

IN-24  
3-7-07

College of Engineering  
Virginia Polytechnic Institute and State University  
Blacksburg, Virginia 24061

October 1998

## **Analysis and Design of Variable Stiffness Composite Cylinders**

Brian F. Tatting<sup>1</sup>  
Zafer Gürdal<sup>2</sup>

Department of Engineering Science and Mechanics

NASA Grant NAG 1-643

Final Technical Report - October 1998

Prepared for:        Structural Mechanics Branch  
                         National Aeronautics and Space Administration  
                         Langley Research Center  
                         Hampton, Virginia 23861-0001

---

<sup>1</sup> Ph. D. Candidate, Department of Engineering Science and Mechanics, Virginia Polytechnic Institute and State University

<sup>2</sup> Professor, Department of Engineering Science and Mechanics & Department of Aerospace and Ocean Engineering, Virginia Polytechnic Institute and State University



# Analysis and Design of Variable Stiffness Composite Cylinders

Brian F. Tatting

(ABSTRACT)

An investigation of the possible performance improvements of thin circular cylindrical shells through the use of the variable stiffness concept is presented. The variable stiffness concept implies that the stiffness parameters change spatially throughout the structure. This situation is achieved mainly through the use of curvilinear fibers within a fiber-reinforced composite laminate, though the possibility of thickness variations and discrete stiffening elements is also allowed. These three mechanisms are incorporated into the constitutive laws for thin shells through the use of Classical Lamination Theory. The existence of stiffness variation within the structure warrants a formulation of the static equilibrium equations from the most basic principles. The governing equations include sufficient detail to correctly model several types of nonlinearity, including the formation of a nonlinear shell boundary layer as well as the Brazier effect due to nonlinear bending of long cylinders. Stress analysis and initial buckling estimates are formulated for a general variable stiffness cylinder. Results and comparisons for several simplifications of these highly complex governing equations are presented so that the ensuing numerical solutions are considered reliable and efficient enough for in-depth optimization studies. Four distinct cases of loading and stiffness variation are chosen to investigate possible areas of improvement that the variable stiffness concept may offer over traditional constant stiffness and/or stiffened structures.

The initial investigation deals with the simplest solution for cylindrical shells in which all quantities are constant around the circumference of the cylinder. This axisymmetric case includes a stiffness variation exclusively in the axial direction, and the only pertinent loading scenarios include constant loads of axial compression, pressure, and torsion. The results for these cases indicate that little improvement over traditional laminates exists through the use of curvilinear fibers, mainly due to the presence of a weak link area within the stiffness variation that limits the ultimate load that the structure can withstand. Rigorous optimization studies reveal that even though slight increases in the critical loads can be produced for designs with an arbitrary variation of the fiber orientation angle, the improvements are not significant when compared to traditional design techniques that utilize ring stiffeners and frames.

The second problem that is studied involves arbitrary loading of a cylinder with a stiffness variation that changes only in the circumferential direction. The end effects of the cylinder are ignored, so that the problem takes the form of an analysis of a cross-section for a short cylinder segment. Various load cases including axial compression, pressure, torsion, bending, and transverse shear forces are investigated. It is found that the most significant improvements in load-carrying capability exist for cases which involve loads that also vary around the circumference of the shell, namely bending and shear forces. The stiffness variation of the optimal designs contribute to the

increased performance in two ways: lowering the stresses in the critical areas through redistribution of the stresses; and providing a relatively stiff region that alters the buckling behavior of the structure. These results lead to an in-depth optimization study involving weight optimization of a fuselage structure subjected to typical design constraints. Comparisons of the curvilinear fiber format to traditional stiffened structures constructed of isotropic and composite materials are included. It is found that standard variable stiffness designs are quite comparable in terms of weight and load-carrying capability yet offer the added advantage of tailorability of distinct regions of the structure that experience drastically different loading conditions.

The last two problems presented in this work involve the nonlinear phenomenon of long tubes under bending. Though this scenario is not as applicable to fuselage structures as the previous problems, the mechanisms that produce the nonlinear effect are ideally suited to be controlled by the variable stiffness concept. This is due to the fact that the dominating influence for long cylinders under bending is the ovalization of the cross-section, which is governed mainly by the stiffness parameters of the cylindrical shell. Possible improvement of the critical buckling moments for these structures is investigated using either a circumferential or axial stiffness variation. For the circumferential case involving infinite length cylinders, it is found that slight improvements can be observed by designing structures that resist the cross-sectional deformation yet do not detract from the buckling resistance at the critical location. The results also indicate that buckling behavior is extremely dependent on cylinder length. This effect is most easily seen in the solution of finite length cylinders under bending that contain an axial stiffness variation. For these structures, the only mechanism that exhibits improved response are those that effectively shorten the length of the cylinder, thus reducing the cross-sectional deformation due to the forced restraint at the ends. It was found that the use of curvilinear fibers was not able to achieve this effect in sufficient degree to resist the deformation, but that ring stiffeners produced the desired response admirably. Thus it is shown that the variable stiffness concept is most effective at improving the bending response of long cylinders through the use of a circumferential stiffness variation.



# Table of Contents

<b>Chapter 1.0 Introduction</b>	1
1.1 Objective of Current Study	1
1.2 Literature Review	2
1.2.1 Variable Stiffness Structures	2
History of Variable Stiffness Analysis and Design	2
Curvilinear Fiber Path Definitions	5
1.2.2 Analysis and Design of Cylindrical Shell Structures	9
Classical Buckling Estimates for Unstiffened Cylindrical Shells	10
Modern Analysis and Design of Shell Structures	20
1.2.3 The Brazier Effect for Long Tubes	22
1.3 Approach of Current Study	26
<b>Chapter 2.0 Governing Equations for Variable Stiffness Cylindrical Shells</b>	28
2.1 Strain-displacement Relations	28
2.1.1 Geometry of the Cylindrical Shell	29
2.1.2 Definition of Strains in Terms of Displacements	32
2.1.3 The Kirchhoff-Love Hypothesis and the Condition of Inextensionality	36
2.2 Constitutive Theory	41
2.2.1 Classical Lamination Theory	41
Stiffness Response	42
Stress Analysis	48
2.2.2 Variable Stiffness Concept	50
Curvilinear Fiber Paths	50
Dropped Plies	53
Discrete Stiffeners	54
Combined Variable Stiffness Concept	56
2.2.3 Classical Membrane and Semi-Membrane Constitutive Theories	57
Classical Membrane Constitutive Theory	57
Semi-membrane Constitutive Theory	58
2.3 Equilibrium Equations	60
2.3.1 Total Potential Energy of a Linearly Elastic System	60
2.3.2 Nonlinear Static Equilibrium Equations	63
2.3.3 Boundary Conditions	65
2.3.4 Stability Equations from the Perturbation of the Equilibrium Solution	67
2.4 Summary of Governing Equations	74

## Table of Contents

<b>Chapter 3.0 Axisymmetric Solution with an Axial Stiffness Variation .....</b>	<b>76</b>
3.1 Static Equilibrium .....	76
3.2 Stability Estimate with Nonlinear Axisymmetric Prebuckling Solution .....	82
3.3 Linear Membrane Approximations .....	84
3.4 Static Response and Stress Analysis .....	87
3.4.1 Curvilinear Fiber Paths.....	88
3.4.2 Ring Stiffeners and Frames .....	94
3.5 Buckling Results .....	95
3.5.1 Effect of Prebuckling Solutions and Nonlinearity .....	96
3.5.2 Curvilinear Fiber Paths.....	102
Axial Compression .....	103
External Pressure .....	105
Torsion.....	107
3.6 Optimization under Axisymmetric Loading .....	111
3.6.1 One Link Variation for Various Cylinder Sizes.....	111
3.6.2 Fiber Path Optimization for Selected Cylinders .....	114
<b>Chapter 4.0 Linear Membrane Solution for a Circumferential Stiffness Variation .....</b>	<b>119</b>
4.1 Static Equilibrium .....	120
4.1.1 Linear Membrane Solution.....	120
4.1.2 Normalization with Respect to Classical Buckling Estimates .....	128
4.2 Stability Estimate using Membrane Prebuckling Solution .....	132
4.3 Material Failure Results for Curvilinear Fiber Paths .....	134
4.3.1 Axisymmetric Loading.....	135
4.3.2 Non-axisymmetric Loading.....	137
4.4 Buckling Results .....	139
4.4.1 General Loading of Constant Stiffness Structures .....	139
4.4.2 Curvilinear Fiber Paths using One Link Variation.....	145
4.4.3 Stiffened Structures .....	151
4.5 Design of Fuselage Cross-section for Minimum Weight.....	154
4.5.1 Design Criteria for General Aircraft Fuselage .....	155
4.5.2 Loading Conditions for Fuselage Cross-section .....	157
4.5.3 Design Strategy for Optimization of Cross-Section.....	160
4.6 Design Study Results .....	163
4.6.1 Traditional Stiffened Structures (Isotropic) .....	164
4.6.2 Traditional Stiffened Structures (Composite) .....	169
4.6.3 Variable Stiffness Skin Designs .....	173

## *Table of Contents*

<b>Chapter 5.0 Bending of Infinite Length Cylinders including the Brazier Effect</b>	177
5.1 Nonlinear Static Solution	178
5.2 Stability Estimate with Nonlinear Prebuckling including the Brazier Effect	183
5.3 Approximate Analyses for Infinite Length Cylinders	186
5.3.1 Linearized Brazier Solution for Constant Stiffness Structures	186
5.3.2 Approximate Stability Analysis Based on Maximum Compressive Stress	187
5.4 Constant Stiffness Results	189
5.4.1 Accuracy of Approximate Analyses	189
5.4.2 Influence of Laminate Stacking Sequence	191
5.4.3 Stacking Sequence Optimization to Maximize Critical Load	194
5.4.4 Influence of Pressure	196
5.5 Variable Stiffness Concept Results	197
<b>Chapter 6.0 Bending of Finite Length Cylinders including the Brazier Effect</b>	200
6.1 Static Equilibrium	202
6.2 Approximate Stability Analysis	207
6.3 Numerical Results and Comparisons	208
6.3.1 General Solution for $\lambda$ and $\mu$	209
6.3.2 Influence of Shear Length Parameter	213
6.3.3 Influence of Boundary Conditions	215
6.3.4 Comparison to Published Results	217
6.4 Variable Stiffness Solutions	219
6.4.1 Curvilinear Fiber Formats	220
6.4.2 Ring Stiffened Structures	222
<b>Chapter 7.0 Concluding Remarks</b>	224
7.1 Analysis of Variable Stiffness Shells	224
7.2 Axial Stiffness Variation for a Cylindrical Shell	225
7.3 Circumferential Stiffness Variation for a Cylindrical Shell	227
7.4 The Brazier Effect for Long Tubes	228
<b>References</b>	230
<b>Appendix A. Numerical Techniques</b>	237
A.1 Finite Difference Techniques for Linear ODE's	237
A.2 Newton's Method for Nonlinear Problems	242
A.3 The Classical Rayleigh-Ritz Method for the Eigenvalue Problem	244
A.4 The Power Method for the Eigenvalue Problem	249
A.5 Finite Difference Techniques versus the Rayleigh-Ritz Method	252

## *Table of Contents*

A.6 Optimization Techniques .....	255
A.6.1 Gradient-Based Methods .....	256
A.6.2 Genetic Algorithms .....	258
<b>Appendix B. Stability Equations for Finite Difference Technique .....</b>	<b>260</b>
B.1 Nonlinear Axisymmetric Prebuckling for an Axial Stiffness Variation .....	260
B.2 Linear Membrane Prebuckling for a Circumferential Stiffness Variation .....	262
B.3 Nonlinear Semi-Membrane Prebuckling for an Infinite Length Cylinder .....	265
<b>Appendix C. Material Data .....</b>	<b>267</b>

# Nomenclature

Standard mathematical conventions are followed. Subscripts using latin letters ( $ij$ ) represent numbers, while greek letters ( $\alpha\beta$ ) stand for coordinate ( $x, \theta, z$ ) designations. Derivatives for each surface direction are expressed through either nondimensional operators ( $d_x, d_\theta$ ) or primes and dots. Normalization is usually denoted by an overbar or a change to lowercase, while a carat ( $\wedge$ ) signifies an average (constant) quantity of the skin. Overbars can also represent quantities applied at the ends of the cylinder, as noted below.

## Shell Geometry

$H$	total thickness of shell skin
$L$	length of cylinder
$R$	radius of cylinder
$X, Y, Z$	global Cartesian coordinates
$\xi, \psi, \zeta$	cross-sectional Cartesian coordinates (nondimensional)
$x, y, z$	cross-sectional cylindrical coordinates
$\theta$	angular coordinate of cross-section ( $\theta = y/R$ )
$\theta_{ref}$	reference angle to locate material centroid of cross-section
$u_x, u_y, u_z$	global Cartesian displacements
$v, \eta, \phi$	cross-sectional Cartesian displacements (nondimensional)
$u, v, w$	cross-sectional displacements in cylindrical coordinates
$A_x, A_\theta, A_{x\theta}$	Lamé parameters of surface
$R_x, R_\theta, R_{x\theta}$	Gaussian radii of curvature of surface
$a_z(x), a_y(x)$	deflection of beam axis (for each transverse direction)
$\Omega_y(x), \Omega_z(x)$	angle of rotation of cross-sectional plane about each axis
$\kappa_y(x), \kappa_z(x)$	curvature of beam axis for each direction
$\overline{\Omega}_y, \overline{\Omega}_z$	end rotation of beam about each axis

## Strain-Displacement Relations

$dS$	increment of arc length
$u^o, v^o, w^o$	middle surface cylindrical displacements
$\omega_x^o, \omega_\theta^o$	rotations of normal, measured at the middle surface
$\epsilon_x, \epsilon_\theta, \gamma_{x\theta}, \gamma_{xz}, \gamma_{\theta z}, \epsilon_z$	total nonlinear strains
$\epsilon_x^o, \epsilon_\theta^o, \gamma_{x\theta}^o, \gamma_{xz}^o, \gamma_{\theta z}^o, \epsilon_z^o$	nonlinear strains measured at middle surface

## Nomenclature

$\kappa_x^o, \kappa_\theta^o, \kappa_{x\theta}^o$	changes of curvature at middle surface
$e_{\alpha\beta}, k_{\alpha\beta}$	linear strains and changes of curvature
$\omega$	inextensional rotation of cross-sectional shell element
$\rho$	radius of curvature for deformed cross-sectional shell element

### Constitutive Theory

$\sigma_1, \sigma_2, \tau_{12}, \tau_{13}, \tau_{23}, \sigma_3$	nonlinear stresses in principal material directions
$\epsilon_1, \epsilon_2, \gamma_{12}, \gamma_{13}, \gamma_{23}, \epsilon_3$	nonlinear strains in principal material directions
$Q_{ij}$	reduced stiffnesses of orthotropic lamina
$E_1, E_2, \nu_{12}, \nu_{21}, G_{12}$	stiffness properties of orthotropic material
$\sigma_x, \sigma_\theta, \tau_{x\theta}$	nonlinear in-plane stresses in surface coordinates
$\varphi$	orientation angle of orthotropic lamina
$\varphi_k, z_k$	ply angle and distance to middle surface for $k^{th}$ layer
$\bar{Q}_{ij}$	transformed reduced stiffnesses of orthotropic lamina
$U_i$	invariant material properties of orthotropic lamina
$N_x, N_\theta, N_{x\theta}$	middle surface force resultants
$M_x, M_\theta, M_{x\theta}$	middle surface moment resultants
$Q_x, Q_\theta$	middle surface shear force resultants
$A_{ij}, B_{ij}, D_{ij}$	extensional, coupling, and bending stiffness terms
$V_{iA}$	integrations of orientation angle through the laminate thickness
$E_x, E_\theta, \nu_{x\theta}, \nu_{\theta x}, G_{x\theta}$	effective stiffness measures for laminate
$X_p, X_c, Y_p, Y_c, S$	strength properties of orthotropic material
$MF$	multiplication factor for material failure criteria
$r, s$	surface coordinates for fiber orientation angle variation
$\Phi$	angle of rotation between $rs$ and $xy$ coordinates
$T_i, \bar{l}_i$	orientation angle and location of linked line segment approach
$N_{seg}$	number of segments in linked line segment approach
$\rho_{min}$	minimum radius of curvature under manufacturing constraint
$t_p, \varphi_p$	thickness and orientation angle of added ply
$w_s, A_s, I_s, J_s, z_s, t_s$	geometric properties of stiffener cross-section
$E_s, G_s$	elastic properties of stiffener
$F_s, M_s, T_s, \epsilon_s, \kappa_s, \phi_s$	loads and deformation quantities of stiffeners

### Equilibrium Equations

$U$	internal energy of elastic shell
$V$	total potential energy of system (with variations $V_1, V_2$ )
$W$	work done on shell by outside forces
$A_1$	area of deformed cross-section
$p$	internal pressure of cylindrical vessel
$V_y(x), V_z(x)$	beam shear forces in horizontal and vertical directions
$M_y(x), M_z(x)$	beam moments about horizontal and vertical axes
$\bar{F}, \bar{T}$	axial compressive force and torque applied at ends of cylinder
$\bar{U}, \bar{V}$	axial displacement and rotation of cross-section at ends
$\bar{V}_y, \bar{V}_z, \bar{M}_y, \bar{M}_z$	beam loads applied at ends of cylinder
$[K], [M]$	stiffness and geometric stiffness matrices for eigensystem
$\Lambda$	eigenvalue representing live load level
$\hat{u}_1, \hat{\epsilon}_1, \hat{\kappa}_1$	vector of perturbed displacements and strain quantities
S1-S4, C1-C4	boundary conditions for perturbed displacements

### Classical Buckling Estimates and Eigenvalue Calculations

$m, n$	axial half wave and circumferential full wave numbers
$\beta$	axial frequency (nondimensional)
$\beta_{min}$	minimum axial frequency for finite length cylinders
$\hat{N}_x^{cl}, \hat{N}_\theta^{cl}, \hat{N}_{x\theta}^{cl}$	classical buckling values for constant stiffness cylindrical shell
$\hat{\beta}_x, \hat{\beta}_{x\theta}$	classical buckling frequencies for axial and shear buckling
$\hat{N}_\theta^\infty, \hat{N}_{x\theta}^\infty$	classical buckling values for infinite length cylindrical shell
$U_I, V_I, W_I$	mode <i>I-IV</i> displacements for assumed buckling deformation
$[K_s], [K_a], [C]$	sub-matrices of stiffness matrix for eigenvalue calculation
$[N_s], [N_a], [S]$	symmetric sub-matrices of geometric stiffness matrix
$[V_s], [V_a], [M_s], [M_a]$	anti-symmetric sub-matrices of geometric stiffness matrix

### Nondimensional Parameters

$l$	axial wavelength parameter
$Z_b$	Batdorf parameter
$\chi$	collapse parameter
$\lambda$	tube length parameter
$\mu$	shear length parameter

### Nondimensional Load Factors

$\bar{u}, \bar{f}$	axial end displacement and compressive force
$\bar{v}, \bar{t}$	cross-sectional rotation and torsional load
$\bar{p}$	internal pressure
$\bar{m}_y, \bar{m}_z$	beam bending moments about each axis
$\bar{v}_y, \bar{v}_z$	transverse beam shear forces in each direction
$\bar{\alpha}$	curvature (infinite length) or end rotation (finite length)
$\phi_{max}$	measure of ovalization of cross-section
$\bar{\alpha}^{-lim}, \bar{m}_y^{-lim}, \phi_{max}^{lim}$	values at limit point of nonlinear load curve
$\bar{\alpha}^{-\infty}, \bar{m}_y^{-\infty}, \phi_{max}^{\infty}$	buckling values for infinite length shell

### Cross-sectional Parameters

$\hat{A}_{ij}, \hat{D}_{ij}$	average stiffness quantities of shell skin
$\theta_{ref}$	reference angle to locate material centroid of cross-section
$\theta_{sc}$	angle to locate shear center of cross-section
$u_w, v_w$	warping displacement functions
$(EA), (EI_y), (EI_z), (GJ)$	global stiffness parameters associated with cylindrical beam
$\bar{I}_y, \bar{I}_z$	normalized bending stiffnesses for cylindrical beam

### Variables for Axial Stiffness Variation Solutions

$u_0, v_0, w_0$	displacements for axisymmetric deformation
$\bar{u}_0, \bar{v}_0, \bar{w}_0$	normalized displacements for axisymmetric deformation
$u_2, v_2, w_2$	Brazier-type displacements for $\cos 2\theta$ deformation
$\bar{u}_2, \bar{v}_2, \bar{w}_2$	normalized Brazier-type displacements for $\cos 2\theta$ deformation
$\alpha$	nondimensional curvature of beam axis

### Numerical Solution Techniques

$\Delta$	distance between finite difference points
$f_i$	value of function $f(x)$ at $i$ th finite difference point
$N$	number of variables in numerical technique
$\vec{X}, \vec{B}$	vectors denoting unknown and forcing term for linear system
$C_{n\theta}, S_{n\theta}, C_x, S_x$	shorthand for trigonometric functions
$X_{IA}^i, k_{IA, JB}^{ij}$	notation for vector and matrices in Rayleigh-Ritz solution
$a_{ij}^k$	Fourier series coefficient for stiffness terms



## *Nomenclature*

$\mathbf{d}_p$	iterated eigenvector for power method
$[A], \mathbf{x}_k$	matrix and $k$ th eigenvector for typical eigensystem
$\mu_s, \lambda_s$	shift and calculated eigenvalue for power method

### **Fuselage Design Study Variables**

$g$	gravitational constant representing unit of acceleration
$W$	weight of aircraft
$n$	load factor compared to weight of aircraft
$M_{0.25}, L_{0.25}$	moment and lift of wing, measured along chord length
$P_t$	vertical force at tail wing
$SF_i$	safety factor for $i$ th load case
$b, h, r, t_s, t_{ts}$	dimensions of inverted hat stiffener and tear strap
$H_{eff}$	effective width of shell computed by smearing stiffeners
$N_{pairs}$	number of pairs of equally spaced longitudinal stiffeners
$\theta_c, \theta_k$	angles to locate transition regions for crown and keel

# List of Figures

Figure 1.1: Baseline Path for $T_0 = 0^\circ$ , $T_1 = 30^\circ$ , $\bar{l}_1 = 1$ .....	6
Figure 1.2: Shifted and Parallel Fiber Methods for 90<30/75> Ply .....	7
Figure 1.3: Example of Buckling Mode under Axial Compression .....	11
Figure 1.4: Contour Plot of Axial Buckling Values for Isotropic Material .....	13
Figure 1.5: Contour Plot of Axial Buckling Values for Orthotropic Material .....	14
Figure 1.6: Contour Plot of Circumferential Buckling Values for Isotropic Material .....	16
Figure 1.7: Example of Buckling Mode under Torsion .....	17
Figure 1.8: Contour Plot of Shear Buckling Values for Isotropic Material .....	19
Figure 1.9: Mechanism of Brazier Effect to Produce Ovalization .....	23
Figure 1.10: Moment and Ovalization vs. Curvature for Long Isotropic Cylinder .....	24
Figure 2.1: Geometry of Undeformed Shell .....	29
Figure 2.2: Geometry of Deformed Shell with Axial Curvature .....	31
Figure 2.3: Derivation of Inextensional Displacements .....	39
Figure 2.4: Orientation of Principal Directions of Orthotropic Material .....	43
Figure 2.5: Stress Measures of Shell Element .....	45
Figure 2.6: Linked Line Segment Approach of Fiber Orientation Angle .....	52
Figure 2.7: Geometry of Dropped Ply Construction .....	53
Figure 2.8: Physical Properties of Stiffeners .....	54
Figure 2.9: Boundary Conditions for Cylindrical Shell .....	66
Figure 3.1: Geometry of Axisymmetric Cylinder .....	78
Figure 3.2: Displacement Profile of Constant Stiffness Cylinder under Axial Compression .....	87
Figure 3.3: Displacement Profiles of Axisymmetric Variable Stiffness Cylinders under Axial Compression .....	89
Figure 3.4: Failure Loads for Cylinders under Axial Compression .....	90
Figure 3.5: Failure Loads for Cylinders under Internal Pressure .....	91
Figure 3.6: Failure Loads for Cylinders under Torsion .....	91
Figure 3.7: Failure vs. Stiffness for Axial Compression .....	93

## List of Figures

Figure 3.8: Failure vs. Stiffness for Torsion .....	94
Figure 3.9: Displacement Profile of Ring Stiffened Cylinder .....	95
Figure 3.10: Nonlinear Displacement Profiles of Constant Stiffness Cylinder under Axial Compression .....	97
Figure 3.11: Nonlinear Displacement Profiles of $[0\pm<15/75>]_{6s}$ Variable Stiffness Cylinder under Axial Compression .....	100
Figure 3.12: Load versus Displacement for Structures under Axial Compression.....	101
Figure 3.13: Mode Shapes of Cylinders under Axial Compression ( $Z_b \approx 800$ ).....	103
Figure 3.14: Contour Plot of Axial Compression Load for One Link Variation ( $Z_b \approx 800$ ) .....	104
Figure 3.15: Mode Shapes of Ring Stiffened Cylinder under External Pressure .....	105
Figure 3.16: Contour Plot of External Pressure Load for One Link Variation ( $Z_b \approx 800$ ) .....	106
Figure 3.17: Comparison of Classical Mode Shape under Torsion .....	108
Figure 3.18: Relative Error of Classical Estimate for Torsion .....	109
Figure 3.19: Contour Plot of Torsional Load for One Link Variation ( $Z_b \approx 800$ ).....	110
Figure 3.20: Mode Shapes of Optimal Designs under Torsion ( $Z_b \approx 800$ ).....	110
Figure 3.21: Mode Shapes of Optimal Designs for External Pressure ( $Z_b \approx 300$ ).....	118
Figure 4.1: Geometry and Loading for Short Cylinder Segment.....	121
Figure 4.2: Failure Loads for Cylinders under Axial Compression.....	135
Figure 4.3: Failure vs. Stiffness for Axial Compression .....	136
Figure 4.4: Failure Loads for Cylinders under Horizontal Bending Moment .....	137
Figure 4.5: Failure vs. Bending Stiffness for Horizontal Bending Moment.....	138
Figure 4.6: Failure Loads for Cylinders under a Vertical Shear Force.....	139
Figure 4.7: Critical Eigenvalue of Major Load Cases versus Axial Frequency $\beta$ .....	140
Figure 4.8: Buckled Mode Shapes for Torsion and Vertical Shear Force, $\beta = \beta_{min}$ .....	145
Figure 4.9: Results for External Pressure using One Link Circumferential Variation .....	146
Figure 4.10: Results for Axial Compression using One Link Circumferential Variation .....	147
Figure 4.11: Results for Torsion using One Link Circumferential Variation.....	148
Figure 4.12: Results for Pure Bending using One Link Circumferential Variation .....	149
Figure 4.13: Results for Vertical Shear Force using One Link Circumferential Variation .....	150

## *List of Figures*

Figure 4.14: Axial Stress Resultant Distribution for Stiffened Fuselage under Bending.....	151
Figure 4.15: Buckled Mode Shape for Stiffened Fuselage under Bending .....	152
Figure 4.16: Shear Stress Resultant Distribution for Stiffened Fuselage under Shear Force .....	153
Figure 4.17: Buckled Mode Shape for Stiffened Structure under Shear Force .....	154
Figure 4.18: Design Criteria for Flight Envelope .....	155
Figure 4.19: Loads and Shear/Bending Moment Diagrams for Fuselage Structure .....	158
Figure 4.20: Geometry of Cross-section and Stiffener Arrangement for Short Segment.....	160
Figure 4.21: Comparison of Weight Optimization Results for All Cases .....	163
Figure 4.22: Optimization Results for Case I1 .....	165
Figure 4.23: Optimization Results for Case I2, $0 \leq N_{\text{pairs}} \leq 26$ .....	166
Figure 4.24: Optimization Results for Case I2, $10 \leq N_{\text{pairs}} \leq 36$ .....	166
Figure 4.25: Optimization Results and Deformed Shape for Case I3.....	167
Figure 4.26: Geometry of Crown/Side/Keel Arrangement.....	168
Figure 4.27: Optimization Results for Case C1 .....	170
Figure 4.28: Optimization Results and Deformed Shape for Case C3 .....	171
Figure 4.29: Optimization Results and Deformed Shape for Case C5 .....	172
Figure 4.30: Description of Curvilinear Fiber Definition.....	174
Figure 4.31: Optimization Results for Variable Stiffness Crown/Side/Keel Arrangement.....	176
Figure 5.1: Geometry of Cross-section for Infinite Length Cylinder .....	178
Figure 5.2: Comparisons between Reissner and Brazier Solutions .....	190
Figure 5.3: Maximum Collapse Parameter vs. Material Orthotropy .....	193
Figure 5.4: Moment vs. Curvature for Long Orthotropic Cylinders.....	193
Figure 5.5: Buckling Curvature and Limit Curvature vs. Collapse Parameter .....	194
Figure 5.6: Moment vs. Curvature for Pressurized Isotropic Cylinders .....	196
Figure 5.7: Buckling Curvature and Limit Curvature vs. Pressure.....	197
Figure 5.8: Optimal Variable Stiffness Design for Long Cylinder under Bending .....	198
Figure 6.1: Geometry of Finite Length Cylinder under Bending .....	202
Figure 6.2: Displacement Profiles for Finite Length Cylinder under Bending.....	209

## *List of Figures*

Figure 6.3: Moment vs. End Rotation for $\lambda = 1$ , Fixed Ends .....	210
Figure 6.4: Moment vs. End Rotation for $\mu = 1$ , Fixed Ends .....	211
Figure 6.5: Critical Curvature vs. $\lambda$ and $\mu$ , Fixed Ends .....	212
Figure 6.6: Critical Curvature vs. $L/R$ and $R/H$ for an Isotropic Cylinder, Fixed Ends .....	213
Figure 6.7: Critical Curvature vs. $\lambda$ for General Material, Fixed Ends .....	214
Figure 6.8: Critical Curvature vs. $\lambda$ for Isotropic Material $\nu = 0.3$ , Fixed Ends .....	214
Figure 6.9: Critical Curvature vs. $\lambda$ for Orthotropic Material AS3501, Fixed Ends .....	215
Figure 6.10: Comparison of Critical Curvature for Fixed and Free End Condition .....	216
Figure 6.11: Moment-End Rotation Curves for Fixed and Free Ends, Isotropic Material .....	216
Figure 6.12: Critical Curvature and Moment vs. $\lambda$ for Fixed and Free Ends .....	217
Figure 6.13: Comparison to Stephens et al. for Moment vs. Radial Displacement .....	218
Figure 6.14: Comparison of Libai & Bert to Present Research .....	219
Figure 6.15: Variable Stiffness Concept Example for Finite Length Cylinder under Bending .....	221
Figure 6.16: Example of Ring Stiffened Cylinder under Bending .....	222
Figure 6.17: Buckling Moments versus Number of Ring Stiffeners for Finite Length Cylinder under Bending .....	223
Figure A.1: Finite Difference Representation of Region of Interest .....	239
Figure A.2: Matrix Structure for Finite Difference Technique .....	241
Figure A.3: Accuracy and Efficiency versus Size Parameter for Numerical Techniques .....	253
Figure A.4: Illustration of Optimization Schemes .....	257

# List of Tables

Table 1.1: Organization of Analysis Scenarios.....	27
Table 3.1: Comparison of Prebuckling Solutions on Axial Compressive Buckling Load .....	98
Table 3.2: Results of Optimization of Linear Variable Stiffness Cylinders .....	112
Table 3.3: Results of Shape Optimization for $Z_b \approx 300$ Variable Stiffness Cylinder .....	116
Table 3.4: Results of Shape Optimization for $Z_b \approx 5000$ Variable Stiffness Cylinder .....	117
Table 4.1: Load Cases for Fuselage Structure .....	159
Table 4.2: Details of Components of Cross-section .....	161
Table 4.3: Description of Optimization Cases for Traditional Stiffened Structures.....	162
Table 4.4: Optimization Results for Composite Skin with Curvilinear Fibers.....	175
Table 5.1: Results of Optimization for Maximum Bending Load (Constant Stiffness) .....	195
Table 6.1: Results of Optimization for Maximum Bending Load (Constant Stiffness) .....	220
Table A.1: Summary of Numerical Technique Comparison . .....	255
Table C.1: Isotropic Material Properties.....	267
Table C.2: Orthotropic Material Properties .....	267

# Chapter 1.0 Introduction

The intended objective of this investigation is set forth in this chapter, and then a review of relevant published work is presented to provide further details of the subject matter. The discussion is then used to define the detailed approach of the present study.

## 1.1 Objective of Current Study

The goal of this investigation is to explore the effectiveness of the variable stiffness concept as applied to cylindrical shell structures, such as an aircraft fuselage. The term “variable stiffness” implies that the stiffness parameters vary spatially throughout the structure. The principal mechanism to produce this stiffness variation will be through the use of curvilinear fiber paths in fiber-reinforced composite laminates, though thickness variation by means of added/dropped plies and the addition of discrete stiffeners are also implemented. The use of these curvilinear fiber paths in a design environment promises great reward, for the novel laminate construction format offers more diverse tailorability opportunities than simply choosing the best stacking sequence for the given loading conditions. A variable stiffness laminate can change its stiffness and strength properties spatially to adapt to the existing stress field and provide the greatest resistance to the local conditions, thereby increasing the load-carrying capability of the structure when compared to constant stiffness laminates. To investigate this fully, some basic problems involving cylindrical shells are studied. However, the presence of the varying stiffness parameters dramatically increases the complexity of the analysis, therefore another goal of this research is to develop solutions that accurately model the physics of the problem while also being efficient numerically so that in-depth design and optimization studies can be conducted. During the development of some of these preliminary analysis tools for cylindrical shells, additional scenarios for which the variable stiffness concept promised improvement were realized, so that the scope of the investigation began to grow. However, the main goal is still based on the effectiveness of curvilinear fiber paths when compared to traditional laminate construction, therefore the analysis techniques will focus on a limited number of cylinder geometries and loading cases that are intended to encompass the most fundamental scenarios for a practical cylindrical structure. In particular, these representative cases include a cylinder with an axial stiffness variation that undergoes axisymmetric loads only, a short cylinder segment with a circumferential stiffness variation that is subjected to arbitrary

beam loads, and long cylinders undergoing predominantly bending loads with a possible stiffness variation in either the axial or circumferential direction. These last two cases both involve some estimation of the Brazier effect, which is a nonlinear phenomena associated with bending of long tubes that can dramatically decrease the failure load of the cylinder. The impact of the Brazier effect on the instability loads of longer cylinders is exceedingly significant yet often misconstrued, therefore the governing shell equations are formulated from first principles so as to correctly model the response due to this highly nonlinear phenomena. Application of the Brazier analysis to realistic cylindrical structures will also be considered.

## **1.2 Literature Review**

This section familiarizes the reader with the relevant topics alluded to in the statement of the objective, namely the variable stiffness concept, modern analysis of cylindrical shell structures, and the Brazier effect. The ensuing information will be used to define the approach of the current study in greater detail, and to provide an idea of the motivation behind this research.

### **1.2.1 Variable Stiffness Structures**

It has long been known that the distribution of the stresses within a structure has a dramatic effect on the structure's load carrying efficiency. As a simple example, a traditional I-beam is designed so that the flanges carry the bulk of the bending loads, while little material is wasted within the web. This results in a structure that carries beam bending loads efficiently while maintaining low weight and material costs. For more complicated structures, such as thin plates and shells that are subject to a greater variety of loading conditions, the possibility of an analogous design surely exists, though the optimal distribution of the stiffness may not be so apparent. Furthermore, the stress analysis for these structures is generally more complex than for a beam, so that determining the best design is not as straightforward. Thus this subsection reviews some earlier work aimed at analyzing structures that contain stiffness variations produced by a variety of methods. The possibility of curvilinear fibers within composite laminates is discussed in greater detail, since it is the primary mechanism that is used in this study.

### **History of Variable Stiffness Analysis and Design**

The earliest use of the variable stiffness concept for shell structures could probably be construed as the analysis of variable thickness plates and shells made from isotropic materials. For instance, Timoshenko & Woinowsky-Krieger's text<sup>1</sup> concerning the theory of plates and shells contains references to variable thickness solutions from as early as 1918. The connection of this work to the variable stiffness concept lies in the relation of the shell thickness to the flexural rigidity (a typical stiffness parameter). For the most part, the solutions were quite simple and assumed



basic variations of the thickness so that direct integration could be performed. Since the materials in use at the time were isotropic, not much investigation into the variation of the material stiffness properties was conducted. However, the work of Mishiku & Teodosiu<sup>2</sup> considered the possibility of inhomogeneity of isotropic materials that could result from damage, imperfections, and temperature changes, and a solution was completed within the theory of elasticity using complex variables. A numerical example of a planar disk under radial tension was included, with the nonhomogeneity being introduced through an idealized variation of the elastic parameters, and it was shown that the stiffness variation produced significant quantitative and qualitative changes in the resulting stress states.

The emergence of composite materials in structural applications during the 1960's lead to new possibilities of stiffness variations within a structure. Traditional composites are usually constructed of a material with high strength and stiffness properties embedded in a resin matrix. The configuration and volume ratios of the two constituents determine the stiffness and strength behavior of the resulting material. For instance, a typical composite material used in the aerospace industry is graphite-epoxy, which contains graphite fibers laid parallel to one another and held in place by an epoxy matrix material. This produces an orthotropic material (one with different stiffness and strength characteristics in orthogonal directions) with higher strength and stiffness properties per unit weight than corresponding isotropic materials (such as aluminum). The most practical application of these composite materials was found to be in the form of laminates, in which a structure is constructed of many layers (laminae) of these directional materials and defined by the ordered layup, or stacking sequence, of its individual plies. Using these composite materials, the potential for stiffness variation increased tremendously, for besides the possibilities of thickness changes due to changing the number of plies throughout the structure, there also existed manufacturing variability with respect to material ratio (volume fractions), fiber spacing and fiber orientation, not to mention unintentional variations of the material properties by way of voids and imperfections within the composite material.

With regards to the most basic stiffness variation for composite materials, the analyses incorporating thickness changes of isotropic shells could be directly applied to their orthotropic counterparts that could be manufactured by adding or dropping plies throughout the structure. For instance, Ashton<sup>3</sup> was one of the first to present a general anisotropic plate analysis technique that allowed for the spatial variation of bending stiffness terms, and as an example suggested dropping plies to produce a tapered plate with variable stiffness coefficients. The analysis relied on approximating the stiffness variation through a series expansion in the spatial directions, where the coefficients for the expansion were determined through integration. Analyses of this type did not

address the fact that the edge effects near the termination of the ply greatly affected the local three-dimensional stress state and often led to decreased failure loads for the structure. However, Dinardo & Lagace<sup>4</sup> showed that where buckling of the structure was concerned, these local stress concerns were not as significant as the global effects due to the large change in stiffness. They substantiated their claims by comparing the buckling loads of laminated composite plates with dropped plies to ones that contained regions with different stacking sequences without thickness changes. Though the relative change in stiffness when using dropped plies was larger and also easier to fabricate (consisting of merely adding plies on the outside of an existing laminate), the buckling and postbuckling response for both cases was analogous, therefore the presence of the ply termination did not provide a significant change in behavior. This result is fortunate, for including the local stress effects due to added/dropped plies in the buckling analysis would lead to extremely complicated and inefficient solutions. Therefore, within this investigation it will be assumed that the effects of the ply termination can be ignored.

Additional methods to achieve spatial variations of the stiffness parameters using composite materials were also investigated, and subsequently new analysis techniques were formulated. Pao<sup>5</sup> found a solution for the momentless design of cylindrical pressure vessels by assuming that the Poissons ratio of the material could be tailored by altering the volume fraction of a composite laminate. An analysis technique by Leissa & Vagins<sup>6</sup> proposed using variable stiffness concepts in terms of a variation of the material properties to produce a homogeneous stress field for certain shell structures constructed of fiber-reinforced composite materials, though they did not propose a suitable method to manufacture these materials. Muser & Hoff<sup>7</sup> provided a closed-form solution for the stress concentration around a hole for a infinite plate s bjected to uniaxial tension that contained a radial variation of the compliances (which are the inverse of the stiffness parameters). Their example revealed that a gradual variation of the compliances defined by designating the laminate stacking sequence at two different radial locations produced a reduction of the stress concentrations near the hole and significantly altered the ensuing stress field. Martin & Leissa<sup>8</sup> allowed the fiber spacing (and thus the fiber volume fraction) of the laminae to vary and analyzed composite sheets using the theory of elasticity and the Ritz method, while Kuo et al.<sup>9</sup> were the first to investigate the change in elastic moduli of composites with curvilinear fibers. Hyer & Charette<sup>10</sup> developed this curvilinear fiber concept even further by proposing that improved designs could be developed by aligning the fibers with the principal directions of the stress field. They provided a finite element solution for a plate with a central hole, and found that the material failure loads did show marked improvement over traditional straight fiber formats, but the variable stiffness designs showed no advantage when buckling was considered. A follow-up work by Hyer

& Lee<sup>11</sup> aimed at improving these buckling loads by using sensitivity analysis and a gradient search method to determine the optimal fiber orientation angles in different regions of the plate. Their results revealed substantial improvements in the buckling load, mostly through the mechanism of transferring the major stresses from the interior region to the edges of the plate.

### Curvilinear Fiber Path Definitions

Further investigation into the potential of curved fiber laminates was required, since it seemed obvious that the use of curvilinear fibers would surely result in an efficient and desirable method to improve the performance of shells. The main advantage of this concept is that the stiffness and strength parameters, which both depend on the fiber orientation angle, can be altered spatially to tailor the structure to the expected loads and stresses. Furthermore, it may be possible to improve the performance of the structure without an increase in weight over traditional laminates, since the volume and weight of a variable stiffness ply should be the same as a constant stiffness layer. However, two questions regarding this variable stiffness concept remain: can we analyze such structures accurately and efficiently?; and can these variable stiffness laminates be manufactured?

As an attempt to answer the first of these questions, the development of an analysis tool for composite panels and cylindrical shells with a spatially varying fiber orientation angle was initiated by Gürdal<sup>12,13,14</sup> of Virginia Tech in the early 1990's, before the manufacturing techniques to produce such structures had even been firmly established. The original idea was that the response of fiber-reinforced laminates could be significantly altered by allowing the fiber orientation angle, which defines the stiffness and strength properties of the laminate, to vary spatially throughout the structure. Such a variation of the fiber orientation angle automatically produces curvilinear fiber paths. The numerical technique to calculate the stress distribution and buckling loads for these variable stiffness plates was subsequently refined during the completion of the M.S. degree by Olmedo<sup>15,16</sup>. Further work by Waldhart<sup>17</sup> utilized the analysis tool to study the possible improvements in performance of the curvilinear fibers over traditional composite laminates. During this investigation, attention was also focused on the producibility of the prototype laminate designs, which generated additional restrictions regarding the variation of the fiber orientation angle.

For instance, the first step of the variable stiffness concept was to conceive of a way to describe a realistic curvilinear fiber path in terms of general variables. The most basic function for the stipulation of the variation of the fiber orientation was used, that being a linear variation in one direction only. Thus the fiber orientation angle for a baseline path was defined as

$$\varphi(r) = (T_1 - T_0) \frac{r}{l_1} + T_0 \quad 0 \leq r \leq l_1 \quad (1.1)$$

Here  $\varphi$  is the fiber orientation angle,  $r$  is the distance along the direction of stiffness variation,  $T_0$  is the value of  $\varphi$  at  $r = 0$ , and  $T_1$  is the prescribed value at some predefined distance  $\bar{l}_1$ . This definition is also assumed to be symmetric about the origin and periodic with a wavelength of  $2\bar{l}_1$  (resembling a sawtooth function) so that the full range of the  $r$ -axis can be encompassed. As an example, shown in Figure 1.1 is the path for a curvilinear fiber with  $T_0 = 0^\circ$  and  $T_1 = 30^\circ$  at  $\bar{l}_1 = 1$ .

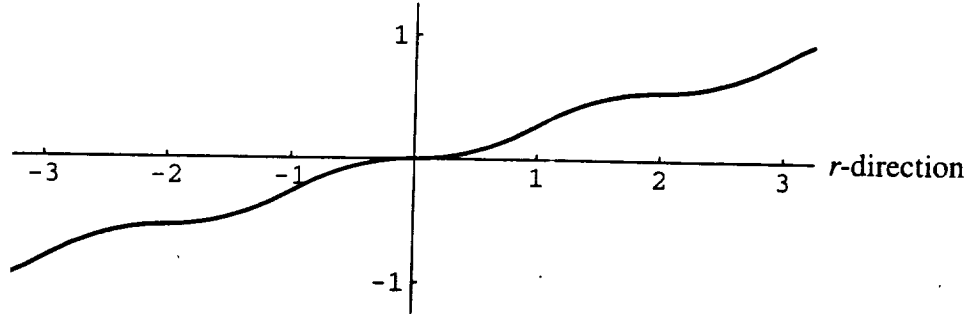


**Figure 1.1: Baseline Path for  $T_0 = 0^\circ$ ,  $T_1 = 30^\circ$ ,  $\bar{l}_1 = 1$**

Note that the linear variation of the fiber orientation angle given in Eq. (1.1) actually produces a curvilinear fiber path, and that the path is smooth and continuous even though it is defined by the non-smooth sawtooth function. It should also be mentioned that the  $r$ -axis can be aligned at any angle  $\Phi$  with respect to the  $xy$ -axes of the plate, so that the preceding definition of the baseline path actually allows a wide range of possible stiffness variations. The notation for the representation of a single layer in the stacking sequence of a variable stiffness laminate using this linear variation is defined as  $\Phi \langle T_0/T_1 \rangle$ .

The production of a complete variable stiffness ply was assumed to be accomplished by the laying down of additional finite width strips of material that referenced the baseline path. It was found that the definition of such a ply could be divided into two strategies, termed the “shifted fiber” and “parallel fiber” methods. Both rely on an initial specification of a baseline path for the variable stiffness ply as given in Eq. (1.1). The shifted method assumes that each additional path has the same shape as the baseline case, but that it is shifted in a direction perpendicular to the stiffness variation so that the whole ply area is covered. An example of a shifted method ply is shown in Figure 1.2a, where the stiffness variation is in the vertical direction and the shift is applied in the horizontal direction. The thick solid lines represent the centerline of each individual path, while the thinner dashed lines denote the edges of the finite width strip of material. Note that due to the variation of the fiber orientation angle, considerable overlap occurs at the edges of the plates. The analysis tool ignored this overlap and assumed a constant thickness for the entire ply. The presence of this overlap condition is quite significant, and its ramifications will be discussed

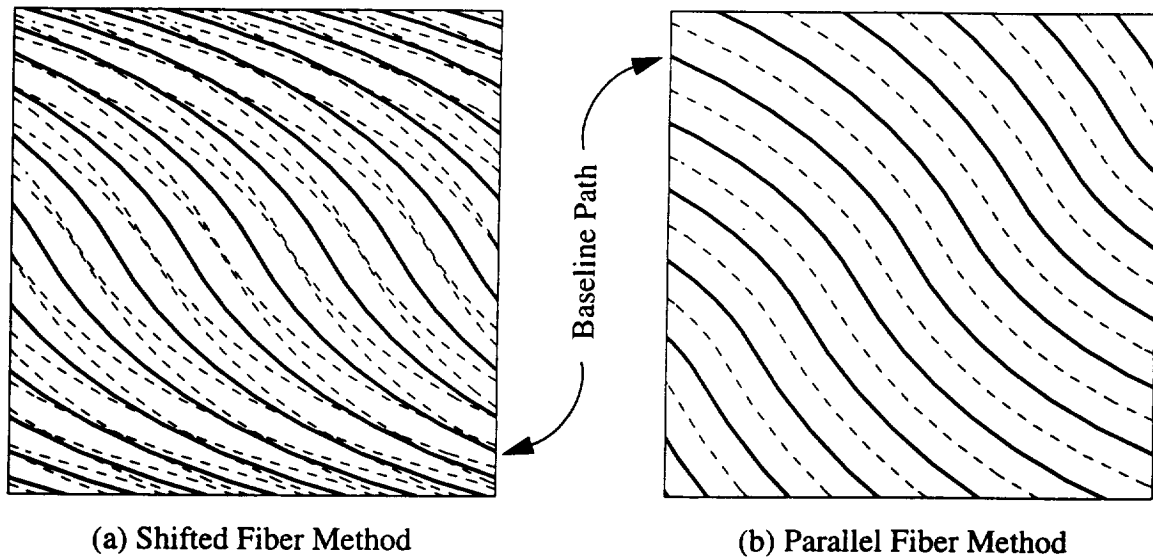


**Figure 1.2: Shifted and Parallel Fiber Methods for 90<30/75> Ply**

later when the manufacturing of the laminates is described. The parallel fiber method is shown in Figure 1.2b. It is based on laying the subsequent material strips exactly parallel to the preceding path, so that no overlap occurs. The additional paths need to be determined using a numerical procedure, therefore the simplicity of the equation defining the fiber orientation variation for the baseline path is lost. Not shown in detail here is the fact that the parallel method produces stiffness variations in both directions, and also that certain curvilinear fiber definitions using the parallel fiber method are infeasible for they produce paths with infinite curvature.

With the basic definitions of the variable stiffness plies in hand, an analysis tool was developed by Olmedo<sup>15</sup> to calculate the stress state and buckling loads of variable stiffness rectangular panels. The static solution utilized a numerical solver called ELLPACK<sup>18</sup>, which is based on Hermite collocation techniques for elliptic partial differential equations, and the buckling estimate was carried out using traditional Rayleigh-Ritz techniques. Specialized computer codes were produced that were able to solve the differential equations accurately and efficiently. Subsequently, design studies were conducted by Waldhart<sup>17</sup> to determine if any performance improvements could be found using these curvilinear fibers for flat plates under compression. The results indicated that the shifted fiber method produced the greatest improvements in load carrying capability (up to 75% increase) when the load was applied to the plate in a direction perpendicular to the stiffness variation. Therefore, the first question concerning curvilinear fibers was answered in the affirmative: the variable stiffness plates could be analyzed effectively and also showed marked improvement over traditional composite laminate designs.

Coordination of these idealized fiber paths with realistic manufacturing tools was completed under the funding of Boeing Helicopters by Gürdal and this author with the help of Cincinnati Milacron and their state-of-the-art fiber tow placement system, VIPER<sup>19,20,21</sup>. Correspondence between the variable stiffness definitions used in the Virginia Tech analysis tools and the controlling software of the tow placement system (ACRAPLACE) was completed by constructing numerical programs that translated the parameters of the analytical designs into appropriate data files that could be interpreted by the ACRAPLACE software. For the shifted method, the coding amounted to defining the centerline path (the dark lines in Figure 1.2a) for each pass of the fiber head individually. The overlap regions were also dealt with as part of this work. The ACRAPLACE programming contains a parameter which determines how much overlap is allowed between successive passes of the tow placement head. If set to 100%, then the overlap regions will produce thickness changes within the variable stiffness plies as expected from Figure 1.2a. However, setting the overlap to 0% introduces the cut-restart capability of the tow placement machine, and it was found that this feature can be used to produce constant thickness plies that maintain the stiffness variation prescribed by the analytical models, though some slight voids do exist within the plies. For the parallel fiber method, perfect correlation was found between the analytical and ACRAPLACE ply constructions and only the baseline path definition was required.

Additionally, the coordination of the theoretical paths with the existing manufacturing techniques revealed that a curvature constraint must also be implemented within the design process. This limit on the change of the fiber path variation exists because for paths with a large curvature, the inner section of the band of fiber will buckle during the placement of the tow. According to tests done with the fiber placement machine by Enders & Hopkins<sup>20</sup> as well as discussions with the Cincinnati Milacron personnel, the minimum radius of curvature that can be allowed without this crimping of the fiber tow (for the specific dimensions of the VIPER machine) is 25", though in the future this constraint may be decreased. Therefore, the availability of the tow placement manufacturing process affirmed the producibility of the prototype parts, as well as providing a realistic constraint on the designs. Similar work using manufacturing constraints of the tape-laying process in a design environment has also been completed by Eschenauer et al.<sup>22</sup>, where they incorporated the potential constraints of ply drops and tow path curvature within a finite element analysis package, and Nagendra et al.<sup>23</sup>, who employed generic path definitions based on splines that could be inserted into finite element codes for analysis.

One major difference between the manufacture of flat panels and cylindrical shells using the tow placement system is that the cylinder surface is continuous in the circumferential direction. This has a specific impact on the definition of the curvilinear fiber paths. To illustrate this point,

recall that a cylindrical surface can be developed from a flat sheet merely by rolling the sheet into a tube and aligning the opposite edges of the panel. Therefore, if one constructed a variable stiffness ply for a cylindrical shell using the shifted and parallel methods defined for the flat plate, the result would be similar to the transformation of the two dimensional planar figures shown in Figure 1.2 into corresponding three dimensional cylindrical structures. For the shifted fiber method, this would seem to work admirably, for when the opposite edges are joined the centerline paths are virtually continuous with respect to orientation angle and curvature. This is true for the development of a cylinder using either a horizontal or vertical rolling action, which would correspond to either an axial or circumferential stiffness variation depending on which way the operation is performed. If no overlaps are allowed in the manufacturing process, the stiffness variation can be regarded as one dimensional, in that the stiffness will change along only one axis. Contrast this to the results for a ply constructed using the parallel fiber method shown in Figure 1.2b. The ply now possesses two dimensional stiffness variation due to the construction process of the parallel method. Furthermore, there is no continuity between the fiber orientation angle or curvature at opposite edges of the plate in either direction. This implies that a seam would be present if the ply were constructed using this method, and the stiffness properties would exhibit a distinct change in character across this boundary. Obviously, this is not a favorable occurrence. Therefore, for cylindrical structures it will be assumed that the shifted fiber method is always used in the construction of the variable stiffness plies, and that the overlap is eliminated (if desired) by using the start/restart capabilities of the tow placement machine. Using the shifted method for cylinders, in essence, ensures that the stiffness change varies only along one axis, which is desirable here since the analysis tools for cylindrical shells is much more complicated than the corresponding solution for flat plates. Further details regarding the definition and constraints of the curvilinear fiber formats for cylindrical shell structures will be presented in Section 2.2.2.

### **1.2.2 Analysis and Design of Cylindrical Shell Structures**

The application of a cylinder as a structural component has been used for centuries, due to its efficiency as a pressure vessel and as a beam or truss element. Static and stability analyses of a cylindrical structure first began appearing in scientific literature in the late 1800's. In the decades that followed, the solutions became more refined and complex, and helped lead to the formulation of various shell theories, which often differed significantly in terms of complexity and accuracy. The richness of the potential avenues for research using the cylindrical shell as a subject has lead to a bountiful collection of investigations throughout history. However, for the purposes of this study, the main topics under investigation are limited to the practical application of cylindrical shell structures in the aerospace industry and how these designs can be enhanced through the use

of the variable stiffness concept. As such, this subsection of the literature review will concentrate on two areas: classical solutions for the stability of cylindrical shells, which are used as illustrations of possible failure mechanisms and later as a comparison to our numerical solutions; and modern analysis and design of stiffened and unstiffened cylindrical shells constructed from composite materials, which serves as a background to the optimization work that will be performed to determine the worth of the variable stiffness concept.

### **Classical Buckling Estimates for Unstiffened Cylindrical Shells**

The term “classical” used as a qualifier for shell theories and analyses indicates that the results originated through the work of the early researchers of the late 1800’s and early 1900’s. Most modern texts on shell theory or stability will ordinarily have some discussion of the history and evolution of these results (for instance, see Brush & Almroth<sup>24</sup> for a discussion of the various shell theories applied to shell stability equations), and it has generally been acknowledged that three distinct (linear) shell theories for cylindrical geometries evolved from this work. In order of decreasing complexity, these shell theories are referred to as Flügge<sup>25</sup>, Sanders<sup>26,27</sup>, and Donnell-Mushtari-Vlasov<sup>28,29</sup> in deference to their originators. The relative accuracy of these theories have been debated for some time, and in summary it has been established that the Flügge equations, though considered exact to the level of their initial assumptions, contain some terms which are not significant for practical problems. Conversely, Donnell-Mushtari-Vlasov theory (also referred to as “shallow shell” theory and denoted hereafter as DMV) has been found to be inaccurate for longer cylindrical shells that do not possess high stress variability in the circumferential direction. However, DMV theory has the advantage that the equations are simple enough so that closed form solutions can often be found (as will be shown shortly). In between these two extremes lies Sanders theory, which does not possess the complexity of Flügge yet resolves the inaccuracies inherent in the shallow shell assumptions, and which is often considered the best first approximation theory for thin shells. Since the forthcoming investigation often deals with long cylinders but also attempts to use the most efficient and accurate solution techniques, the resulting equations of Chapter 2.0 correspond in essence to the Sanders type.

As an illustration of possible failure modes of cylindrical shells due to instability, some classical buckling estimates for unstiffened cylindrical shells under fundamental loads will be developed here. “Buckling” and “instability” are often used interchangeably, and represent the transition from one equilibrium state of the structure to a new radically different form due to the slight increase of a load. The calculation to find the loads that produce such changes is usually in the form of an eigenvalue problem. As mentioned earlier, the standard DMV equations used to estimate the stability of cylindrical shells can actually be solved analytically for the basic loadings



of axial compression, external pressure, and torsion. Without going into too great of detail, we will present similar results for orthotropic shells, while also augmenting some aspects of the equations to include the terms of Sanders so that the results are still accurate for longer shells. Classical buckling estimates for finite and infinite length shells will be formulated for each type of basic loading. These solutions, along with some additional assumptions, will later be used to generate estimates for the failure loads of variable stiffness cylinders under loading conditions including bending and transverse shear forces.

First buckling of a cylinder under axial compression is considered. The classical solution assumes that under this type of loading, the shell will buckle from an undeformed surface into one with sinusoidal waves in both the axial and circumferential directions. This is represented as:

$$w(x, \theta) \propto \sin\left(\frac{m\pi x}{L}\right) \cos(n\theta) \quad (1.2)$$

where  $x$  and  $\theta$  denote the axial and circumferential coordinates,  $w$  is the radial displacement, and  $L$  is the length of the cylinder. The parameters  $m$  and  $n$  represent the number of half-waves in the axial direction and the number of full waves in the circumferential direction, respectively. The mode shape given in Eq. (1.2) implies that the surface of the shell buckles into a checkerboard-shaped pattern. For example, shown in Figure 1.3 is the buckled shape of a cylinder with  $m = 4$

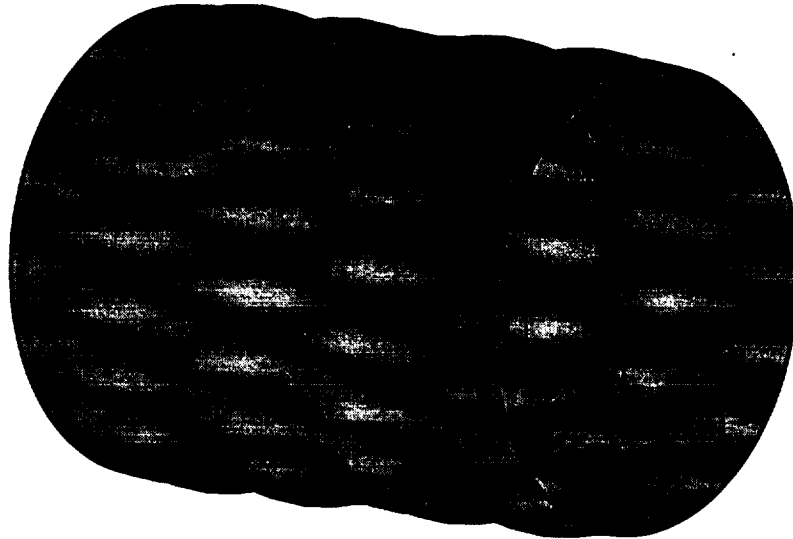


**Figure 1.3: Example of Buckling Mode under Axial Compression**

and  $n = 19$ . However, this mode shape is not necessarily the one that the shell will deform into when it becomes unstable, for there actually exists an infinite number of mode shapes corresponding to any integer value (with a few restrictions) for the parameters  $m$  and  $n$ . For each of these pos-

sible combinations of  $m$  and  $n$ , there is also an associated buckling load (calculated from an eigenvalue problem) which depends on the values of these wave numbers, and the critical buckling load and mode shape are thus defined from the smallest eigenvalue among these possibilities.

To illustrate, it can be shown that using DMV theory for a cylindrical shell constructed from an orthotropic laminate, the buckling load under axial compression can be estimated as

$$(-\hat{N}_x) = \frac{\beta^4 \hat{D}_{11} + 2\beta^2 n^2 (\hat{D}_{12} + 2\hat{D}_{66}) + n^4 \hat{D}_{22}}{\beta^2 R^2} + \frac{\beta^2 \hat{E}_\theta H}{\beta^4 + 2\beta^2 n^2 \left( \frac{\hat{E}_\theta}{2\hat{G}_{x\theta}} - \hat{\nu}_{\theta x} \right) + n^4 \frac{\hat{E}_\theta}{\hat{E}_x}} \quad (1.3)$$

Most of these symbols will be defined later in more precise terms, so that for now  $(-\hat{N}_x)$  is defined as a measure of the compressive axial load and is called the axial stress resultant,  $R$  and  $H$  are the radius and thickness of the cylindrical shell,  $\beta$  replaces the axial wave number  $m$  through the relation  $\beta = m\pi R/L$  and is often referred to as the axial frequency, and the rest of the terms with a carat represent some stiffness quantity and are constants that can be determined from the shell material and geometry. Therefore, the only unknown variables on the right hand side of Eq. (1.3) are the wave number parameters  $\beta$  and  $n$ , and the critical buckling value is determined by finding the minimum value of the eigenvalue  $(-\hat{N}_x)$  within all these possibilities. Since, in general, this cannot be done analytically for unknown values of the stiffness parameters, the value of  $n$  is chosen to be zero, which corresponds to an axisymmetric state in which the deformed shape varies only in the axial direction, and assume that  $\beta$  can attain any positive value. Finding the critical axial wave number and eigenvalue is then easily accomplished through basic calculus:

$$\begin{aligned} n = 0 \Rightarrow (-\hat{N}_x) &= \frac{\beta^2 \hat{D}_{11}}{R^2} + \frac{\hat{E}_\theta H}{\beta^2} \\ \frac{d}{d\beta}(-\hat{N}_x) = 0 \text{ for minimum} \Rightarrow \hat{\beta}_x &= \sqrt[4]{\frac{\hat{E}_\theta H R^2}{\hat{D}_{11}}}, \quad (-\hat{N}_x^{cl}) = \frac{2\sqrt{\hat{D}_{11} \hat{E}_\theta H}}{R} \end{aligned} \quad (1.4)$$

The superscript *cl* denotes the classical estimate, while the carats will later be defined to designate an average quantity related to the shell skin.

To check the accuracy of the  $n = 0$  assumption, the level curves of Eq. (1.3) for  $(-\hat{N}_x)$  using an isotropic material are plotted as functions of the wave number parameters  $\beta$  and  $n$ , which are assumed to be continuously valued numbers as opposed to ones based on discrete valued integers. The result is shown in Figure 1.4, where normalization with respect to the values of Eq. (1.4) are used for the load and both of the wave number parameters (this figure was actually constructed

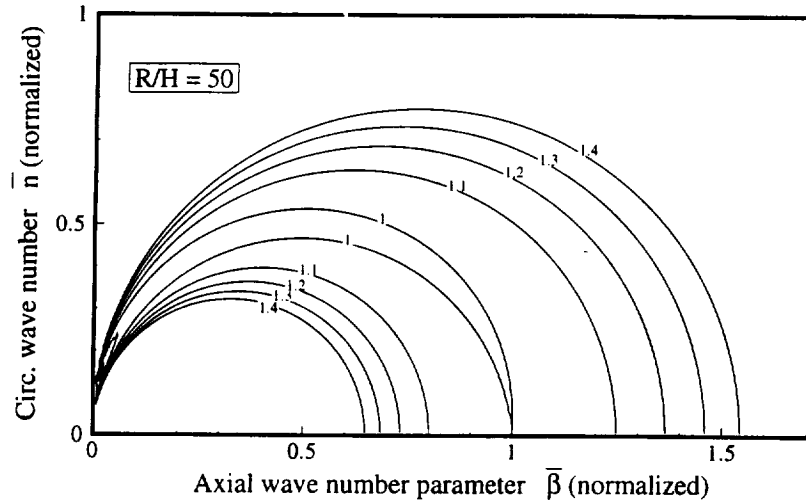


**Figure 1.4: Contour Plot of Axial Buckling Values for Isotropic Material**

using the Sanders theory solution so as to be accurate for all values of  $n$ ). Figure 1.4 reveals that these contour lines are in the approximate shape of semi-circles, first described by Koiter<sup>30</sup> in his doctoral thesis in 1945. In fact, if Eq. (1.3) based on DMV theory is used instead of the Sanders theory solution, then it can be shown that for isotropic materials the level curves are *exactly* semi-circles. Each level curve represents a constant value of the eigenvalue, so that multiple buckling modes exist for each load level. Note that the critical (lowest) value of the normalized buckling load is near one, yet no definite minimum exists (except for the singular case near the origin, which is not a realistic mode). Therefore the value of  $(-\hat{N}_x)$  at  $n = 0$ , where the parameter  $\beta$  and the eigenvalue correspond to their classical values, gives a fair estimate of the critical eigenvalue of the isotropic skin, so that the assumption used to find the classical buckling load for isotropic materials under axial compression can be considered reliable. Of course for realistic cylinders, the value of  $\beta$  is not infinitely valued but depends on the number of half-waves along the length of the structure (since  $\beta = m\pi R/L$ ). However, since the magnitude of  $\hat{\beta}_x$  is large for most thin shells, there usually exists some value of  $m$  which ensures that the number of half-waves is an integer without unduly changing the amplitude of the buckling load. This occurrence also implies that the classical estimate is just as accurate for infinite length shells, since the additional length of the shell will not alter the critical axial frequency or influence the value of the buckling load.

For orthotropic materials or composite laminates with arbitrary stacking sequences, the level curves of  $(-\hat{N}_x)$  are not necessarily circular, since the orthotropy of the laminate leads to different stiffness characteristics in each direction. For instance, the level curves for buckling under axial compression using an orthotropic material with properties corresponding to a typical fiber-reinforced composite (see Table C.2 in Appendix C) are shown in Figure 1.5. Note that now a definite minimum exists, and that its location is nowhere near the assumed values of  $(\bar{\beta} = 1, \bar{n} = 0)$ , nor

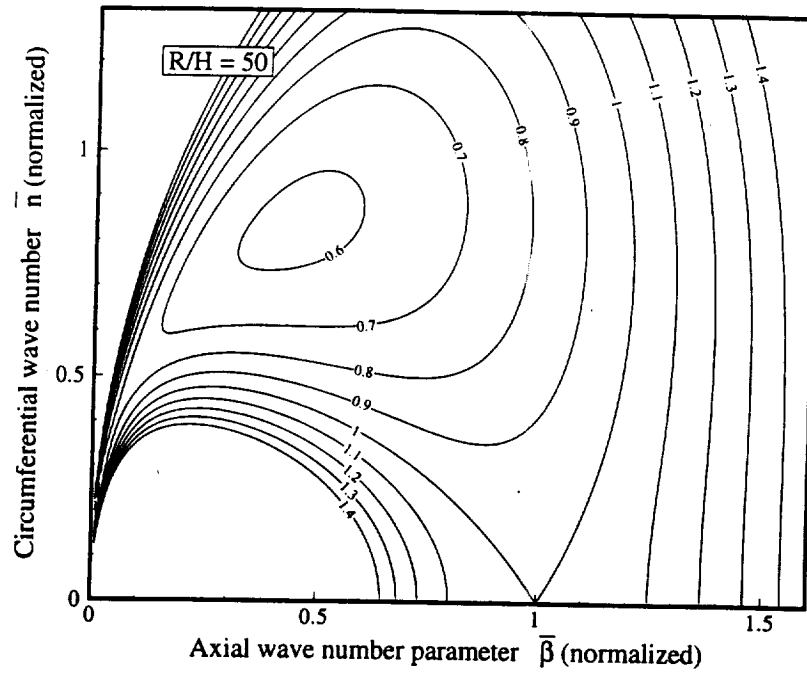


**Figure 1.5: Contour Plot of Axial Buckling Values for Orthotropic Material**

is its normalized eigenvalue near the classical estimate. However, the actual location and magnitude of this minimum for an arbitrary laminate is a complicated expression involving the roots of high order polynomials, and cannot be expressed as succinctly as Eq. (1.4). Therefore, even though the orthotropic skins may possess distinctively different critical buckling modes as in Figure 1.5, the  $n = 0$  case will still be used as the classical value due to its simplicity, while noting its inaccuracy for highly orthotropic laminates. Moreover, the values used here for the orthotropic material case are quite extreme, in that practical laminates possess stacking sequences which tend to reduce the orthotropic effect displayed in Figure 1.5.

It should be mentioned here that it is quite significant that for an isotropic material so many modes exist which possess similar eigenvalues when compared to the critical one. This property of coincident modes is a major factor in the imperfection sensitivity of cylinders under axial compression, for it increases the likelihood that a geometric imperfection will coincide to the shape of a possible buckling mode and lead to catastrophic failure. Conversely, the contours of Figure 1.5 reveal that such an orthotropic laminate may be comparably imperfection *insensitive*, since fewer modes that correspond to the critical eigenvalue exist. The importance of this point has a direct correlation to the fact that the classical solution for axial compression of cylindrical shells is not considered accurate for practical design. This topic will be discussed in more detail in the review of modern analysis techniques for cylindrical shells and also in the results of Chapter 3.0.

For a cylinder under external pressure, the calculation of the critical circumferential stress resultant  $\hat{N}_\theta$  can be performed in a similar manner. First the classical estimate is derived for buckling of an infinitely long cylinder. With this specification, the end conditions can be effectively ignored and the ensuing problem exactly corresponds to a ring buckling under the action of a centrally directed pressure, where the ring represents the cross-section of the cylinder. The buckled shape does not change along the length of the cylinder, therefore the axial frequency  $\beta$  is zero. The form of the radial displacement is assumed as in Eq. (1.2) with the  $\sin(m\pi x/L)$  term removed. Using Sanders shell theory, the eigenvalue calculation can be reduced to

$$(-\hat{N}_\theta) = \frac{\hat{D}_{22}}{R^2} \frac{(n^2 - 1)}{(1 + \hat{D}_{22}/\hat{A}_{22}R^2)} \quad (1.5)$$

To determine the critical buckling value, notice that increasing the wave number  $n$  also increases the eigenvalue, so that the lowest permissible value of  $n$  should correspond to the critical value. Here  $n = 0$  is not a possibility since it does not represent a realistic buckled shape. The case for  $n = 1$  conforms to a translation of the cross-section, which is a degenerate case and is not present once the cylinder is constrained against rigid body motion. The critical eigenvalue is then for  $n = 2$ , so that the classical estimate for an infinitely long cylinder under a circumferential stress is

$$(-\hat{N}_\theta^\infty) = \frac{3\hat{D}_{22}}{R^2} \frac{1}{(1 + \hat{D}_{22}/\hat{A}_{22}R^2)} \quad (1.6)$$

The superscript now designates the classical value for an infinite length cylinder. This answer conforms exactly to the theoretical value for the ring under external pressure, as opposed to the DMV shallow shell solution which differs from this exact answer by a factor of 4/3.

The classical buckling value for a constant circumferential stress given in Eq. (1.6) is valid for infinitely long cylindrical shells which act as a ring under external pressure. However, for finite length cylinders with realistic end conditions, the axial frequency  $\beta$  is not zero since the end conditions restrain the radial displacement of the cylinder, therefore an estimate involving the axial frequency must be developed. This is accomplished by again assuming the deformed shape to be of the form given in Eq. (1.2), and applying a constant circumferential stress instead of an axial stress. Thus an analogue to the stability equation (1.3) for cylinders under axial compression can be found for buckling under external pressure using DMV shell theory:

$$(-\hat{N}_\theta) = \frac{\beta^4 \hat{D}_{11} + 2\beta^2 n^2 (\hat{D}_{12} + 2\hat{D}_{66}) + n^4 \hat{D}_{22}}{n^2 R^2} + \frac{\beta^4 \hat{E}_\theta H / n^2}{\beta^4 + 2\beta^2 n^2 \left( \frac{\hat{E}_\theta}{2\hat{G}_{x\theta}} - \hat{\nu}_{\theta x} \right) + n^4 \frac{\hat{E}_\theta}{\hat{E}_x}} \quad (1.7)$$

For shorter cylinders, it can be shown that the correct value of  $\beta$  will be determined by the condition that only one axial half-wave is present along the length of the cylinder. Then  $\beta = \pi R/L$  and the number of circumferential waves is not necessarily two. However, choosing the correct value of  $n$  for the polynomial given in Eq. (1.7) so as to produce the smallest eigenvalue cannot be completed analytically, though it can easily be accomplished numerically once the shell parameters are determined by merely calculating the eigenvalues for each possibility of the wavenumber. In practice, this is the method used here to determine the classical buckling value for finite length shells under external pressure, though the buckling equation is based on Sanders theory as opposed to the shallow shell assumptions. Therefore the classical estimate for external pressure loading for finite length cylinders is represented as:

$$(-\hat{N}_\theta^{\epsilon^I}) = \text{minimum}[-\hat{N}_\theta(n)] \quad (1.8)$$

To illustrate the dependence of the buckling value on cylinder length and the circumferential wave number, the level curves of the circumferential stress resultant normalized with respect to its infinite length value in Eq. (1.6) are shown in Figure 1.6 as a function of  $\beta$  and  $n$  for an isotropic

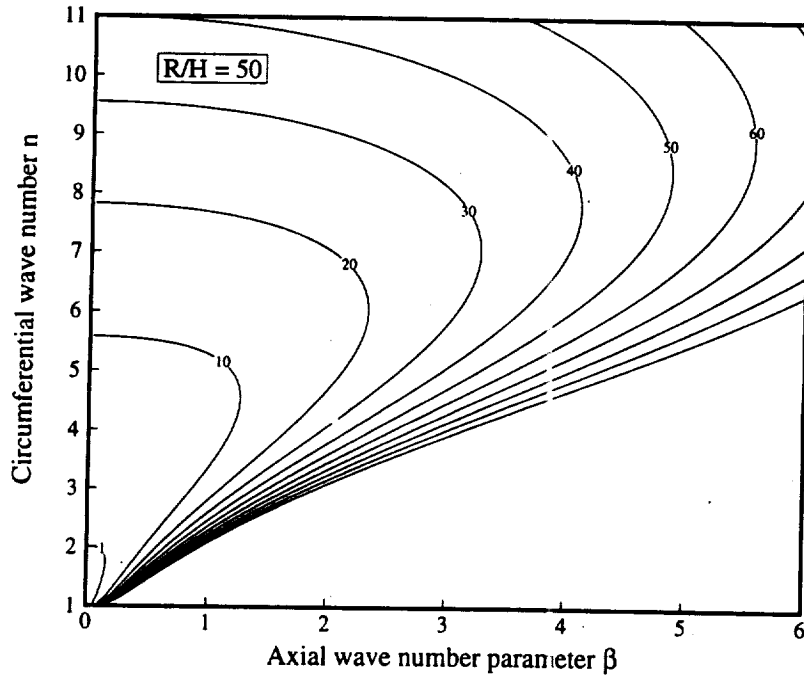


**Figure 1.6: Contour Plot of Circumferential Buckling Values for Isotropic Material**

material. This contour plot is based on the Sanders theory solution. Note that for very small values of  $\beta$  (corresponding to an infinite length shell), the critical eigenmode corresponds to a buckled mode shape of  $n = 2$  and the normalized eigenvalue is equal to one, as expected. For a finite length cylinder with a known value of  $\beta = \pi R/L$  corresponding to one axial half-wave, it is easily seen in

the figure that the minimum eigenvalue and the number of circumferential waves increase dramatically as the length decreases. The number of circumferential waves in the eigenmode can be surmised from Figure 1.6 by imagining a vertical line located at the particular value of  $\beta = \pi R/L$ , and determining where the eigenvalue is a minimum along the vertical line. For instance, if  $\beta = 4$ , the critical mode would correspond to  $n = 8$  with a normalized eigenvalue equal to around 40. Since decreasing the length of the shell increases the number of circumferential waves, which implies high variability in the circumferential direction for the resulting stresses and strains, the DMV shallow shell estimate given in Eq. (1.7) can be considered accurate for cases involving longer shells. Incidentally, the level curves for an orthotropic material follow the same general shape of the contours of Figure 1.6, so that the preceding discussions hold true for a general cylindrical shell. Therefore, for a cylindrical shell under external pressure, two classical estimates are used: Eq. (1.6) for an infinite length shell; and a solution for finite length shells based on Eq. (1.8).

For a cylinder under a constant shear load (torsion), the solutions closely follow that of the external pressure load. However, the assumed doubly periodic function of Eq. (1.2) no longer corresponds to a realistic buckled shape. Instead, the radial displacement is assumed to vary in the form of a spiral so as to produce a twisted buckled shape. This eigenfunction is defined mathematically as

$$w(x, \theta) \propto \sin\left(\frac{\beta x}{R} + n\theta\right) \quad (1.9)$$

An example of such a shape is displayed in Figure 1.7 with  $n = 2$ . The surface can be construed as

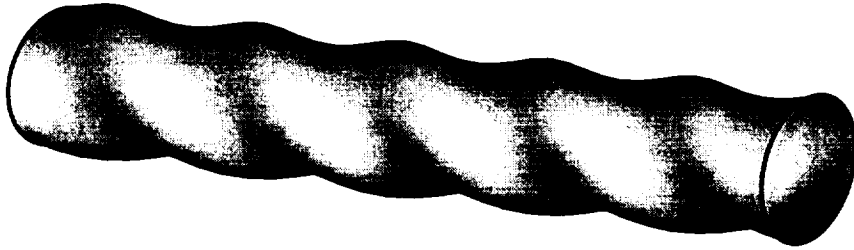


**Figure 1.7: Example of Buckling Mode under Torsion**

being composed of successive cross-sections with  $n$  circumferential waves that are being rotated about the axis of the cylinder with frequency  $\beta$ . However, it should be noted that at each end of the cylinder, the cross-section still contains  $n$  circumferential waves and does not satisfy the boundary condition of radial restraint that is typically enforced at the ends. This is due to the assumed form of the radial displacement, given in Eq. (1.9). A proper form that *does* satisfy the end conditions is usually represented by a summation of sine terms in the axial direction. Comparison of such a

solution to the estimate generated by the assumption of Eq. (1.9) is detailed in Section 3.5.2.

Using the assumed displacement field given in Eq. (1.9), a closed form estimate of the torsional buckling load can again be developed. For DMV theory, this expression is given as:

$$(-\hat{N}_{x\theta}) = \frac{\beta^4 \hat{D}_{11} + 2\beta^2 n^2 (\hat{D}_{12} + 2\hat{D}_{66}) + n^4 \hat{D}_{22}}{2\beta n R^2} + \frac{\beta^3 \hat{E}_\theta H / (2n)}{\beta^4 + 2\beta^2 n^2 \left( \frac{\hat{E}_\theta}{2\hat{G}_{x\theta}} - \hat{\nu}_{\theta x} \right) + n^4 \frac{\hat{E}_\theta}{\hat{E}_x}} \quad (1.10)$$

Here  $(-\hat{N}_{x\theta})$  is defined as the shear stress resultant, and the negative sign appears due to the definition of the direction of the assumed mode shape in Eq. (1.9). A similar Sanders theory solution exists, though it cannot be expressed as succinctly as Eq. (1.10). As with the circumferential case, estimates for infinite and finite length shells can be formulated independently based on the assumption of the value of the axial frequency.

For infinite length cylindrical shells, the axial frequency  $\beta$  is assumed to be small. Then the higher order terms associated with small values of  $\beta$  in Eq. (1.10) can be ignored, especially when multiplied by the factor  $(H/R)$ , which is small for thin shells. The Sanders theory solution for the torsional buckling load using this approximation can then be shown to be

$$(-\hat{N}_{x\theta}) = \frac{\hat{D}_{22} n (n^2 - 1)}{R^2} \frac{1}{2\beta} + \frac{\hat{E}_x H \beta^3}{2n^3 (n^2 - 1)} \quad (1.11)$$

Note that this expression differs slightly from a direct reduction of Eq. (1.10) assuming small  $\beta$  due to the different shell theory that is used. Direct minimization of Eq. (1.11) with respect to the axial frequency  $\beta$  yields

$$\hat{\beta}_{x\theta} = \sqrt[4]{\frac{\hat{D}_{22}}{\hat{E}_x H R^2} \frac{n^4 (n^2 - 1)^2}{3}} \quad (-\hat{N}_{x\theta}^\infty) = 2 \sqrt{\frac{n^2 - 1}{3}} \sqrt[4]{\frac{\hat{D}_{22}^3 \hat{E}_x H}{3 R^6}} \quad (1.12)$$

As in the circumferential case, the minimum eigenvalue corresponds to a value of  $n = 2$  for a long cylinder, so that the classical values for torsion of a long cylindrical shell become

$$\hat{\beta}_{x\theta} = \sqrt[4]{\frac{48 \hat{D}_{22}}{\hat{E}_x H R^2}} \quad (-\hat{N}_{x\theta}^\infty) = \sqrt[4]{\frac{16 \hat{D}_{22}^3 \hat{E}_x H}{3 R^6}} \quad (1.13)$$

This solution agrees exactly with the classical solution for isotropic cylinders derived by Timoshenko & Gere<sup>31</sup>, whereas the solution using the approximate DMV shallow shell equations would overestimate the buckling load by around fifteen percent.



For finite length cylinders, the value of  $\beta$  is not necessarily small. Furthermore, since the end conditions using the assumed shape of Eq. (1.9) are not rigidly satisfied, an accurate solution for shorter cylinders actually requires a more general shape for the eigenfunction in the form of a linear combination of similar sinusoidal functions, as mentioned earlier. This solution is beyond the scope required for a simple classical estimate, but it is of some interest to investigate the solution of  $(-\hat{N}_{x\theta})$  for larger values of  $\beta$ , which corresponds to torsional buckling of shorter cylinders which allow warping at the ends. Under these assumptions, it can be shown that the value of  $\beta$  again corresponds to the existence on only one half-wave along the length of the shell, therefore the finite length solution is based on finding the correct value of  $n$  in Eq. (1.10) with  $\beta = \pi R/L$ . This estimate cannot be expressed in closed form. Therefore, in practice the classical estimate is found from the Sanders theory solution as:

$$(-\hat{N}_{x\theta}^{cl}) = \text{minimum}[-\hat{N}_{x\theta}(n)] \quad (1.14)$$

For completeness, the level curves for the critical torsional load using Sanders theory are shown in Figure 1.8, where the axial frequency  $\beta$  has been normalized with respect to the value in

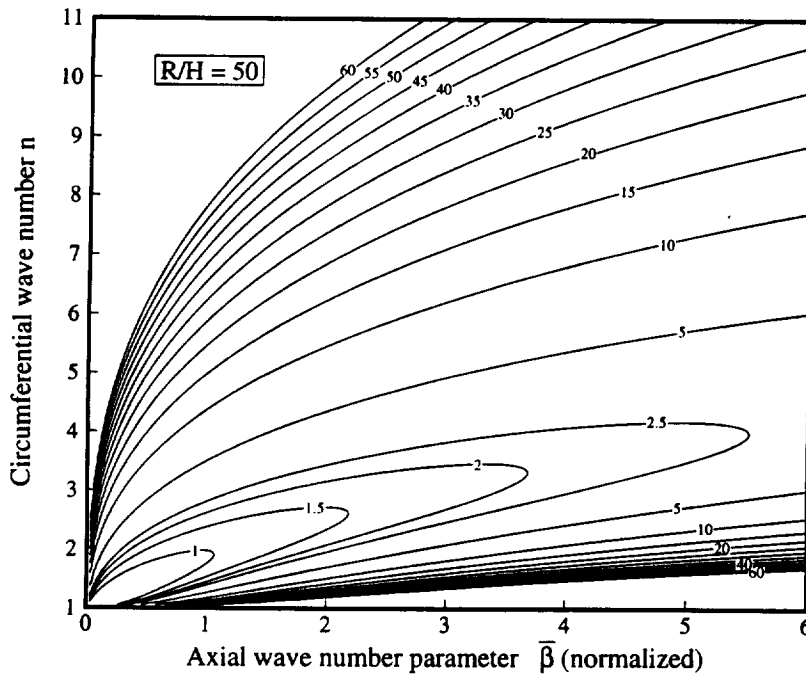


**Figure 1.8: Contour Plot of Shear Buckling Values for Isotropic Material**

Eq. (1.13). Note that the critical value for  $n = 2$  is located at  $\bar{\beta} = 1$ , and that increasing the value of the axial wavelength parameter increases the buckling load and the number of circumferential waves, much like the case of the constant circumferential stress. The relative increase in the buckling load and number of circumferential waves by decreasing the length of the cylinder is not as

great for torsion as compared to the external pressure case, however the basic mechanisms that produce this effect are identical. It should be again noted that this estimate for torsion is somewhat unreliable for shells with any type of end restraint, and that the inclusion of this effect requires a more thorough analysis. A comparison of such a solution to the rough estimate represented by Eq. (1.14) will be performed in Section 3.5.2.

The preceding calculations have provided classical buckling solutions for axial compression, external pressure, and torsion of an unstiffened composite cylindrical shell. The estimate for axial compression, Eq. (1.4), applies to cylinders of arbitrary length, while the solutions for external pressure and torsion, Eq. (1.8) and (1.14) respectively, are only correct for finite length cylinders. However, history has shown that these estimates may not be accurate when compared to the experimental buckling loads of actual cylinders. The next subsection discusses some improvements to the analysis that may be needed to provide better correlation to the experimental results.

### **Modern Analysis and Design of Shell Structures**

As with all analytical predictions, the accuracy of the classical buckling estimates must be measured by comparisons to experiments performed on actual cylinders. Such results for isotropic cylinders under the three basic loadings of axial compression, external pressure, and torsion can be found in the references by Batdorf<sup>32</sup> or Brush & Almroth<sup>24</sup>, and show that for the external pressure and torsional loading the classical estimates are well within the bounds of engineering approximation. However, experimental buckling loads for cylinders under axial compression are well below the calculated estimate, sometimes as low as 15% of that value. As such, the design of cylinders under axial compression had to take these discrepancies into account, and therefore several design guidelines and knockdown factors were empirically formulated to avoid disastrous failure scenarios. Of course, concurrent research in the field strived to explain these differences between theory and experiment, and a thorough history of the studies performed can be found in Hoff<sup>33</sup>, Brush & Almroth<sup>24</sup>, and Bushnell<sup>34</sup>. Some of the relevant discoveries of these studies that apply to this investigation are now discussed.

Many of the earliest hypotheses presented to account for the discrepancy between the theoretical and experimental buckling loads involved the accuracy of the prebuckling state of stress of the shell. In the classical solutions, this prebuckling deformation was approximated by membrane theory, in which the bending of the shell wall was neglected and the surface was assumed to be flat until the buckling load was reached. However, realistic shell problems usually possess some kind of end restraint that produces a boundary layer that grows nonlinearly with respect to the magnitude of the applied load. Therefore, increased accuracy of the eigenvalue problem was

accomplished by including the effects of various boundary conditions and the presence of the nonlinear prebuckled state. Some landmark papers concerning these topics include the work of Stein<sup>35</sup>, Sobel<sup>36</sup>, and Almroth<sup>37</sup>. Though these investigations did produce eigenvalues significantly less than the classical results, the agreement with experiments was still not consistent. The issue was finally resolved when it was accepted that the imperfection sensitivity of the shells played an enormous role in the failure loads and postbuckling response of cylindrical shells. This was first demonstrated experimentally by Donnell & Wan<sup>38</sup>, while the theory of postbuckling response had first been formulated within the doctoral work of Koiter<sup>30</sup>. Shape imperfections of actual specimens often resulted from the inherent inaccuracies of manufacturing techniques. It was discovered that shape imperfections that loosely corresponded to the mode shape of the critical buckling load produced drastic reductions in the load carrying capability of the structure. Since the axial buckling load for isotropic cylinders possessed so many coincident modes (as revealed in Figure 1.4), then the chance that a slight imperfection of the cylinder would correspond to one of these shapes was high. Postbuckling theory also explained why the assumed checkerboard pattern given by the classical eigenmode was rarely seen in experiments. This deformation state is unstable, and when a bifurcation point is reached the configuration of the shell follows a stable path that corresponds to a different postbuckled state. Further details of postbuckling theory applied to elastic structures can be found in Hutchinson & Koiter<sup>39</sup>.

Though postbuckling theory and the imperfection sensitivity phenomenon explained the discrepancy between theory and experiment for cylinders under axial compression, it offered no immediate help to the designer, since the determination of the imperfection sensitivity and the possibilities of the manufacturing flaws of a given shell configuration were not easily calculated because of the complexity and enormity of the problem. Due to this setback, most optimization work for stiffened and unstiffened shells utilized analyses that only determined the bifurcation load for the perfect structure and never delved into the postbuckling regime. However, it was demonstrated by several authors (Singer & Baruch<sup>40</sup>, Tennyson & Hansen<sup>41</sup>) that designing a structure for the maximum bifurcation load often lead to designs with increased imperfection sensitivity, since the optimizer tended to find structures with many closely spaced eigenvalues. For our purposes, we will ignore this aspect within the optimization studies, since our main goal is to determine the applicability of the variable stiffness concept to the improvement of shell structures. If sufficient improvement is discovered, then more detailed analyses and optimization studies that include these aspects of imperfection sensitivity may need to be addressed.

A remark must also be made concerning the modern analysis of shell structures that contain stiffeners. For cylindrical structures that are subjected to possible destabilizing loads, both cir-

cumferential and longitudinal stiffeners are typically used, for they are structurally efficient and often contribute to the postbuckling strength of the structure. The earliest solutions incorporating stiffeners usually relied on “smearing” their effect throughout the shell so that the structure could be considered an unstiffened shell and could be analyzed by techniques that already existed. However, it was subsequently determined that this practice was often too crude for the accurate representation of the buckling of stiffened structures, since complicating factors such as modal interaction between the skin and stiffener played an important role in the instability modes of the structure. A discussion regarding the levels of complexity that the stiffeners can possess, and their relative merits and drawbacks, can be found in the survey paper of Bushnell<sup>34</sup>. In general, the level of detail in present day analyses ranges from the smeared approach to representing the stiffener with nonlinear shell elements, though for most problems this high level of detail is not required. It will be shown in Section 2.2.2 that the variable stiffness concept possibly provides a suitable method of incorporating stiffeners without increasing the level of complexity of the analysis.

### 1.2.3 The Brazier Effect for Long Tubes

One phenomenon that the modern solutions for cylindrical shells often fail to address is the Brazier effect, which is a nonlinear phenomenon that applies to long tubes subjected to bending. In truth, this is quite understandable, for most realistic cylindrical shell structures possess end restraints or closely spaced ring stiffeners which render the effect insignificant. Possible exceptions include underwater pipes and medical tubing. However, recent advances in the aerospace industry have considered increasing the spacing of the ring stiffening elements along the length of the fuselage to save weight, and in such a case the Brazier effect becomes an important consideration with regards to the optimal construction of the fuselage skin and the size and spacing of the stiffeners. Since most existing analysis techniques do not consider the Brazier-type deformation for cylindrical shells, this study also attempts to produce an accurate, efficient solution to the Brazier problem that can be used as a guideline for relevant structural designs. The spacing of ring stiffeners for a long cylinder under bending also provides another area in which the variable stiffness analysis can be used, since the modelling of the ring stiffeners is easily incorporated into the solution techniques.

The Brazier effect can be easily demonstrated by simply bending a drinking straw or rubber hose by hand. As the curvature of the tube increases, one can feel that the additional applied moment needed to produce this extra curvature begins to lessen, and often a change in the shape of the cross-section of the tube may be observed. Finally, the tube will form a kink and collapse. This phenomena was first investigated by L.G. Brazier in 1926<sup>42</sup>, and he formulated a solution to explain the flattening behavior of infinite length isotropic circular cylinders under bending. The

Brazier phenomena differs from usual nonlinear shell problems in that the nonlinear response is induced by the macroscopic rotation of the structure, as opposed to classical boundary layer effects due to the local rotations of shell elements near the boundaries. To illustrate, shown in Figure 1.9 is an exaggerated view of an infinitesimal section of a deformed circular cylinder along

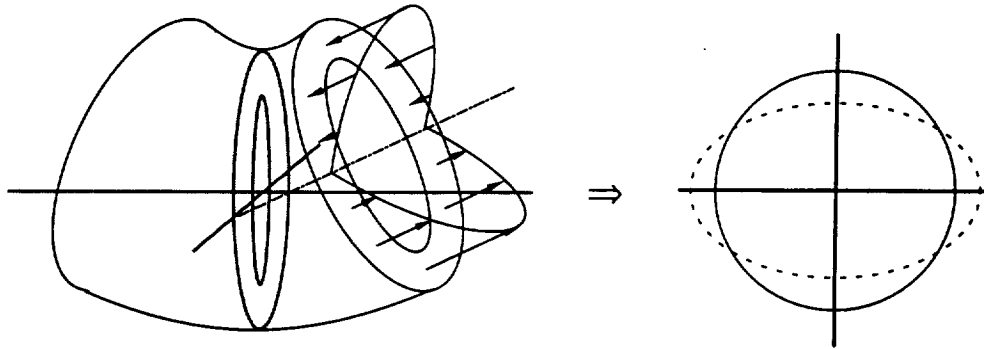


**Figure 1.9: Mechanism of Brazier Effect to Produce Ovalization**

with the linear stress state associated with pure bending. Due to the curvature of the tube axis, the compressive and tensile stresses act at an angle to the lighter cross-section and deform the original circular shape into an oval. This ovalization, in turn, decreases the moment of inertia of the cross-section and leads to a nonlinear load-displacement relation. Additionally, the deformation of the cross-section increases the axial bending stresses and lowers the structure's buckling load.

The investigation of this nonlinear behavior for an *infinite length* cylindrical shell is the problem originally studied by Brazier<sup>42,43</sup>. His approximate solution determined that the cross-sectional displacements varied as a function of  $\cos(2\theta)$ , and with this result the nonlinear moment-curvature relation could be expressed as a succinct third-order polynomial. Over thirty years later, Wood<sup>44</sup> expanded the results of Brazier to include the possibility of internal or external pressure. Within the next few years, the renowned mechanician E. Reissner attacked the problem in a series of papers<sup>45,46,47</sup> and generated a more exact solution using variational energy methods. The result was a highly nonlinear equation that he could not solve analytically, though some attempts using perturbation techniques and simple numerical solutions were performed. Attentive simplification of Reissner's equation converges to the approximate solutions of Brazier and Wood. By 1975, numerical techniques had developed that could accurately solve the nonlinear equations, and this was first completed for the Brazier problem in an excellent paper by Fabian<sup>48</sup>. His numerical solution of Reissner's equation is compared to Brazier's solution for the moment and cross-sectional deformation versus end rotation in Figure 1.10. The ovalization is a measure of the radial displacement at the top and bottom of the cross-section, and one can see that Brazier's approxima-

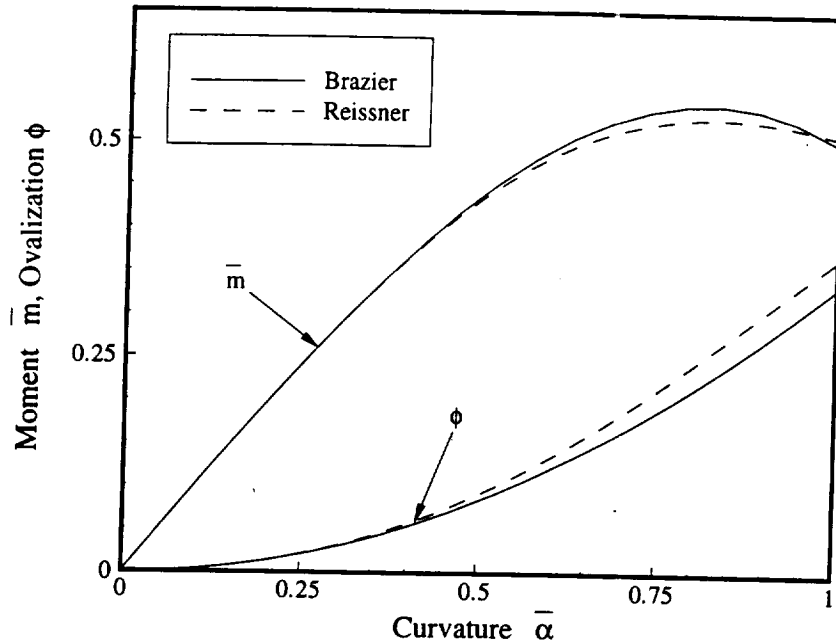


**Figure 1.10: Moment and Ovalization vs. Curvature for Long Isotropic Cylinder**

tion underestimates the deformation by around 12% at the limit point, while overestimating the moment by approximately 3%. However, the gains in analytical simplicity and computational efficiency for the approximate solution are well worth the small errors. In fact, Brazier's original solution is often considered quite serendipitous, for the gross assumptions that he invoked do not seem to warrant the resulting accuracy for such a highly nonlinear problem. Throughout this investigation we refer to these original approximations to justify neglecting certain terms, such as powers or derivatives of certain functions. It can be shown that retaining these higher order terms will result in significant disagreement between Brazier's solution and the accurate nonlinear solution of Reissner. For example, Bannister<sup>49</sup> studied the load-displacement response and vibrations of a long cylindrical shell subjected to whipping loads (bending) and used a variational approach analogous to Wood's formulation that included all the quadratic terms that are usually neglected as per the original approximate solution. The resulting moment-curvature relations underestimate the nonlinearity considerably and predict a limit moment with over 30% error. The reasons for discrepancies of this nature can be found in the discussion by Calladine<sup>50</sup>.

Additional work regarding the moment-curvature relationship for infinite length cylinders incorporating the Brazier effect was completed by several authors. Kedward<sup>51</sup> extended Brazier's analysis to include orthotropic materials. Spence & Toh<sup>52</sup> investigated elliptical cross-sections under bending, and also included experimental results which verified the nonlinear moment-curvature relationship yet revealed that the structures failed due to buckling and at a lower load than

expected. Birman & Bert<sup>53</sup> calculated the vibrations of a long cylindrical beam using Brazier's solution. Stockwell & Cooper<sup>54</sup> also attempted to incorporate orthotropic materials into Brazier's solution, though their results were not consistent with the correct solutions of Kedward<sup>51</sup> and this author<sup>55</sup>. Baruch et al.<sup>56</sup> examined the sensitivity of the limit moment to circumferential imperfections, while Li<sup>57</sup> and Molyneaux & Li<sup>58</sup> investigated the dynamic instability of elastic tubes under pure bending.

Some of the aforementioned papers dealing with the Brazier effect contain one common flaw: the assumption that the limit moment of the nonlinear load-displacement curve (as shown in Figure 1.10) is the determining collapse load of the structure. However, it was originally noticed by Brazier that the characteristic of the failure mode more properly resembles local bifurcation on the compressive side of the shell. This failure mode was first investigated by Aksel'rad in 1965<sup>59</sup>, who employed Brazier's approximate solution to determine the effect of the cross-sectional deformation on the structure's buckling load. Fabian<sup>48</sup> also included this local bifurcation possibility (as well as some postbuckling estimations) in his robust numerical solution of Reissner's equation, and he concluded that for thinner isotropic shells, bifurcation always occurs before the limit moment is reached. This observation lead other researchers, most notably Reddy<sup>60,61</sup>, Calladine<sup>50</sup>, Aksel'rad & Emmerling<sup>62</sup>, and Corona & Rodrigues<sup>63</sup> (who also included a material failure constraint) to re-evaluate the failure characteristics of cylindrical shells under nonlinear bending, and their results revealed that the major contribution of the ovalization of the cross-section toward failure was the lowering of the critical local buckling stress. These conclusions were later reaffirmed through experimental testing by Ju & Kyriakides<sup>64</sup> and Karam & Gibson<sup>65</sup>. Similar analytical results and conclusions will be presented in this investigation.

The investigation of the Brazier effect for *finite length* cylindrical shells was initiated with the original work of Aksel'rad<sup>59</sup>. To obtain solvable equations, he employed semi-membrane constitutive theory to reduce the order of the analysis, and along with his follow-up work<sup>62</sup> he determined the prebuckling deformation and an estimation of the buckling moment for cylindrical shells of finite length. Stephens et al.<sup>66</sup> also contributed toward the finite length solutions through the use of the emerging nonlinear finite element code STAGS, and subsequent finite length solutions utilizing the semi-membrane assumptions by Libai & Bert<sup>67</sup> and this author<sup>68,69</sup> used the finite element results as a comparison to their solutions. It should also be noted here that Libai & Bert were the first to notice the importance of shear deformation due to the Brazier effect for finite length shells.

Most of the concerns discussed here regarding the Brazier effect will be included as part of this investigation. Both the exact nonlinear solution and an approximate solution based on the

assumptions of Brazier will be used, and the collapse loads for infinite and finite length cylinders will be fully investigated. Applications of these results for practical structures will also be addressed.

### 1.3 Approach of Current Study

With reference to the previous discussions in this chapter, the approach for this investigation will focus on the application of the variable stiffness concept to the design of cylindrical shells under various types of loading. The stiffness variation will predominantly be defined through the use of curvilinear fibers, though discrete stiffening elements and thickness changes may also be employed. When these additional stiffening mechanisms are employed, basic assumptions are used so that they can be incorporated into the variable stiffness concept without adding significant complexity to the solution techniques. Specific restrictions on the geometry and loading conditions will be made in order to reduce the stiffness variation to be in either the axial or circumferential direction, since this will facilitate the ensuing analysis techniques by transforming the two dimensional problems into one dimensional ones. Particular boundary conditions, application of the loads, and the degree of nonlinearity for each load case will be determined independently for each case. In general, each problem will contain a static solution to determine the prebuckling stress state and estimate material failure loads, and a stability analysis based on bifurcation loads that takes the form of a numerical eigenvalue problem. Postbuckling phenomenon will not be investigated, however the final designs will be analyzed with the most rigorous nonlinear solutions available to give some insight into the higher order details of the response. Rigorous optimization studies for practical cylindrical structures will be performed using the most efficient analysis techniques to determine the relative worth of the variable stiffness concept.

To understand the motivation behind this work, a quick sketch of the evolution of the analysis techniques is necessary. It was originally believed that the added tailorability that the variable stiffness concept provides should produce designs that exhibit increased performance compared to traditional constant stiffness laminates. This idea applies not only to cylindrical shells, but to any structure constructed of thin laminates. The earliest work was actually applied to flat plates, and the positive results discovered for compression of square panels lead to the application of the concept to shell structures. The initial attempt for the analysis of variable stiffness cylinders consisted of a simple investigation of the deformed shape and stress state of an axisymmetric cylinder. This analysis was subsequently expanded to include the buckling response of a cylinder with a stiffness variation in either the axial or circumferential direction. The preliminary results indicated that the most significant by-products of the stiffness variation were the redistribution of the loads and the production of deformed shapes that were quite atypical when compared to standard



structures. This second finding created a desire to find realistic problems for which the resulting deformation was quite large, so that the stiffness variation could be designed to control the deformation and improve the performance of the cylinder. Such a scenario existed for long cylinders under bending, thus the investigation was broadened to include many aspects of this interesting problem. However, the main motivation of this research remains focused on determining if the curvilinear fiber format is a viable alternative for the design of cylindrical shell structures, and thus four major cases encompassing the most basic loading conditions of a variable stiffness cylinder are included.

A summary of the particulars for each case are presented in Table 1.1, where the case designations correspond, respectively, to a cylinder with an axial stiffness variation that undergoes axisymmetric loads only, a short cylinder segment with a circumferential stiffness variation that can handle arbitrary beam loads, and long tubes undergoing predominantly bending loads including the Brazier effect with a possible stiffness variation in either direction.

Case designation	Stiffness variation	Level of analysis	Load cases	Nonlinear effects	End conditions
Axisymmetric	Axial	Nonlinear solution with bifurcation analysis	Axial force, pressure, torsion	Boundary layer, shell rotations	Exact
Short Segment	Circumferential	Linear membrane prebuckling solution with bifurcation analysis	General beam loads	None	Warping allowed
Infinite Length Brazier	Circumferential	Nonlinear prebuckling solution with bifurcation analysis	Bending, pressure, axial force	Exact Brazier effect	None
Finite Length Brazier	Axial	Nonlinear semi-membrane solution with approximate stability analysis	Bending, pressure	Approximate Brazier effect	Membrane

**Table 1.1: Organization of Analysis Scenarios**

## **Chapter 2.0 Governing Equations for Variable Stiffness Cylindrical Shells**

The governing equations for composite circular cylindrical shells are derived in this chapter along the lines of classical nonlinear shell theory, together with the assumption that the material properties may vary as a continuous function throughout the surface of the shell. The first section investigates the physical aspects of the problem by defining the geometry of the shell structure and the assumed relationship between strain and displacements. The second section outlines the constitutive theory for the stiffness response and stress analysis of thin shells constructed from laminae of orthotropic materials. This leads to the introduction of the variable stiffness concept, which allows for the stiffness characteristics to vary spatially in the structure by means of curvilinear fiber paths, dropped plies, and discrete ring stiffeners or stringers. The assumptions of classical membrane and semi-membrane constitutive theory are also discussed, which are utilized to simplify the governing equations for special cases by applying limiting assumptions to the constitutive equations. The last section combines the geometric and stiffness concepts of the first two sections to develop the governing equations for the static response and stability estimations of composite cylinders with stiffness characteristics varying in both the axial and circumferential direction. Thus the goal of this chapter is to formulate the governing equations for general loading of a cylindrical shell with arbitrary stiffness variations. The specialization of these equations into four distinct sub-problems is implemented in the succeeding chapters.

### **2.1 Strain-displacement Relations**

This section presents the physical geometry and kinematics for a circular cylindrical shell. The three-dimensional structure is expressed as a two-dimensional surface through the application of the geometry of surfaces for thin shells. The strains are defined through the use of first-order transverse shear deformation shell theory, and are formulated in terms of the displacements and rotations at the middle surface of the shell. The Kirchhoff-Love hypothesis is then introduced, which reduces the number of field variables of the problem by assuming that deformation through the thickness of the shell can be ignored. In addition, circumferential inextensionality of the cross-section, which is a typical deformation state for several of the load cases considered, is discussed.

### 2.1.1 Geometry of the Cylindrical Shell

The structure under study is a thin cylindrical shell of length  $L$ , radius  $R$ , and skin thickness  $H$  (see Figure 2.1), where we assume  $H/R \ll 1$ . The shell can be constructed of any combination of

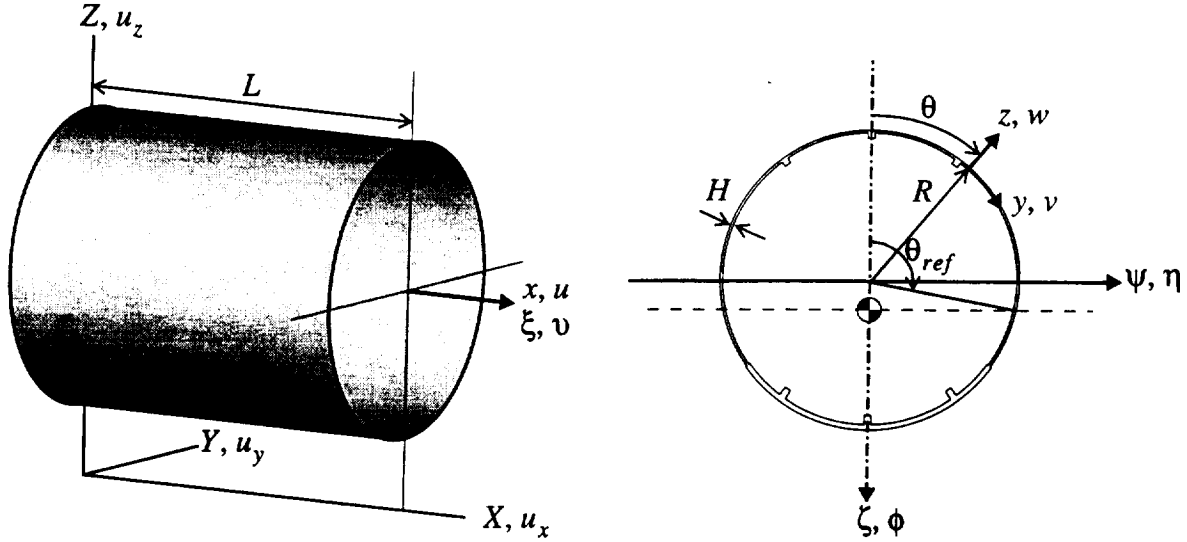


**Figure 2.1: Geometry of Undeformed Shell**

isotropic or orthotropic materials, including either longitudinal or circumferential stiffeners, and is required to have “material symmetry” about two vertical planes:  $X = L/2$  and  $Y = 0$ . The skin is assumed to be composed of a symmetric, balanced composite laminate which may contain curvilinear fibers and dropped or added plies. Due to these construction possibilities the cross-section is not necessarily symmetric about the horizontal plane, therefore the material centroid of the cross-section is located at some angle  $\theta_{ref}$  which defines the reference line of the cylinder axis.

The three dimensional structure can be referenced in terms of several coordinate systems using a Lagrangian, or “material”, frame of reference: a global Cartesian system defined by  $(X, Y, Z)$ ; and two local systems for the cylinder cross-section in terms of rectangular  $(\xi, \psi, \zeta)$  and cylindrical  $(x, y, z)$  coordinates. These directions are displayed in Figure 2.1, along with their corresponding displacements. For this work, the circumferential arc-length coordinate  $y$  is usually replaced by the polar angle  $\theta$ , where  $y = R\theta$ , and it should also be noted that the Cartesian cross-sectional coordinates  $(\xi, \psi, \zeta)$  and displacements  $(v, \eta, \phi)$  are normalized with respect to some cylinder dimension. Then with regards to the undeformed shell, the coordinates are related by

$$X_0 = (L/2)\xi = x \quad Y_0 = R\psi = (R+z)\sin\theta \quad Z_0 = -R\zeta = (R+z)\cos\theta \quad (2.1)$$

where the zero subscript denotes the undeformed configuration. Since the shell is assumed to be

thin ( $H/R \ll 1$ ), the three-dimensional body can also be represented as a two-dimensional structure through the theory of surfaces (see, for instance, Novoshilov<sup>70</sup>). For this purpose, the skin middle surface is chosen as the reference surface, and the coordinates  $(x, \theta)$  are used to define any point on this surface. The Lamé parameters and Gaussian curvatures (which are parameters measuring the arc-length and radii of curvature at each point in terms of the surface coordinates) using this coordinate system are

$$\begin{aligned} A_x &= 1 & A_\theta &= R & A_{x\theta} &= 0 \\ 1/R_x &= 0 & 1/R_\theta &= 1/R & 1/R_{x\theta} &= 0 \end{aligned} \quad (2.2)$$

which qualifies the chosen directions as principal coordinates, since they are orthogonal ( $A_{x\theta} = 0$ ) and conjugate ( $1/R_{x\theta} = 0$ ). The benefit of these surface coordinates is that they transform a three-dimensional body into a two-dimensional surface. Since the shell is thin, standard shell theory assumptions regarding the functional form of displacements and strains through the thickness of the shell can be utilized, thereby decreasing the complexity of the equations.

As mentioned in the introduction, the basic equations of classical nonlinear shell theory have previously been derived by many authors in terms of arbitrary curvilinear surface coordinates, in varying degrees of complexity, nonlinearity, and notation (this was first completed by Novoshilov<sup>70</sup>, while other authors that have employed tensor analysis to formulate these general shell equations include Leonard<sup>71</sup>, Sanders<sup>27</sup>, Naghdi & Nordgren<sup>72</sup>, and Budiansky<sup>73</sup>). To utilize these derivations, all that is needed is the calculation of the Lamé parameters and Gaussian curvatures for the specific geometry. However, it will be shown that using the typical expressions of Eq. (2.2) for a circular cylindrical shell does not correctly model the nonlinear bending response of longer shells. To this end, the governing equations will be derived for the specific geometry of a long cylindrical shell, and the differences between these equations and standard cylindrical shell equations will be discussed.

To formulate the relationship between the strains and the displacements of the cylindrical shell, the current state of the structure must be defined in terms of general variables that accurately represent all the desired details of the deformation. For the distorted state of the cylindrical shell, we therefore assume a general displacement field  $(u, v, w)$  along with a rotation of the cross-section due to beam bending. The tube axis, taken at the centroid where  $Y_0 = 0$  and  $Z_0 = R \cos(\theta_{ref})$ , undergoes deflection and curvature due to the bending of the cylinder as a “classical” beam (see Figure 2.2). Here the “classical” stipulation implies that warping of the beam cross-section due to shear is not included, so that planes normal to the axis remain flat and perpendicular to the axis after deformation. Therefore, for classical beam bending the cylinder cross-section translates

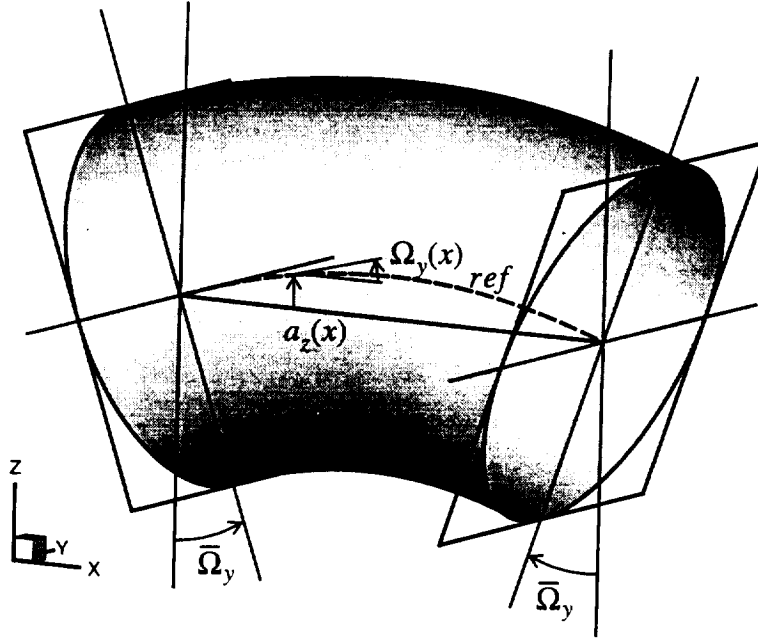


**Figure 2.2: Geometry of Deformed Shell with Axial Curvature**

an amount  $a_z(x)$  while undergoing a rotation  $\Omega_y(x)$ , where the two functions are related by

$$\tan \Omega_y(x) = \frac{da_z}{dx} \quad (2.3)$$

Furthermore, the curvature of the beam is defined as the derivative of the angle of rotation, and its sign is chosen so that a positive end rotation produces positive curvature (a prime denotes a derivative with respect to  $x$ )

$$\kappa_y(x) = -\Omega_y'(x) = \frac{-a_z''}{[1 + a_z']^{3/2}} \quad (2.4)$$

The angle of rotation at the ends is denoted by  $\bar{\Omega}_y$ , and the assumption of symmetry about  $X = L/2$  generates its definition in terms of the angle of rotation or curvature:

$$\Omega_y(0) = -\Omega_y(L) = \bar{\Omega}_y \quad \bar{\Omega}_y = \int_0^{L/2} \kappa_y(x) dx \quad (2.5)$$

Note that these expressions for  $a_z$ ,  $\Omega_y$ , and  $\kappa_y$  are derived for a beam rotation about the  $Y$ -axis, which is the customary state of bending for our shell structure. Similar equations arise for beam bending about the  $Z$ -axis (using the variables  $a_y$ ,  $\Omega_z$ , and  $\kappa_z$ ), however we need not include that possibility here for the nonlinear bending cases will be assumed to be symmetric about the  $Z$ -axis.

The expression for the deformed state of the cylinder subjected to classical beam bending is

$$\begin{aligned} X_1 &= x + u \cos \Omega_y(x) - [(R + z + w) \cos \theta - R \cos \theta_{ref} - v \sin \theta] \sin \Omega_y(x) \\ Y_1 &= (R + z + w) \sin \theta + v \cos \theta \\ Z_1 &= a_z(x) + u \sin \Omega_y(x) + [(R + z + w) \cos \theta - R \cos \theta_{ref} - v \sin \theta] \cos \Omega_y(x) \end{aligned} \quad (2.6)$$

where the displacements  $(u, v, w)$  are all functions of  $(x, \theta, z)$ . The deformed state can also be expressed in terms of the Cartesian cross-sectional displacements through the vector relations

$$\begin{aligned} R\eta &= v \cos \theta + w \sin \theta \\ R\phi &= v \sin \theta - w \cos \theta \end{aligned} \quad \Leftrightarrow \quad \begin{aligned} v/R &= \eta \cos \theta + \phi \sin \theta \\ w/R &= \eta \sin \theta - \phi \cos \theta \end{aligned} \quad (2.7)$$

so that Eq. (2.6) becomes

$$\begin{aligned} X_1 &= x + u \cos \Omega_y(x) + R(\zeta + \phi + \cos \theta_{ref}) \sin \Omega_y(x) \\ Y_1 &= R(\psi + \eta) \\ Z_1 &= a_z(x) + u \sin \Omega_y(x) - R(\zeta + \phi + \cos \theta_{ref}) \cos \Omega_y(x) \end{aligned} \quad (2.8)$$

The *global* displacements can be simply calculated as the change from the undeformed condition, Eq. (2.1), to the deformed state, Eq. (2.6) or (2.8).

### 2.1.2 Definition of Strains in Terms of Displacements

The expressions for the undeformed and deformed configurations are now used to calculate the strains of the shell. *Normal* strains are defined as an elongation per unit length, while *shear* strains measure the change in shape of a shell element. Thus, some measure of the arc lengths and angles of a typical shell element is needed. A suitable method is to calculate the incremental change as the shell deforms from its original undeformed state to a distorted geometry. As such, an increment of arc length defined through the use of differential geometry is

$$dS^2 = dX^2 + dY^2 + dZ^2 \quad (2.9)$$

The original arc length for the undeformed case using Eq. (2.1) is

$$dS_0^2 = dx^2 + (R + z)^2 d\theta^2 + dz^2 \quad (2.10)$$

The strains are defined by the change of this quantity during deformation. The strains are assumed to be small when compared to unity, and are calculated using a Cauchy concept of strain:

$$\varepsilon \equiv \frac{dS_1 - dS_0}{dS_0} \quad \Rightarrow \quad dS_1^2 = dS_0^2(1 + \varepsilon)^2 \approx dS_0^2(1 + 2\varepsilon) \quad (2.11)$$

Therefore, all that is needed to derive expressions for the strain-displacement relations is the calculation of  $dS_1$  in terms of the displacements. However, first an assumption is used to decrease the complexity of the equations. The displacements  $(u, v, w)$  in terms of the three dimensions  $(x, \theta, z)$  are replaced by a linear approximation in the transverse  $(z)$  direction, such that

$$\begin{aligned} u(x, \theta, z) &= u^o(x, \theta) + z\omega_x^o(x, \theta) \\ v(x, \theta, z) &= v^o(x, \theta) + z\omega_\theta^o(x, \theta) \\ w(x, \theta, z) &= w^o(x, \theta) + ze_{zz}(x, \theta) \end{aligned} \quad (2.12)$$

The superscript  $^o$  denotes quantities at the middle surface of the shell ( $z = 0$ ), while the variables  $(\omega_x^o, \omega_\theta^o, e_{zz})$  represent a rotation of the normal in the  $x$ -direction, a rotation of the normal in the  $\theta$ -direction, and the linear transverse normal strain, respectively. Eq. (2.12) in terms of the six middle surface field variables conforms to first-order transverse shear deformation, where the linear transverse normal strain  $e_{zz}$  is usually considered to be negligible. Insertion of these relations into Eq. (2.6) and collecting terms according to powers of  $z$  yields:

$$\begin{aligned} X_1 &= \{u^o \cos \Omega_y(x) - [(R + w^o) \cos \theta - R \cos \theta_{ref} - v^o \sin \theta] \sin \Omega_y(x)\} + \\ &\quad \{\omega_x^o \cos \Omega_y(x) - [(1 + e_{zz}) \cos \theta - \omega_\theta^o \sin \theta] \sin \Omega_y(x)\} z \\ Y_1 &= \{(R + w^o) \sin \theta + v^o \cos \theta\} + \{(1 + e_{zz}) \sin \theta + \omega_\theta^o \cos \theta\} z \\ Z_1 &= \{u^o \sin \Omega_y(x) + [(R + w^o) \cos \theta - R \cos \theta_{ref} - v^o \sin \theta] \cos \Omega_y(x)\} + \\ &\quad \{\omega_x^o \sin \Omega_y(x) + [(1 + e_{zz}) \cos \theta - \omega_\theta^o \sin \theta] \cos \Omega_y(x)\} z \end{aligned} \quad (2.13)$$

The expression for the deformed arc length using Eq. (2.9) has the form:

$$dS_1^2 = dS_0^2 + 2[\epsilon_x dx^2 + \epsilon_\theta R^2 d\theta^2 + \gamma_{x\theta} dx R d\theta + \gamma_{xz} dx dz + \gamma_{\theta z} R d\theta dz + \epsilon_z dz^2] \quad (2.14)$$

where terms involving products of  $z$  are neglected since  $H/R \ll 1$ . This limits the shell theory to first-order, since the omission of any powers of  $z$  greater than one maintains that the strains are at most linear in  $z$ . Also note that this implies that the transverse strains must be constant through the thickness. The transformations from the actual strains to their middle surface counterparts are

$$\begin{aligned} \epsilon_x(x, \theta, z) &= \epsilon_x^o(x, \theta) + z\kappa_x^o(x, \theta) & \gamma_{xz}(x, \theta, z) &= \gamma_{xz}^o(x, \theta) \\ \epsilon_\theta(x, \theta, z) &= \epsilon_\theta^o(x, \theta) + z\kappa_\theta^o(x, \theta) & \gamma_{\theta z}(x, \theta, z) &= \gamma_{\theta z}^o(x, \theta) \\ \gamma_{x\theta}(x, \theta, z) &= \gamma_{x\theta}^o(x, \theta) + z\kappa_{x\theta}^o(x, \theta) & \epsilon_z(x, \theta, z) &= \epsilon_z^o(x, \theta) \end{aligned} \quad (2.15)$$

The middle surface strains and curvatures are generally nonlinear functions of  $x$  and  $\theta$ , and can be expressed in terms of the six unknown field variables (plus the beam deflection  $a_z(x)$  and its associated derivatives) through linear counterparts, denoted by  $e_{\alpha\beta}$  and  $k_{\alpha\beta}$ . Thus the expressions for the middle surface strains are written as

$$\begin{aligned}\epsilon_x^o &= \frac{e_{xx}}{\cos\Omega_y} + \frac{1}{2}(e_{xx}^2 + \tan^2\Omega_y + e_{x\theta}^2 + e_{xz}^2) \\ \epsilon_\theta^o &= e_{\theta\theta} + \frac{1}{2}(e_{\theta x}^2 + e_{\theta\theta}^2 + e_{\theta z}^2) \quad \gamma_{x\theta}^o = \frac{e_{\theta x}}{\cos\Omega_y} + e_{x\theta} + e_{xx}e_{\theta x} + e_{x\theta}e_{\theta\theta} + e_{xz}e_{\theta z} \\ \gamma_{xz}^o &= e_{xz} + \left(\frac{1}{\cos\Omega_y} + e_{xx}\right)\omega_x^o + e_{x\theta}\omega_\theta^o + e_{xz}e_{zz} \\ \gamma_{\theta z}^o &= e_{\theta z} + e_{\theta x}\omega_x^o + (1 + e_{\theta\theta})\omega_\theta^o + e_{\theta z}e_{zz} \quad \epsilon_z^o = e_{zz} + \frac{1}{2}(\omega_x^{o2} + \omega_\theta^{o2} + e_{zz}^2)\end{aligned}\quad (2.16)$$

where the linear strain expressions are

$$\begin{aligned}e_{xx} &= \frac{\partial u^o}{\partial x} + \kappa_y[(R + w^o)\cos\theta - R\cos\theta_{ref} - v^o\sin\theta] & e_{x\theta} &= \frac{\partial v^o}{\partial x} + u^o\kappa_y\sin\theta \\ e_{xz} &= \frac{\partial w^o}{\partial x} - u^o\kappa_y\cos\theta & e_{\theta x} &= \frac{1}{R}\frac{\partial u^o}{\partial\theta} & e_{\theta\theta} &= \frac{1}{R}\left(\frac{\partial v^o}{\partial\theta} + w^o\right) & e_{\theta z} &= \frac{1}{R}\left(\frac{\partial w^o}{\partial\theta} - v^o\right)\end{aligned}\quad (2.17)$$

The middle surface curvatures become

$$\begin{aligned}\kappa_x^o &= \frac{k_{xx}}{\cos\Omega_y} + e_{xx}k_{xx} + e_{x\theta}k_{x\theta} + e_{xz}k_{xz} & \kappa_\theta^o &= e_{\theta x}k_{\theta x} + (1 + e_{\theta\theta})k_{\theta\theta} + e_{\theta z}k_{\theta z} + e_{\theta\theta}/R \\ \kappa_{x\theta}^o &= \left(\frac{1}{\cos\Omega_y} + e_{xx}\right)k_{\theta x} + (1 + e_{\theta\theta})k_{x\theta} + e_{\theta x}k_{xx} + e_{x\theta}k_{\theta\theta} + e_{xz}k_{\theta z} + e_{\theta z}k_{xz} + \frac{e_{x\theta}}{R}\end{aligned}\quad (2.18)$$

and the linear curvature functions ( $k_{\alpha\beta}$ ) are

$$\begin{aligned}k_{xx} &= \frac{\partial\omega_x^o}{\partial x} + \kappa_y[e_{zz}\cos\theta - \omega_\theta^o\sin\theta] + \kappa_y\cos\theta \\ k_{x\theta} &= \frac{\partial\omega_\theta^o}{\partial x} + \omega_x^o\kappa_y\sin\theta & k_{xz} &= \frac{\partial e_{zz}^o}{\partial x} - \omega_x^o\kappa_y\cos\theta \\ k_{\theta x} &= \frac{1}{R}\frac{\partial\omega_x^o}{\partial\theta} & k_{\theta\theta} &= \frac{1}{R}\left(\frac{\partial\omega_\theta^o}{\partial\theta} + e_{zz}\right) & k_{\theta z} &= \frac{1}{R}\left(\frac{\partial e_{zz}^o}{\partial\theta} - \omega_\theta^o\right)\end{aligned}\quad (2.19)$$



These expressions, Eq. (2.16)-(2.19), are accurate up to the error of the qualifying assumptions of small strains, moderate rotations, and a first-order (linear) variation of displacements and strains through the thickness of the shell. These shell equations conform roughly to the type first proposed by Flügge<sup>25</sup>, except that these equations also contain the possibility for the nonlinear response of the cylindrical shell acting as a beam. For the problems investigated here, these strain-displacement relations are unduly complex, and therefore will be slightly simplified.

One notable feature concerning a cylindrical shell under beam loading is the possibility for the flexural stiffness of the structure to change under large axial curvatures. This capability actually exists for any long structure designed to carry large bending loads that is constructed of a cross-section that can deform easily in its own plane. Therefore, for this investigation the nonlinear strain-displacement equations are simplified as much as possible without omitting this possibility of large distortion of the original circular cross-section. To this end, the following assumptions regarding the deformation of the cylindrical shell are employed: (a) the beam rotation  $\Omega_y(x)$  is considered small; (b) any products of axial strains, rotations, or displacements may be ignored; (c) nonlinear terms involving strains not dealing with cross-sectional deformation are neglected; and (d) axial rotations are considered small in comparison to circumferential rotations. Application of these simplifying assumptions to the expressions of Eq. (2.15)-(2.18) yields the final form of the strain-displacement relations according to first-order transverse shear shell theory:

$$\begin{aligned}
 \epsilon_x^o &= e_{xx} + \frac{1}{2}(e_{xz}^2) & \kappa_x^o &= k_{xx} \\
 \epsilon_\theta^o &= e_{\theta\theta} + \frac{1}{2}(e_{\theta z}^2 + \overline{e_{\theta\theta}^2}) & \kappa_\theta^o &= (1 + \overline{e_{\theta\theta}})k_{\theta\theta} + \overline{e_{\theta z}k_{\theta z}} + \overline{e_{\theta\theta}/R} \\
 \gamma_{x\theta}^o &= e_{\theta x} + e_{x\theta} + e_{xz}e_{\theta z} & \kappa_{x\theta}^o &= k_{\theta x} + k_{x\theta} \\
 \gamma_{xz}^o &= e_{xz} + \omega_x^o & \gamma_{\theta z}^o &= e_{\theta z} + (1 + \overline{e_{\theta\theta}})\omega_\theta^o + \overline{e_{\theta z}e_{zz}} & \epsilon_z^o &= e_{zz} + \frac{1}{2}(\overline{\omega_\theta^{o2}} + e_{zz}^2)
 \end{aligned} \tag{2.20}$$

The linear expressions are reduced to:

$$\begin{aligned}
e_{xx} &= \frac{\partial u^o}{\partial x} + \kappa_y [(R + w^o) \cos \theta - R \cos \theta_{ref} - v^o \sin \theta] & k_{xx} &= \frac{\partial \omega_x^o}{\partial x} + \kappa_y \cos \theta \\
e_{x\theta} &= \frac{\partial v^o}{\partial x} & k_{x\theta} &= \frac{\partial \omega_\theta^o}{\partial x} & e_{xz} &= \frac{\partial w^o}{\partial x} & k_{xz} &= \frac{\partial e_{zz}}{\partial x} \\
e_{\theta x} &= \frac{1}{R} \frac{\partial u^o}{\partial \theta} & k_{\theta x} &= \frac{1}{R} \frac{\partial \omega_x^o}{\partial \theta} & e_{\theta\theta} &= \frac{1}{R} \left( \frac{\partial v^o}{\partial \theta} + w^o \right) \\
k_{\theta\theta} &= \frac{1}{R} \left( \frac{\partial \omega_\theta^o}{\partial \theta} + e_{zz} \right) & e_{\theta z} &= \frac{1}{R} \left( \frac{\partial w^o}{\partial \theta} - v^o \right) & k_{\theta z} &= \frac{1}{R} \left( \frac{\partial e_{zz}}{\partial \theta} - \omega_\theta^o \right)
\end{aligned} \tag{2.21}$$

The terms with an overbar in Eq. (2.20) and (2.21) denote deviations from classical first-order nonlinear shell theory and need to be retained when the cross-sectional deformation is large. Additionally, the presence of the beam curvature  $\kappa_y$  in the definition of the axial strain is required for the accurate modelling of the nonlinear Brazier effect. Removal of these two types of terms results in the level of approximation used by Sanders theory when in-plane nonlinear rotations are neglected.

It should be noted here that the derivation of these nonlinear strain-displacement relations, Eq. (2.20) and (2.21), represents a significant deviation from the classical cylindrical shell equations used by most authors. As mentioned previously, the formulation of the nonlinear strain-displacement relations using the standard Lamé parameters and Gaussian curvatures of Eq. (2.2) will *not* correspond to the equations just presented. The main difference between the two sets of equations lies in the inclusion of the beam curvature  $\kappa_y$  in the definition of the linear axial strain  $e_{xx}$ . However, for the specific problem of a long tube under bending, the beam curvature does become significant and is the primary contributor to the mechanism known as the Brazier effect. Failure to properly include the effect of the beam curvature in the axial strain relation leads to an erroneous factor of 2/3 in the resulting governing equations. Mathematically, this considerable inaccuracy can be traced to an incorrect definition of the Lamé parameters for a cylindrical shell when the magnitude of the beam curvature becomes significant (in particular, the equation for  $A_1$  in Eq. (2.2) should also contain a term due to  $\kappa_y$ , as shown in an article by this author<sup>55</sup>). Therefore, a significant result of this investigation is the presentation of the correct governing equations for the solution of a cylindrical shell of *arbitrary* length under bending, since our formulation is accurate for both long and short cylinders.

### 2.1.3 The Kirchhoff-Love Hypothesis and the Condition of Inextensionality

The Kirchhoff-Love hypothesis is a theory used for thin shells to reduce the number of field

variables of the problem by invoking assumptions about the state of deformation through the thickness of the shell. Its application is for very thin shells, or ones in which the transverse stiffness of the shell wall is roughly of the same order as the other stiffnesses (e.g. sandwich structures with a pliable inner core often require the inclusion of shear deformation). The Kirchhoff-Love hypothesis states that (a) the shell remains inextensional in the transverse direction, and (b) that normals to the middle surface remain straight and normal to the surface after deformation. The first assumption stipulates that the length of the normal remains the same, and is customarily invoked when thin shells are being considered, while the latter is only used when transverse shear effects are not considered. Physically, these two assumptions imply that the three transverse strains must be zero, and reduces the number of unknown variables by the application of these constraints. This is expressed mathematically as

$$\begin{aligned}\epsilon_z(x, \theta, z) = 0 & \Rightarrow \epsilon_z^o(x, \theta) = 0 \\ \gamma_{xz}(x, \theta, z) = 0 & \Rightarrow \gamma_{xz}^o(x, \theta) = 0 \\ \gamma_{\theta z}(x, \theta, z) = 0 & \Rightarrow \gamma_{\theta z}^o(x, \theta) = 0\end{aligned}\tag{2.22}$$

These constraints can be manipulated such that they relate the linear transverse strain ( $e_{zz}$ ) and the rotations of the normal ( $\omega_x^o, \omega_\theta^o$ ) to the middle surface displacements. Standard first-order shell theories typically only satisfy the above equations in the *linear* sense. However, certain circumstances regarding large distortion of the cylinder cross-section require the Kirchhoff-Love hypothesis to be applied to the *nonlinear* equations to be consistent with the omission and inclusion of certain terms.

The nonlinear transverse strains from Eq. (2.20) are

$$\begin{aligned}\gamma_{xz}^o &= e_{xz} + \omega_x^o \\ \gamma_{\theta z}^o &= e_{\theta z} + (1 + e_{\theta\theta})\omega_\theta^o + e_{\theta z}e_{zz} \\ \epsilon_z^o &= e_{zz} + \frac{1}{2}(\omega_\theta^{o2} + e_{zz}^2)\end{aligned}\tag{2.23}$$

Applying the assumptions of the Kirchhoff-Love hypothesis, Eq. (2.22), and solving for the rotations and linear strain yields

$$\omega_x^o = -e_{xz} \quad \omega_\theta^o = \sin \omega \quad e_{zz} = \cos \omega - 1\tag{2.24}$$

where the intermediate variable  $\omega$  is created for ease of expression and is defined as

$$\tan \omega = \frac{-e_{\theta z}}{1 + e_{\theta\theta}} \quad (2.25)$$

When the cross-sectional deformation is considered small, the linearized version of Eq. (2.24) can be used, which states

$$\omega_x^o = -e_{xz} \quad \omega_\theta^o = -e_{\theta z} \quad e_{zz} = 0 \quad (2.26)$$

Therefore, the strain-displacement relations of Eq. (2.20) must be augmented by the relations of Eq. (2.24) or (2.26), according to the level of nonlinearity present. This results in the middle surface strains and curvatures being expressed completely in terms of the middle surface displacements ( $u^o$ ,  $v^o$ ,  $w^o$ ) and the beam curvature  $\kappa_y(x)$ .

One final assumption that remains to be discussed for the strain-displacement relations involves the inextensionality of the cross-section. Typically, cylindrical shells are loaded through the ends of the cylinder (on planes perpendicular to the axis), thereby resulting in axial and shear strains from the action of these boundary conditions. Shells with "closed contours" for cross-sections do not contain any boundary conditions on a circumferential face, since the cross-section is continuous in the circumferential direction, thus circumferential strains due to applied loads at the circumferential boundaries do not exist. Therefore, the presence of circumferential strain can most often be attributed to two other sources: (a) the Poisson effect when large axial strains exist; and (b) surface tractions acting on the shell surface in the form of pressure or circumferential shear traction. Whenever these two contributions can be considered small in comparison to other strains, the shell is said to be inextensional in the circumferential direction because the length of the perimeter of the cross-section does not change. The instances where this inextensionality condition can be invoked will be discussed elsewhere, so that this section will only detail the simplifications to the strain-displacement relations that can be achieved through this assumption.

To envision the concept of an inextensional cross-section, imagine a thin circular ring of a stiff elastic material lying on a flat surface. The shape of the ring as a circular contour represents the original undeformed cross-section. If the ring is compressed between points across its diameter, it deforms into an oval shape, yet the length of the ring (the perimeter of the contour) remains the same in that there is no appreciable circumferential extension. The oval shape is developed merely through individual rotations and changes of curvature of the ring elements. Thus, the inextensional circumferential rotation of the shell element has the property of changing the curvature of the contour without changing its length, and therefore this rotation (defined here as  $\omega$ ) will be used as the desired field variable of the derivation. Much like the Kirchhoff-Love hypothesis elim-

inated variables from the governing equations by expressing the rotations of the normal in terms of middle surface displacements, as in Eq. (2.24), this inextensionality condition decreases the number of unknown variables by one, either as a parametric representation in terms of the inextensional rotation, or by a direct substitution in terms of a middle surface displacement.

The derivation of the inextensionality condition is performed on an arbitrary slice of the cylinder cross-section. An increment of the undeformed cross-sectional contour is shown as arc  $AB$  in Figure 2.3. Note that the reference system is in terms of the rectangular cross-sectional coordinate

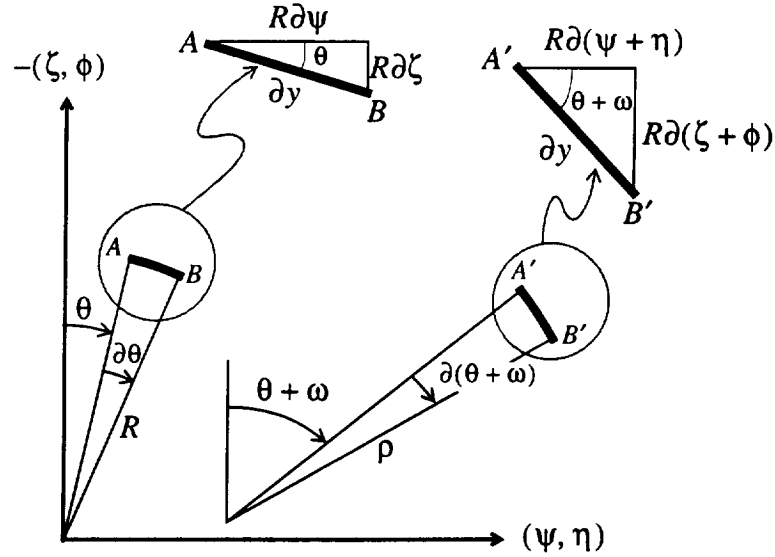


**Figure 2.3: Derivation of Inextensional Displacements**

system, and that the sign of the vertical axis is in the downward direction. The original coordinates of the end points of the arc (normalized with respect to the radius  $R$ ) are

$$A = (\psi, \zeta) \quad B = (\psi + \partial\psi, \zeta + \partial\zeta) \quad (2.27)$$

The close-up of the geometry, where  $\partial y = R\partial\theta$ , reveals that

$$\cos\theta = \frac{\partial\psi}{\partial\theta} \quad \sin\theta = \frac{\partial\zeta}{\partial\theta} \quad (2.28)$$

During inextensional deformation, the original circular arc length  $AB$  displaces to a new position  $A'B'$ , which is rotated at an angle  $(\theta+\omega)$  to the vertical axis and has a different center and radius of curvature. Since the deformation is assumed as inextensional, the length of the differential arc remains the same, and can be calculated for each case.

$$\partial y = R\partial\theta = \rho\partial(\theta + \omega) \quad (2.29)$$

The coordinates of the new end points in terms of the rectangular displacements are

$$A' = (\psi + \eta, \zeta + \phi) \quad B' = (\psi + \partial\psi + \eta + \partial\eta, \zeta + \partial\zeta + \phi + \partial\phi) \quad (2.30)$$

and the close-up gives the geometric relation as

$$\cos(\theta + \omega) = \frac{\partial(\psi + \eta)}{\partial\theta} \quad \sin(\theta + \omega) = \frac{\partial(\zeta + \phi)}{\partial\theta} \quad (2.31)$$

Expressions for the middle surface displacements and circumferential change of curvature can now be derived in terms of the inextensional rotation  $\omega$ .

The curvatures of each arc in Figure 2.3 are readily found from the inverse of the radii of curvatures, and naturally the change in curvature is simply the difference of the deformed state with respect to the undeformed configuration, so that, using Eq. (2.29)

$$\kappa_\theta^o = \frac{1}{\rho} - \frac{1}{R} = \frac{1}{R} \frac{\partial\omega}{\partial\theta} \quad (2.32)$$

The inextensional displacements can be found from the solution of Eq. (2.31), whereby

$$\frac{\partial\eta}{\partial\theta} = \cos(\theta + \omega) - \cos\theta \quad \frac{\partial\phi}{\partial\theta} = \sin(\theta + \omega) - \sin\theta \quad (2.33)$$

Enforcing symmetry and measuring the vertical displacement from the reference surface

$$\eta(x, \theta)|_{\theta=0} = 0 \quad \phi(x, \theta)|_{\theta=\theta_{ref}} = 0 \quad (2.34)$$

results in integral equations for the rectangular displacements:

$$\eta(x, \theta) = \int_0^\theta [\cos(\theta + \omega) - \cos\theta] d\theta \quad \phi(x, \theta) = \int_{\theta_{ref}}^\theta [\sin(\theta + \omega) - \sin\theta] d\theta \quad (2.35)$$

These parametric expressions can also be obtained for the cylindrical displacements ( $v^o, w^o$ ) by using the usual vector transformation of Eq. (2.7). Of more interest, however, is the representation of some of the linear strain quantities of Eq. (2.21) in terms of this inextensional rotation  $\omega$ . For instance, the combination of Eq. (2.35) and (2.7) gives

$$e_{\theta\theta} = \frac{1}{R} \left( \frac{\partial v^o}{\partial\theta} + w^o \right) = \cos\omega - 1 \quad e_{\theta z} = \frac{1}{R} \left( \frac{\partial w^o}{\partial\theta} - v^o \right) = -\sin\omega \quad (2.36)$$

These expressions on the right hand sides should look familiar, since they correspond (except for

a sign change) to the parameterization used to satisfy the nonlinear Kirchhoff-Love assumptions of Eq. (2.24). In fact, insertion of the solution for these linear strain quantities into Eq. (2.25) produces an identity, proving that the inextensional rotation  $\omega$  is equivalent to the parameter used in the Kirchhoff-Love hypothesis (which of course is why it was chosen to have the same symbol). Furthermore, calculation of the *nonlinear* circumferential strain and curvature at the middle surface, Eq. (2.20), reveals

$$\varepsilon_{\theta}^o = 0 \quad \kappa_{\theta}^o = \frac{1}{R} \frac{\partial \omega}{\partial \theta} \quad (2.37)$$

which exactly corresponds to the original assumption (zero circumferential strain) and partial solution, Eq. (2.32), of the inextensionality condition. The results of Eq. (2.36) also substantiate the use of the nonlinear application of the Kirchhoff-Love hypothesis, since the assumption of inextensionality equates the order of the circumferential and transverse strains. Therefore whenever this inextensional condition is considered relevant, the simplifications to the strain-displacement relations, Eq. (2.36) and (2.37), will be employed.

## 2.2 Constitutive Theory

This section defines the physical laws of the shell material that relate the structure's stresses to the strains. The material is assumed to be linear elastic and constructed of either isotropic materials or fiber-reinforced orthotropic composite materials, which usually consist of a high-stiffness fiber surrounded by a soft polymer matrix. The cylindrical shell is constructed of multiple layers (laminae) of these materials, and the resulting structure is defined by the orientation angle of each orthotropic layer. Since the shell is assumed to be thin, we neglect the strains and stresses through the thickness of the laminate and formulate the stiffness and strength characteristics for the surface directions only. This is the basic premise of Classical Lamination Theory (CLT). The variable stiffness concept is an extension of this theory which allows for the orientation angles to be a function of spatial location (in terms of the surface coordinates) in addition to the transverse direction through the thickness (the stacking sequence). It also includes other types of construction techniques which can be regarded as a variation in stiffness, such as thickness changes, dropped plies, or directional stiffeners attached to the skin laminate. The various modifications of these variable stiffness concepts to the equations of CLT are subsequently detailed. Additionally, the assumptions of classical membrane and semi-membrane theory are discussed, which are simplified constitutive theories that are employed for specific problems in later chapters.

### 2.2.1 Classical Lamination Theory

In Section 2.1.2, the strains in terms of the three dimensions ( $x, \theta, z$ ) were transformed into

two-dimensional quantities evaluated at the middle surface through the assumptions of first-order shell theory. Additionally, the Kirchhoff-Love hypothesis was introduced, which maintains that the strains in the transverse direction are relatively small. Classical Lamination Theory uses similar premises to represent the stiffness properties of a three-dimensional body in terms of middle surface quantities only. The effect of shear deformation in the transverse direction will be ignored in the derivation of these constitutive laws. However, it should be noted that the strain-displacement relations of Section 2.1.2 and, subsequently, the equilibrium equations of Section 2.3.2 are formulated in terms of general first-order shell theory. Therefore, if transverse shear effects are to be included, only this section outlining the stress-strain relations need be augmented. A more thorough discussion of the assumptions and details of Classical Lamination Theory can be found in the text of Jones<sup>74</sup>, while a general review of transverse shear deformation (applied to flat plates) is presented by Reddy<sup>75</sup>.

### Stiffness Response

For our purposes, we begin with the definition of the three-dimensional state of stress for a thin shell constructed of an orthotropic material. The Kirchhoff-Love hypothesis states that the transverse strains are negligible, and it can be shown that these constraints provide an estimation of the relative size of the corresponding transverse stresses with respect to the surface stresses. In particular, the stipulation that the transverse shear strains are zero implies that some transverse shear stresses (though small) must exist to ensure this condition. Furthermore, the thinness of the shell, which led to the assumption that the transverse normal strain was negligible, can also be used to determine that the magnitude of the transverse normal stress is small when compared to the other stress quantities. Therefore, regarding the transverse quantities:

$$\begin{aligned}\gamma_{13} &= 0 & \Rightarrow & \tau_{13} \neq 0 \\ \gamma_{23} &= 0 & \Rightarrow & \tau_{23} \neq 0 \\ \epsilon_3 &= 0 & \Rightarrow & \sigma_3 \approx 0\end{aligned}\tag{2.38}$$

Note that the subscripts of Eq. (2.38) now correspond to the principal material directions of an orthotropic material, with “3” representing the transverse direction. These principal material directions are not necessarily parallel to the surface coordinates  $(x, \theta)$ , but depend on the properties of the orthotropic material. Traditionally, the 1 direction represents the maximum stiffness in the plane of the surface, while the 2 direction is aligned to the minimum value. For a material to be orthotropic, these directions are necessarily perpendicular, and the stiffnesses in an arbitrary in-plane direction can be found through a standard tensorial rotation of these properties.

With regard to the constitutive equations, the results of Eq. (2.38) greatly simplify the stress-



strain relations since the transverse stresses, even though they are non-zero, can be effectively removed from the constitutive equations due to their relative magnitude (if transverse shear effects are to be included, additional constitutive laws must be used to relate the transverse stresses to their respective strains). Thus, the only significant stresses are those that occur in the plane of the middle surface. Using the notation of the principal directions, these stresses are related to the corresponding strains along the principal material directions of the orthotropic material as

$$\begin{bmatrix} \sigma_1 \\ \sigma_2 \\ \tau_{12} \end{bmatrix} = \begin{bmatrix} Q_{11} & Q_{12} & 0 \\ Q_{12} & Q_{22} & 0 \\ 0 & 0 & Q_{66} \end{bmatrix} \begin{bmatrix} \varepsilon_1 \\ \varepsilon_2 \\ \gamma_{12} \end{bmatrix} \quad (2.39)$$

The quantities  $Q_{ij}$  are referred to as the reduced stiffnesses of an orthotropic lamina, and are related to the engineering stiffness quantities measured along the principal directions:

$$Q_{11} = \frac{E_1}{1 - \nu_{12}\nu_{21}} \quad Q_{12} = \frac{\nu_{12}E_2}{1 - \nu_{12}\nu_{21}} \quad Q_{22} = \frac{E_2}{1 - \nu_{12}\nu_{21}} \quad Q_{66} = G_{12} \quad (2.40)$$

To project the principal stresses and stiffness quantities along the directions of the surface coordinates, a tensorial rotation about the normal to the surface is performed. For example, the transformation from the stresses in the material coordinates to the surface coordinates is represented as:

$$\begin{bmatrix} \sigma_x \\ \sigma_\theta \\ \tau_{x\theta} \end{bmatrix} = \begin{bmatrix} \cos^2\varphi & \sin^2\varphi & -2\sin\varphi\cos\varphi \\ \sin^2\varphi & \cos^2\varphi & 2\sin\varphi\cos\varphi \\ \sin\varphi\cos\varphi & -\sin\varphi\cos\varphi & \cos^2\varphi - \sin^2\varphi \end{bmatrix} \begin{bmatrix} \sigma_1 \\ \sigma_2 \\ \tau_{12} \end{bmatrix} \quad (2.41)$$

The sign of this rotation is displayed in Figure 2.4, where the principal directions of the orthotro-

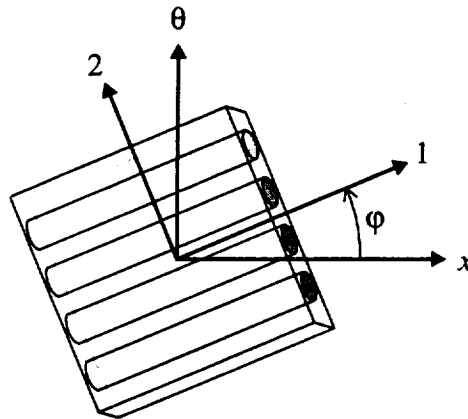


**Figure 2.4: Orientation of Principal Directions of Orthotropic Material**

pic material are aligned at some orientation angle  $\phi$  to the surface coordinates. Similar transformations can be applied to the strains and material properties of the shell.

Tensorial rotations such as Eq. (2.41) are applied to both the stresses and strains in the principal material directions in Eq. (2.39), thereby producing the stress-strain relations for an arbitrary lamina in terms of the surface coordinates:

$$\begin{bmatrix} \sigma_x \\ \sigma_\theta \\ \tau_{x\theta} \end{bmatrix} = \begin{bmatrix} \bar{Q}_{11} & \bar{Q}_{12} & \bar{Q}_{16} \\ \bar{Q}_{12} & \bar{Q}_{22} & \bar{Q}_{26} \\ \bar{Q}_{16} & \bar{Q}_{26} & \bar{Q}_{66} \end{bmatrix} \begin{bmatrix} \epsilon_x \\ \epsilon_\theta \\ \gamma_{x\theta} \end{bmatrix} \quad (2.42)$$

The transformed reduced stiffness  $\bar{Q}_{ij}$  are dependent on the reduced stiffnesses  $Q_{ij}$  and the orientation angle  $\phi$  of the orthotropic material. For ease of representation, Tsai & Pagano<sup>76</sup> have formulated these relations in terms of invariant material properties, such that

$$\begin{aligned} \bar{Q}_{11} &= U_1 + U_2 \cos 2\phi + U_3 \cos 4\phi & \bar{Q}_{12} &= U_4 - U_3 \cos 4\phi \\ \bar{Q}_{22} &= U_1 - U_2 \cos 2\phi + U_3 \cos 4\phi & \bar{Q}_{66} &= U_5 - U_3 \cos 4\phi \\ \bar{Q}_{16} &= -(U_2/2) \sin 2\phi - U_3 \sin 4\phi & \bar{Q}_{26} &= -(U_2/2) \sin 2\phi + U_3 \sin 4\phi \end{aligned} \quad (2.43)$$

The invariant properties  $U_1$ – $U_5$  are defined in terms of the reduced stiffnesses:

$$\begin{aligned} U_1 &= (3/8)Q_{11} + (3/8)Q_{22} + (1/4)Q_{12} + (1/2)Q_{66} \\ U_2 &= (1/2)Q_{11} - (1/2)Q_{22} \\ U_3 &= (1/8)Q_{11} + (1/8)Q_{22} - (1/4)Q_{12} - (1/2)Q_{66} \\ U_4 &= (1/8)Q_{11} + (1/8)Q_{22} + (3/4)Q_{12} - (1/2)Q_{66} \\ U_5 &= (1/8)Q_{11} + (1/8)Q_{22} - (1/4)Q_{12} + (1/2)Q_{66} \end{aligned} \quad (2.44)$$

For an isotropic material, the invariants  $U_2$  and  $U_3$  are zero.

The stress-strain relations of Eq. (2.42) lead to the definition of middle surface stress resultants that correspond to the middle surface strains and curvatures derived from first-order shell theory. Since the surface strains are assumed to vary linearly through the thickness of the shell, the surface stresses for each lamina should also conform to such a linear variation. Throughout the total thickness of the laminate, the stresses actually vary in a piecewise linear function, since each layer may possess different stiffness parameters due to a rotation of the principal material directions. Determining the possible variation of the transverse quantities in this way enables integration to be performed through the thickness. Resultant forces and moments are therefore defined as

$$\begin{aligned}
N_x &= \int_H \sigma_x dz & M_x &= \int_H \sigma_x z dz \\
N_\theta &= \int_H \sigma_\theta dz & M_\theta &= \int_H \sigma_\theta z dz \\
N_{x\theta} &= \int_H \tau_{x\theta} dz & M_{x\theta} &= \int_H \tau_{x\theta} z dz
\end{aligned} \tag{2.45}$$

where the integration expressed as  $\int_H$  represents limits from  $-H/2$  to  $H/2$ . The resultant stress quantities are functions of the surface coordinates  $(x, \theta)$  only, and their units are force per unit length and moment per unit length, respectively. They represent an equivalent force and moment from the stress distribution through the thickness of the shell, and their signs and orientation are displayed in Figure 2.5. Also included in the figure are the shear force resultants  $Q_x$  and  $Q_\theta$ , which

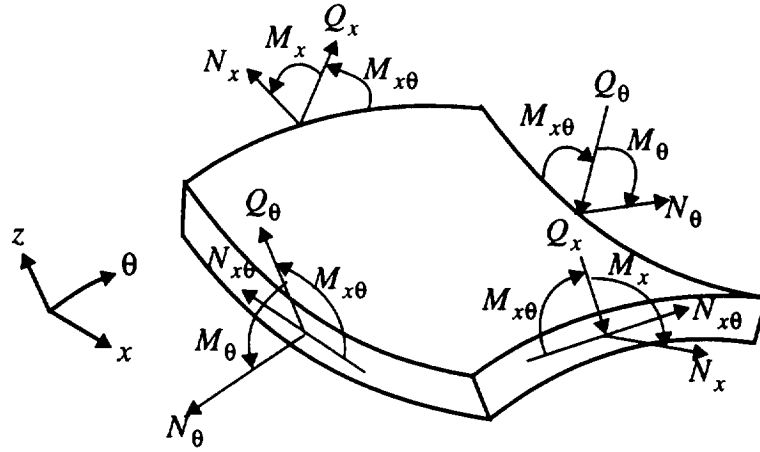


**Figure 2.5: Stress Measures of Shell Element**

do not follow a constitutive law (since we are neglecting transverse shear deformation) and are derived from consideration of the equilibrium equations in Section 2.3.1. The force and moment resultants are related to the middle surface strains and curvatures through the integration of the general constitutive law of Eq. (2.42), which results in:

$$\begin{aligned}
\begin{bmatrix} N_x \\ N_\theta \\ N_{x\theta} \end{bmatrix} &= \begin{bmatrix} A_{11} & A_{12} & A_{16} \\ A_{12} & A_{22} & A_{26} \\ A_{16} & A_{26} & A_{66} \end{bmatrix} \begin{bmatrix} \epsilon_x^o \\ \epsilon_\theta^o \\ \gamma_{x\theta}^o \end{bmatrix} + \begin{bmatrix} B_{11} & B_{12} & B_{16} \\ B_{12} & B_{22} & B_{26} \\ B_{16} & B_{26} & B_{66} \end{bmatrix} \begin{bmatrix} \kappa_x^o \\ \kappa_\theta^o \\ \kappa_{x\theta}^o \end{bmatrix} \\
\begin{bmatrix} M_x \\ M_\theta \\ M_{x\theta} \end{bmatrix} &= \begin{bmatrix} B_{11} & B_{12} & B_{16} \\ B_{12} & B_{22} & B_{26} \\ B_{16} & B_{26} & B_{66} \end{bmatrix} \begin{bmatrix} \epsilon_x^o \\ \epsilon_\theta^o \\ \gamma_{x\theta}^o \end{bmatrix} + \begin{bmatrix} D_{11} & D_{12} & D_{16} \\ D_{12} & D_{22} & D_{26} \\ D_{16} & D_{26} & D_{66} \end{bmatrix} \begin{bmatrix} \kappa_x^o \\ \kappa_\theta^o \\ \kappa_{x\theta}^o \end{bmatrix}
\end{aligned} \tag{2.46}$$

$[A]$ ,  $[B]$ , and  $[D]$  are referred to as the extensional, coupling, and bending stiffness matrices, respectively. The stiffness terms are calculated by the integration of the material properties through the thickness (the  $z$ -direction) of the laminate

$$\{A_{ij}, B_{ij}, D_{ij}\} = \int_H \bar{Q}_{ij} \{1, z, z^2\} dz \quad (2.47)$$

The integration of the transformed reduced stiffnesses  $\bar{Q}_{ij}$  through the thickness of the shell wall is easily accomplished when typical composite laminates are used. Laminated composites are constructed from multiple layers of orthotropic materials, called laminae, that are bonded together on their faces. Each individual lamina can be constructed of isotropic or orthotropic materials, and can have unequal orthotropic orientation angles as well. Usually the construction of a composite laminate is defined by its "stacking sequence" or "layup", which lists the various orientation angles of the chosen orthotropic material as it changes through the thickness (starting from the top layer). For example, a laminate denoted as  $[0/\pm 45/90]_S$  is constructed of eight layers, consisting of  $\{0^\circ, +45^\circ, -45^\circ, 90^\circ, 90^\circ, -45^\circ, +45^\circ, 0^\circ\}$  plies through the thickness (the subscript  $S$  denotes symmetry about the middle surface). Other conventions for the definition of stacking sequences include numbered subscripts, indicating multiple layers of the same orientation angle, and the subscript  $T$ , which denotes that the total layup of the laminate is listed, as opposed to a partial list for symmetric laminates.

If each layer is composed of the same material, the integration of Eq. (2.47) can be performed for the stiffness matrices in terms of the orientation angle alone. The following notation for the stiffness matrices is attributed to Tsai & Pagano<sup>76</sup> and Miki<sup>77</sup>, and expresses the stiffness terms through the invariant material properties and some stacking sequence parameters, such that:

$$[A, B, D] = \begin{bmatrix} U_1 V_0 + U_2 V_1 + U_3 V_3 & U_4 V_0 - U_3 V_3 & \frac{-U_2 V_2}{2} - U_3 V_4 \\ U_4 V_0 - U_3 V_3 & U_1 V_0 - U_2 V_1 + U_3 V_3 & \frac{-U_2 V_2}{2} + U_3 V_4 \\ \frac{-U_2 V_2}{2} - U_3 V_4 & \frac{-U_2 V_2}{2} + U_3 V_4 & U_5 V_0 - U_3 V_3 \end{bmatrix} \quad (2.48)$$

where the integration of the stacking sequence is represented as:

$$\begin{aligned} V_{0\{A, B, D\}} &= \{H, 0, H^3/12\} \\ V_{1\{A, B, D\}} &= \int_H \cos 2\phi \{1, z, z^2\} dz & V_{2\{A, B, D\}} &= \int_H \sin 2\phi \{1, z, z^2\} dz \\ V_{3\{A, B, D\}} &= \int_H \cos 4\phi \{1, z, z^2\} dz & V_{4\{A, B, D\}} &= \int_H \sin 4\phi \{1, z, z^2\} dz \end{aligned} \quad (2.49)$$

These integrated quantities are termed in-plane stiffness coefficients. Furthermore, for typical composite laminates, the integration is made even easier since the material properties are constant throughout the thickness of each individual lamina, so that the integration can be replaced by a summation in the  $z$ -direction. For example, the integration of  $V_{1D}$  can also be represented as

$$V_{1D} = \int_H \cos 2\phi \ z^2 dz = \sum_{k=1}^{K_{layers}} \cos 2\phi_k \frac{z_k^3 - z_{k-1}^3}{3} \quad (2.50)$$

where  $K_{layers}$  is the total number of plies,  $(z_k, z_{k-1})$  are the distances from the middle surface to the faces of the  $k$ th layer, and  $\phi_k$  is the orientation angle of that layer.

By restricting ourselves to shells constructed of balanced, symmetric laminates we can further simplify some of the terms of Eq. (2.49). A “balanced” laminate implies that for every non-zero  $+\phi$  angle of the stacking sequence, there exists a corresponding  $-\phi$  angle to balance the anisotropic nature of a rotated orthotropic layer. If such is the case then the integrals  $V_{2A}$  and  $V_{4A}$  are equal to zero, since they do not depend on the location of the layers but only the value of the sine of the orientation angles, which cancel if the laminate is balanced. “Symmetric” means that the layup is a reflection of itself about  $z = 0$ , and since in Eq. (2.49) any odd function as an integrand is equal to zero, all terms  $V_{iB}$  vanish. Incidentally, the combination of balance and symmetry for a multi-layered laminate stacking sequence often renders  $V_{2D}$  and  $V_{4D}$  small when compared to the other  $V_{iD}$  terms, and often these terms are ignored, though they will not be for this investigation. Therefore, the contribution to the laminate stiffness for multi-layered composites under these restrictions becomes:

$$\begin{bmatrix} N_x \\ N_\theta \\ N_{x\theta} \end{bmatrix} = \begin{bmatrix} A_{11} & A_{12} & 0 \\ A_{12} & A_{22} & 0 \\ 0 & 0 & A_{66} \end{bmatrix} \begin{bmatrix} \epsilon_x^o \\ \epsilon_\theta^o \\ \gamma_{x\theta}^o \end{bmatrix} \quad \begin{bmatrix} M_x \\ M_\theta \\ M_{x\theta} \end{bmatrix} = \begin{bmatrix} D_{11} & D_{12} & D_{16} \\ D_{12} & D_{22} & D_{26} \\ D_{16} & D_{26} & D_{66} \end{bmatrix} \begin{bmatrix} \kappa_x^o \\ \kappa_\theta^o \\ \kappa_{x\theta}^o \end{bmatrix} \quad (2.51)$$

where the stiffness terms are calculated as per Eq. (2.48).

Lastly, we define the effective moduli and Poisson's ratios of the laminate in terms of the extensional stiffness measures as:

$$E_x = \frac{A_{11}A_{22} - A_{12}^2}{A_{22}H} \quad E_\theta = \frac{A_{11}A_{22} - A_{12}^2}{A_{11}H} \quad G_{x\theta} = \frac{A_{66}}{H} \quad (2.52)$$

$$v_{x\theta} = \frac{A_{12}}{A_{22}} \quad v_{\theta x} = \frac{A_{12}}{A_{11}}$$

These quantities provide a method of comparing the principal stiffness measures of multi-layered composites to traditional single-layered orthotropic or isotropic materials. Additionally, these stiffness expressions often appear in certain cases of the governing equations and will be used extensively to make the notation more concise.

### Stress Analysis

Along with the stiffness concepts just discussed, Classical Lamination Theory contains information about the assumed stress state in each layer of the laminate due to the assumptions of the Kirchhoff-Love hypothesis. Thus the strains in terms of the three dimensions ( $x, \theta, z$ ) as defined by Eq. (2.15) can be used to determine the state of strain at any location in the body. The stresses can likewise be found through the orthotropic constitutive relations of Eq. (2.42). Orthotropic materials, along with their directional stiffness characteristics, possess unequal failure characteristics along perpendicular material directions. Therefore, to fully analyze the feasibility of a given stress state, the stresses and strains along the principal material directions need to be calculated. Note, however, that the neglect of the transverse shear stresses in the constitutive laws does limit the accuracy of the stress analysis, for multi-layered composites often fail due to interlaminar stresses which Classical Lamination Theory cannot account for. This topic will not be addressed in this study. Instead, the failure loads for the in-plane stress components will be the only criteria used to investigate the strength of the laminated structure.

For orthotropic materials, failure will be based on a first-ply-failure mode in conjunction with maximum stress or maximum strain failure criterion. This means that the laminate is considered to have failed in a material sense when a stress or strain in a principal material direction attains its strength value. Though first-ply-failure does not usually imply total collapse of the structure, it does produce a substantial drop in performance and is often used as a design criterion. To estimate the load to achieve first-ply-failure, the state of stress for a given load level must be determined, i.e. the governing equations must be solved. Once this is completed, the most direct method to extract the actual stresses and strains for each lamina is to calculate the total surface strains from the middle surface quantities as in Eq. (2.15). The value of  $z$  in this equation determines for which layer the strain is being calculated. Since each layer can have a different orthotropic orientation angle, the strains in the surface coordinates must be transformed to principal material directions for each ply. This is accomplished through a tensorial rotation as before:

$$\begin{bmatrix} \epsilon_1 \\ \epsilon_2 \\ \gamma_{12}/2 \end{bmatrix} = \begin{bmatrix} \cos^2 \varphi & \sin^2 \varphi & 2 \sin \varphi \cos \varphi \\ \sin^2 \varphi & \cos^2 \varphi & -2 \sin \varphi \cos \varphi \\ -\sin \varphi \cos \varphi & \sin \varphi \cos \varphi & \cos^2 \varphi - \sin^2 \varphi \end{bmatrix} \begin{bmatrix} \epsilon_x \\ \epsilon_\theta \\ \gamma_{x\theta}/2 \end{bmatrix} \quad (2.53)$$

The stresses can be found through the orthotropic relations of Eq. (2.39), if required. To determine when failure is imminent, each laminae must be examined separately. Since the stresses and strains vary linearly within each layer, the critical values of these quantities must be located at the interface between layers, thus the first-ply-failure criteria is applied at each of these boundaries.

To determine the critical load for which failure is likely, the stresses or strains must be compared to the material failure estimates for the material. For most cases, a “dead” load is initially applied to the structure, such that the magnitude of these applied dead loads does not change. Secondly, proportional “live” loads are applied, which need not be of the same load type as the dead loads. Proportional loading means that the magnitude of the different live loads are assumed to increase at proportional rates, where their ratio is determined beforehand. For example, fuselage structures must usually withstand a dead load of interior pressure, while live loads including bending, torsion, and shear vary throughout flight and their relative magnitudes are determined by the global geometry and loading of the structure. Therefore, to determine the critical load for failure, two stress states must be determined: the initial state due to the dead loads (denoted by a superscript  $d$ ), and a progressive state which increases linearly and is proportional to the live loads (superscript  $l$ ). Once the stresses (or strains) are known throughout the structure for these conditions, a material failure estimation (using maximum stress or maximum strain criterion) can be determined using the formula:

$$MF = \text{minimum} \left[ \frac{X_t - \sigma_1^d}{\sigma_1^l}, \frac{X_c - \sigma_1^d}{\sigma_1^l}, \frac{Y_t - \sigma_2^d}{\sigma_2^l}, \frac{Y_c - \sigma_2^d}{\sigma_2^l}, \frac{S - \tau_{12}^d}{\tau_{12}^l} \right] \quad (2.54)$$

where the material failure parameter  $MF$  is usually positive and represents the amount of increase of the live loads to produce failure. The five possible modes of failure in Eq. (2.54) correspond to tensile ( $X_t$ ) and compressive ( $X_c$ ) failure in the fiber direction, tensile ( $Y_t$ ) and compressive ( $Y_c$ ) failure in the transverse direction, and shear failure ( $S$ ) for in-plane shear deformation. These five modes of failure must be investigated at all locations in the structure. The material failure load can also be formulated in terms of the strains, in which case the failure constraints would correspond to maximum strains in each direction. If the value of  $MF$  is less than or equal to zero, the laminate has failed due to the dead loads only. This case often occurs for nonlinear problems, in which the dead loads are calculated at equilibrium of the static solution, and the live loads are represented by

the rate of change of these loads along the nonlinear load path. For highly nonlinear problems, the material failure analysis should be performed at each load step to be considered accurate.

For isotropic materials, no principal material directions exist, therefore the preceding calculations have no relevance. Instead, the traditional Tresca criterion (see a basic strength of materials reference such as Gere & Timoshenko<sup>78</sup>) will be used to determine material failure, which depends on the magnitudes of the principal middle surface stresses for a given stress state. Using this criterion, a similar calculation for  $MF$  representing the yielding of the isotropic material can easily be formulated.

### 2.2.2 Variable Stiffness Concept

One distinguishing aspect of this work is that the solution of the cylindrical shell problem includes the effect of variable  $[A, B, D]$  matrices throughout the shell. By considering cylinders with this feature, we should be able to design the stiffness characteristics to take full advantage of the orthotropic material properties in regards to the applied loading and improve the performance of the structure as a whole. The mathematical modelling employed for this endeavor is to define the orthotropic stiffness parameters at discrete spatial locations along the variation, and then to use these representative values to formulate the stiffness terms and their derivatives along that direction. To simplify the solution techniques for this preliminary investigation of the variable stiffness concept, stiffness variations are constrained to be in only one direction. We thus present the three techniques used in this investigation to produce stiffness matrices which are functions of the surface coordinates  $x$  and  $\theta$ .

#### Curvilinear Fiber Paths

The stiffness variation within a composite laminate is based on the fiber orientation angle  $\phi$  of each ply. This is the basic building block of each stiffness term of Eq. (2.51), which are usually calculated through the in-plane stiffness coefficients of Eq. (2.49). When the fiber orientation angle for each lamina is the same for all locations within the structure, these coefficients are constants for the given stacking sequence of the laminate. These "constant stiffness" laminates can be referred to as straight fiber formats, since the path of an individual fiber is a linear function of the surface coordinates. The path of the fiber is found by simple integration (here we will employ  $r$ - $s$  coordinates which are rotated by an angle  $\Phi$  with respect to the  $x$ - $\theta$  surface directions to remain consistent with the curvilinear fiber discussion presented in Section 1.2.1):

$$\frac{ds}{dr} = \tan \phi \quad \Rightarrow \quad s(r) = (\tan \phi)r + C \quad (2.55)$$

The constant  $C$  merely represents a shift in the  $s$ -direction that is incremented as successive fiber



paths are laid down alongside each other. Since each path is a straight line, the edges of the paths will be aligned perfectly and no overlap will occur.

Within the variable stiffness concept, the fiber orientation angle  $\varphi$  is allowed to vary along the  $r$ -direction, thus the stiffness terms are no longer constants but become a function of location. Now the path of an individual fiber is not a linear function of the  $r$ - $s$  coordinates. For instance, consider the standard linear variation of the fiber orientation angle mentioned earlier, with  $T_0$  being the value of  $\varphi$  at the origin and  $T_l$  being the value at some distance  $l_1$ :

$$\varphi(r) = (T_l - T_0) \frac{r}{l_1} + T_0 \quad 0 \leq r \leq l_1 \quad (2.56)$$

The fiber path for this equation is again found through integration:

$$\frac{ds}{dr} = \tan \varphi(r) \quad \Rightarrow \quad s(r) = \frac{-l_1 \ln(\cos[\varphi(r)])}{(T_l - T_0)} + C \quad (2.57)$$

Examples of the curvilinear paths produced by this equation have previously been displayed in Figure 1.1 and Figure 1.2. The constant  $C$  in Eq. (2.57) is chosen so that no gaps exist between adjacent fibers for each successive pass of the tow placement machine. However, since the fiber path is not a straight line, some overlap will occur unless ply drops are allowed, as seen in Figure 1.2a. For this study, we will assume that this capability of the tow placement machine is used, so that the curvilinear fiber paths produce the desired stiffness variation without any thickness change in the laminate.

To include an *arbitrary* variation of stiffness, several functions were considered to serve as a basis for representation of the fiber orientation angle, such as an expression of the variation in terms of an expansion by Legendre polynomials or trigonometric (Fourier) functions. However, it was found that the best general representation of the fiber orientation angle is in terms of the linear variation of Eq. (2.56). Two reasons motivated this choice: (a) to represent the *stiffness* terms in a Fourier expansion, functions similar to  $\cos[\varphi(r)]$  must be integrable, and this can only be done analytically for a linear function of  $\varphi$ ; and (b) to include the possibility of multiple constant stiffness areas that are connected at their edges, for instance a crown/side/keel arrangement around the circumference in which each component is allowed a different stacking sequence. This leads to a “linked” line segment approach shown in Figure 2.6, where the fiber orientation angle for each segment is defined by its endpoint values (the  $rs$  subscript denotes the rotated coordinate system). The ply angles and endpoint locations are both variable, and can approximate any function if enough segments are used. Within the total range, the fiber orientation angle is thus defined as

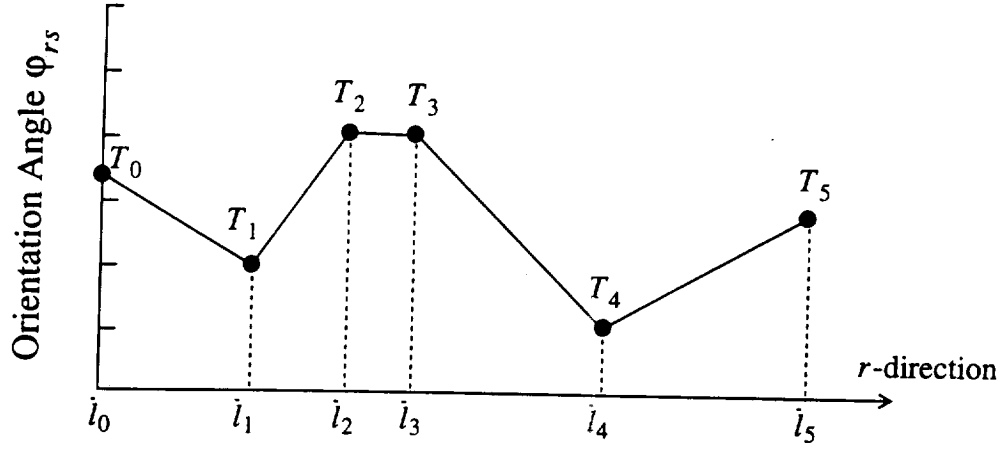


Figure 2.6: Linked Line Segment Approach of Fiber Orientation Angle

$$\phi_{rs}(r) = (T_i - T_{i-1}) \frac{r - \bar{l}_{i-1}}{\bar{l}_i - \bar{l}_{i-1}} + T_{i-1} \quad \bar{l}_{i-1} \leq r \leq \bar{l}_i \quad (i = 1, N_{seg}) \quad (2.58)$$

The endpoint values  $\bar{l}_i$  are typically normalized with respect to some meaningful distance in the direction of the stiffness variation. For a cylinder, a stiffness variation in the axial direction will have  $\bar{l}_0 = 0$  at one end and  $\bar{l}_{N_{seg}} = 1$  located at  $x = L/2$ , and the definition will be symmetric about the half-length to cover the entire cylinder axis. Similarly, for a circumferential variation the fundamental distance will be equal to  $\pi$  measured in the  $\theta$ -direction, so that the stiffness variation will be symmetric about the  $Y = 0$  line in Figure 2.1. Typically, the locations of the endpoint will be at regularly spaced intervals within the appropriate domain, and the designation of a variable stiffness ply in the stacking sequence will be of the form

$$\Phi < T_0 | T_1 | T_2 | \dots | T_{N_{seg}} > \quad \text{which implies} \quad \bar{l}_i = i / N_{seg} \quad \phi = \Phi + \phi_{rs} \quad (2.59)$$

Here  $\Phi$  is the rotation angle between the direction of the stiffness variation and the  $x$ -axis, and it is equal to  $0^\circ$  or  $90^\circ$  for an axial or circumferential variation, respectively. The fiber orientation angle in  $x$ - $\theta$  coordinates is then equal to  $\Phi + \phi_{rs}$ . Additionally, for circumferential stiffness variations a crown/side/keel arrangement is often considered, in which there are three areas of constant (but possibly different) stiffness characteristics. This can be constructed using the notation of Figure 2.6 with the stipulation that  $T_0 = T_1$ ,  $\bar{l}_1 = \bar{l}_2$ ,  $T_2 = T_3$ ,  $\bar{l}_3 = \bar{l}_4$ , and  $T_4 = T_5$ .

Finally, there also exists a limit on the variables of the linked line segment approach due to manufacturing considerations. In the introduction it was mentioned that one such constraint dealt with the minimum radius of curvature of the fiber tows for flat panels. A similar constraint will be used here for cylindrical shells, and takes the form of

$$\rho_{\min} \leq \frac{(\bar{l}_i - \bar{l}_{i-1})}{|T_i - T_{i-1}| \cos[\varphi_{rs}(r)]} \quad \text{for } \bar{l}_{i-1} \leq r \leq \bar{l}_i, \quad i = 1, N_{seg} \quad (2.60)$$

The value of  $\rho_{\min}$ , the minimum radius allowable by the tow placement machine, will be assumed to be the same as the flat panel value of 25", though it is believed that smaller values actually exist for curved surfaces.

### Dropped Plies

Another mechanism to change the stiffness of a thin laminate is by adding or removing plies, which changes the thickness as well as the stiffness characteristics of the shell. Since Classical Lamination Theory integrates through the thickness to calculate the stiffness matrices, the effect of this change is wholly contained within the  $[A, B, D]$  matrices. An argument against this approach is that it does not apply at the end of the dropped plies, where the free edge effects will produce three-dimensional stress states that lead to failure. However, the inclusion of these free edge effects demands a more rigorous three-dimensional analysis that is beyond the scope of this study, and therefore will be ignored.

The construction of the added ply configuration is shown in Figure 2.7, where the thickness of



**Figure 2.7: Geometry of Dropped Ply Construction**

each individual ply is designated as  $t_p$ . For reference purposes, the value of  $H$  for such a structure is based on the original laminate without the thickness variation. The plies are assumed to be symmetric about the middle surface and composed of a  $+\varphi_p$  and  $-\varphi_p$  layer so that the structure remains balanced. Then for all locations within the domain of the added ply, the addition to the stiffness terms of the original laminate can be calculated as

$$\begin{aligned} A_{ij} &= 4t_p \cdot \bar{Q}_{ij}(\varphi_p) & B_{ij} &= 0 & D_{ij} &= \frac{1}{12}[(H + 4t_p)^3 - H^3] \cdot \bar{Q}_{ij}(\varphi_p) & j \neq 6 \\ A_{ij} &= 0 & B_{ij} &= 0 & D_{ij} &= \frac{2}{3}[3Ht_p^2 + 7t_p^3] \cdot \bar{Q}_{ij}(\varphi_p) & j = 6 \end{aligned} \quad (2.61)$$

where the transformed reduced stiffnesses  $\bar{Q}_{ij}$  are calculated from Eq. (2.43). Note that the plies are constrained to be symmetric about the middle surface and therefore produce no contribution to the  $[B]$  matrix, which facilitates the analysis though limits the applicability of the added/dropped

ply analysis. Thus the effect of the thickness change is reflected in the value of the stiffness terms, for they have been altered proportionally to the thicker structure. This method for dropped/added plies can also apply to standard thickness changes using an isotropic material, where the thickness can vary smoothly over a region by introducing multiple dropped plies of varying thicknesses. Material failure can also be estimated by simply regarding the added material as a change in shell thickness, and using the standard method to find the stress state at the given shell location.

### Discrete Stiffeners

As discussed in Section 1.2.2, the inclusion of stiffeners for shell analysis has often been accomplished by “smearing” the stiffness properties over the total structure so that the solutions for unstiffened cylindrical shells can be applied. Since our premise is that the stiffness is automatically a function of location, we can more accurately model the stiffeners by defining their stiffness characteristics at the point of attachment to the laminate skin. The stiffeners are treated as discrete beams, which for the variable stiffness concept means the obvious: the stiffener produces a discrete change in stiffness at the point of attachment equivalent to a one-dimensional beam. Though this treatment of the stiffeners does contain some degree of approximation in the resulting solutions (see Bushnell<sup>34</sup> for a discussion of the influence of nonlinear and prebuckling effects for stiffened shell structures), the obvious inclusion within the variable stiffness concept is warranted for the type of problems that we are investigating. The beam is assumed to withstand only axial stresses and torsional loads, and the resistance to these loads is calculated from the stiffness of the beam material as well as the shape of the cross-section, which is arbitrary. Therefore, to incorporate the characteristics of the stiffener into the variable stiffness concept, an estimation of the elastic behavior of a beam under extension, flexure, and torsion is required (see Figure 2.8). The

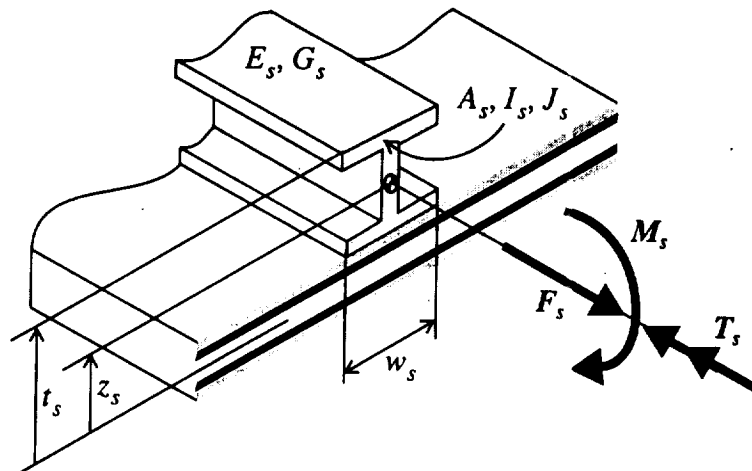


Figure 2.8: Physical Properties of Stiffeners

relevant quantities required to calculate these attributes from elementary beam theory include the extensional and torsional moduli  $E_s$  and  $G_s$ , cross-sectional area  $A_s$ , distance to the centroid  $z_s$ , and the moment of inertia  $I_s$  and torsional constant  $J_s$  measured about this centroid. The stiffeners can be attached on the exterior of the cylinder (for which  $z_s > 0$ ) or the interior ( $z_s < 0$ ). Also needed is the maximum height  $t_s$ , which is used for material failure considerations, and the width  $w_s$  over which the stiffener is attached to the laminate, since for wide attachments the stiffness properties will be smeared over this distance. The stiffener material is assumed to be either isotropic or a constant stiffness composite laminate defined by effective moduli parameters and corresponding material failure characteristics. An example of a composite stiffener is outlined in Appendix C.

The cross-sectional parameters are used to relate the applied loading of the beam to strain measures of the beam, including the axial strain  $\epsilon_s$ , axial curvature  $\kappa_s$ , and angle of twist per unit length  $\phi_s$  (which are in the same direction as the force, moment, and torque in Figure 2.8):

$$F_s = E_s A_s \epsilon_s \quad M_s = E_s I_s \kappa_s \quad T_s = G_s J_s \phi_s \quad (2.62)$$

These strain and force quantities of the beam must both be related to appropriate middle surface shell quantities so that they can be included in the stiffness characteristics of the shell. This is accomplished by finding the equivalent shell force and moment resultants that are acting at the centroid of the stiffener, as well as defining the beam strains at the centroid through the middle surface strain quantities. For instance, the equivalent system acting on the centroid of a beam aligned to the cylinder axis in terms of the axial stress resultants  $N_x$ ,  $M_x$ , and  $M_{x\theta}$  acting at the middle surface of the shell and smeared over the width of the beam is

$$F_s = N_x w_s \quad M_s = (M_x + N_x z_s) w_s \quad T_s = M_{x\theta} w_s \quad (2.63)$$

Note that the shear stress resultant  $N_{x\theta}$  is not included, since the beam is assumed to only withstand shear loads due to torsion. The axial strain, curvature, and twist at the centroid of the beam are found from Eq. (2.15) in terms of the middle surface strain quantities, so that

$$\epsilon_s = \epsilon_x^o + z_s \kappa_x^o \quad \kappa_s = \kappa_x^o \quad \phi_s = \kappa_{x\theta}^o \quad (2.64)$$

Insertion of these transformations into Eq. (2.62) generates the appropriate additions to the CLT stiffness matrices. The stiffeners are restricted to be either ring stiffeners, which alter the  $[A, B, D]$  matrices along the length, or axial stringers, which are used for a circumferential variation of stiffness. Therefore the additions to the stiffness matrices (for either ring stiffeners or longitudinal stringers, respectively) for locations within the width of the attachment are calculated as

$$\begin{aligned}
A_{22}(x) = A_{11}(\theta) &= \frac{E_s A_s}{w_s} & B_{22}(x) = B_{11}(\theta) &= \frac{E_s A_s z_s}{w_s} \\
D_{22}(x) = D_{11}(\theta) &= \frac{E_s (I_s + A_s z_s^2)}{w_s} & D_{66}(x) = D_{66}(\theta) &= \frac{G_s J_s}{w_s}
\end{aligned} \tag{2.65}$$

For material failure considerations, the axial stresses in the beams are calculated using the beam constitutive relations

$$\sigma_s = E_s \varepsilon_s = E_s (\varepsilon_x^o + z \kappa_x^o) \tag{2.66}$$

For the axial stress to attain its maximum or minimum value, the  $z$ -location in Eq. (2.66) should correspond to either  $(H/2)$  or  $(H/2 + t_s)$ . For the beam under torsion, the value of the shear stress at these locations depends heavily on the shape of the stiffener cross-section. However it can be shown that the magnitude of these shear stresses is small when compared to the axial stresses of the beam, mostly due to the fact that the shell skin carries most of the shear loads, and therefore the contribution of the shear stresses in the beam will be ignored for simplicity in the material failure analysis.

### Combined Variable Stiffness Concept

The three mechanisms just presented can be combined into one general relation for the total laminate constitutive laws, where each stiffness term is calculated from the sum total of Eq. (2.51), (2.61), and (2.65), which correspond to curvilinear fibers, dropped plies, and discrete stiffeners, respectively.

$$\begin{aligned}
\begin{bmatrix} N_x \\ N_\theta \\ N_{x\theta} \end{bmatrix} &= \begin{bmatrix} A_{11} & A_{12} & 0 \\ A_{12} & A_{22} & 0 \\ 0 & 0 & A_{66} \end{bmatrix} \begin{bmatrix} \varepsilon_x^o \\ \varepsilon_\theta^o \\ \gamma_{x\theta}^o \end{bmatrix} + \begin{bmatrix} B_{11} & 0 & 0 \\ 0 & B_{22} & 0 \\ 0 & 0 & 0 \end{bmatrix} \begin{bmatrix} \kappa_x^o \\ \kappa_\theta^o \\ \kappa_{x\theta}^o \end{bmatrix} \\
\begin{bmatrix} M_x \\ M_\theta \\ M_{x\theta} \end{bmatrix} &= \begin{bmatrix} B_{11} & 0 & 0 \\ 0 & B_{22} & 0 \\ 0 & 0 & 0 \end{bmatrix} \begin{bmatrix} \varepsilon_x^o \\ \varepsilon_\theta^o \\ \gamma_{x\theta}^o \end{bmatrix} + \begin{bmatrix} D_{11} & D_{12} & D_{16} \\ D_{12} & D_{22} & D_{26} \\ D_{16} & D_{26} & D_{66} \end{bmatrix} \begin{bmatrix} \kappa_x^o \\ \kappa_\theta^o \\ \kappa_{x\theta}^o \end{bmatrix}
\end{aligned} \tag{2.67}$$

These stiffness matrices are in general a function of  $x$  and  $\theta$ . Note that the stiffness coupling terms  $B_{11}$  and  $B_{22}$  are only present for ring and axial stiffeners, respectively. The importance of these coupling terms becomes apparent in the determination of the buckling loads.

### 2.2.3 Classical Membrane and Semi-Membrane Constitutive Theories

This subsection introduces two common approximations to the constitutive laws of Eq. (2.67) that result in signification reduction in the complexity of the governing equations. Both rely on the assumption that the shell walls are thin enough to neglect certain stiffness terms. The first theory is applicable to short shells and is employed predominantly for the analysis of Chapter 4.0, while the second theory is used for longer shells that are subjected to inextensional deformation, such as the problems involving the Brazier effect under bending.

#### Classical Membrane Constitutive Theory

Classical membrane theory is a simplified constitutive theory that is commonly used in the analysis of shells because the solution can frequently be completed analytically. The results are often quite accurate when compared to more rigorous analyses, especially when applied to very thin and short shells. The basic premise of membrane theory is that the shell carries loads only through the action of the surface stresses, and that the “membrane” is incapable of resisting changes in curvature of the shell surface. The standard analogy for this constitutive theory is that of a balloon, which resists stretching but deforms easily to any load applied normal to the surface. The assumptions of membrane theory are enforced through the constitutive equations, whereby the terms that represent bending of the shell wall, the  $[B]$  and  $[D]$  stiffness matrices of Eq. (2.67), are assumed to be zero. Since these stiffness terms are of order  $(H/R)$  and  $(H/R)^2$ , respectively, when compared to the in-plane stiffness measures, membrane theory is considered a reliable first-order approximation for thin shells. However, any membrane solution should be tested for validity by determining if the original suppositions of the theory hold. For instance, the solution of a shell whose loading produces large curvatures but relatively small in-plane strains would not be applicable under the guises of membrane theory.

Utilization of the membrane assumptions guarantees that the strains are constant through the thickness of the shell, and that the moment and shear force stress resultants of the shell are negligible. Since membrane theory effectively ignores localized bending of the shell, it also neglects the boundary conditions at the ends which are related to this effect. These boundary conditions correspond to the specification of the radial displacement, and either the shell rotation or moment stress resultant present at the ends (this will be detailed further in Section 2.3.3). Furthermore, the absence of the  $[B]$  and  $[D]$  stiffness terms in the governing equations reduces the order of the equations from eight to four, thereby making the differential equations much easier to solve. The reduced order of the equations corresponds to the neglecting of the boundary conditions just mentioned, so that the cross-section at the ends may deform from a non-circular state. This is one of the major limitations of membrane theory: the inability to account for radial restraint.

A second limitation of membrane theory is also a result of this reduction of order of the governing equations. It can be shown that under membrane theory, the system of equilibrium equations for a cylindrical shell maintains that the variation of the axial and shear stress resultants is totally determined by the stipulation of these quantities at any location along the length. Thus the stress distribution is not allowed to diffuse along the length of the shell, which contradicts the intuitive result referred to as the St. Venant effect. Therefore, the membrane solution is only valid for shorter cylinders which do not undergo drastic stress redistribution.

Bearing these limitations in mind, the constitutive laws of classical membrane theory under the definitions of CLT are written here in terms of the effective stiffness measures of Eq. (2.52):

$$\begin{bmatrix} N_x \\ N_\theta \\ N_{x\theta} \end{bmatrix} = \begin{bmatrix} \frac{E_x H}{1 - \nu_{x\theta} \nu_{\theta x}} & \frac{\nu_{\theta x} E_x H}{1 - \nu_{x\theta} \nu_{\theta x}} & 0 \\ \frac{\nu_{x\theta} E_\theta H}{1 - \nu_{x\theta} \nu_{\theta x}} & \frac{E_\theta H}{1 - \nu_{x\theta} \nu_{\theta x}} & 0 \\ 0 & 0 & G_{x\theta} H \end{bmatrix} \begin{bmatrix} \epsilon_x^o \\ \epsilon_\theta^o \\ \gamma_{x\theta}^o \end{bmatrix} \quad (2.68)$$

### Semi-membrane Constitutive Theory

Semi-membrane, or semi-moment, theory is an alternate form of membrane theory that neglects bending of the shell wall in the axial direction only, thereby eliminating the boundary layer present in usual shell problems. It was first introduced by V. Z. Vlasov<sup>79</sup>, and its application is for long shells or ones in which the variation of the stresses and strains is slow in the axial direction. The difference between *classical* membrane theory and the semi-membrane approach is that the latter includes the cross-sectional deformation associated with changes of curvature in the circumferential direction. By including this additional contribution, the limitation involving the variation of the stress distribution along the length is removed (though the inability to account for radial restraint still exists). Semi-membrane theory also ignores the Poisson effect and assumes that the circumferential strain is negligible, thereby making the deformation inextensional in that direction. Thus, the earlier derivation of the condition of circumferential inextensionality (Section 2.1.3) has direct relevance here. Often the shear strain is taken to be zero as well, though we will discover that this assumption may be invalid for some of our specific problems. Further details of semi-membrane theory are discussed in the reference by Vasiliev<sup>80</sup>. Our application of semi-membrane theory will only be for the problem of nonlinear bending due to the Brazier effect. The majority of the published research into this problem has utilized this constitutive theory to render the equations more manageable and often solvable for approximate systems.



We first assume that Classical Lamination Theory has been used to express the force resultants in terms of the middle surface strain quantities. The variable stiffness concept is also utilized, so that the equations of the last two sections produce the general relations of Eq. (2.67). We now invoke the assumptions of semi-membrane constitutive theory. First, shell bending in the axial direction and twisting are ignored. This can be expressed mathematically as

$$B_{11}, B_{22}, D_{11}, D_{12}, D_{66}, D_{16}, D_{26} \rightarrow 0 \quad (2.69)$$

Since semi-membrane theory neglects the Poisson effect, the in-plane stress resultants depend only on their corresponding strain measures, and can be found from Eq. (2.68) by letting the Poisson's ratios go to zero:

$$N_x = E_x H \epsilon_x^o \quad N_\theta = E_\theta H \epsilon_\theta^o \quad N_{x\theta} = G_{x\theta} H \gamma_{x\theta}^o \quad (2.70)$$

The inextensionality condition is satisfied at the constitutive level by the assumption that  $E_\theta \rightarrow \infty$ . Typical semi-membrane theory also often assumes zero shear strain (i.e.  $G_{x\theta} \rightarrow \infty$ ), though for the general problem of Brazier deformation this assumption is invalid. The importance of shear strain for nonlinear bending with the Brazier effect was first surmised by Libai & Bert<sup>67</sup> for arbitrary beam loading of finite length tubes. Though the shear stress is obviously significant when transverse beam forces are present, it will be shown that its inclusion is also warranted for the pure bending case, since shear deformation does exist near the ends of the structure due to the presence of the end restraints which maintain the circular shape of the cross-section. In fact, the production of shear stresses near this boundary is the driving force that transforms the deformed cross-sectional shape into a circle at the ends. Therefore, the neglecting of the shear strain does not apply for the nonlinear bending of finite length cylinders, and the necessary constitutive relations for semi-membrane theory become

$$N_x = E_x H \epsilon_x^o \quad N_{x\theta} = G_{x\theta} H \gamma_{x\theta}^o \quad M_\theta = D_{22} \kappa_\theta^o \quad (2.71)$$

One final remark is needed concerning the circumferential stress. Though the deformation is assumed inextensional around the circumference, this does not imply that the stress resultant is zero as well. Instead  $N_\theta$  is merely an intermediate stress measure that does not follow a constitutive law, much like the shear forces  $Q_x$  and  $Q_\theta$  for shell theory that neglects transverse shear deformation. However, calculation of the three-dimensional stresses for each layer must include the fact that this circumferential stress exists. This is accomplished by assuming that each lamina carries the circumferential stress proportional to its stiffness in that direction, thus

$$\sigma_{\theta} = \bar{Q}_{22} \cdot \frac{N_{\theta}}{A_{22}} \quad (2.72)$$

This applies to the semi-membrane solution of the Brazier problem only.

## 2.3 Equilibrium Equations

This section derives the equations for static equilibrium and stability for cylindrical shells in terms of the middle surface stress and strain quantities. The derivation will be performed using energy methods, which state that the total potential energy of the system must be a minimum to achieve equilibrium. Variational techniques are employed to translate this condition into suitable differential equations which must be satisfied for static equilibrium of the system. Boundary conditions for the problem are also obtained in this manner. Furthermore, a system to estimate the stability of the equilibrium state is generated by the assumption of a small perturbation from the equilibrium solution.

### 2.3.1 Total Potential Energy of a Linearly Elastic System

The cylindrical shell under the action of end loads and surface tractions is chosen as the system under study. The loads associated with this system are assumed to be conservative, which means that the work done in moving from one configuration to another is independent of the path taken. This implies that the state of the system can be represented in terms of a potential energy, which is equivalent to the negative amount of the work done in displacing from some reference configuration. For a linearly elastic body, the total potential energy is separated into an internal energy portion, which represents the work done by the deformation of the elastic body (strain energy), and a contribution from external forces acting on the system that produce displacements at their point of application, so that

$$\text{Total Potential Energy} = \text{Internal Energy} - \text{Work done by External Forces} \quad (2.73)$$

Furthermore, the principle of stationary potential energy states that for a conservative system, the variation of this total potential energy must be a minimum for the system to be in equilibrium. Therefore, if the internal energy and external work are expressed in terms of the field variables of the cylindrical shell, the application of the principle of stationary potential energy will generate the necessary conditions for equilibrium.

The internal energy of a linearly elastic cylindrical shell can be expressed (see Langhaar<sup>81</sup>) as

$$U = \frac{1}{2} \iiint [\sigma_x \epsilon_x + \sigma_{\theta} \epsilon_{\theta} + \tau_{x\theta} \gamma_{x\theta} + \tau_{xz} \gamma_{xz} + \tau_{\theta z} \gamma_{\theta z} + \sigma_z \epsilon_z] dx R d\theta dz \quad (2.74)$$

Using the assumptions of first-order shell theory, this integral can be evaluated through the thickness and represented in terms of the middle surface stress resultants and strain quantities. The strains are represented in terms of their middle surface counterparts through Eq. (2.15), and the integration can be carried out for the stresses as defined in Eq. (2.45). Note that the stress-strain relations and the Kirchhoff-Love assumption are not explicitly used, so that the following derivation could include any linear constitutive laws allowable under first-order shell theory, such as transverse shear deformation. Actually, the equilibrium equations are formulated along these lines so that the contributions from the transverse shear force resultants (discussed below) are more apparent, yet this derivation also enables the theory to be easily expanded to include such transverse shear deformation.

Returning to the integration of the strain energy, note that the last three terms of Eq. (2.74) contain some expressions for stress which do not have a corresponding middle surface definition under Classical Lamination Theory. This is due to the presumption that the transverse strains are negligible under the auspices of the Kirchhoff-Love assumption. Since we are not employing this assumption at this time, we define two new stress resultants, termed shear force resultants, as

$$Q_x = \int_H \tau_{xz} dz \quad Q_\theta = \int_H \tau_{\theta z} dz \quad (2.75)$$

With first-order transverse shear deformation theory, these force resultants will have a constitutive law to relate them to their respective strain quantities, however under CLT these quantities are merely intermediate variables that arise in the equations of equilibrium, though they also represent a physical quantity corresponding to the transverse shear force applied to the shell. For the final term of Eq. (2.74), the evaluation through the thickness results in the expression:

$$\int_H \sigma_z dz \quad (2.76)$$

It can be shown that integration of this term and application of the boundary conditions at the top and bottom of the surface leads to a quantity proportional to the pressure applied to the surface, but that the magnitude of the contribution to the internal energy is of the order of the square of  $(H/R)$ . Thus the small effect of this term, even when compared to the other transverse quantities, enables it to be effectively ignored. This result also substantiates the claim made in Eq. (2.38) that the transverse normal stress is small when compared to the other stresses. Therefore, the expression for the internal energy for the cylindrical shell after integration can be represented as

$$U = \frac{1}{2} \iint [N_x \epsilon_x^o + N_\theta \epsilon_\theta^o + N_{x\theta} \gamma_{x\theta}^o + M_x \kappa_x^o + M_\theta \kappa_\theta^o + M_{x\theta} \kappa_{x\theta}^o + Q_x \gamma_{xz}^o + Q_\theta \gamma_{\theta z}^o] dx R d\theta \quad (2.77)$$

The work done on the shell by external forces that produce displacements consists of surface



tractions and body forces in each of the three directions ( $x, \theta, z$ ). For this investigation, we limit the contributions of these general loadings to only include transverse pressure applied perpendicular to the surface. Furthermore, since we expect large cross-sectional deformation for some cases, the transverse pressure is chosen so as to always act normal to the surface as it deforms. Thus the total work done by this pressure is determined by the change in area of the cross-sectional contour integrated along the length of the shell. The area of the undeformed cross-section is, of course,  $\pi R^2$ . The deformed area is calculated through the use of a line integral in terms of the rectangular cross-sectional coordinates (see Figure 2.1 for the coordinate definitions), such that

$$A_1 = \frac{R^2}{2} \oint [\psi_1 d\zeta_1 - \zeta_1 d\psi_1] \quad (2.78)$$

The deformed rectangular coordinates are expressed in terms of the middle surface cylindrical variables using Eq. (2.1) and (2.7), which after employing the linear strain measures of Eq. (2.21) become

$$\begin{aligned} \psi_1 &= (v^o/R)\cos\theta + (1 + w^o/R)\sin\theta & d\psi_1 &= [(1 + e_{\theta\theta})\cos\theta + e_{\theta z}\sin\theta]d\theta \\ \zeta_1 &= (v^o/R)\sin\theta - (1 + w^o/R)\cos\theta & d\zeta_1 &= [(1 + e_{\theta\theta})\sin\theta - e_{\theta z}\cos\theta]d\theta \end{aligned} \quad (2.79)$$

Insertion of these relations into Eq. (2.78) and noting that

$$\oint \frac{\partial v^o}{\partial \theta} d\theta = 0 \quad (2.80)$$

due to the periodicity of the function  $v^o$  gives the final result for the deformed area as

$$A_1 = \pi R^2 + \oint \left[ w^o + \frac{1}{2}(w^o e_{\theta\theta} - v^o e_{\theta z}) \right] R d\theta \quad (2.81)$$

Then the work done by the internal pressure on the surface (positive for an increase in area) is

$$W = p \int (A_1 - \pi R^2) dx = p \iint \left[ w^o + \frac{1}{2}(w^o e_{\theta\theta} - v^o e_{\theta z}) \right] dx R d\theta \quad (2.82)$$

The total potential energy of the cylindrical shell under pressure loading is  $V = U - W$ , or

$$\begin{aligned} V &= \frac{1}{2} \iint [N_x \epsilon_x^o + N_\theta \epsilon_\theta^o + N_{x\theta} \gamma_{x\theta}^o + M_x \kappa_x^o + M_\theta \kappa_\theta^o + M_{x\theta} \kappa_{x\theta}^o + Q_x \gamma_{xz}^o + Q_\theta \gamma_{\theta z}^o] dx R d\theta - \\ &\quad p \iint \left[ w^o + \frac{1}{2}(w^o e_{\theta\theta} - v^o e_{\theta z}) \right] dx R d\theta \end{aligned} \quad (2.83)$$

This integral is in terms of seven independent field variables: the middle surface displacements

$(u^o, v^o, w^o)$ ; the middle surface rotations  $\omega_x^o, \omega_\theta^o$ ; the linear transverse strain  $e_{zz}$ ; and the deflection of the beam axis  $a_z(x)$  and its derivatives. For an equilibrium state, the energy of the system must be a minimum for any allowable change of the independent field variables. This can also be expressed as the fact that the first variation of the potential energy must equal zero. This condition of equilibrium is formulated mathematically using the calculus of variations. For example, a surface integral in terms of an independent function and its first-order derivatives is expressed as

$$V = \iint F[x, \theta, g, g', \dot{g}] dx d\theta \quad (2.84)$$

where the prime and dot represent derivatives with respect to the  $x$  and  $\theta$  coordinates, respectively, and the function  $F$  is generally nonlinear. To calculate the first variation of this integral, a perturbation to the dependent variable ( $\delta g$ ) and its derivatives is assumed, and integration by parts is performed until the integrand involves only terms directly related to the perturbation  $\delta g$ . This procedure also generates evaluations at the limits, which become the boundary conditions of the problem. For a general nonlinear function as in Eq. (2.84), the calculus of variations states that the supposition that the first variation of this integral must be zero is equivalent to the condition that

$$\frac{\partial F}{\partial g} - \frac{\partial}{\partial x} \left[ \frac{\partial F}{\partial g'} \right] - \frac{\partial}{\partial \theta} \left[ \frac{\partial F}{\partial \dot{g}} \right] = 0 \quad (2.85)$$

along with the boundary conditions which are expressed as

$$\begin{aligned} g &= g^\dagger \quad \text{or} \quad \frac{\partial F}{\partial g'} = 0 && \text{on edge } x = \text{constant} \\ g &= g^\dagger \quad \text{or} \quad \frac{\partial F}{\partial \dot{g}} = 0 && \text{on edge } \theta = \text{constant} \end{aligned} \quad (2.86)$$

The dagger denotes some known quantity at that location. The first condition of Eq. (2.86) is often referred to as a “forced” or “geometric” boundary condition, which means that the variable there is constrained to be a certain value (often zero), while the latter choice is termed a “natural” condition, implying that the resulting expression must be zero to correctly minimize the integral of Eq. (2.84). These equations can be expanded in terms of several independent variables and/or higher order derivatives in an obvious manner (see Langhaar<sup>31</sup> for details).

### 2.3.2 Nonlinear Static Equilibrium Equations

Applying Eq. (2.85) of the calculus of variations to the potential energy expression Eq. (2.83) results in the following six differential equations of equilibrium for the shell variables. Much like the strains of Eq. (2.20), the overbar signifies the highly nonlinear terms that are only needed for drastic cross-sectional deformation:

Axial displacement  $u^o$ :

$$\frac{\partial N_x}{\partial x} + \frac{1}{R} \frac{\partial N_{x\theta}}{\partial \theta} = 0 \quad (2.87)$$

Circumferential displacement  $v^o$ :

$$\begin{aligned} \frac{\partial N_{x\theta}}{\partial x} + \frac{N_{x\theta}}{R} e_{xz} + \frac{1}{R} \frac{\partial}{\partial \theta} [N_\theta (1 + \overline{e_{\theta\theta}})] + \frac{N_\theta}{R} e_{\theta z} + \frac{1}{R} \frac{\partial}{\partial \theta} [\overline{Q_\theta \omega_\theta^o}] + \frac{Q_\theta}{R} (1 + \overline{e_{zz}}) + \\ \frac{1}{R} \frac{\partial}{\partial \theta} \left[ \overline{M_\theta \left( \frac{1}{R} + k_{\theta\theta} \right)} \right] + \frac{\overline{M_\theta}}{R} k_{\theta z} + N_x \kappa_y \sin \theta - p e_{\theta z} = 0 \end{aligned} \quad (2.88)$$

Transverse displacement  $w^o$ :

$$\begin{aligned} \frac{\partial Q_x}{\partial x} + \frac{1}{R} \frac{\partial}{\partial \theta} [Q_\theta (1 + \overline{e_{zz}})] - \frac{\overline{Q_\theta}}{R} \omega_\theta^o + \frac{1}{R} \frac{\partial}{\partial \theta} [\overline{M_\theta k_{\theta z}}] - \frac{\overline{M_\theta}}{R} \left( \frac{1}{R} + k_{\theta\theta} \right) + \\ \left[ \frac{\partial N_{x\theta}}{\partial x} + \frac{1}{R} \frac{\partial N_\theta}{\partial \theta} \right] e_{\theta z} + N_x \left[ \frac{\partial e_{xz}}{\partial x} - \kappa_y \cos \theta \right] + N_{x\theta} \left[ \frac{\partial e_{\theta z}}{\partial x} + \frac{1}{R} \frac{\partial e_{xz}}{\partial \theta} \right] + \\ \frac{N_\theta}{R} \left[ \frac{\partial e_{\theta z}}{\partial \theta} - (1 + \overline{e_{\theta\theta}}) \right] + p (1 + \overline{e_{\theta\theta}}) = 0 \end{aligned} \quad (2.89)$$

Axial rotation  $\omega_x^o$ :

$$\frac{\partial M_x}{\partial x} + \frac{1}{R} \frac{\partial M_{x\theta}}{\partial \theta} - Q_x = 0 \quad (2.90)$$

Circumferential rotation  $\omega_\theta^o$ :

$$\frac{\partial M_{x\theta}}{\partial x} + \frac{1}{R} \frac{\partial}{\partial \theta} [M_\theta (1 + \overline{e_{\theta\theta}})] + \frac{\overline{M_\theta}}{R} e_{\theta z} - Q_\theta (1 + \overline{e_{\theta\theta}}) = 0 \quad (2.91)$$

Linear transverse strain  $e_{zz}$ :

$$\frac{1}{R} \frac{\partial}{\partial \theta} [\overline{M_\theta e_{\theta z}}] - \frac{\overline{M_\theta}}{R} (1 + \overline{e_{\theta\theta}}) - \overline{Q_\theta} e_{\theta z} = 0 \quad (2.92)$$

Eq. (2.87) - (2.92) are the equilibrium equations conforming to first-order classical nonlinear shell theory. Together with the application of the Kirchhoff-Love condition, the constitutive equations, and the strain-displacement relations, these equations define the equilibrium state of the cylindrical shell system in terms of the middle surface displacements. Further simplifications will be made in later sections for specific loading and material definitions.

In addition to the above system, a differential equation for the beam deflection  $a_z(x)$  is derived along the same lines. However, since the function  $a_z$  is only dependent on the axial coordinate, the

integration in the circumferential direction can only be evaluated symbolically. This results in:

$$\frac{d^2}{dx^2} \left\{ \oint N_x [(R + w^o) \cos \theta - R \cos \theta_{ref} - v^o \sin \theta] R d\theta \right\} \equiv \frac{d^2}{dx^2} [M_y(x)] = 0 \quad (2.93)$$

This equation corresponds to the beam equation of the cylindrical shell. The integral involving  $N_x$  is actually the definition of the beam moment  $M_y$ , and the equation conforms to the classical beam equation as expected. The beam shear force  $V_z(x)$  will also be defined here as

$$V_z(x) \equiv -\frac{d}{dx} [M_y(x)] \quad (2.94)$$

which follows from classical beam theory. Note that Eq. (2.93) is actually a fourth-order ordinary differential equation in terms of the beam deflection  $a_z(x)$ , since  $N_x$  is proportional to  $\kappa_y(x)$ , the second derivative of  $a_z(x)$ . Similar equations for bending about the Z-axis exist, with the exception that sine and cosine functions are interchanged.

### 2.3.3 Boundary Conditions

To generate the boundary conditions for the system, Eq. (2.86) of the calculus of variations is employed in the same manner as was used for the equilibrium equations. The general equations for the unknown shell variables which must be evaluated at  $x = 0, L$  are then:

$$\begin{aligned} u^o &= u^\dagger \quad \text{or} \quad N_x = 0 & \omega_x^o &= \omega_x^\dagger \quad \text{or} \quad M_x = 0 \\ v^o &= v^\dagger \quad \text{or} \quad N_{x\theta} = 0 & \omega_\theta^o &= \omega_\theta^\dagger \quad \text{or} \quad M_{x\theta} = 0 \\ w^o &= w^\dagger \quad \text{or} \quad Q_x = 0 & e_{zz} &= e_{zz}^\dagger \end{aligned} \quad (2.95)$$

The beam variable  $a_z(x)$  requires two boundary conditions at each end, given as:

$$a_z = a_z^\dagger \quad \text{or} \quad V_z = 0 \quad \Omega_y = \Omega_y^\dagger \quad \text{or} \quad M_y = 0 \quad (2.96)$$

Corresponding equations for  $a_y(x)$  are expressed by exchanging  $z \leftrightarrow y$  in Eq. (2.96).

The boundary conditions given above established for our particular problem are derived from examination of Figure 2.9. Here the general loading consists of a simply supported beam under arbitrary beam loading which is symmetric about  $x = L/2$ . The symmetric plane located at the mid-length is assumed to be able to slide horizontally and vertically, but remain fixed for axial translation as well as with regards to rotation in any of the three directions. To formulate these simply supported beam conditions in terms of the displacement variables, the horizontal and vertical beam displacements ( $a_y$  and  $a_z$ ) are zero at the ends, while the other displacement ( $\bar{U}$ ) and



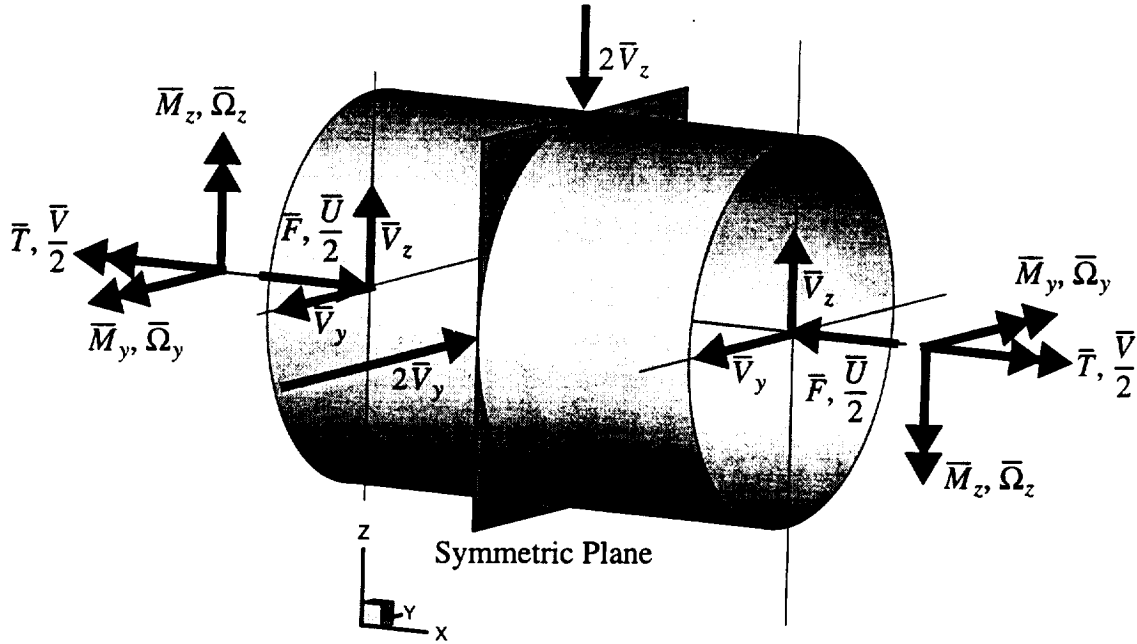


**Figure 2.9: Boundary Conditions for Cylindrical Shell**

rotation quantities ( $V, \Omega_y, \Omega_z$ ) are of opposite sign at each end, and are shown in the figure with their corresponding load quantity and symbol. Also note that the end displacement  $\bar{U}$  and axial rotation  $\bar{V}$  also contain a factor of one-half, so that the global deformation for the whole shell equals the value of the applied displacement. Additionally, the shell is constrained to remain circular at the ends, so that any variables which would produce cross-sectional deformation must be zero there. Under these stipulations, attention need only be focused on one half of the cylinder.

The specific boundary conditions for the shell variables are given as:

Shell variables at  $x = 0$ :

$$\begin{aligned} u^o &= \bar{U}/2 \quad \text{or} \quad N_x = 0 & v^o &= \bar{V}/2 \quad \text{or} \quad N_{x\theta} = 0 & w^o &= 0 \\ \omega_x^o &= -\bar{\Omega}_y \cos \theta - \bar{\Omega}_z \sin \theta \quad \text{or} \quad M_x = 0 & \omega_\theta^o &= 0 & e_{zz} &= 0 \end{aligned} \quad (2.97)$$

Shell variables at  $x = L/2$ :

$$\begin{aligned} u^o &= 0 & v^o &= 0 & Q_x &= 0 \\ \omega_x^o &= 0 & M_{x\theta} &= 0 & e_{zz} &= 0 \end{aligned} \quad (2.98)$$

Note that these expressions come directly from the variational techniques in terms of the six unknown field variables. Therefore if any supplementary assumptions are to be invoked, these boundary conditions may also change slightly to accommodate these assumptions. For example,

enforcement of the Kirchhoff-Love hypothesis results in the combination of the boundary conditions for  $v^o$  and  $\omega_\theta^o$  into one equation, as well as the condition that  $e_{zz} = 0$ . If a membrane constitutive theory is being used, then the only relevant boundary conditions here would correspond to  $u^o$  and  $v^o$ , which are termed the *membrane* boundary conditions. Semi-membrane theory also considers circumferential bending of the shell, so that the equation governing  $\omega_\theta^o$  will also be needed.

Concerning the boundary conditions for the beam variables in Figure 2.9, the problem has heretofore been formulated in terms of the beam deflections and rotations, and the proper variational procedure generates boundary conditions in terms of these variables:

Beam variables at  $x = 0$ :

$$\begin{aligned} a_z &= 0 & \Omega_y &= \bar{\Omega}_y \text{ or } M_y = 0 \\ a_y &= 0 & \Omega_z &= \bar{\Omega}_z \text{ or } M_z = 0 \end{aligned} \quad (2.99)$$

Beam variables at  $x = L/2$ :

$$\begin{aligned} a_z|_{x \rightarrow L/2^+} &= a_z|_{x \rightarrow L/2^-} & \Omega_y &= 0 \\ a_y|_{x \rightarrow L/2^+} &= a_y|_{x \rightarrow L/2^-} & \Omega_z &= 0 \end{aligned} \quad (2.100)$$

The boundary conditions concerning the beam deflections in Eq. (2.100) are required to preserve continuity of the beam across the discontinuity produced by the applied shear loads. However, for most stress analysis problems, the actual values of the deflections need not be calculated, for the resulting stresses and strains from the applied loads are wholly contained in the higher derivatives of the deflections (the beam rotations and curvatures). Therefore the integration to find the deflections need not be performed and, subsequently, only three boundary conditions are required for the beam structure. These are expressed in an alternate form in terms of the beam load variables:

Beam variables at  $x = 0$ :

$$\begin{aligned} \Omega_y &= \bar{\Omega}_y \text{ or } M_y = 0 \\ \Omega_z &= \bar{\Omega}_z \text{ or } M_z = 0 \end{aligned} \quad (2.101)$$

Beam variables at  $x = L/2$ :

$$\begin{aligned} V_z &= \bar{V}_z & \Omega_y &= 0 \\ V_y &= \bar{V}_y & \Omega_z &= 0 \end{aligned} \quad (2.102)$$

### 2.3.4 Stability Equations from the Perturbation of the Equilibrium Solution

The preceding two sections supplied the necessary conditions for static equilibrium of the

shell in the form of a boundary value problem, that is, a system of differential equations with specific constraints applied at certain locations. The solution of this system provides the displacements, strains, and stresses of the loaded shell, and can be used to investigate the stiffness and strength response of the cylindrical shell under arbitrary loading conditions. However, another consideration that must be addressed is the concept of stability. In mathematical terms, stability determines if the calculated equilibrium state is necessarily a minimum of the total potential energy of the system. In more physical language, instability implies that a small perturbation from the equilibrium configuration may lead to a drastic change in the state of the structure. If the equilibrium state is “stable”, the effect of this small perturbation decays and the configuration returns to the original static equilibrium solution. However, an “unstable” equilibrium state may bifurcate to a new equilibrium solution, one which is of quite different character than the original, but which also satisfies the equilibrium equations. This possibility is due to the nonlinearity of the equilibrium solutions, such that more than one solution to the equations for a given loading condition may exist. Therefore, the stability analysis relies on determining the result when a small perturbation from the equilibrium state is introduced. Since this perturbation is arbitrarily small, we use the equations already developed with the stipulation that the perturbed displacements, rotations, and strains are small. This greatly simplifies the equations, as we shall see, and leads to the formulation of an eigenvalue problem to determine the stability of the shell.

To determine stability, the equilibrium solution of the nonlinear boundary value problem is perturbed through an amount  $\delta$ . For example, the solution in terms of the cylindrical displacements is represented by a vector such that

$$\hat{u} = \{u^o, v^o, w^o\}^T = \hat{u}_0 + \delta \hat{u}_1 \quad (2.103)$$

where the 0 subscript denotes the “0 state” configuration and the 1 denotes the perturbed displacements. Insertion of the equations for the displacements and strains into the expression for the total potential energy  $V$  of Eq. (2.83) yields a similar expansion expressed as

$$V = V_0 + \delta V_1 + \delta^2 V_2 + O(\delta^3) \quad (2.104)$$

The first term in this expansion is a constant for a given displacement configuration and is a measure of the total potential energy of the system at the 0 state. As stated earlier, for such a state to be considered in equilibrium, the total potential energy must be a minimum. In mathematical terms, the minimization of this quantity can be expressed as two necessary and sufficient conditions: that the first variation is zero, and that the second variation is positive. The stipulation that the  $V_1$  term in the above expansion will vanish produces the equilibrium equations for the 0 state variables,

which was earlier derived using the calculus of variations. Thus the second variation  $V_2$  measures the stability of the equilibrium state for an arbitrary configuration of the 1 state variables, so that as long as the quantity remains positive the equilibrium state is valid. However, for certain values of destabilizing loads, there will exist some configuration of the perturbed displacements that will render the second variation zero. In theory, at this point the third variation of the total potential energy must be examined to determine the viability of the equilibrium state, however in practice the load level at which the second variation first becomes non-positive is usually defined as the critical load due to instability.

For the physical system derived in this investigation, the second variation of the total potential energy takes the form of a linear system of equations in terms of the perturbed displacements and the 0 equilibrium state variables. It is represented mathematically as

$$[K]\delta_1 = 0 \quad (2.105)$$

For a valid equilibrium state, the determinant of this matrix must be positive definite. However, for a given structure and load condition the  $[K]$  matrix, termed the stiffness matrix, is strictly a function of the magnitude of the loading, defined as the load level  $\Lambda$ . Therefore the determination of the critical load level for the system of Eq. (2.105) consists of finding the zero of the determinant as a function of the load level  $\Lambda$ . Numerically, this process does not lend itself to traditional root finding methods. Instead, the method of finding the critical determinant is reformulated as an eigenvalue problem. The initial equilibrium state is defined as the load  $\Lambda_0$ . An incremental change in this load level and a standard Taylor expansion of  $K(\Lambda)$  generates the eigenvalue problem:

$$\begin{aligned} \{[K] + \delta\Lambda[M] + O(\delta\Lambda^2)\} \cdot \delta = 0 \\ [K] = [K(\Lambda_0)] \quad [M] = \left. \frac{d}{d\Lambda}[K] \right|_{\Lambda = \Lambda_0} \quad \Lambda_1 = \Lambda_0 + \delta\Lambda \end{aligned} \quad (2.106)$$

The terms in the  $[M]$  matrix, referred to as the geometric stiffness matrix, are simply the terms in the stiffness matrix  $[K]$  that change when the load is increased. The solution of the eigenvalue problem produces an eigenvalue  $\delta\Lambda$  which can be regarded as a correction to the load factor which produces instability. The procedure is then repeated for an initial load value of  $\Lambda_1 + \delta\Lambda$  until the ensuing eigenvalue  $\delta\Lambda$  is considered to be effectively zero, at which point it can be concluded that the equilibrium state is unstable for the load level  $\Lambda_1$ . This numerical procedure to find the eigenvalue is much more reliable than finding the root of the determinant of  $[K]$  (see the work of Thurston<sup>82</sup>). It should also be noted here that for some systems, the stiffness matrix  $[K]$  is exactly linear with respect to the load level  $\Lambda$ . These particular cases are much simpler to solve than the

general problem, since the eigenvalue problem need be solved at only one load level to determine the correct value of the destabilizing loads. In this investigation, this occurs when the prebuckling analysis is linear and the stability estimation ignores the prebuckling deformations. These details will be clarified in the formulation of the stability equations.

To generate the detailed mathematical form of the eigenvalue problem for the cylindrical shell, we assume a small perturbation in the shell displacement variables as defined by Eq. (2.103). Perturbations of the beam displacements will not be considered, so that the buckling mode will consist of “local” buckling of the shell only. Though “global” buckling is a possibility, the estimation of these critical modes can usually be expressed theoretically and need not be calculated numerically. For this formulation, we also assume that the Kirchhoff-Love hypothesis has been applied. The middle surface strains and curvatures after the perturbation of the displacements given in Eq. (2.103) are represented as

$$\begin{aligned}\bar{\epsilon} &= \{\epsilon_x^o, \epsilon_\theta^o, \gamma_{x\theta}^o\}^T = \bar{\epsilon}_0 + \delta\bar{\epsilon}_1 + \delta^2\bar{\epsilon}_2 \\ \bar{\kappa} &= \{\kappa_x^o, \kappa_\theta^o, \kappa_{x\theta}^o\}^T = \bar{\kappa}_0 + \delta\bar{\kappa}_1\end{aligned}\tag{2.107}$$

Here the 0 subscripted quantities denote the expressions already derived for the nonlinear strain-displacement relations as given in Eq. (2.20), while the others are defined as

$$\begin{aligned}
\varepsilon_{x_1}^o &= \frac{\partial u_1}{\partial x} + \overline{\kappa_y(w_1 \cos \theta - v_1 \sin \theta)} + \left( \frac{\partial w_0^o}{\partial x} \right) \left( \frac{\partial w_1}{\partial x} \right) & \varepsilon_{x_2}^o &= \frac{1}{2} \left( \frac{\partial w_1}{\partial x} \right)^2 \\
\varepsilon_{\theta_1}^o &= \left[ 1 + \left( \frac{1}{R} \frac{\partial v_0^o}{\partial \theta} + \frac{w_0^o}{R} \right) \right] \left( \frac{1}{R} \frac{\partial v_1}{\partial \theta} + \frac{w_1}{R} \right) + \left( \frac{v_0^o}{R} - \frac{1}{R} \frac{\partial w_0^o}{\partial \theta} \right) \left( \frac{v_1}{R} - \frac{1}{R} \frac{\partial w_1}{\partial \theta} \right) \\
\gamma_{x\theta_1}^o &= \frac{1}{R} \frac{\partial u_1}{\partial \theta} + \frac{\partial v_1}{\partial x} + \left( \frac{\partial w_0^o}{\partial x} \right) \left( \frac{v_1}{R} - \frac{1}{R} \frac{\partial w_1}{\partial \theta} \right) + \left( \frac{v_0^o}{R} - \frac{1}{R} \frac{\partial w_0^o}{\partial \theta} \right) \left( \frac{\partial w_1}{\partial x} \right) \\
\varepsilon_{\theta_2}^o &= \frac{1}{2} \left( \frac{v_1}{R} - \frac{1}{R} \frac{\partial w_1}{\partial \theta} \right)^2 + \frac{1}{2} \left( \frac{1}{R} \frac{\partial v_1}{\partial \theta} + \frac{w_1}{R} \right)^2 & \gamma_{x\theta_2}^o &= \left( \frac{\partial w_1}{\partial x} \right) \left( \frac{v_1}{R} - \frac{1}{R} \frac{\partial w_1}{\partial \theta} \right) \\
\kappa_{x_1}^o &= \frac{\partial^2 w_1}{\partial x^2} & \kappa_{x\theta_1}^o &= \frac{1}{R} \left( \frac{\partial v_1}{\partial x} - 2 \frac{\partial^2 w_1}{\partial x \partial \theta} \right) \\
\kappa_{\theta_1}^o &= \left[ 1 + \left( \frac{1}{R} \frac{\partial v_0^o}{\partial \theta} + \frac{w_0^o}{R} \right) \right] \frac{1}{R^2} \left( \frac{\partial v_1}{\partial \theta} - \frac{\partial^2 w_1}{\partial \theta^2} \right) + \frac{1}{R} \left( 1 + \frac{\partial w_0^o}{\partial \theta} + e_{zz_0} \right) \left( \frac{1}{R} \frac{\partial v_1}{\partial \theta} + \frac{w_1}{R} \right) + \\
&\quad \frac{1}{R} \left( \frac{v_0^o}{R} - \frac{1}{R} \frac{\partial w_0^o}{\partial \theta} + \omega_{\theta_0}^o - \frac{\partial e_{zz_0}}{\partial \theta} \right) \left( \frac{v_1}{R} - \frac{1}{R} \frac{\partial w_1}{\partial \theta} \right) & \kappa_{\theta_2}^o &= \left( \frac{1}{R} \frac{\partial v_1}{\partial \theta} + \frac{w_1}{R} \right) \frac{1}{R^2} \left( \frac{\partial v_1}{\partial \theta} - \frac{\partial^2 w_1}{\partial \theta^2} \right)
\end{aligned} \tag{2.108}$$

The overbars again signify the highly nonlinear terms that are only required for problems with significant cross-sectional deformation. The expression for the second variation of the total potential energy is found by retaining terms of order  $\delta^2$  after insertion of these expansions into Eq. (2.83). After some manipulation the equation for  $V_2$  becomes

$$\begin{aligned}
V_2 &= \frac{1}{2} \iint [A_{11} \varepsilon_{x_1}^{o^2} + 2A_{12} \varepsilon_{x_1}^o \varepsilon_{\theta_1}^o + A_{22} \varepsilon_{\theta_1}^{o^2} + A_{66} \gamma_{x\theta_1}^{o^2} + 2B_{11} \varepsilon_{x_1}^o \kappa_{x_1}^o + 2B_{22} \varepsilon_{\theta_1}^o \kappa_{\theta_1}^o + \\
&\quad D_{11} \kappa_{x_1}^{o^2} + 2D_{12} \kappa_{x_1}^o \kappa_{\theta_1}^o + D_{22} \kappa_{\theta_1}^{o^2} + D_{66} \kappa_{x\theta_1}^{o^2} + 2D_{16} \kappa_{x_1}^o \kappa_{x\theta_1}^o + 2D_{26} \kappa_{\theta_1}^o \kappa_{x\theta_1}^o + \\
&\quad N_{x_0} \left( \frac{\partial w_1}{\partial x} \right)^2 + N_{\theta_0} \left[ \left( \frac{v_1}{R} - \frac{1}{R} \frac{\partial w_1}{\partial \theta} \right)^2 + \left( \frac{1}{R} \frac{\partial v_1}{\partial \theta} + \frac{w_1}{R} \right)^2 \right] + 2N_{x\theta_0} \left( \frac{\partial w_1}{\partial x} \right) \left( \frac{v_1}{R} - \frac{1}{R} \frac{\partial w_1}{\partial \theta} \right) + \\
&\quad \frac{2M_{\theta_0}}{R} \left( \frac{1}{R} \frac{\partial v_1}{\partial \theta} + \frac{w_1}{R} \right) \left( \frac{1}{R} \frac{\partial v_1}{\partial \theta} - \frac{1}{R} \frac{\partial^2 w_1}{\partial \theta^2} \right) + \frac{2M_{\theta_0}}{R} \left( \frac{1}{R} \frac{\partial v_1}{\partial \theta} + \frac{w_1}{R} \right) - \\
&\quad \frac{p}{R} \left( v_1^2 - v_1 \frac{\partial w_1}{\partial \theta} + w_1 \frac{\partial v_1}{\partial \theta} + w_1^2 \right) ] dx R d\theta
\end{aligned} \tag{2.109}$$

The eigenvalue problem is formulated from Eq. (2.109) by maintaining that the variation of  $V_2$  with respect to each degree of freedom for the 1 state variables is zero. For numerical techniques such as the Rayleigh-Ritz method, the elements of the stiffness matrix are most easily calculated through integration of the terms in this equation. This method is outlined in Appendix B. More thorough expressions in terms of the perturbed displacements and the CLT stiffness terms can be found in the succeeding chapters, when the general problem given above is specialized in terms of loading conditions and the direction of the stiffness variation.

An alternative method of formulating the stability equations is to employ the calculus of variations to the integral to produce three differential equations in terms of the perturbed displacements. This is often useful if closed form solutions exist or if numerical methods that operate on differential equations are to be used. These equations are written here without the nonlinear cross-sectional deformation terms (those with an overbar in the preceding equations) for brevity.

Axial direction:

$$\frac{\partial}{\partial x}[N_{x_1}] + \frac{1}{R} \frac{\partial}{\partial \theta}[N_{x\theta_1}] = 0 \quad (2.110)$$

Circumferential direction:

$$\begin{aligned} \frac{\partial}{\partial x}\left[N_{x\theta_1} + \frac{M_{x\theta_1}}{R}\right] + \frac{1}{R} \frac{\partial}{\partial \theta}\left[N_{\theta_1} + \frac{M_{\theta_1}}{R}\right] + \left(p - \frac{N_{\theta_0}}{R}\right)\left(\frac{v_1}{R} - \frac{1}{R} \frac{\partial w_1}{\partial \theta}\right) + \\ \frac{N_{x\theta_0}}{R} \left(\frac{\partial w_1}{\partial x}\right) + \left(\frac{\partial w_0}{\partial x}\right) \frac{N_{x\theta_1}}{R} - \left(\frac{v_0}{R} - \frac{1}{R} \frac{\partial w_0}{\partial \theta}\right) \frac{N_{\theta_1}}{R} = 0 \end{aligned} \quad (2.111)$$

Radial direction:

$$\begin{aligned} \frac{\partial^2}{\partial x^2}[M_{x_1}] + \frac{2}{R} \frac{\partial^2}{\partial x \partial \theta}[M_{x\theta_1}] + \frac{1}{R^2} \frac{\partial^2}{\partial \theta^2}[M_{\theta_1}] - \frac{N_{\theta_1}}{R} - N_{x_0}[\kappa_{x_1}] - N_{\theta_0}[\kappa_{\theta_1}] + \\ p\left(\frac{1}{R} \frac{\partial v_1}{\partial \theta} + \frac{w_1}{R}\right) - N_{x\theta_0}[\kappa_{x\theta_1}] - \left[\frac{\partial N_{x\theta_0}}{\partial x} + \frac{1}{R} \frac{\partial N_{\theta_0}}{\partial \theta}\right]\left(\frac{v_1}{R} - \frac{1}{R} \frac{\partial w_1}{\partial \theta}\right) - \\ \kappa_{x_0}[N_{x_1}] - \kappa_{\theta_0}[N_{\theta_1}] - \kappa_{x\theta_0}[N_{x\theta_1}] - \left(\frac{v_0}{R} - \frac{1}{R} \frac{\partial w_0}{\partial \theta}\right)\left[\frac{\partial N_{x\theta_1}}{\partial x} + \frac{1}{R} \frac{\partial N_{\theta_1}}{\partial \theta}\right] = 0 \end{aligned} \quad (2.112)$$

Here the perturbed resultant forces and moments (with a 1 subscript) are related to the perturbed strain quantities using the standard Classical Lamination Theory equations, Eq. (2.57).

The presentation of the stability equations in this differential form also reveals some important facts about the eigenvalue problem. Due to the fact that we neglected terms with order greater

than  $\delta^2$ , the eigenvalue problem is linear with respect to the perturbed variables, as expected. The loading of the prebuckled state is mainly introduced through the membrane stress resultants, though prebuckling deformation in terms of rotations and curvatures is also present. When a nonlinear prebuckled state is used, the critical load must be calculated using the numerical technique as outlined in Eq. (2.106), in which several eigensystems must be solved along the nonlinear load path to obtain an accurate result for the buckling load. However, what is not as evident is that this iterative technique for the eigenvalue problem must also be used whenever the effects of the prebuckling deformation are included. This is due to the presence of several terms that are quadratic with respect to the prebuckling deformations, such as those in the last line of both Eq. (2.111) and (2.112). The prebuckling rotations and curvatures are coefficients of the perturbed stress measures, which also contain multiples of the prebuckling rotations through the constitutive relations and the perturbed strains of Eq. (2.108). Therefore, even if a linear prebuckling solution is obtained, these quadratic terms generate a nonlinear eigenvalue problem that is most efficiently solved using the numerical technique outlined earlier. Unfortunately, it was shown by Bushnell<sup>83</sup> that neglecting these nonlinear prebuckling terms while retaining their linear aspects can lead to errors that may be greater than those resulting from neglecting the prebuckling deformations altogether. Therefore though it is advantageous from a numerical efficiency standpoint to ignore these prebuckling rotations, the loss of accuracy that this generates may be prohibitive. This will be discussed in more detail in Section 3.5 when we compare the results for buckling under axial compression using different prebuckling solutions.

The boundary conditions for the perturbed system are also found using the equations of the calculus of variations. At the ends, it is assumed that the radial displacement is always constrained to be zero, and the combination of the other three conditions results in eight distinct possibilities for end conditions. They are classified here according to the definitions proposed by Almroth<sup>37</sup>:

$$\begin{array}{ll}
 \text{S1:} & u_1 = v_1 = M_{x_1} = 0 \\
 \text{S2:} & N_{x_1} = v_1 = M_{x_1} = 0 \\
 \text{S3:} & u_1 = N_{x\theta_1} = M_{x_1} = 0 \\
 \text{S4:} & N_{x_1} = N_{x\theta_1} = M_{x_1} = 0 \\
 \text{C1:} & u_1 = v_1 = w_1' = 0 \\
 \text{C2:} & N_{x_1} = v_1 = w_1' = 0 \\
 \text{C3:} & u_1 = N_{x\theta_1} = w_1' = 0 \\
 \text{C4:} & N_{x_1} = N_{x\theta_1} = w_1' = 0
 \end{array} \tag{2.113}$$

The 'S' denotes simply supported conditions, while 'C' implies clamped ends. Usually, these end conditions correspond to the constraints imposed on the prebuckling solution. At the mid-length, the buckled configuration is not necessarily symmetric in the axial direction. However, an arbitrary condition can be achieved by assuming a linear combination of a symmetric and anti-sym-



metric portion. These are defined for each case as:

$$\begin{aligned} \text{Symmetric case} \quad & u_1 = N_{x\theta_1} = Q_{x_1} = w_1' = 0 \\ \text{Unsymmetric case} \quad & N_{x_1} = v_1 = w_1 = M_{x_1} = 0 \end{aligned} \quad (2.114)$$

## 2.4 Summary of Governing Equations

The three basic building blocks governing the physics of a thin cylindrical shell subjected to general beam loading have now been formulated, namely the strain-displacement relations, constitutive laws, and equilibrium equations. Each portion contains some distinctive deviations from the standard first-order cylindrical equations. Firstly, the strain-displacement relations were derived by the combination of global displacements associated with beam bending along with the more traditional variables representing the surface of the shell. Particular nonlinear terms were retained that correctly model the nonlinear Brazier effect for all lengths of cylinders, which led to a nonlinear enforcement of the Kirchhoff-Love assumption and the condition of inextensionality of the cross-section. Secondly, Classical Lamination Theory was expanded to include three mechanisms to produce a structure with variable stiffness properties: curvilinear fibers; dropped/added plies or thickness changes; and discrete stiffeners. The introduction of these concepts into the equilibrium equations produced additional terms which do not exist in the standard cylindrical shell equations. These include extra nonlinear terms that give the correct response for the Brazier effect, and the presence of derivatives of stiffness parameters in the surface directions. Furthermore, the governing equations still remain general enough so that transverse shear effects can easily be included by the definition of additional constitutive laws. The development of the particular shell equations that correctly model these phenomena is quite a substantial work, and represents a major percentage of this investigation. However, the actual solution of these governing equations must also be performed so that the unique behavior of these concepts can be further investigated.

The system of governing equations derived in this chapter presents quite a formidable boundary value problem, an eighth order nonlinear partial differential equation with variable coefficients. The numerical solution of such a system is quite laborious and time intensive. Since one of the main goals of this investigation is the exploration of the variable stiffness concept as a design environment, more efficient solutions that still accurately model the physics of the problem need to be employed. The basic technique to achieve this end is to reduce the dimension of the solution by transforming the partial differential equations into ordinary ones. This can be accomplished by using two procedures: limiting the stiffness variation to be in one surface direction only; and utilizing a simplifying assumption so that the solution can be performed analytically in the other direction. Along these lines, the next four chapters specialize the general governing equations of a

variable stiffness cylindrical shell derived in Chapter 2.0 into four distinct sub-problems with specific stiffness variations and loading conditions. These sub-problems consist of (a) the axisymmetric problem, in which the stiffness variation and loading do not change in the circumferential direction; (b) a linear membrane solution for a short cylinder segment, with the stiffness varying in the circumferential direction only; (c) nonlinear bending of infinite length tubes, which utilizes the highly nonlinear shell equations and a circumferential stiffness variation is allowed; and (d) nonlinear bending of finite length cylinders, where the linearized Brazier solution is employed along with an axial stiffness variation.

## Chapter 3.0 Axisymmetric Solution with an Axial Stiffness Variation

In this chapter, the governing equations will be simplified by assuming that the cylinder contains a stiffness variation only in the axial direction, produced by the standard mechanisms of the variable stiffness concept as outlined in the last chapter. Further specialization will be performed by imposing the constraint that the loading and boundary conditions follow the nature of the stiffness properties by being axisymmetric. The term “axisymmetric” implies that quantities do not change around the circumference of the shell. Therefore, any quantities which indicate any variation in the circumferential direction cannot be considered. This includes bending of the cylinder as a beam and shear forces acting transverse to the cross-section, since these loads manifest themselves as sinusoidal variations of stress and strain in terms of the circumferential coordinate  $\theta$ . As such the only loads that are considered axisymmetric include a longitudinal force, internal pressure, and an axial torque. The solution technique for these specialized conditions will consist of a nonlinear static equilibrium solution which determines the stresses, strains, and displacements of the cylinder due to these axisymmetric loads, and a stability estimate which can take into account the nonlinear prebuckled state of the shell. A linear membrane solution, which is merely a subset of the full analysis, is also detailed. Comparisons of this approximate technique to the full analysis are presented, as well as some interesting results of the variable stiffness concept under axisymmetric loading. Initial optimization of variable stiffness cylinders with curvilinear fibers is conducted using the membrane prebuckling stability solution to determine the loading cases which offer the best possibilities for increased performance over constant stiffness laminates. These results lead to optimization of the fiber path itself, which is accomplished using the linked segment approach for the variable stiffness concept as explained in Section 2.2.2.

### 3.1 Static Equilibrium

Regarding the static solution under axisymmetric conditions, significant simplifications to the governing equations exist. In mathematical terms, the stipulation of axisymmetry means that all derivatives with respect to the circumferential direction equal zero. This implies that all variables are only functions of  $x$ , and it transforms the partial differential equations into ordinary differen-

Note that for a stiffened structure, this axial stiffness variation allows ring stiffeners and frames along the length of the cylinder which can produce a coupling stiffness term  $B_{22}$ . The equilibrium equations and boundary conditions under the axisymmetric conditions follow.

Equilibrium Equations, Eq. (2.87)-(2.92):

$$\frac{dN_x}{dx} = 0 \quad \frac{dN_{x\theta}}{dx} = 0 \quad \frac{dQ_x}{dx} + N_x \frac{d^2 w_0}{dx^2} - \frac{N_\theta}{R} + p = 0 \quad Q_x = \frac{dM_x}{dx} \quad (3.4)$$

Boundary Conditions, Eq. (2.97) and (2.98):

$$\begin{aligned} u_0(0) = \bar{U} \quad \text{or} \quad N_x(0) = 0 \quad u_0(L/2) = 0 \\ v_0(0) = \bar{V} \quad \text{or} \quad N_{x\theta}(0) = 0 \quad v_0(L/2) = 0 \\ w_0(0) = 0 \quad Q_x(L/2) = 0 \\ \frac{dw_0}{dx}(0) = 0 \quad \text{or} \quad M_x(0) = 0 \quad \frac{dw_0}{dx}(L/2) = 0 \end{aligned} \quad (3.5)$$

The resulting configuration with its relevant loads, end displacements, and coordinate directions is displayed in Figure 3.1, where the actual structure is a surface of revolution produced by the rota-

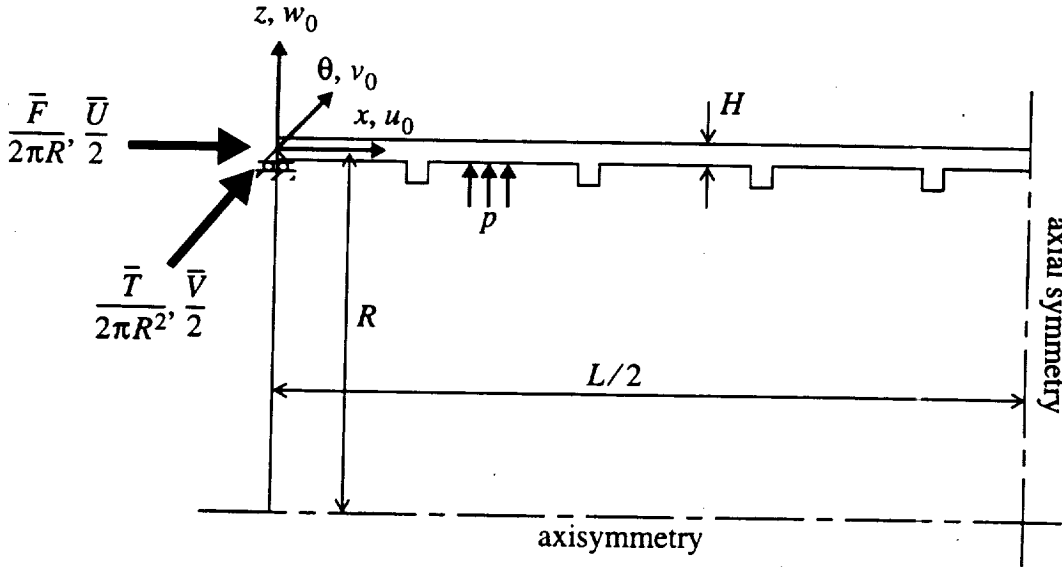


Figure 3.1: Geometry of Axisymmetric Cylinder

tion of the slice of the shell around the line of axisymmetry. Symmetry also exists about  $x = L/2$ , so that only half of the structure need be considered. This axisymmetric cylinder corresponds to the classical elasticity problem of a beam on an elastic foundation.

Basic substitution and integration of the governing equations enables further simplification.

For instance, the first two equilibrium equations of Eq. (3.4) are easily integrated to reveal that the axial and shear stress resultants are constants. Integration of these constant axial and shear stress resultants around the circumference of the cylinder relates them to their corresponding beam loads of axial force and torsion. These loads will be treated as unknown variables and will consequently be determined from the end conditions in terms of the applied displacements.

$$\begin{aligned} \oint N_x(x) R d\theta &= -\bar{F} & \Rightarrow & N_x(x) = \frac{-\bar{F}}{2\pi R} \\ \oint N_{x\theta}(x) R^2 d\theta &= -\bar{T} & \Rightarrow & N_{x\theta}(x) = \frac{-\bar{T}}{2\pi R^2} \end{aligned} \quad (3.6)$$

The circumferential stress resultant  $N_\theta$  expressed in terms of the constant axial load and the radial displacement  $w_0$ , utilizing the effective stiffness expressions of Eq. (2.52) and the definition of the circumferential strain from Eq. (3.3), is

$$N_\theta(x) = E_\theta(x) H \frac{w_0(x)}{R} - \nu_{\theta x}(x) \frac{\bar{F}}{2\pi R} \quad (3.7)$$

Substitution of this relation, along with the remaining constitutive laws and the expression for the intermediate variable  $Q_x$ , into the third equilibrium equation results in an ordinary differential equation in terms of  $w_0$ :

$$\frac{d^2}{dx^2} \left[ D_{11}(x) \frac{d^2 w_0}{dx^2} \right] + \frac{\bar{F}}{2\pi R} \left( \frac{d^2 w_0}{dx^2} \right) + \frac{E_\theta(x) H}{R^2} w_0 = p + \nu_{\theta x}(x) \frac{\bar{F}}{2\pi R^2} \quad (3.8)$$

Note that the only unknowns in this equation are the radial displacement and the applied loads. Since the differential equation is fourth order, the stipulation of proper boundary conditions for  $w_0$  at each end provides the necessary requirements to solve the system.

Expressions for the axial and shear strains in terms of the middle surface stress resultants and stiffness quantities, all of which are known once the differential equation of Eq. (3.8) has been solved, are found through inversion of the constitutive relations, Eq. (3.3).

$$\epsilon_x^o = \frac{N_x - \nu_{x\theta} N_\theta}{E_x H} \quad \gamma_{x\theta}^o = \frac{N_{x\theta}}{G_{x\theta} H} \quad (3.9)$$

These strain quantities each contain an isolated derivative of one of the middle surface displacements ( $u_0, v_0$ ) as revealed by Eq. (3.2), and integration can be performed for each variable in terms of the loads, stiffness terms, and radial displacement  $w_0$ . The boundary conditions for  $u_0$  and  $v_0$  from Eq. (3.5) are applied as part of the integral equations, so that the constant end displacements

representing the total axial extension and twist of the cylinder can be expressed in a simple form:

$$\begin{aligned} u_0(x) &= 2 \int_x^{L/2} \left[ \frac{(1 - \nu_{x\theta} \nu_{\theta x})}{E_x H} \frac{\bar{F}}{2\pi R} + \nu_{\theta x} \frac{w_0}{R} + \frac{1}{2} \left( \frac{dw_0}{dx} \right)^2 \right] dx & u_0(0) &= \bar{U} \\ \nu_0(x) &= \frac{\bar{T}}{\pi R^2} \int_x^{L/2} \frac{dx}{G_{x\theta} H} & \nu_0(0) &= \bar{V} \end{aligned} \quad (3.10)$$

Note that the axial displacement  $u_0$  still depends on the radial displacement  $w_0$ , while the circumferential displacement  $\nu_0$  is totally uncoupled from the other displacements and depends only on the applied torque. The boundary conditions containing equations for the end displacements  $\bar{U}$  and  $\bar{V}$  can be treated in two different ways with regards to the application of the loads: the end loads  $\bar{F}$  and  $\bar{T}$  can be prescribed (possibly zero) and the unknown end displacements can be found using Eq. (3.10); or the displacements can be provided and the resulting forces found through integration. Here the latter approach is used whenever loading is introduced, corresponding to "displacement control", since nonlinear load-displacement curves often contain a limit load which leads to difficulties if "load control" is used. Whenever loading is introduced this way, the boundary condition will be classified as "fixed" since the value of the displacement of the end is predetermined. The alternative is a "free" boundary, where the axial force or torque is zero and the end is allowed to displace in an unrestrained manner. For this condition, the free end displacements are not determined and therefore replace the loads as an unknown in the solution.

Let us now perform some normalization. To remain consistent, notation for the nondimensional variables will generally conform to that of the unnormalized variable by either an addition of an overbar or a change to lower case. First the nondimensional axial coordinate  $\xi$  is established, and an average stiffness quantity is introduced which depends on the skin properties only. These average skin values will be used in the estimation of classical buckling parameters, as well as providing a global estimate of structural stiffness that can be compared to constant stiffness shells.

$$\xi = \frac{2x}{L} \quad \hat{A}_{ij} = \int_0^1 A_{ij}^{skin}(\xi) d\xi \quad \bar{A}_{ij} = A_{ij} / \hat{A}_{ij} \quad (3.11)$$

The compressive axial force, internal pressure, and torque, as well as their corresponding membrane stress resultants, are normalized with respect to their classical buckling values for a finite length cylinder, found from Eq. (1.4), (1.8), and (1.14), respectively:

$$\bar{f} = \frac{\bar{F}}{2\pi R N_x^{cl}} \quad \bar{p} = \frac{pR}{N_{\theta}^{cl}} \quad \bar{i} = \frac{\bar{T}}{2\pi R^2 N_{x\theta}^{cl}} \quad (3.12)$$

The axial and circumferential displacements can also be normalized with respect to their classical estimates by using the integral equations of Eq. (3.10) to find similar critical values at the end of the cylinder, while the radial displacement will be normalized with respect to a parameter which is proportional to the skin thickness.

$$\bar{u}_0(\xi) = \frac{\hat{E}_x H}{L \hat{N}_x^{cl}} u_0(x) \quad \bar{v}_0(\xi) = \frac{\hat{G}_{x\theta} H}{L \hat{N}_{x\theta}^{cl}} v_0(x) \quad \bar{w}_0(\xi) = \sqrt{\frac{\hat{E}_\theta H}{4 \hat{D}_{11}}} w_0(x) \quad (3.13)$$

Insertion of these normalizing factors into the governing equation results in the generation of a nondimensional parameter  $l$  involving the length-to-radius ratio and a measure of the boundary layer near the ends:

$$l = \sqrt[4]{\frac{\hat{E}_\theta H L^4}{64 \hat{D}_{11} R^2}} = \frac{L}{2R} \cdot \frac{\hat{\beta}_x}{\sqrt{2}} \quad (3.14)$$

Notice that this parameter is proportional to the classical estimate for the critical half-wavelength for buckling under axial compression.

The governing equations for the axisymmetric cylinder with an axial stiffness variation are displayed in their final form below, where a prime represents differentiation with respect to  $\xi$ .

$$\begin{aligned} \bar{u}_0(\xi) &= \int_{\xi}^1 \left[ \frac{\bar{f}}{\bar{E}_x} + \frac{\nu_{x\theta}}{\bar{E}_x} (\bar{E}_\theta \bar{w}_0 - \nu_{\theta x} \bar{f}) + \frac{\hat{E}_x \bar{w}_0'^2}{\hat{E}_\theta 2l^2} \right] d\xi & \bar{v}_0(\xi) &= i \int_{\xi}^1 \frac{d\xi}{\bar{G}_{x\theta}} \\ \frac{(\bar{D}_{11} \bar{w}_0'')''}{4l^4} + \frac{\bar{f} \bar{w}_0''}{l^2} + \bar{E}_\theta \bar{w}_0 - \nu_{\theta x} \bar{f} &= \frac{\hat{N}_\theta^{cl}}{\hat{N}_x^{cl}} \bar{p} & (3.15) \\ \bar{n}_x(\xi) &= -\bar{f} & \bar{n}_\theta(\xi) &= \frac{\hat{N}_x^{cl}}{\hat{N}_\theta^{cl}} (\bar{E}_\theta \bar{w}_0 - \nu_{\theta x} \bar{f}) & \bar{n}_{x\theta}(\xi) &= -i \end{aligned}$$

The boundary conditions along with their relevant geometrical interpretations are

$x$ -direction	Fixed	$\bar{u}_0(0) = \bar{u}$	or	Free	$\bar{f} = 0$
$\theta$ -direction	Fixed	$\bar{v}_0(0) = \bar{v}$	or	Free	$i = 0$
$z$ -direction	Radial restraint	$\bar{w}_0(0) = 0$			
	Clamped	$\bar{w}_0'(0) = 0$	or	Simply supported	$\bar{w}_0''(0) = 0$
symmetry		$\bar{w}_0'(1) = 0$			$\bar{w}_0'''(1) = 0$

(3.16)

This system is well-posed and consistent with standard derivations. For constant stiffness laminates, the differential equation can actually be solved in closed form. This analytical solution is instructive with regards to the expected response of the shell, and will also be used as a basis of comparison for approximate techniques. It can be found by assuming constant stiffness quantities in Eq. (3.15) and solving the ordinary differential equation for  $\bar{w}_0$  using traditional methods. The solution is

$$\bar{w}_0(\xi) = \left( \frac{\hat{N}_\theta^{cl}}{\hat{N}_x^{cl}} \bar{p} + v_{\theta x} \bar{f} \right) \times \quad (3.17)$$

$$\{ 1 + C_1 \cosh[l(1 - \bar{f})\xi] \cos[l(1 + \bar{f})\xi] + C_2 \sinh[l(1 - \bar{f})\xi] \cos[l(1 + \bar{f})\xi] + C_3 \cosh[l(1 - \bar{f})\xi] \sin[l(1 + \bar{f})\xi] + C_4 \sinh[l(1 - \bar{f})\xi] \sin[l(1 + \bar{f})\xi] \}$$

The constants  $C_1$ - $C_4$  are determined once the four boundary conditions for  $\bar{w}_0$  given in Eq. (3.16) are applied. For a general variable stiffness cylinder, however, the problem must be solved numerically. The numerical solution using a finite difference technique is outlined in Appendix A. Estimation of stability of this equilibrium state is addressed in the next section.

### 3.2 Stability Estimate with Nonlinear Axisymmetric Prebuckling Solution

The equations of Section 2.3.2 that govern instability of a cylindrical shell can also be specialized for the case of axisymmetric loading. Here, the energy method formulation employing the second variation of the total potential energy will be used. The perturbed strain quantities for an axisymmetric prebuckled state are defined from Eq. (2.108) as:

$$\begin{aligned} \epsilon_{x_1}^o &= \frac{\partial u_1}{\partial x} + \left( \frac{dw_0^o}{dx} \right) \left( \frac{\partial w_1}{\partial x} \right) & \epsilon_{\theta_1}^o &= \frac{1}{R} \frac{\partial v_1}{\partial \theta} + \frac{w_1}{R} \\ \gamma_{x\theta_1}^o &= \frac{1}{R} \frac{\partial u_1}{\partial \theta} + \frac{\partial v_1}{\partial x} + \left( \frac{dw_0^o}{dx} \right) \left( \frac{v_1}{R} - \frac{1}{R} \frac{\partial w_1}{\partial \theta} \right) \\ \kappa_{x_1}^o &= \frac{\partial^2 w_1}{\partial x^2} & \kappa_{\theta_1}^o &= \frac{1}{R^2} \left( \frac{\partial v_1}{\partial \theta} - \frac{\partial^2 w_1}{\partial \theta^2} \right) & \kappa_{x\theta}^o &= \frac{1}{R} \left( \frac{\partial v_1}{\partial x} - 2 \frac{\partial^2 w_1}{\partial x \partial \theta} \right) \end{aligned} \quad (3.18)$$

These expressions, together with the integral for the second variation of the total potential energy, Eq. (2.109), generate a system of equations for the unknown perturbed displacements. As detailed in Section 2.3.2, the determination of the critical mode shape and load that satisfies the resulting system takes the form of an eigenvalue problem. An additional simplification to this technique due to the axisymmetric prebuckling state involves the assumed form of the perturbed displacements. It can be shown that the resulting system can be decoupled in the axial and circumferential



directions by assuming that

$$\begin{aligned} u_1(\xi, \theta) &= U_I(\xi) \cos(n\theta) + U_{II}(\xi) \sin(n\theta) \\ v_1(\xi, \theta) &= V_I(\xi) \sin(n\theta) - V_{II}(\xi) \cos(n\theta) \\ w_1(\xi, \theta) &= W_I(\xi) \cos(n\theta) + W_{II}(\xi) \sin(n\theta) \end{aligned} \quad (3.19)$$

Using this form of the displacements, the periodicity condition of the cylinder is automatically satisfied, and the integration in the circumferential direction can be carried out analytically. The parameter  $n$  represents the number of circumferential waves in the buckled shape, and to preserve the periodicity condition it must be an integer (including the  $n = 0$  possibility). In reality, the general form of the displacements should be able to represent any arbitrary function, so that the assumed form in Eq. (3.19) should properly be an infinite sum of such functions in terms of the integer values of  $n$ . However, for an axisymmetric prebuckling solution it can be easily shown that the problem becomes separable for each value of  $n$ , therefore the assumed form given above is sufficient with the stipulation that the wavenumber  $n$  is now a variable.

The specification of two modes for each displacement in Eq. (3.19) ensures that the assumed form has the capability to accommodate any general function of the buckled shape. This is accomplished by prescribing each group of displacements specified by mode  $I$  or  $II$  to conform to the symmetric and anti-symmetric mid-length boundary conditions of Eq. (2.114). For the axisymmetric case, these mid-length conditions can be written as:

$$\begin{aligned} \text{Symmetric case} \quad & U_I(1) = V_I'(1) = W_I'(1) = W_I'''(1) = 0 \\ \text{Unsymmetric case} \quad & U_{II}'(1) = V_{II}(1) = W_{II}(1) = W_{II}''(1) = 0 \end{aligned} \quad (3.20)$$

Both modes must also satisfy the particular end conditions from Eq. (2.113), which are reproduced here with respect to the modal quantities.

Radial restraint for all cases  $W_i(0) = 0$

$$\begin{array}{ll} \text{S1:} & U_i(0) = V_i(0) = M_{x_i}(0) = 0 \\ \text{S2:} & N_{x_i}(0) = V_i(0) = M_{x_i}(0) = 0 \\ \text{S3:} & U_i(0) = N_{x\theta_i}(0) = M_{x_i}(0) = 0 \\ \text{S4:} & N_{x_i}(0) = N_{x\theta_i}(0) = M_{x_i}(0) = 0 \end{array} \quad \begin{array}{ll} \text{C1:} & U_i(0) = V_i(0) = W_i'(0) = 0 \\ \text{C2:} & N_{x_i}(0) = V_i(0) = W_i'(0) = 0 \\ \text{C3:} & U_i(0) = N_{x\theta_i}(0) = W_i'(0) = 0 \\ \text{C4:} & N_{x_i}(0) = N_{x\theta_i}(0) = W_i'(0) = 0 \end{array} \quad (3.21)$$

Insertion of the assumed form of the displacements into the expression for the total potential energy and invoking the condition that the variation of this integral must be a minimum leads to a

system of linear ordinary differential equations with variable coefficients, which now contain the additional unknown parameter  $n$ . This system can be denoted as

$$\begin{bmatrix} K_s & C \\ -C & K_a \end{bmatrix} + \begin{bmatrix} N_s & S \\ -S & N_a \end{bmatrix} \begin{bmatrix} I \\ II \end{bmatrix} = \begin{bmatrix} 0 \\ 0 \end{bmatrix} \quad (3.22)$$

where the uppercase letters represent  $3 \times 3$  matrices of linear differential operators and the roman numerals denote the modal displacements of Eq. (3.19). The full matrix in parentheses is a function of the load level of the equilibrium state as well as stiffness and geometric parameters, and is divided into a stiffness and loading portion to make the notation easier to understand. The first matrix represents the stiffness terms, where  $K_s$ ,  $K_a$ , and  $C$  symbolize the symmetric, anti-symmetric, and coupling ( $D_{16}$  and  $D_{26}$ ) portions. The subscripts for  $K$  denote slight differences in the submatrices resulting from either the symmetric or anti-symmetric stipulation for the pertinent buckling mode. The loading matrix consists of  $N_s$  and  $N_a$ , which contain the normal loads acting on the symmetric and anti-symmetric portions, and  $S$ , produced by the presence of a shear load. The mathematical expressions for the linear operators are supplied in Appendix B.1. The stability of the equilibrium state can be numerically estimated through a perturbative technique as outlined in Section 2.3.4, which requires a calculation of the change in the loading matrices with respect to the given load level. This leads to a differential eigenvalue problem for the displacements, which will be solved numerically using an iterative technique called the power method along with the finite difference technique. These numerical methods are discussed in Appendix A.

### 3.3 Linear Membrane Approximations

The full solution of the equilibrium equations along with the estimation of the critical buckling load can be completed analytically for constant stiffness laminates, as shown in Eq. (3.17). However, insertion of this prebuckling solution into the stability equations produces a complex system of variable coefficient equations that cannot be solved in closed form and thus require a numerical solution. On the other hand, implementation of classical membrane constitutive theory *does* provide a basic closed form stability estimate, for the equilibrium state can be represented in a simpler analytical form and the eigenvalue problem can be solved if appropriate boundary conditions are used (as in the classical solution discussed in Section 1.2.2). Furthermore, the use of this constitutive theory for the prebuckling solution generates a much simpler method for eigenvalue calculations than the one represented by Eq. (3.22). Thus an approximate solution to the systems presented in the previous two sections using classical membrane theory is used for two reasons: to provide a more efficient method for eigenvalue calculations so that rigorous optimiza-

tion may be performed; and to serve as a comparison to the more complex nonlinear system, so that the regions where the two solutions disagree can be determined.

The easiest way to apply the restrictions of classical membrane theory for static equilibrium is to remove any terms associated with nonlinearity or shell bending in the full nonlinear systems. Thus Eq. (3.15), with these terms removed, is rearranged and the unknown displacements and membrane stress resultants are explicitly solved for in terms of the normalized loads:

$$\begin{aligned}\bar{u}_0(\xi) &= \bar{f} \int_{\xi}^1 \left[ \frac{d\xi}{\bar{E}_x(\xi)} \right] + \frac{N_{\theta}^{cl}}{N_x^{cl}} \bar{p} \int_{\xi}^1 \left[ \frac{v_{x\theta}(\xi) d\xi}{\bar{E}_x(\xi)} \right] \\ \bar{v}_0(\xi) &= i \int_{\xi}^1 \frac{d\xi}{\bar{G}_{x\theta}(\xi)} \quad \bar{w}_0(\xi) = \frac{v_{\theta x}(\xi)}{\bar{E}_{\theta}(\xi)} \bar{f} + \frac{N_{\theta}^{cl}}{N_x^{cl}} \frac{\bar{p}}{\bar{E}_{\theta}(\xi)} \\ \bar{n}_x(\xi) &= -\bar{f} \quad \bar{n}_{\theta}(\xi) = \bar{p} \quad \bar{n}_{x\theta}(\xi) = -i\end{aligned} \quad (3.23)$$

As can be readily seen, once the stiffness distribution is defined, the displacements can be easily calculated through integration. The applied end displacements are consequently related to the end loads in an obvious manner once the membrane boundary conditions of Eq. (3.16) are applied:

$$\bar{u} = \bar{f} \int_0^1 \left[ \frac{d\xi}{\bar{E}_x(\xi)} \right] + \frac{N_{\theta}^{cl}}{N_x^{cl}} \bar{p} \int_0^1 \left[ \frac{v_{x\theta}(\xi) d\xi}{\bar{E}_x(\xi)} \right] \quad \bar{v} = i \int_0^1 \frac{d\xi}{\bar{G}_{x\theta}(\xi)} \quad (3.24)$$

Note that the “fixed” versus “free” boundary conditions for the end loads can both be satisfied using the above equation, and also that the boundary conditions for  $\bar{w}_0$  in Eq. (3.16) are not needed since a membrane state is assumed.

Using classical membrane theory for the prebuckling solution also provides some significant simplifications of the stability equations. First, note in Eq. (3.23) that for traditional constant stiffness structures, the radial displacement  $\bar{w}_0$  is constant along the length since the stiffness parameters do not vary. Thus the prebuckling deformation of the cylinder does not produce any rotations or curvatures in the axial direction, as they are defined as axial derivatives of the radial displacement. Therefore, the prebuckling rotations contained in the perturbed strain quantities of Eq. (3.18) disappear and the prebuckling state for the eigenvalue problem is introduced solely through the simple definition of the stress resultants, as given in Eq. (3.23). For variable stiffness structures, derivatives of the radial displacement *do* exist due to the axial variation of the stiffness terms, therefore it is proper to retain the prebuckling deformation in the stability equations. However, to simplify the stability estimation using membrane prebuckling, this investigation will conform to the typical practice of neglecting these terms and introduce the prebuckled state only

through the stress resultants. Though this may produce significant error for variable stiffness structures with large prebuckling deformation, the simplification makes the formulation of the numerical eigenvalue problem much more straightforward. Comparisons to the full nonlinear eigenvalue problem, which retains the effect of prebuckling rotations, will be conducted in Section 3.5.1 to determine if this simplification is warranted for variable stiffness structures.

The second significant simplification from the full nonlinear estimate is the fact that the prebuckling solution is linear. For the linear membrane solution the loading matrix, as given in Eq. (3.22), can be determined analytically from Eq. (3.23) in terms of the loads of axial force, pressure, and torsion which are applied proportionally. Thus, instead of the numerical algorithm used to determine the point along the nonlinear load path that produces a "zero" eigenvalue, only one eigenvalue calculation need be computed, and this result will always produce the same estimation of the critical loads. For more complex loading cases, the proportional loading is also divided into two parts: a "dead" and "live" portion, where the dead loads are assumed to be applied up to their prescribed values using the membrane prebuckling solution, and the ratio of the live loads designates the loads that will produce buckling. Thus the loading matrix can be decomposed into these two portions as well, so that the resulting eigenvalue can be written in traditional form as

$$[K] \cdot \hat{u}_1 = \Lambda [M] \cdot \hat{u}_1 \quad (3.25)$$

The stiffness matrix  $[K]$  contains the stiffness sub-matrices and the dead loading, and the geometric stiffness matrix  $[M]$  contains the derivatives of the live loads with respect to the load level  $\Lambda$ . These derivatives are calculated analytically once the ratio of the proportional loading for the live loads is determined. For example, under hydrostatic pressure with no torsion present, the ratio of live loads is given as

$$\frac{d}{d\Lambda}[N_{x_0}^I] = \frac{-R}{2} \quad \frac{d}{d\Lambda}[N_{\theta_0}^I] = -R \quad \frac{d}{d\Lambda}[N_{x\theta_0}^I] = 0 \quad (3.26)$$

so that the resulting eigenvalue problem solves for the critical buckling value under hydrostatic pressure. The simplicity of these equations is even more evident when constant stiffness laminates are used along with the S2 boundary condition, for in this case the buckling equations can be expressed in closed form, such as the classical solutions presented in Section 1.2.2. Further details of the form of the linear stability equations for the membrane simplification are offered in Appendix B.1.

### 3.4 Static Response and Stress Analysis

This section is intended to present the basic results of the equilibrium solutions for variable stiffness cylinders under axisymmetric loading. As such, the prebuckling solutions with regard to deformation and material failure considerations is investigated first, and the static response of particular variable stiffness structures is also examined to develop an understanding of the physical mechanisms involved. It should also be mentioned here that these stress analysis results are predominantly based on the *linear* solution of the governing equations. This is considered accurate and sufficient for two reasons. In the first case, the simplifications of classical membrane theory should never be used for in-depth stress analysis, since the critical location for failure depends largely on where the shell bending effects, which membrane theory neglects, are the largest. Secondly, *linear* analysis is also justified here, since the nonlinear effects for cylindrical shells become most significant when the applied loads generate an unstable configuration. If non-destabilizing loads such as tension or internal pressure are being applied, material failure is the limiting constraint that governs the design of the shell. Though the development of the nonlinear boundary layer does have some effect on the failure loads of the shell, its contribution can be neglected here without loss of generality.

Material failure of most cylinders generally occurs because of the large bending moments within the shell that are present due to the enforcement of zero radial displacement at the ends. For instance, the radial displacement of a typical constant stiffness cylinder under axial compression is shown in Figure 3.2. Away from the restraint generated by the support at  $\xi = 0$ , the radial

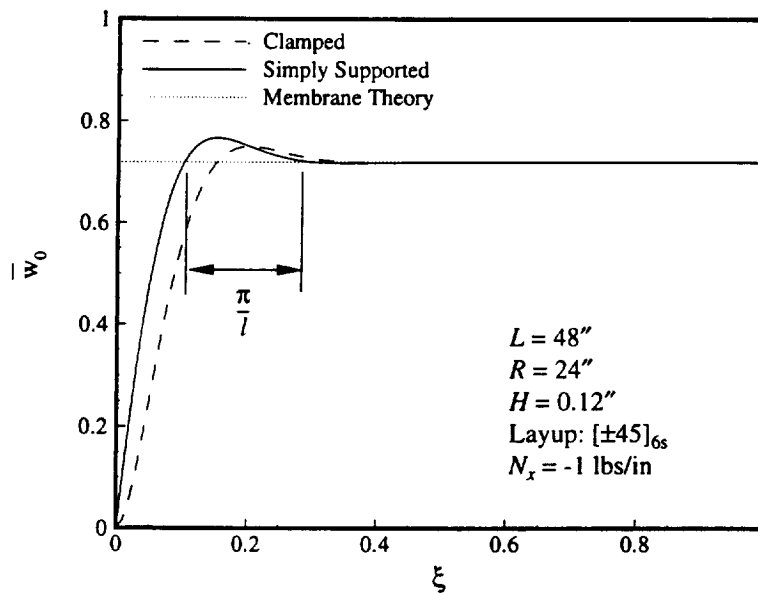


Figure 3.2: Displacement Profile of Constant Stiffness Cylinder under Axial Compression

displacement is a constant as per the membrane solution of Eq. (3.23). However, as one approaches the end, a boundary layer appears to facilitate the enforcement of the boundary conditions for the fourth order differential equation of Eq. (3.15). As shown in Eq. (3.17), the variation of the radial displacement within this boundary layer, for small values of  $\bar{f}$ , follows that of functions like  $\cosh(l\xi) \sin(l\xi)$ , so that the distance between successive intersections of the membrane and boundary layer solutions can be expressed as a function of  $l$ , as shown in Figure 3.2. The non-dimensional parameter  $l$  can also be regarded as an indicator of the relative length of the boundary layer based on the attenuation of the hyperbolic functions. Within the boundary layer region, the variation of the radial displacement will produce rotations and curvatures (and therefore bending moments) of the middle surface. These moments produce high axial strains at the extreme surfaces of the laminate ( $z = \pm H/2$ ). Away from the ends, the shell response is dictated by the membrane effect of the shell, which manifests itself as middle surface axial, circumferential, and shear strains. Thus the highest stresses are generated where both the bending and membrane effects are significant, and material failure usually occurs near the ends of the cylinder. With implementation of the variable stiffness concept, the distribution of the stresses can possibly be altered, thereby changing the critical location and perhaps the magnitude of the material failure load as well. Therefore this section investigates the state of stress produced by various implementations of the variable stiffness concept, and determines their worth when compared to conventional laminates.

### 3.4.1 Curvilinear Fiber Paths

The first study of strength properties for variable stiffness laminates will be based on a simple one link linear variation of the fiber orientation angle. Two angles are needed to define the stiffness variation:  $T_0$  being the value at each end of the cylinder, and  $T_1$  which is located at the mid-length. The stacking sequence will be assumed to be of the form  $[\pm\phi]_{6s}$ , so as to highlight the maximum effect of the variable stiffness concept. As mentioned, failure of cylindrical shells most often occurs near the ends, where the gradients produced by the boundary layer result in large bending moments within the shell wall. However, by selectively varying the stiffness of the cylinder as it approaches the supports, the location of material failure can be altered by smoothing out the displacement gradients that produce these areas of high stress.

As an illustration of this hypothesis, radial displacement profiles of some simply supported cylinders under a unit load of axial compressive force are shown in Figure 3.3. Also shown are the membrane theory solutions (as dotted lines), to provide an idea of the boundary layer length for each cylinder. The solid line represents the radial displacement versus axial location for a  $[\pm 45]_{6s}$  cylinder ( $L = 48"$ ,  $R = 24"$ ). The filled circle represents the material failure site where the stresses reach their critical strength value, and it is located where the membrane and bending effects are

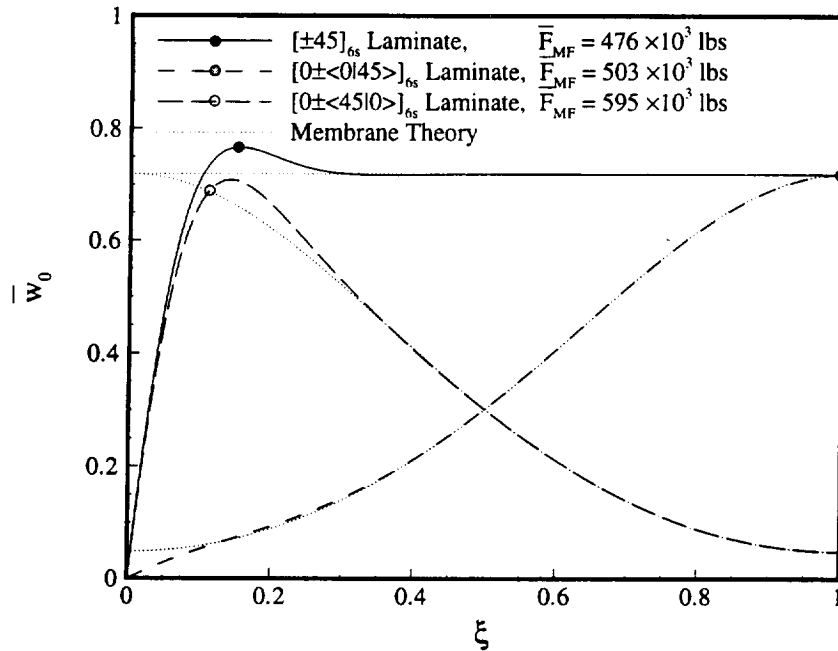


**Figure 3.3: Displacement Profiles of Axisymmetric Variable Stiffness Cylinders under Axial Compression**

both significant. The other two curves of Figure 3.3 represent variable stiffness cylinders using two particular linear variations of the fiber orientation angle. The symbols for each denote the material failure location, and the ultimate failure loads assuming a linear response are also reported. Note that for the second case, the critical location has moved to the mid-length of the cylinder.

The movement of the failure location can be attributed to two factors. First, the variation of the stiffness can smooth out the large displacement gradients that occur near the ends of clamped and simply supported cylinders. This relieves the high stresses produced by the bending moments at the ends of the cylinder. The short dashed line in Figure 3.3 is an excellent example of this phenomena. As is readily seen, the variation of the stiffness terms produce a membrane solution that roughly approaches zero near the support, so that the effect of the boundary conditions does not produce the large displacement gradients that are common to the other cases. Therefore, the resulting bending moments within the shell wall that lead to failure are not as significant. Secondly, since the strength of an angle ply laminate is related to the fiber orientation angle (based on the maximum stress or strain criterion), a change in the fiber orientation angle also changes the laminate's resistance to certain types of stress (i.e. strength) as a function of the spatial coordinates. This implies that for loads that produce constant stress along the length of the cylinder (such as axial loads or torsion), failure will occur where the strength is the lowest as determined

by the fiber orientation angle. For instance, if the stress state is axial tension, a  $0^\circ$  orientation will be much stronger than any other fiber orientation angle, and therefore the cylinder will most likely fail at the location that possesses the weakest resistance to the tensile stress state. This is also illustrated in Figure 3.3. For the  $T_0 = 0^\circ$ ,  $T_1 = 45^\circ$  variable stiffness cylinder that exhibits no substantial boundary layer, the stress state is predominantly pure axial compression along the entire length. The failure location ( $\xi = 1$ ) coincides with the weakest fiber orientation angle under compression within the given configuration ( $\varphi = 45^\circ$ ).

To determine the relative merits of optimum designs of variable stiffness cylinders, a simple design study was performed to determine the material failure loads of variable stiffness cylinders under the three basic axisymmetric loads using the one link linear variation of the fiber orientation angle. The results are displayed in graphical form for axial compression (Figure 3.4), internal pressure (Figure 3.5) and torsion (Figure 3.6). For each figure, the material failure load is plotted

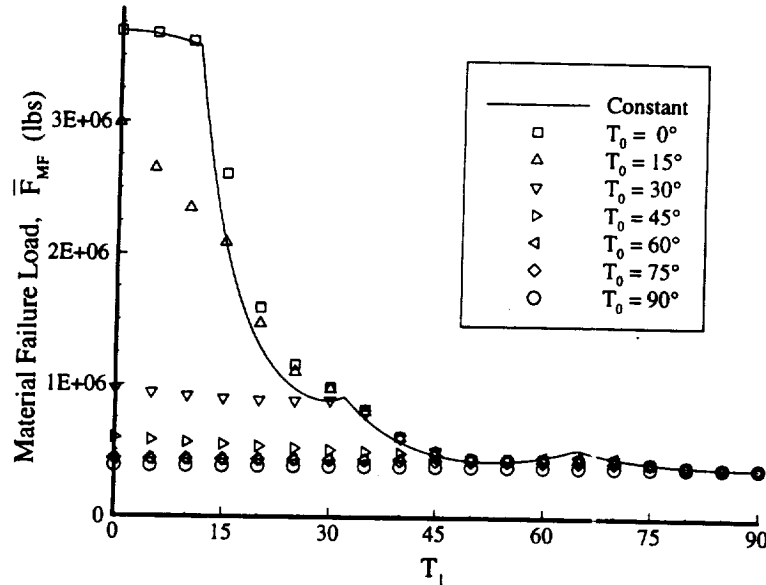


Figure 3.4: Failure Loads for Cylinders under Axial Compression

as a function of the mid-length angle  $T_1$  for a given value of the end point angle  $T_0$ , and denoted by symbols. Note that the manufacturing constraint limiting the allowable variation of the fiber orientation angle is not implemented here. The solid line in each figure represents the failure loads of constant stiffness laminates for which  $T_0 = T_1$ . For each case, the results indicate that the highest material failure load is achieved by a constant stiffness laminate. Combined loadings including various ratios of tension, internal and external pressure, and torsion were also investigated to determine the advantage of the variable stiffness concept compared to the constant stiffness laminates. It was discovered that if material failure is the biggest concern, the variable stiffness cylin-



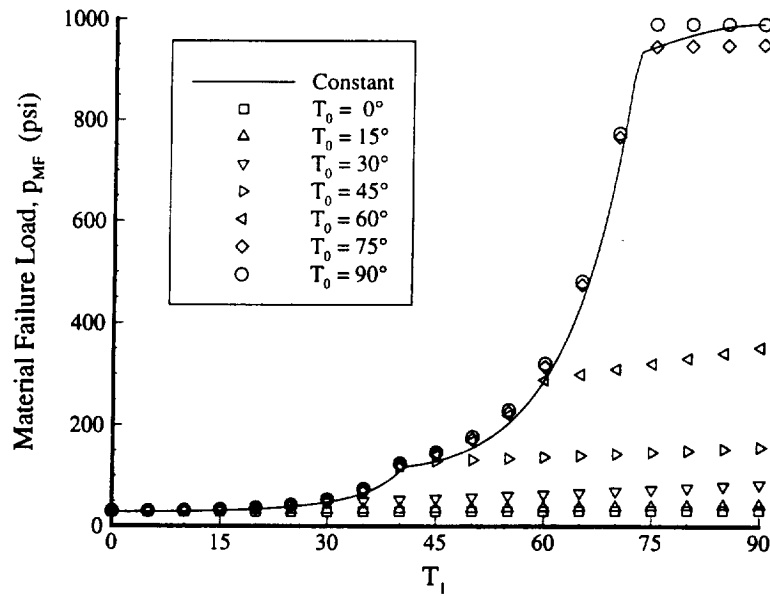


Figure 3.5: Failure Loads for Cylinders under Internal Pressure

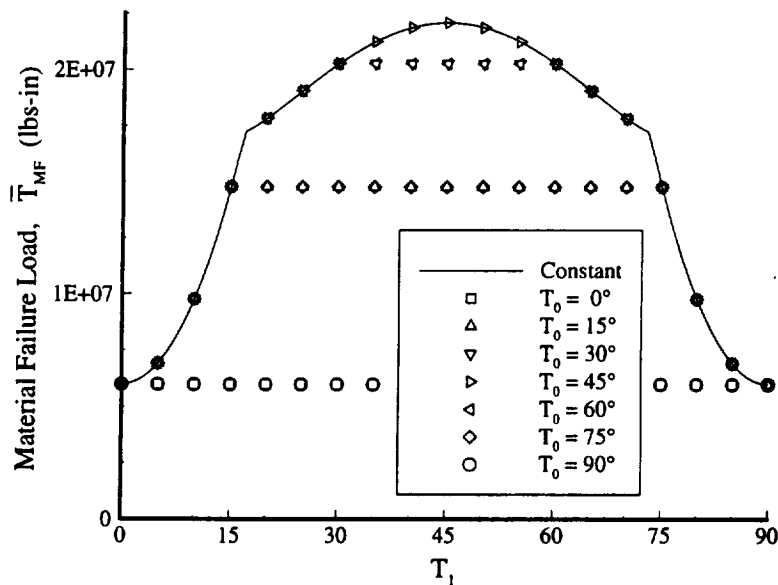


Figure 3.6: Failure Loads for Cylinders under Torsion

ders exhibit no improvement over the straight fiber format. Often the variable stiffness concept can change the location and/or mode of failure, but a significant strength increase over the optimum constant stiffness laminate does not exist.

These results can be explained through the use of a “weak link” analogy. For axisymmetric loads applied to a cylindrical shell with an axial stiffness variation, one distinguishing aspect of the solution is the fact that the dominant membrane stress resultants do not vary along the length of the shell. This is evident in the solutions for the stress resultants in Eq. (3.15), where it is shown

that the axial and shear stress resultant are both exactly a constant, and the circumferential stress resultant is proportional to the constant pressure loading along with some secondary effects due to the variation of the radial displacement. Therefore, the stress state at any location along the length is basically the same, the only exception being near the ends where the boundary layer effects are significant, so that the axial variation of the stiffness does not actually redistribute the stresses at all. This condition can be regarded as the variable stiffness cylinder carrying the loads in "series", where each infinitesimal segment of the structure must be able to withstand the applied loads independently. Of course, for the particular ratio of loads being applied, there exists some optimal stacking sequence that is best suited to withstand the resulting stress state, as well as some layups that are expected to behave quite poorly under the same conditions. For example, under axial tension a  $0^\circ$  orientation would be expected to be the strongest, since the fibers are aligned exactly with the largest stresses, while a  $90^\circ$  ply would fail easily in this case since the tensile stresses would be carried predominantly by the weaker matrix component of the composite material. When curvilinear fibers are used, the failure location will generally occur where the stacking sequence is least suited to carry the applied loads, and thus this "weak link" location will be the limiting factor on the material failure load. To achieve the best performance, a designer would avoid these weak links and replace them with a more favorable stacking sequence. Since there exists some layup that withstands the stress state better than all others, the resulting optimal design would be composed of a constant stiffness laminate with this particular stacking sequence.

Fortunately, the conclusion regarding the weak link aspect for the axisymmetric problem does not imply that the axial stiffness variation is not useful. In the first case, it is quite possible to load the cylinder such that the axisymmetric loads *do* vary along the length, which is most easily accomplished with an axial variation of the pressure or by external loads being applied at certain axial location. For such loading, varying the fiber orientation angle along the length will enable the optimal stacking sequence to be used for the specific loading at that location, and obviously will produce designs that outperform conventional straight fiber cylinders. Investigation of these types of loading cases will not be included here. Secondly, it must be realized that for almost all of the thin cylinders analyzed, the critical failure mechanism (for destabilizing loads) was buckling and not material failure. Therefore, some performance improvements may still be attainable under axisymmetric loading, which will be looked at in the next subsection. Lastly, comparisons between cylindrical shells are not always based only on strength but often include stiffness criteria. Thus a cylinder design may need to have a minimum load capability as well as a required displacement constraint or, conversely, be defined for a given failure load with the overall stiffness of the structure being the quantity that is to be maximized. The variable stiffness cylinder can

become advantageous in this instance because it can offer designs that exhibit the same stiffness properties yet have different strength characteristics, or vice versa.

To demonstrate this last idea, the material failure loads under axial compression shown in Figure 3.4 are plotted versus the overall axial stiffness of the cylinder structure in Figure 3.7.

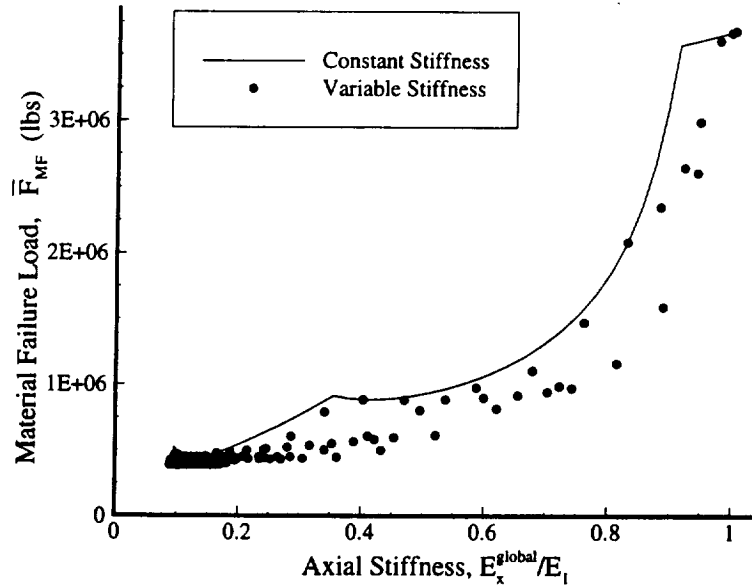


**Figure 3.7: Failure vs. Stiffness for Axial Compression**

Again the solid line represents the constant stiffness laminates, while the filled circles now denote variable stiffness designs using the one link linear variation of the fiber orientation angle. The global axial stiffness quantity is found through integration along the length using the appropriate stiffness quantities, and relates the axial end displacement  $\bar{U}$  to the applied end load  $\bar{F}$  as surmised from Eq. (3.10). As expected from the earlier results, the best performance is exhibited by a constant stiffness laminate with  $0^\circ$  plies only, and all variable stiffness designs fail at a lower load level. However, if a particular stiffness response is desired, then any variable stiffness design that is above the constant stiffness curve is considered advantageous because the variable stiffness cylinder has a higher strength with the same stiffness characteristics. Similarly, if an exact failure load is defined and the stiffness is meant to be maximized, then any circle to the right of the curve demonstrates improved performance. Examination of Figure 3.7 reveals that there is still no noticeable improvement for a prescribed stiffness design, though some gains can be achieved for the second (less practical) case. The results for a similar treatment of a cylinder under torsion are shown in Figure 3.8. The torsional stiffness relates the overall twist of the cylinder to the torsional load applied at the end, and is again found through integration as given by Eq. (3.10). Again, the

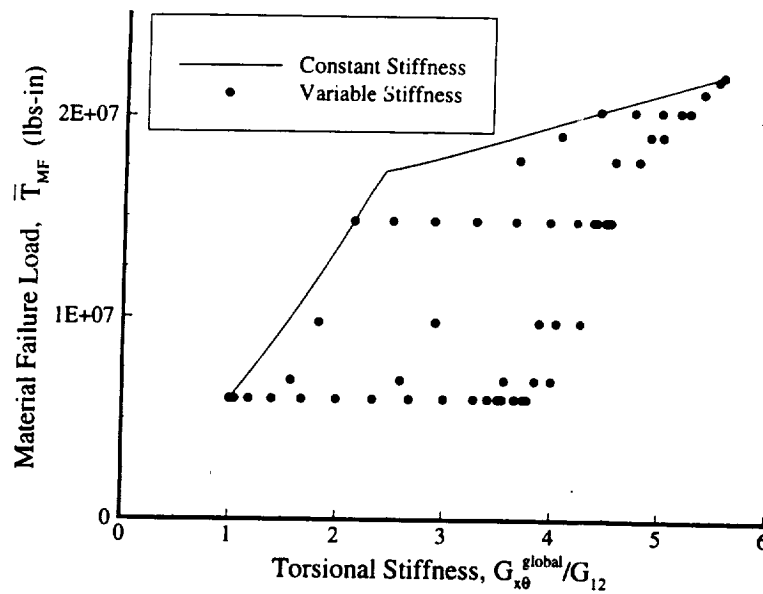


**Figure 3.8: Failure vs. Stiffness for Torsion**

only noticeable gains exist for the case in which the failure load is prescribed and the stiffness is maximized. Investigations of similar scenarios using combinations of the axisymmetric loads generate comparable results, though the magnitude of the possible improvements are never that substantial. However, the results do indicate that for some highly constrained designs, the variable stiffness concept is valuable because of the greater flexibility that it gives to the designer.

### 3.4.2 Ring Stiffeners and Frames

Though the foremost objective of this investigation is determining the possible performance improvements from using curvilinear fibers, the preponderance of stiffeners as additional components of cylindrical structures does warrant some discussion. With regards to the static response of axisymmetric cylinders, the inclusion of stiffeners is limited to ring stiffeners and frames that do not vary in terms of shape or stiffness characteristics around the circumference of the cylinder. This results in the addition of a discrete jump in stiffness for some of the stiffness measures where the stiffener is attached (see Section 2.2.2). The radial displacement profile from a linear solution of the axisymmetric problem which now includes some basic stiffeners is shown in Figure 3.9. The shaded portion shows the axisymmetric geometry of the stiffened shell, which is constructed of a  $[\pm 45]_6$  laminate skin. The cylinder is loaded by external pressure, and both the clamped and simply supported cases are included (the simply supported case is shown by the dashed curve). One can readily see that the major consequence of a ring stiffener is that it effectively divides the long cylinder into a series of shorter ones, such that a ring stiffener or frame imitates an end restraint (a *clamped* condition according to Figure 3.9). Of course, this is only true if the stiffener

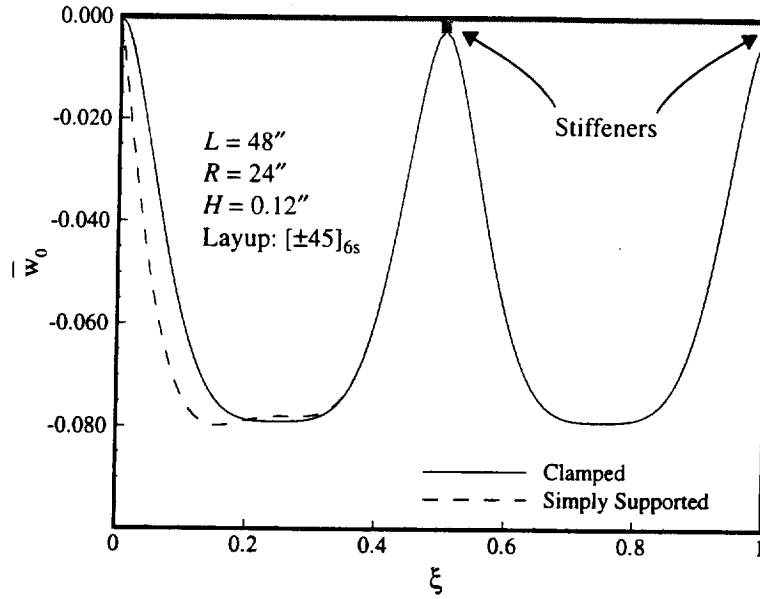


**Figure 3.9: Displacement Profile of Ring Stiffened Cylinder**

is sturdy enough with respect to the rest of shell, since flimsier elements often deform significantly in the radial direction as well. The point that is intended to be made here is that the addition of ring stiffeners, much like the axial variation of the fiber orientation angle, does not actually redistribute any of the axisymmetric loads, therefore an increase in material failure strength of the resulting shell will not be observed. In fact, the failure load for some loading may decrease, since the stiffeners produce additional boundary layer regions. However, ring stiffeners do serve a useful purpose, for it will be shown later in this chapter that the division of long cylindrical structures into a series of shorter elements can provide significant increases in buckling loads for certain types of axisymmetric loading. Furthermore, a long cylinder under bending provides another area where circumferential stiffeners become an efficient concept that improves performance by resisting the ovalization of the cross-section. This will be investigated in more detail in Chapter 6.0.

### 3.5 Buckling Results

The failure of cylinders due to buckling by axisymmetric loading has been studied throughout the evolution of modern shell analysis techniques. As mentioned in Section 1.2.2, the agreement between the classical theoretical solutions and actual experiments has been excellent for cylinders subjected to torsion and external pressure. However, no such correlation was found for the axial compression case, predominantly due to the effect of geometric imperfections on the critical buckling load. Though the inclusion of the postbuckling analysis required to thoroughly investigate the imperfection phenomenon is beyond the scope of this study, some aspects of the nonlinear buckling problem are addressed here. In particular, the development of the shell boundary

layer for constant and variable stiffness cylinders is discussed, and conclusions are drawn regarding the need of a full nonlinear prebuckling analysis for the initial investigation of the variable stiffness concept. The buckling results for laminates with curvilinear fibers are then presented along the same lines as the material failure results, in that a one link linear variation is utilized to demonstrate the failure trends of the structure. Optimization of the curvilinear fiber path is completed in the next section for the load cases which show the most promise.

### 3.5.1 Effect of Prebuckling Solutions and Nonlinearity

The choices for the prebuckling state of the buckling calculation are determined from the level of complexity used in the static solution of the governing equations for axisymmetric cylinders. The simplest choice employs linear membrane constitutive theory, which in the classical formulation also neglects the prebuckling rotations in the strain-displacement relations for the perturbed displacements, displayed in Eq. (3.18). The main motivation for neglecting these rotations is that it produces a linear eigenvalue problem which only needs to be solved once for each design, as opposed to the nonlinear eigensystem, represented by Eq. (2.104), which must be evaluated at successive points along the load path. Of course, for constant stiffness laminates the membrane solution results in an unrotated deformation pattern anyway, so that neglecting the prebuckling deformation is justified mathematically. However, as seen in Figure 3.3 the membrane solution for variable stiffness cylinders does not necessarily produce an equilibrium state without shell rotations due to the variation of the stiffness parameters, yet the prebuckling deformation will still be neglected to conform to the classical assumptions and to warrant using the simpler eigenvalue solution technique. This clearly leads us to the next level of complexity for the prebuckling state in which the prebuckling rotations of the equilibrium solution *are* considered in the buckling equations. If this addition is included, then to remain consistent the end conditions of the prebuckling solution should be identical to the ones used by the buckling estimate. Membrane theory does not consider the boundary conditions in the transverse direction (related to  $w_0$  and its derivatives), therefore it should not be considered adequate if the prebuckling rotations are to be included. Instead the next choice of prebuckling states will be for a linear solution of the equilibrium equations that adhere to the same end constraints as the stability estimate, where the prebuckling deformation due to the stiffness variation and the boundary layer effect is taken into account in the stability estimate. As implied earlier, since the eigenvalue problem is actually nonlinear with respect to the prebuckling rotations, the numerical computation of the critical eigenvalue must now follow the complex nonlinear method to be considered accurate. The final improvement to the prebuckling state involves the full nonlinear solution of the equilibrium equations, along with the effect on the bifurcation load due to the nonlinearity of the deformation as the magnitude of

the applied loads increases. Again an eigenvalue problem must now be solved at each step along the load path to determine an accurate buckling load. This nonlinear stability solution is not considered numerically efficient when compared to the (linear) membrane solution. However, since the more efficient stability estimate is planned to be used for optimization studies, some explanation and error estimate is needed to justify using the simpler technique.

To this end, the radial displacement profile of the standard  $[\pm 45]_{6s}$  constant stiffness laminate under axial compression is shown in Figure 3.10 for several values of the load parameter (the last

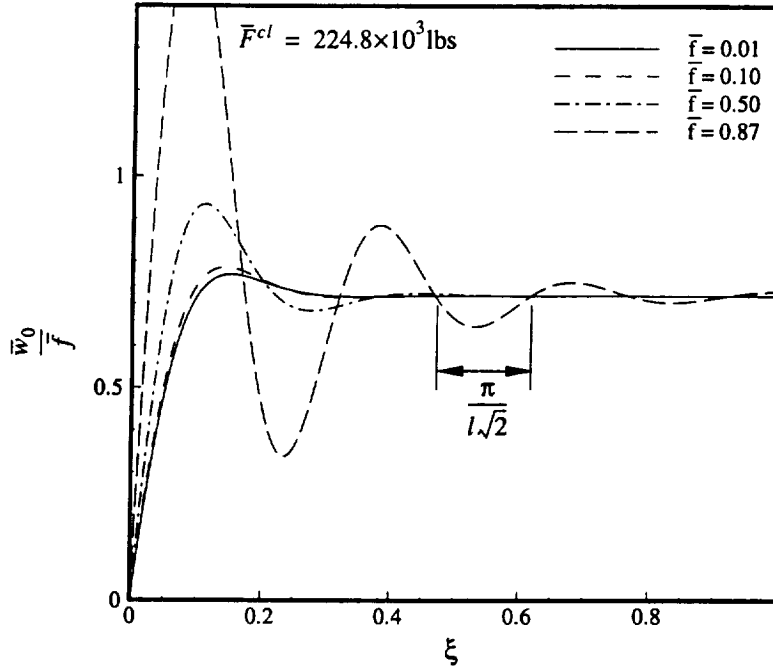


**Figure 3.10: Nonlinear Displacement Profiles of Constant Stiffness Cylinder under Axial Compression**

load level actually corresponds to the critical buckling load). These results were formulated using the full nonlinear solution of Eq. (3.15), and note that the radial displacement is also normalized with respect to the value of the applied load. For small values of the load parameter, the linear solution first shown in Figure 3.2 is considered adequate. As the magnitude of the compressive load increases, the influence of the nonlinearity increases dramatically. The nonlinear character of the boundary layer for a constant stiffness laminate can be surmised from the analytical solution of the ordinary differential equation given by Eq. (3.15). As the load increases, the effect of the exponential portion begins to spread further into the interior of the domain (since the frequency for the hyperbolic functions decreases), while the sinusoidal terms begin to vary faster and approach a frequency that corresponds to the classical buckling estimate  $\hat{\beta}_x$ , where the parameters  $\hat{\beta}_x$  and  $l$  are related through Eq. (3.14). The resulting wavelength of the buckled pat-

tern as  $\bar{f}$  approaches one is shown in Figure 3.10. It is quite evident that substantial differences exist between the assumed “flat” state from classical membrane theory and the actual deformation from the nonlinear solution, therefore the effect of this prebuckling deformation on the critical buckling load must be investigated in more detail.

Consideration of the nonlinear prebuckling solution when calculating an accurate estimate of the bifurcation load has already been performed by other authors for constant stiffness laminates, most notably by Almroth<sup>37</sup>. His results (using Donnell-Mushtari-Vlasov buckling equations) indicate that the calculated buckling load can be around 15% lower than the classical solution that employs linear membrane prebuckling, though the general trends and characteristics of the buckled state remain the same. For comparison purposes, Almroth’s results are displayed in Table 3.1 along with calculations based on the equations derived here (using Sanders shell theory) for all possibilities of boundary conditions, designated in Eq. (2.113). To conform to Almroth’s results, the cylinder is assumed to be made of an isotropic material with  $\nu = 0.3$ ,  $L/R = 3.2$ , and  $R/H = 100$ . The buckling loads are normalized with respect to the classical value, and the number in parentheses is  $n$ , the number of circumferential waves in the buckled shape.

Boundary Condition	Almroth <sup>37</sup> (DMV Theory)	Membrane (Sanders Theory)	Linear (Sanders Theory)	Nonlinear (Sanders Theory)
S1	0.868 (9)	0.9947 (9)	0.9950 (9)	0.8670 (9)
S2	0.844 (9)	0.9528 (4)	0.9565 (4)	0.8480 (9)
S3	0.510 (2)	0.5064 (2)	0.5057 (2)	0.5072 (2)
S4	0.510 (2)	0.5044 (2)	0.5054 (2)	0.5072 (2)
C1	0.928 (9)	0.9950 (9)	0.9950 (9)	0.9262 (9)
C2	0.911 (8)	0.9618 (4)	0.9667 (4)	0.9066 (8)
C3	0.928 (9)	0.9945 (9)	0.9949 (9)	0.9262 (9)
C4	0.909 (8)	0.9605 (4)	0.9663 (4)	0.9050 (8)

**Table 3.1: Comparison of Prebuckling Solutions on Axial Compressive Buckling Load**

The first thing to note from these results is the close agreement between the DMV and Sanders shell theory solutions. This is due to the fact that the mode shapes possess a large number of circumferential waves, so that the shallow shell assumptions invoked by DMV theory are acceptable. Discrepancies between the two theories tend to increase for shorter cylinders. Also note the low buckling value for the S3 and S4 cases. This has been attributed to the minimal support provided



by these idealized end conditions, in which the shell is simply supported and also free to displace in the circumferential direction. The membrane prebuckling solution agrees remarkably well with the full nonlinear solution for these cases, since the major factor producing this low buckling value is not nonlinearity but the (unrealistic) conditions applied at the ends. For the other six cases, the membrane and linear prebuckling solutions yield similar results, which tend to overestimate the nonlinear calculation for all cases. This, in essence, removes the possibility of using linear theory for the prebuckling solution, since its accuracy is no greater than the membrane solution while its decreased numerical efficiency is comparable to the more accurate nonlinear case. Therefore the choice for prebuckling solutions comes down to a trade-off between the numerical efficiency of the membrane case and the accuracy of the full nonlinear solution. If the magnitude of the relative error when using the membrane solution could be shown to be bounded by the results of Table 3.1, then its use would be considered acceptable. In fact, investigation of constant stiffness cylinders constructed of composite laminates reveals that even greater agreement exists between the membrane and nonlinear estimates for many cases. This is due to the fact that for certain stacking sequences, the nonlinear boundary layer effect is greatly reduced when compared to isotropic cylinders. However, when using variable stiffness cylinders conclusions regarding the effect of the prebuckling state cannot be drawn as easily, since the membrane deformation is no longer rotation-free. Thus it must be determined if the nonlinear effects are more or less significant when applied to the novel variable stiffness designs.

As discussed in Section 1.2.2 and evidenced by Table 3.1, including the effect of the prebuckling nonlinearity substantially increases the accuracy of the critical load calculation for most cylinders. However, this improvement in the analytical estimation of the critical axial compressive load does still not account for the discrepancy that exists with the experimental results. It is believed that the reason for the disagreement is due to initial shape imperfections of the shell. Though the rigorous postbuckling analysis to include the imperfection sensitivity of the critical load is beyond the scope of this study, some conclusions regarding the effects of these imperfections can still be estimated. The motivation behind this is that the prebuckling deformation of variable stiffness cylinders somewhat resembles an imperfection, and if this leads to greater discrepancy between the membrane and nonlinear buckling estimates than the more complex eigenvalue solution must be used, even if the cylinder is assumed to be imperfection free. Thus it must be shown that the simpler membrane results will still convey the essence of the true buckling load of the structure. This claim is substantiated in two ways: first it will be shown that the basic character of the nonlinear boundary layer is the same for variable stiffness designs as compared to conventional laminates; and secondly that the magnitude of this radial deformation of variable

stiffness cylinders is small enough so that it does not resemble a geometric imperfection and therefore does not require a more thorough analysis. Substantiation of these facts implies that the ensuing relative errors of the simpler analysis will be of comparable magnitude to those of Table 3.1, which will be acceptable for this investigation of the variable stiffness concept.

As an example of the nonlinear static solution of a variable stiffness cylinder, the radial displacement profile for a  $[0\pm<15/75>]_{6s}$  variable stiffness cylinder under axial compression is shown in Figure 3.11 for various values of the load parameter. Again the last load level is the one at

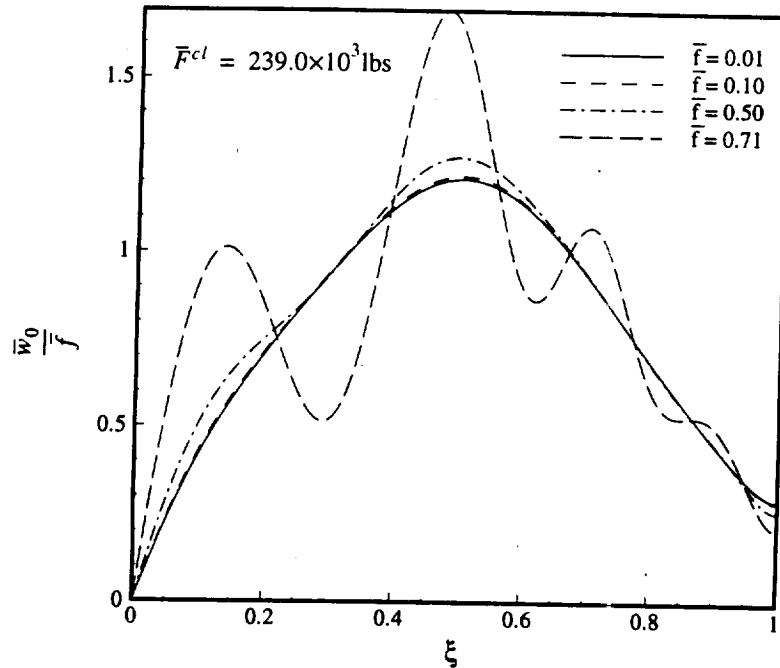


**Figure 3.11: Nonlinear Displacement Profiles of  $[0\pm<15/75>]_{6s}$  Variable Stiffness Cylinder under Axial Compression**

which buckling occurs, though it should be noted that its relative magnitude when compared to unity is mainly due to the normalization parameters used. Comparison of the nonlinear effects in Figure 3.11 with the constant stiffness laminate of Figure 3.10 reveals that, except for the atypical membrane response due to the stiffness variation, the influence and magnitude of the nonlinear boundary layer is equivalent. For small load values, the linear solution can be considered accurate. As the load is subsequently increased, the boundary layer extends further into the interior of the shell and oscillates about the underlying membrane solution. Though some slight vestiges of boundary layer effects do exist away from the ends, the relative magnitude of the nonlinear end effects appears to diminish its significance. Similar results were found for a variety of variable stiffness designs, so that the conclusion stating that the nonlinear boundary layer effect has the same influence as for constant stiffness laminates is considered justified.

The other alternative that would produce a discrepancy between variable and constant stiffness cylinders involves the non-flat prebuckling state of the variable stiffness laminates. If the deformation acts as an geometric imperfection, then the membrane solution may be unacceptably inaccurate for loading under axial compression. To determine if this scenario is present, a plot of load versus displacement is displayed in Figure 3.12 for both the constant and variable stiffness structures previously discussed. Three load curves are shown, which terminate at their calculated

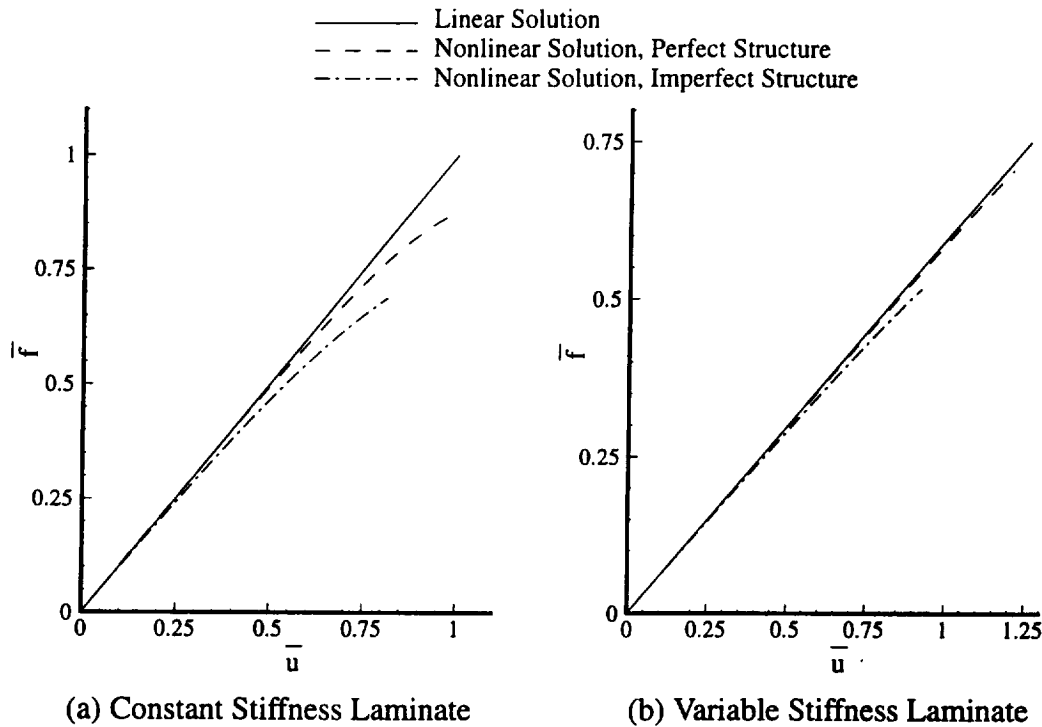


**Figure 3.12: Load versus Displacement for Structures under Axial Compression**

critical buckling loads. The first two represent the membrane and nonlinear prebuckling solutions for a perfect structure. The dash-dot curve denotes a nonlinear analysis for a cylinder with an initial geometric imperfection. For both structures, the imperfection was assumed to be axisymmetric with an axial frequency corresponding to the classical value  $\hat{\beta}_x$  for each cylinder, while the magnitude of the imperfection was chosen to be 10% of the laminate thickness. First notice in Figure 3.12 that for the perfect structures, the amount of nonlinearity for the constant stiffness case seems greater than the variable stiffness laminate. This is due to the fact that the  $45^\circ$  plies in the constant stiffness layup generate a more active boundary layer than the  $15^\circ$  plies that are present near the supports for the variable stiffness case, leading to more significant nonlinear effects when the load is increased. However, the relative magnitude of the nonlinearity for the perfect structures is largely overshadowed when a small imperfection is introduced. For the imperfect structures, the drop in buckling load and increased nonlinearity are quite significant, and conform

to the expected results of postbuckling analysis. It is thus surmised from Figure 3.12 that if the prebuckling shape of the variable stiffness cylinder acted like an effective imperfection, the nonlinearity present in the load-displacement curve and the resulting decrease in the critical load would be much more pronounced. Therefore, the added complexity to compute the buckling load using the nonlinear prebuckled state is not warranted here, since the relative error when compared to the membrane estimate should remain within the errors demonstrated in Table 3.1 for perfect structures. Of course, using this approximate theory for design optimization of cylinders under axial compression may lead to other problems, such as increasing the imperfection sensitivity of the structure by finding structures with many coincident buckling modes, however these concerns should be postponed until after the initial investigation into the possible improvements using the variable stiffness concept is complete.

The results presented in this subsection have dealt exclusively with cylinders under axial compression. This is due to the fact that it is under this loading condition that the nonlinear effects and imperfection sensitivity have been found to be most influential on the calculated buckling load. Experiments have shown that cylinders buckling under external pressure and torsion agree with the theoretical estimations that use either the membrane or nonlinear prebuckling solutions. Therefore, the choice of the membrane prebuckling is warranted for all axisymmetric loading.

### 3.5.2 Curvilinear Fiber Paths

Now that the appropriate solution technique to use for the eigenvalue problem has been determined, the buckling response of laminates with curvilinear fibers can be investigated. As with the material failure results,  $[\pm\phi]_n$  stacking sequences will be used to highlight the variable stiffness effects. A one link linear variation will be used initially with no manufacturing constraints considered, and the S2 boundary condition will be used unless specifically mentioned otherwise. The discussion is divided into general results for various sizes of cylindrical shells under the basic loadings of axial compression, external pressure, and torsion. Relative dimensions of cylindrical shells are often defined in terms of the Batdorf parameter, which is given as

$$Z_b^2 = \frac{L^4}{12R^2} \frac{\hat{A}_{11}\hat{A}_{22} - \hat{A}_{12}^2}{\sqrt{\hat{A}_{11}\hat{A}_{22}\hat{D}_{11}\hat{D}_{22}}} \quad (3.27)$$

This expression was originally derived for isotropic shells by Batdorf<sup>32</sup>, and the definition above in terms of orthotropic stiffness quantities was supplied by Nemeth<sup>84</sup>. This parameter will be used to define the sizes of the variable stiffness cylinders through the use of their average skin stiffness quantities of Eq. (3.11). The actual dimensions for the cylinders are given in Table 3.2.

### Axial Compression

In general, a variable stiffness cylinder defined by a one link variation with  $T_0$  and  $T_1$  under axial compression is found to behave like a constant stiffness cylinder with the fiber orientation angle being the average of the two angles, especially for cylinders in which the axisymmetric state is the critical buckling mode. For instance, the buckled mode shape of an axially compressed cylinder with end angle  $T_0 = 15^\circ$  and mid-length angle  $T_1 = 45^\circ$  is shown in Figure 3.13 along with

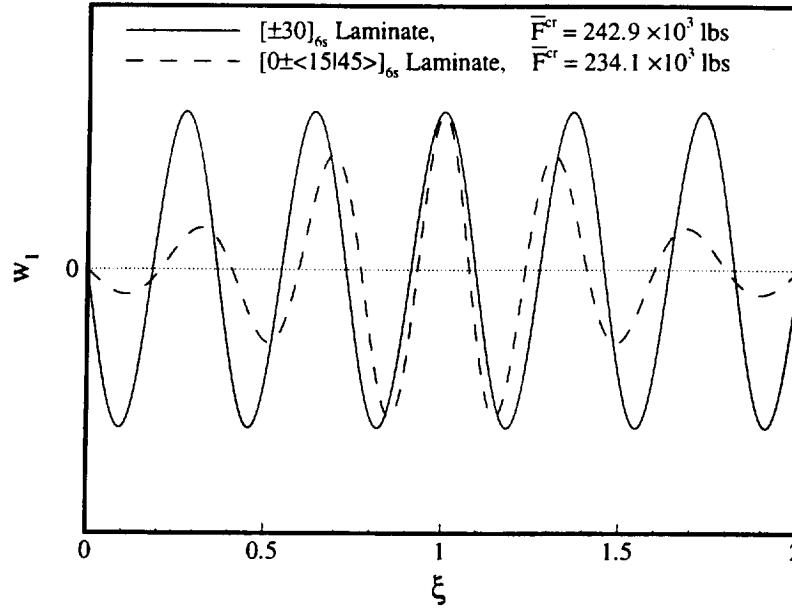


**Figure 3.13: Mode Shapes of Cylinders under Axial Compression ( $Z_b \approx 800$ )**

the mode shape of a constant stiffness shell with  $\phi = 30^\circ$ . Both cylinders buckle at similar load levels and deform into a mode shape with  $m = 11$ ,  $n = 0$  being the dominant harmonic term, however the variable stiffness shell has other harmonic terms that also contribute to the mode shape. For constant stiffness laminates under the S2 boundary condition, the harmonic frequencies in terms of the axial wavenumber  $m$  are decoupled, much like the situation for the circumferential wavenumber  $n$ . This produces mode shapes that are completely defined by the wave numbers  $m$  and  $n$ , much like the classical solutions derived in Section 1.2.2, Eq. (1.3), (1.7), and (1.10). However for variable stiffness cylinders, the spatial variation of the stiffness terms couples the harmonics to produce a mode shape with variable wavelengths in the  $x$ -direction. As one would expect, the character of these wavelengths is dependent on the local values of the stiffness parameters. For example, the classical buckling frequency of a  $[\pm 15]_{6s}$  laminate is  $\hat{\beta}_x = 14.8$ , while for a  $[\pm 45]_{6s}$  layup it increases to 21.9. This is reflected in Figure 3.13, where the middle of the cylindrical shell experiences a higher buckling frequency due to the local stiffness properties. This trend of the stiffness properties defining the resulting frequency is observed for nearly all variable stiffness cylinders under axial compression. Since the buckling frequencies for most laminates are

relatively high, the failure of axially compressed cylinders through instability is often characterized by the weakest areas dominating the buckling response. For instance, the critical load of the  $[\pm 0/15/45]_{6s}$  laminate in Figure 3.13 is analogous to the value for a  $[\pm 45]_{6s}$  cylinder and the most significant aspect of the buckled shape occurs in the middle of the cylinder. This buckling failure characteristic somewhat resembles the “weak link” concept of the material failure results, though the global nature of the buckling results somewhat alters the nature of the failure mode.

To see this effect in greater detail, a contour plot of the buckling load under axial compression with respect to the endpoint angles  $T_0$  and  $T_1$  is shown in Figure 3.14. The critical loads are nor-

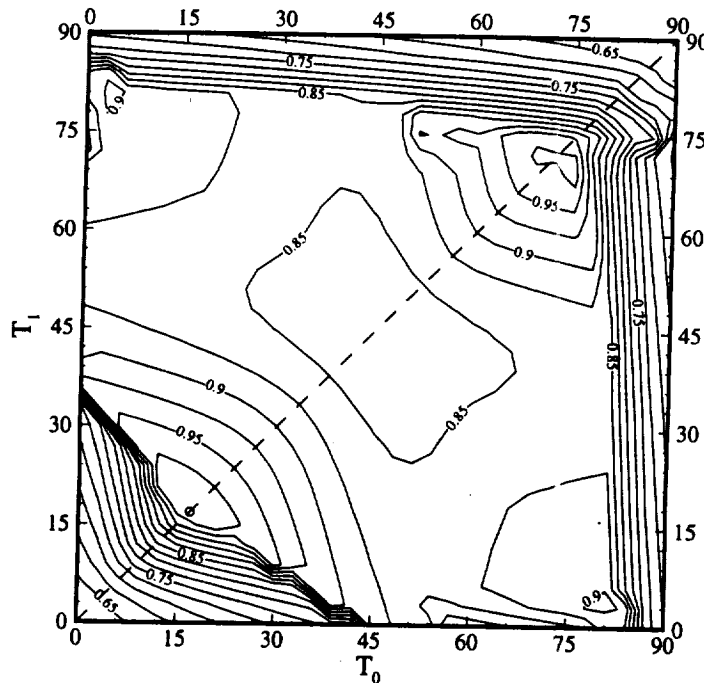


**Figure 3.14: Contour Plot of Axial Compression Load for One Link Variation ( $Z_b \approx 800$ )**

malized with respect to the optimal buckling load of the best constant stiffness laminate, so that each contour line represents a change of 2.5% of this value. The dashed diagonal line indicates designs that are constant stiffness laminates ( $T_0 = T_1$ ) and the empty and filled circles represent the variable stiffness and constant stiffness shells with the maximum buckling load found through standard optimization techniques. As one can see from Figure 3.14, the optimum design for buckling under axial compression (for this geometry) is actually a straight fiber cylinder with  $\phi \approx 17^\circ$ , so that the empty and filled circles are at the same location. The “weak link” phenomenon is best represented by the top and right hand portions of the contour plot, where the horizontal and vertical contour lines indicate that the critical load is determined by the least resistant areas of the stiffness distribution. Furthermore, the diagonal contour lines at the bottom left region resemble the

averaging property that was introduced through the results of Figure 3.13. Also note that the contour plot is nearly symmetric about the constant stiffness design line. This indicates that the axial variation of the stiffness does not improve the buckling load for axially compressed cylinders. This proved to be the case for virtually all cylinders under axial compression due to the two methods of failure just discussed.

### External Pressure

Perhaps the greatest possibility for an improvement in the buckling load by using an axial variation of the stiffness exists for cylinders under external pressure. This is surmised from the fact that the effective length of the cylinder has an enormous influence on the critical pressure, and also through the belief that the stiffness variation can be designed to imitate the response of a shorter cylinder and therefore improve the buckling load. This has been most easily accomplished in the past through the use of ring stiffeners. It was mentioned in the introduction that constant stiffness cylinders under external pressure will always buckle into a mode with one axial half wave ( $m = 1$ ). The largest deflection for this mode shape occurs at the middle of the cylinder. Also proven in Section 1.2.2 (in the discussion of Figure 1.6) was that shorter cylinders always have a higher critical pressure load than longer ones because of the smaller distance between the restrained ends. One way to improve the buckling performance under this loading condition is to include ring stiffeners, which in essence decrease the span between supports by separating the long cylinder into shorter ones. This is demonstrated in Figure 3.15, where the mode shapes are displayed for an unstiffened and stiffened cylinder subjected to external pressure. The geometry

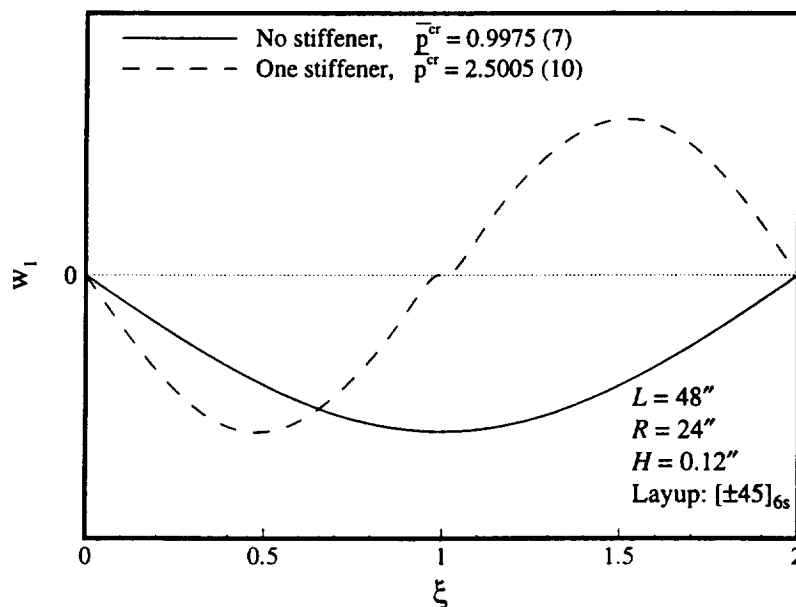


Figure 3.15: Mode Shapes of Ring Stiffened Cylinder under External Pressure

of the shell corresponds to the one of Figure 3.9, except that only one stiffener located at the mid-length is included, and the number in parentheses in the legend represents the number of circumferential waves in the buckled shape. The unstiffened shell buckles into one axial half wave as expected, with the critical value being close to the predicted classical value (the slight deviation from unity is due to the presence of the  $D_{16}$  and  $D_{26}$  terms that the classical estimate ignores). Placing a sturdy ring stiffener at the location of the largest displacement cuts the effective length of the cylinder in half, and significantly increases the critical load and the number of circumferential waves in the buckled mode shape. It then logically follows that if the variable stiffness shell is designed to have a high circumferential stiffness near the middle ( $90^\circ$  plies) this area will approximate a ring stiffener, and the buckled cylinder should behave as if it had a central ring stiffener. The mode shape should then change from a  $m = 1$  configuration to  $m = 2$  because the stiff center will not permit large deflections.

To see if this actually happens, several geometries of cylinders were investigated to determine if such a change in mode shape could be produced through the use of curvilinear fibers, and if any other mechanisms exist that can improve the buckling performance of cylinders loaded by external pressure. The results are again displayed in the form of a contour plot for the end and mid-length angles, as shown in Figure 3.16. Note that the contour lines are basically diagonal, which again represents the averaging concept for the one link variable stiffness designs. Also note that

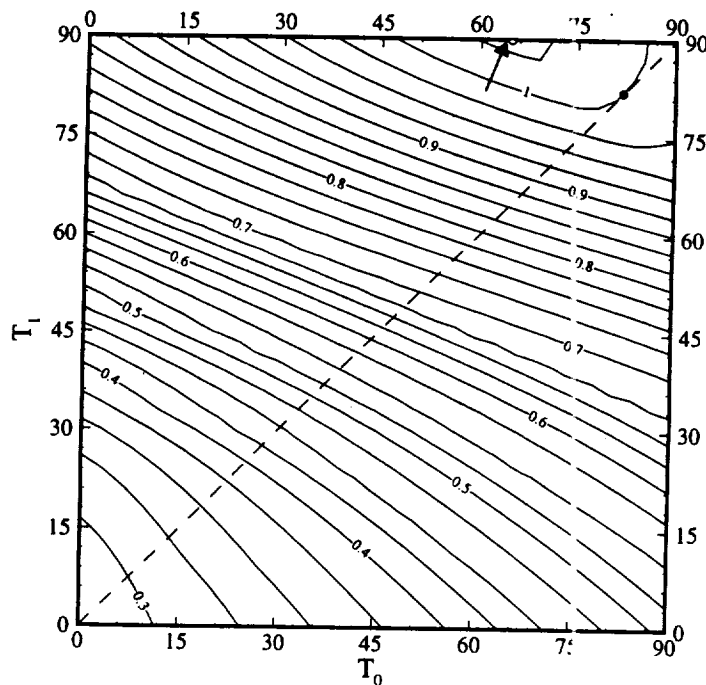


Figure 3.16: Contour Plot of External Pressure Load for One Link Variation ( $Z_b \approx 800$ )



the maximum value now occurs as a variable stiffness design (shown by the arrow), with a relative increase over the straight fiber format of around three percent. However, the desired mechanism to improve the performance of laminates under external pressure, namely the reduction of the effective length of the cylinder, was not found to occur for any of the geometries investigated. The main reason for this is that the axial variation of the stiffness parameters through the use of curvilinear fibers is not able to produce a drastic enough stiffness change that will act as a ring stiffener. Instead the stiffness variation produces a buckling mode that is still predominantly an  $m = 1$  mode. However, the results shown in Figure 3.16 do provide some hope, since there does exist slight improvement over the constant stiffness laminates even with the simple one link variation. Optimization of designs with more general variations of the fiber orientation angle will be performed in Section 3.6.2 to determine the extent of the possible improvements.

### Torsion

For cylinders with an axial stiffness variation loaded by torsion, the results are expected to be similar to the pressure loaded case due to the sensitivity of cylinder length on the buckling load. Though the dependence on the length is not as considerable for torsion (as noted in the discussion of Figure 1.6 and Figure 1.8 in Section 1.2.2), there still exists similar promise for improvement by decreasing the effective length of the structure. However, this conclusion is based on the results of the classical estimate of the torsional buckling load as presented in Section 1.2.2, which ignores the boundary conditions at the ends and allows warping of the cross-section. Nevertheless, since the solution in the next chapter does allow warping at the ends, the relative error associated with this non-realistic mode shape must be determined.

Our classical estimation for buckling under torsion is briefly reviewed here for ease of comparison. In essence, the solution assumes that deformed shape is composed of successive cross-sections with  $n$  circumferential waves that are rotated about the axis of the cylinder with an axial frequency  $\beta$ . For short and intermediate length cylinders, the axial frequency can be shown to correspond to one half wave along the length of the axis, while the value of  $n$  is chosen so that the resulting eigenvalue is a minimum. Mathematically, such an assumed shape for the radial displacement (from Eq. (1.9) with  $\beta = m\pi R/L$ ) can be written as

$$w_1(\xi, \theta) = \sin\left(\frac{m\pi\xi}{2}\right)\cos(n\theta) - \cos\left(\frac{m\pi\xi}{2}\right)\sin(n\theta) \quad (3.28)$$

Comparison of this result to Eq. (3.19) supplies the classical solution for the perturbed displacement functions  $W_I$  and  $W_{II}$ . Note that Eq. (3.28) does not satisfy any realistic boundary conditions at the ends of the cylinder, since  $W_{II}$  does not equal zero there.

The rigorous and classical solutions for the radial displacement functions  $W_I$  and  $W_{II}$  are shown in Figure 3.17 for a typical intermediate length cylinder with the S2 end condition. The

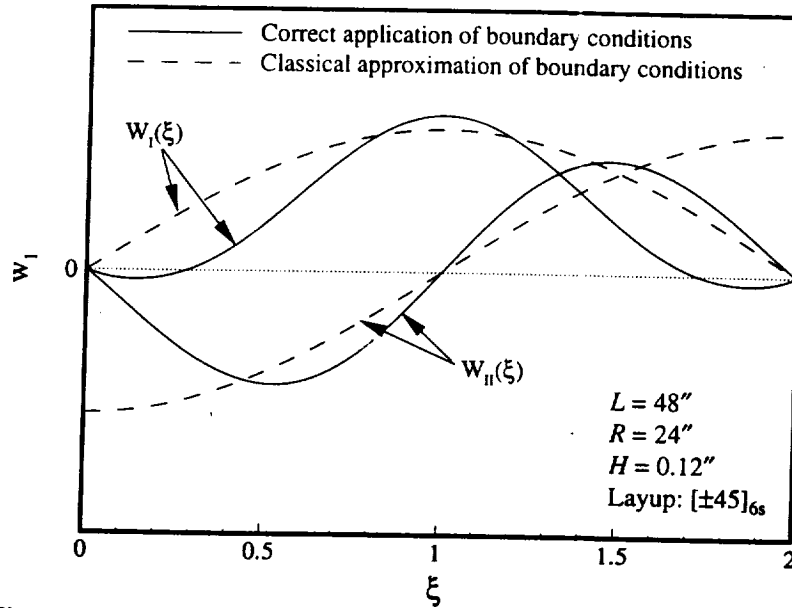


**Figure 3.17: Comparison of Classical Mode Shape under Torsion**

dashed lines represent the classical estimate, which for this geometry produces a mode with one axial half wave ( $m = 1$ ) and six circumferential waves ( $n = 6$ ). Note that the radial displacement is not zero at the ends for the  $W_{II}$  solution. Conversely, the rigorous application of the boundary conditions for the deformed shape, using a membrane prebuckling solution as outlined earlier in this chapter, is denoted by the solid lines in Figure 3.17. Now the buckled mode shape contains nine circumferential waves, and the critical load is calculated to be greater than the classical estimate by a factor of 2.05. Also notice that though the shapes of the curves basically resemble the classical approximation, the differences near the ends are quite substantial and lead to the large error between the solutions. Because of this discrepancy, most of the literature devoted to torsion of cylindrical shells uses some form of the rigorous solution to calculate the "classical" buckling load. Usually this is accomplished by an assumed form of the displacements as an expansion of sine functions in the axial direction which automatically satisfy the end conditions. The rigorous solution shown above agrees exactly with these results.

As the length of the cylinder increases, the effect of the end conditions should diminish and the rigorous solution should approach that of the infinite length solution with  $n = 2$  and the axial frequency corresponding to the classical value  $\hat{\beta}_{x\theta}$ . The relative error between the classical estimate and the rigorous solution should also diminish. This is demonstrated in Figure 3.18, where the torsional buckling load is plotted as a function of the Batdorf parameter for two isotropic cyl-

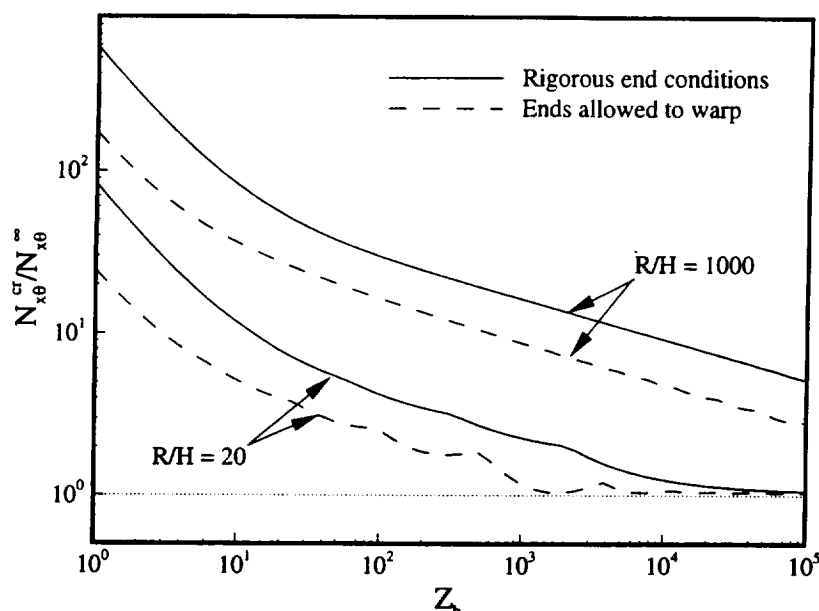


**Figure 3.18: Relative Error of Classical Estimate for Torsion**

inders with different  $R/H$  ratios. Note that both axes are logarithmic, and that the critical shear stress resultant is normalized with respect to the infinite length value of Eq. (1.13). As the length is increased, the relative difference between the two solutions decreases, though the effect is definitely more apparent for the thicker shell. For the thinner shell, the error seems to remain at a factor of around two, while for very short cylinders the correct application of the boundary conditions tends to overshoot the classical estimation by a factor of three, irrespective of the radius-to-thickness ratio. Therefore, it can be concluded that the effect of the end conditions is quite significant for short and intermediate length cylinders, and that it increases for thinner shells. The classical estimation can be regarded as following the basic trends of the rigorous solution, though when used for analysis its inherent error due to the neglect of the end restraints must be considered.

Returning to the application of the variable stiffness concept as applied to torsion, the results of Figure 3.17 and Figure 3.18 indicate that the dependence on length may offer some improvement possibilities over constant stiffness laminates. Firstly, as opposed to the pressure loaded case that possess a maximum displacement at the mid-length of the cylinder, the cyclic nature of the torsional buckling mode generates a large area over which large deformation occurs. Therefore an axial stiffness variation that can resist deformation in these areas have a greater possibility of improving the buckling load. Also, the expected sensitivity of length on the torsional buckling load implies that artificial ring stiffeners should also add to the resistance to instability. For curvilinear fibers using a one link variation, the results are displayed in Figure 3.19, which is the typi-

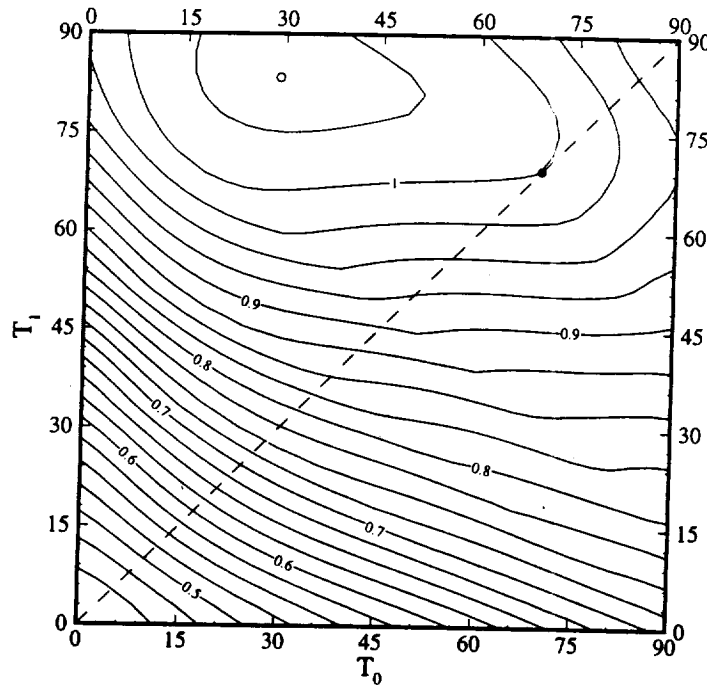


**Figure 3.19: Contour Plot of Torsional Load for One Link Variation ( $Z_b \approx 800$ )**

cal contour plot of the critical load in terms of the end point angles. Again note the averaging effect for the designs at the bottom right of the figure, however now there also exists a definite maximum which occurs as a variable stiffness design. The mode shapes for the radial displacement for both of the maximum designs, variable and constant stiffness, are shown in Figure 3.20. Notice how the stiffness variation forces the maximum deformation to be concentrated in the mid-

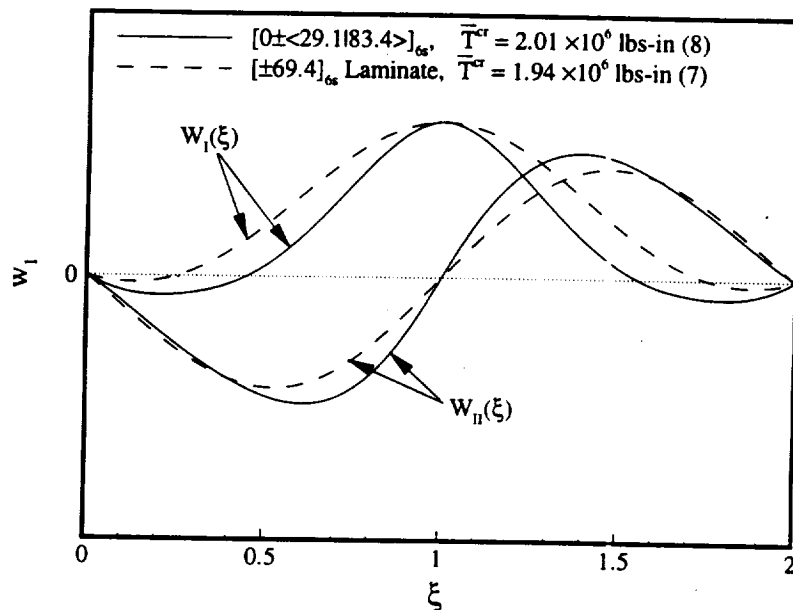


**Figure 3.20: Mode Shapes of Optimal Designs under Torsion ( $Z_b \approx 800$ )**

dle of the cylinder even more than usual. This, in essence, shortens the cylinder and thereby produces the higher buckling load, though not to the extent desired. Further improvements may be possible for more general variations of the fiber orientation angle, which is investigated in the next section.

### 3.6 Optimization under Axisymmetric Loading

The basic trends and optimization results demonstrated in the last section for curvilinear fibers under axisymmetric loading is expanded in this section to more practical design problems. In the first subsection, the one link variation is used for several geometries of cylinders to determine the sizes that show the most promise for the use of curvilinear fibers. These results lead to optimization of the critical loads using a more general variation of the fiber path. Emphasis for this design study is on the longer cylinders, which give the curvilinear fibers more freedom to vary within the manufacturing constraints. Also included in this portion is stacking sequence optimization, since the general  $[\pm\phi]$  symmetric layup may not be the best choice. Finally, a quick comparison between the curvilinear fiber designs and a constant stiffness laminate with a central ring stiffener is conducted to determine which mechanism has a greater effect on improving the performance of composite laminates.

#### 3.6.1 One Link Variation for Various Cylinder Sizes

The general material failure and buckling results presented in the last two sections dealt primarily with a specific size cylinder constructed with a  $[\pm\phi]$  stacking sequence. This subsection extends on these results by finding the optimal configurations for several geometries of variable stiffness cylinders that utilize the one link curvilinear fiber path definition. The results should indicate general trends about the usefulness of the variable stiffness concept as applied to cylinder sizes under particular axisymmetric loading conditions. For these design studies, the  $[\pm\phi]_{ns}$  stacking sequence will be the only layup considered, and the manufacturing constraints will be ignored. These considerations are implemented to highlight the stiffness variation and to fully explore the possibilities of the curvilinear fiber format. More practical laminate constructions that fall within the manufacturing guidelines for curvilinear fibers will be utilized in the next subsection for the geometries that show the most promise using these simple guidelines.

Six representative values of the Batdorf parameter  $Z_b$  are chosen for the initial study. The optimization is designed to find the configuration of the one link fiber orientation angle that produces the greatest value of the critical load (that being the smaller of the material failure load and the buckling load) for the cases of axial compression, external pressure, and torsion. The curvilinear fiber path is defined by two variables: the fiber orientation angle at the end of the cylinder ( $T_0$ ),

and at the mid-length ( $T_1$ ), and these quantities are constrained to remain between  $0^\circ$  and  $90^\circ$ . For such a simple optimization problem, traditional gradient-based strategies are used to find the optimal designs. These techniques are likely to only find local optima, therefore for problems with multiple optima such as these (note the several optima in Figure 3.14) various starting points for the optimization process are used, and the ultimate designs are determined as the best design from these local optima. The results of the design studies are reported in Table 3.2:

$R = 24''$ for all cylinders	Axial Compression ( $\times 10^3$ lbs)	External Pressure (psi)	Torsion ( $\times 10^6$ lbs-in)
$Z_b \approx 2$ $L = 2.4'', 24$ plies	$T_0 = 0^\circ, T_1 = 0^\circ$ $\bar{F}^{cr} = 724.0$ Increase = 0.0%	$T_0 = 43.2^\circ, T_1 = 32.2^\circ$ $p^{cr} = 400.9$ Increase = 4.5%	$T_0 = 45.0^\circ, T_1 = 45.0^\circ$ $\bar{T}^{cr} = 72.10$ Increase = 0.0%
$Z_b \approx 50$ $L = 12'', 24$ plies	$T_0 = 21.0^\circ, T_1 = 18.6^\circ$ $\bar{F}^{cr} = 284.3$ Increase = 0.0%	$T_0 = 37.6^\circ, T_1 = 90^\circ$ $p^{cr} = 34.66$ Increase = 8.7%	$T_0 = 41.7^\circ, T_1 = 52.4^\circ$ $\bar{T}^{cr} = 5.273$ Increase = 0.48%
$Z_b \approx 300$ $L = 24'', 16$ plies	$T_0 = 73.3^\circ, T_1 = 73.3^\circ$ $\bar{F}^{cr} = 120.3$ Increase = 0.0%	$T_0 = 61.4^\circ, T_1 = 90^\circ$ $p^{cr} = 5.675$ Increase = 4.6%	$T_0 = 30.7^\circ, T_1 = 71.2^\circ$ $\bar{T}^{cr} = 1.168$ Increase = 4.7%
$Z_b \approx 800$ $L = 48'', 24$ plies	$T_0 = 17.0^\circ, T_1 = 17.0^\circ$ $\bar{F}^{cr} = 269.7$ Increase = 0.0%	$T_0 = 64.7^\circ, T_1 = 90^\circ$ $p^{cr} = 7.821$ Increase = 3.2%	$T_0 = 29.1^\circ, T_1 = 83.4^\circ$ $\bar{T}^{cr} = 2.005$ Increase = 3.4%
$Z_b \approx 5,000$ $L = 120'', 24$ plies	$T_0 = 72.3^\circ, T_1 = 72.3^\circ$ $\bar{F}^{cr} = 269.2$ Increase = 0.0%	$T_0 = 90^\circ, T_1 = 90^\circ$ $p^{cr} = 3.201$ Increase = 0.0%	$T_0 = 69.2^\circ, T_1 = 90^\circ$ $\bar{T}^{cr} = 1.266$ Increase = 0.88%
$Z_b \approx 20,000$ $L = 170'', 12$ plies	$T_0 = 71.7^\circ, T_1 = 71.7^\circ$ $\bar{F}^{cr} = 65.71$ Increase = 0.0%	$T_0 = 90^\circ, T_1 = 90^\circ$ $p^{cr} = 0.3997$ Increase = 0.0%	$T_0 = 90^\circ, T_1 = 90^\circ$ $\bar{T}^{cr} = 0.2294$ Increase = 0.0%

**Table 3.2: Results of Optimization of Linear Variable Stiffness Cylinders**

For only two cases ( $Z_b \approx 2$  for pressure and torsional loading) is the material failure load significant. Buckling is the critical failure mode for all other cases by a considerable margin.

The first conclusion from the results shown in Table 3.2 concerns the lack of improvement of an axial stiffness variation for the load case of axial compression, in which the optimal configurations correspond to constant stiffness laminates for all cylinder sizes. This result can be explained through the known behavior of constant stiffness laminates under axial compression. As discussed in Section 1.2.3 with regards to the Koiter circles of Figure 1.4, there exist numerous possibilities for the buckled shape of an axially compressed cylinder in terms of the axial frequency  $\beta$  and the

circumferential wavenumber  $n$ . Furthermore, many of these eigenmodes possess similar eigenvalues, especially for thin laminates in which the buckling frequencies are relatively high. As a consequence of these multiple possibilities for the dominant mode shape, axially compressed cylinders that contain an axial stiffness variation deform into a linear combination of these coincident modes, thereby generating a buckled shape that reflects the local stiffness properties (as evidenced by Figure 3.13) but does not increase the resultant buckling load. Therefore it is concluded that an axial stiffness variation will do little to improve the buckling load under axial compression, since the stiffness variation will neither redistribute the applied load nor alter the buckled shape in an advantageous manner.

The foregoing explanation of the buckling characteristics for the axial compression case also offers insight as to why there *is* relative improvement for an axial stiffness variation under loads of external pressure and torsion. As discussed earlier, the critical mode shape for both of these transverse loads ordinarily contains only one half-wave ( $m = 1$ ) in the axial direction. Furthermore, eigenvalues corresponding to mode shapes that contain multiple axial half-waves ( $m > 1$ ) are significantly higher than the critical buckling value (as exemplified in Figure 3.15). Therefore, when a cylinder with an axial stiffness variation is subjected to external pressure or torsion, the resulting critical eigenmode attempts to deform into the  $m = 1$  shape with some local variations due to the local stiffness properties. This, in effect, activates the modes corresponding to  $m > 1$  and thereby increases the buckling load by altering the deformed shape of the buckled cylinder. Though the relative increases for a one link variation are not that significant for either load case, as evidenced by Table 3.2, their improvements can be attributed to this mechanism. More general variations of the fiber orientation angle should produce even greater increases in buckling performance. This will be addressed in the next subsection.

A few remarks are also needed to explain the poor results in Table 3.2 for the longer cylinders under external pressure and torsion. On one hand, the one link variation of the fiber orientation angle is not that effective at varying the stiffness over such a long span. More general variations need to be included. Furthermore, constraining the stacking sequence to  $[\pm\phi]_{ns}$  laminates is severely limiting for optimization purposes. For instance, the buckling of longer cylinders under external pressure and torsion is dominated circumferential bending, therefore the layup that produces the highest buckling load should contain many  $90^\circ$  plies that best resist this type of deformation. This leaves very little room for the variable stiffness effects to work. Employing arbitrary stacking sequences should alleviate this problem, since without the  $[\pm\phi]_{ns}$  layup constraint several (constant stiffness)  $90^\circ$  plies can easily be included in the stacking sequence. Both of these considerations are investigated in the next subsection.

### 3.6.2 Fiber Path Optimization for Selected Cylinders

The results of Section 3.6.1 have indicated that the best hope to improve the performance of cylinders under axisymmetric conditions is to find an axial stiffness variation that effectively alters the shape of the resulting eigenmode to increase the buckling load. The load cases of external pressure and torsion show the most promise, and longer cylinders are intuitively believed to offer the greatest improvement since they provide more opportunity for the curvilinear fiber paths to vary. Therefore, this subsection utilizes a more general definition of the fiber orientation angle through the use of the linked line segment approach, defined earlier in Figure 2.6, and investigates the possible gains in failure loads for two specific geometries from Table 3.2. The specific cylinder sizes correspond to  $Z_b \approx 300$ , which showed the greatest consistent increase for the relevant loading conditions, and a longer cylinder with  $Z_b \approx 5,000$  (it was chosen over the  $Z_b \approx 20,000$  case due to the greater number of possibilities for stacking sequences). Though increased failure loads are only expected for the transversely loaded cases, axial compression is also investigated for completeness.

The optimization problem is represented as:

$$\begin{aligned} & \text{maximize} \quad \text{critical load}(T_i, \varphi_k) \\ & \text{such that} \quad \text{manufacturing constraints are satisfied} \end{aligned} \tag{3.29}$$

The design variables are the endpoint values of the fiber orientation angle using the linked line segment approach, and the designation of each laminae within the stacking sequence. The endpoints of the line segments are evenly spaced within the half-length of the cylinder, and the design cases are arranged so that each successive scenario increases the number of line segments in the definition of the fiber orientation angle. The possibilities for each ply include a positively or negatively aligned variable stiffness ply (denoted as  $+\varphi$  or  $-\varphi$ , respectively) and a constant stiffness layer with either a  $0^\circ$  or  $90^\circ$  ply angle. The laminate is assumed to be symmetric so that only half of the stacking sequence need be considered, and the two outermost plies of the laminate are stipulated to be  $\pm\varphi$  so as to provide the greatest effect of the variable stiffness concept. The discrete nature of these ply designation variables precludes the use of standard gradient-based optimization techniques, therefore the numerical optimization will be performed through the use of a genetic algorithm, which is ideally suited for problems involving discrete variables. Details of this optimization technique are provided in Appendix A, Section A.6.2.

The manufacturing constraints alluded to in the statement of the optimization problem include two criteria: a stipulation that the laminate be balanced; and a curvature limit on the curvilinear fiber path. The balancing constraint is enforced through the use of a penalty function within the



optimization scheme, in which laminates that do not have an equal number of  $+\phi$  and  $-\phi$  plies are penalized to lower their relative worth. The latter constraint, based on the limit on the curvature of the fiber path due to the manufacturing process, helps to define the form of the endpoint design variables within the optimization scheme. Traditional methods would suggest that each endpoint angle should be designated as a separate design variable, and the manufacturing limit on curvature would then be incorporated as an inequality constraint within the optimization problem. However, it was found that when using a genetic algorithm, this technique produced many designs that were infeasible due to the curvature constraint, thereby wasting computing time. Therefore, an alternate method to define the values of the fiber angle variables is used.

The procedure is predicated on establishing a base angle as one independent variable, and then defining the subsequent fiber orientation angle variables as positive or negative changes from the reference value. The base angle is chosen as  $T_0$ , and it is limited to discrete values to remain consistent with the genetic algorithm technique. Each remaining endpoint angle  $T_i$  is given the possibility of either no change from its predecessor, or a positive or negative step. The size of the step is limited to remain within the manufacturing constraints, thus every design is feasible in a manufacturing sense. For longer cylinders or designs using only a few line segments, the curvature constraint may not be significant, therefore an upper limit of  $15^\circ$  is also prescribed for the step size. This is expressed mathematically in Eq. (3.30):

$$\begin{aligned} T_0 &\in \{5^\circ, 15^\circ, 30^\circ, 40^\circ, 45^\circ, 50^\circ, 60^\circ, 75^\circ, 85^\circ\} \\ T_i &= T_{i-1} \pm \text{step} \quad i = 1, N_{\text{seg}} \\ \text{step} &\in \left\{ 0, \min \left[ 15^\circ, \frac{180^\circ \cdot L}{2\pi N_{\text{seg}} \rho_{\min} \cos T_{\min}} \right] \right\} \end{aligned} \quad (3.30)$$

Here  $N_{\text{seg}}$  is the number of line segments in the half-length, which increases for each optimization case to track the evolution of the fiber path. Also note that when  $N_{\text{seg}} = 0$ , the problem reduces to standard (constant stiffness) stacking sequence optimization with the value of the fiber orientation angle for the  $\pm\phi$  plies being limited to the choices shown in Eq. (3.30).

The results of the fiber path optimization for the axial compressive case corroborate the expected outcome. The final designs when using the linked line segment approach are constant stiffness laminates that produce the best resistance to buckling under axial compression. The stacking sequence optimization also provides a significant increase over the basic  $[\pm\phi]_{\text{ns}}$  layups reported in Table 3.2. In detail, the solutions for each geometry under axial compression are:

$$\begin{aligned}
 Z_b \approx 300 & \rightarrow [\pm 45/0/90_2/0/\pm 45]_s & \bar{F}^{cr} &= 175.9 \times 10^3 \text{ lbs} \\
 Z_b \approx 5000 & \rightarrow [\pm 45/90/0_2/90/\pm 45_2/90/0]_s & \bar{F}^{cr} &= 395.7 \times 10^3 \text{ lbs}
 \end{aligned}
 \quad (3.31)$$

The results for external pressure and torsion for each geometry are reported in Table 3.3 and Table 3.4. The stiffness variation for each case is defined by a small plot of the fiber orientation angle (marked at  $15^\circ$  intervals) versus location within the half-length.

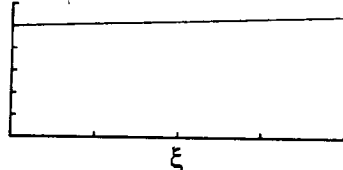
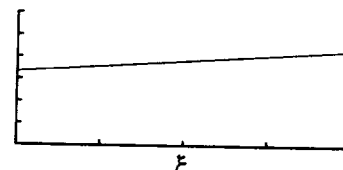
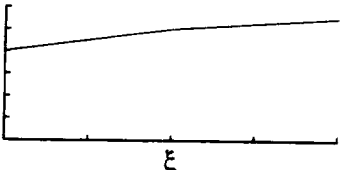
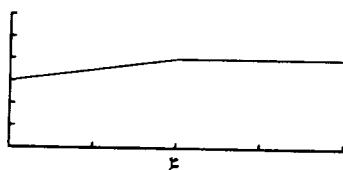
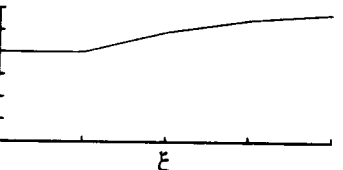
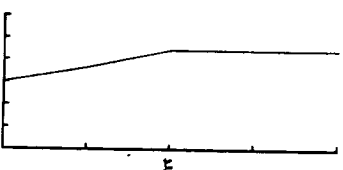
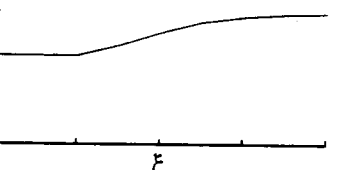
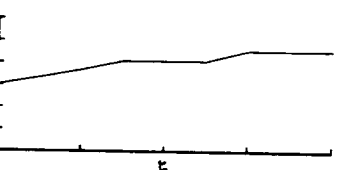
	External Pressure	Torsion
Constant Stiffness	$[\pm 85/90/\pm 85/0_3]_s$ $p^{cr} = 6.9131 \text{ psi}$	$[\pm 60/90/\pm 60/0_3]_s$ $\bar{T}^{cr} = 1.419 \times 10^6 \text{ lbs-in}$
1 Segment	 $[\pm \phi/90/\pm \phi/0_3]_s$ Increase = 1.84%	 $[\pm \phi/90/\pm \phi/0_3]_s$ Increase = 1.05%
2 Segments	 $[\pm \phi/90/\pm \phi/0_3]_s$ Increase = 4.27%	 $[\pm \phi/90/\pm \phi/0_3]_s$ Increase = 1.07%
4 Segments	 $[\pm \phi/90/\pm \phi/0_3]_s$ Increase = 5.79%	 $[\pm \phi_3/0_2]_s$ Increase = 0.92%
8 Segments	 $[\pm \phi/90/\pm \phi/0_3]_s$ Increase = 6.57%	 $[\pm \phi_3/0_2]_s$ Increase = 0.78%

Table 3.3: Results of Shape Optimization for  $Z_b \approx 300$  Variable Stiffness Cylinder

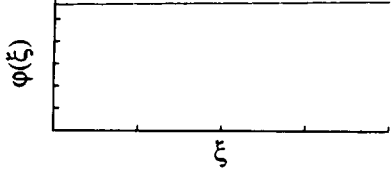
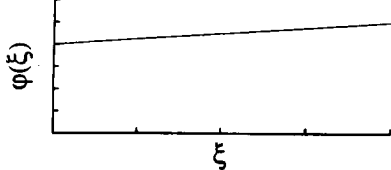
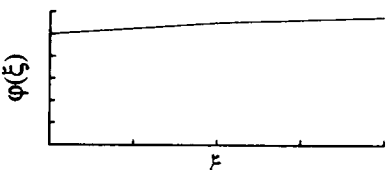
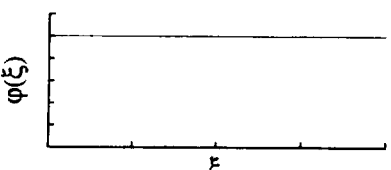
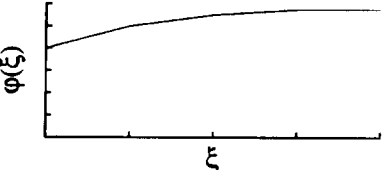
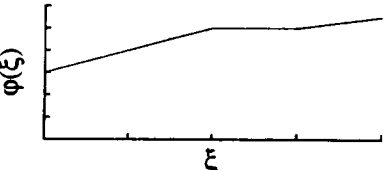
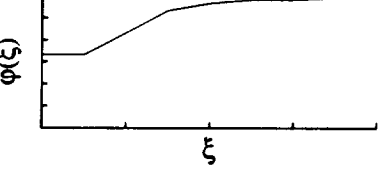
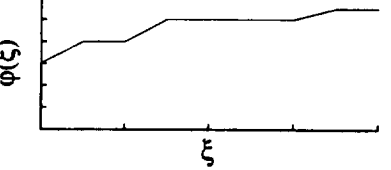
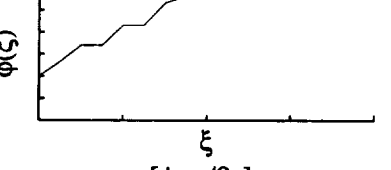
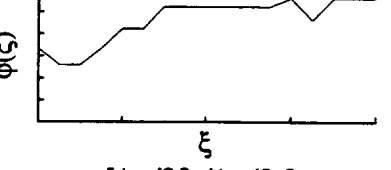
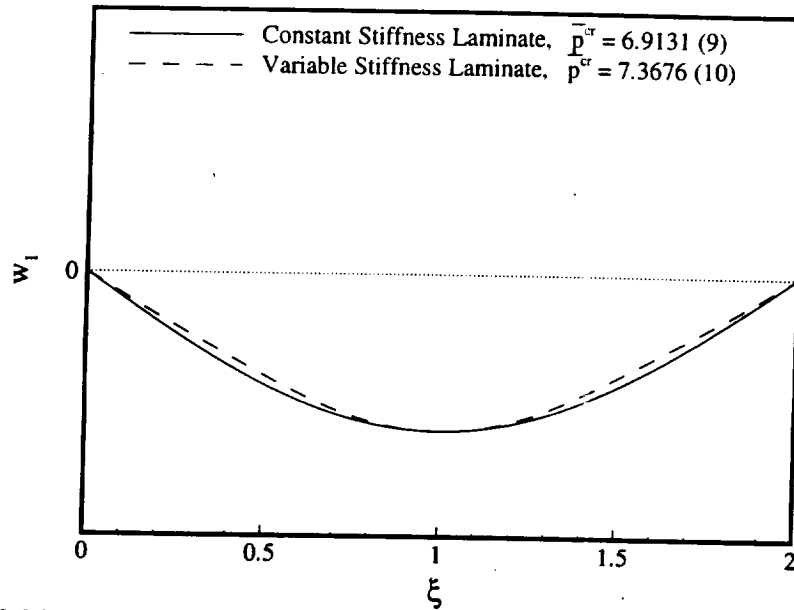
	External Pressure	Torsion
Constant Stiffness	$[\pm 85/90_5/0_5]_s$ $p^{cr} = 4.0885 \text{ psi}$	$[\pm 75/90_3/\pm \varphi/0_5]_s$ $\bar{T}^{cr} = 1.924 \times 10^6 \text{ lbs-in}$
1 Segment	 $[\pm \varphi/90_2/\pm \varphi/0_6]_s$ Increase = 1.23%	 $[\pm \varphi/90_3/\pm \varphi/0_5]_s$ Increase = 0.78%
2 Segments	 $[\pm \varphi_3/0_6]_s$ Increase = 2.16%	 $[\pm \varphi/90_3/\pm \varphi/0_5]_s$ Increase = 0.00%
4 Segments	 $[\pm \varphi/+ \varphi/90/- \varphi/0_7]_s$ Increase = 2.92%	 $[\pm \varphi/90_2/\pm \varphi/0_6]_s$ Increase = 1.30%
8 Segments	 $[\pm \varphi/+ \varphi/90_2/- \varphi/0_6]_s$ Increase = 3.98%	 $[\pm \varphi_2/90/\pm \varphi/0_5]_s$ Increase = 1.30%
16 Segments	 $[\pm \varphi_3/0_6]_s$ Increase = 4.54%	 $[\pm \varphi/90_2/\pm \varphi/0_6]_s$ Increase = 0.99%

Table 3.4: Results of Shape Optimization for  $Z_b \approx 5000$  Variable Stiffness Cylinder

As evidenced by the tables, the relative increase over constant stiffness laminates is not overly impressive. The optimal designs are typified by a gradual change from the value at the ends to a fiber orientation angle in the middle that shows the best resistance to the applied load. The torsionally loaded cylinders exhibit the least amount of improvement, while the case of external pressure does show slight promise. The buckling mode for the best constant stiffness laminate and the optimal variable stiffness design (8 segment case) for the  $Z_b \approx 300$  geometry are displayed in Figure 3.21. Notice that the variable stiffness design still buckles in the basic mode corresponding



**Figure 3.21: Mode Shapes of Optimal Designs for External Pressure ( $Z_b \approx 300$ )**

to one axial half-wave. The stiffness variation does slightly change the deformation pattern by limiting the maximum deformation to the middle area of the cylinder. The number of circumferential waves also increases, albeit slightly, so that the buckling frequencies of the variable stiffness laminate are higher than the constant stiffness design and thus the variable stiffness cylinder require a larger load to become unstable. The curvilinear fiber path mechanism does not seem to be able to produce enough stiffness variation that could actually generate a critical eigenmode that contained two axial half-waves as the dominant mode. A more traditional mechanism to produce this effect is through the use of ring stiffeners and frames. In fact, the inclusion of only one ring stiffener for the constant stiffness design shown in Figure 3.21 produces an increase in the buckling frequency of over 90%, with the mode shape deforming into two axial half-waves much like the example of Figure 3.15. Therefore, it is concluded that in a practical manufacturing environment, the use of ring stiffeners is much more effective than the curvilinear fiber format, since the buckling performance is substantially increased without the added complexity of the manufacturing process required for curvilinear fibers.

## Chapter 4.0 Linear Membrane Solution for a Circumferential Stiffness Variation

This investigation now changes direction ninety degrees by examining the response of cylindrical shells with a circumferential stiffness variation. Besides the standard curvilinear fiber format, the variable stiffness concept now can also incorporate longitudinal stiffeners, including stringers and longerons, but does not contain ring stiffeners or any variation which will produce different characteristics of the cross-section anywhere along the length. Since the stiffness now varies circumferentially, the resulting analysis will contain greater detail in this direction and simplifying assumptions will be used in the axial direction so that one-dimensional solution techniques are still applicable. Unfortunately, the possible simplifications associated with the analysis in the axial direction are quite limited, with the results that the response is assumed to be basically constant along the length. At first glance, this severely limits the practical applications of the analysis, for real structures almost certainly have end conditions which contribute significantly to the stiffness response. By neglecting these effects, we limit the scope of the problem to either very long cylinders that do not depend on the boundary conditions, or an approximate solution of only a thin slice of the cylinder cross-section in which the end conditions are ignored. Fortunately, there exist opportunities within these restrictions that can still be considered worthwhile for a cylinder with a circumferential stiffness variation. These include (1) the nonlinear Brazier effect for infinitely long cylinders; and (2) linear stability analysis of cross-sections of short cylinders subjected to general loading that can be considered constant along the length. Of these two options, the latter choice is the simpler and will be investigated first, while the former case will be studied in the next chapter.

Therefore, this chapter investigates the linear membrane solution for general loading of a short cylinder segment with a circumferential stiffness variation. Several remarks regarding the chosen restrictions for this specific problem should be addressed. Firstly, linear membrane theory is used since it was shown that it was a good first approximation for the axisymmetric problem in the previous chapter. The property of membrane theory to disregard the end conditions can also be utilized so that an accurate solution in the axial direction need not be performed. This also removes the nonlinearity associated with the boundary layer near the ends, so that a linear solution is con-

sidered adequate. Secondly, since the solution method must already be more complex in the circumferential direction due to the stiffness variation, loads which produce non-axisymmetric stress distributions can easily be included. This includes bending moments and shear forces in each direction. Finally, the restriction that the cylinder segment be short is regulated by the use of classical membrane theory (discussed in Section 2.2.3), and we can therefore choose a segment that is so short that any beam loads that change along the length can be considered constant. The prebuckling solution and stability analysis of such a shell are detailed in the next two sections, and numerical results and design studies using these analyses are also presented.

## 4.1 Static Equilibrium

This section presents an analytical solution for the stress state of the shell in terms of the applied beam loads. Linear membrane constitutive theory is used, and equations for the stress resultants and average cross-sectional displacements are developed and normalized with respect to their classical buckling estimations. These quantities represent the prebuckling state of the shell, which is used to calculate the material failure load and is also needed to estimate stability.

### 4.1.1 Linear Membrane Solution

The linear membrane solution begins with the specialization of the general governing equations of Chapter 2.0. All expressions are stipulated to be linear, and the constitutive laws follow classical membrane theory which assumes that the shell only deforms under extension and shear within the middle surface of the shell. We also include the possibility of beam bending and transverse shear loads in both directions. Under these constraints, the system of equations becomes:

Strain-displacement relations, Eq. (2.20):

$$\begin{aligned}\epsilon_x^o &= \frac{\partial u^o}{\partial x} + \kappa_y(x)R(\cos\theta - \cos\theta_{ref}) + \kappa_z(x)R\sin\theta \\ \epsilon_\theta^o &= \frac{1}{R}\left(\frac{\partial v^o}{\partial\theta} + w^o\right) \quad \gamma_{x\theta}^o = \frac{1}{R}\frac{\partial u^o}{\partial\theta} + \frac{\partial v^o}{\partial x}\end{aligned}\quad (4.1)$$

Membrane constitutive theory using effective stiffness measures, Eq. (2.68):

$$\begin{bmatrix} N_x \\ N_\theta \\ N_{x\theta} \end{bmatrix} = \begin{bmatrix} \frac{E_x H}{1 - \nu_{x\theta}\nu_{\theta x}} & \frac{\nu_{\theta x} E_x H}{1 - \nu_{x\theta}\nu_{\theta x}} & 0 \\ \frac{\nu_{x\theta} E_\theta H}{1 - \nu_{x\theta}\nu_{\theta x}} & \frac{E_\theta H}{1 - \nu_{x\theta}\nu_{\theta x}} & 0 \\ 0 & 0 & G_{x\theta} H \end{bmatrix} \begin{bmatrix} \epsilon_x^o \\ \epsilon_\theta^o \\ \gamma_{x\theta}^o \end{bmatrix} \quad (4.2)$$

Equilibrium equations, Eq. (2.87)-(2.94):

$$\begin{aligned} \frac{\partial N_x}{\partial x} + \frac{1}{R} \frac{\partial N_{x\theta}}{\partial \theta} &= 0 & \frac{\partial N_{x\theta}}{\partial x} + \frac{1}{R} \frac{\partial N_\theta}{\partial \theta} &= 0 & \frac{N_\theta}{R} &= p \\ \frac{d^2}{dx^2}[M_y] &= 0 & V_z &= -\frac{d}{dx}[M_y] & \frac{d^2}{dx^2}[M_z] &= 0 & V_y &= \frac{d}{dx}[M_z] \end{aligned} \quad (4.3)$$

Boundary conditions Eq. (2.97)-(2.102):

$$\begin{aligned} u^o(0, \theta) &= \bar{U}/2 \quad \text{or} \quad N_x(0, \theta) = 0 & u^o(L/2, \theta) &= 0 \\ v^o(0, \theta) &= \bar{V}/2 \quad \text{or} \quad N_{x\theta}(0, \theta) = 0 & v^o(L/2, \theta) &= 0 \\ \Omega_y(0) &= \bar{\Omega}_y \quad \text{or} \quad M_y(0) = 0 & V_z(L/2) &= \bar{V}_z & \Omega_y(L/2) &= 0 \\ \Omega_z(0) &= \bar{\Omega}_z \quad \text{or} \quad M_z(0) = 0 & V_y(L/2) &= \bar{V}_y & \Omega_z(L/2) &= 0 \end{aligned} \quad (4.4)$$

We need not include the boundary conditions for the radial displacement since membrane theory neglects these constraints. The sign conventions for the possible loads applied to the cylinder segment are displayed in Figure 4.1 for a generic cross-section of a short cylinder segment. Note that these loads correspond to the assumed directions shown in Figure 2.9, where the short cylinder section is located within the region to the left of the symmetric plane.

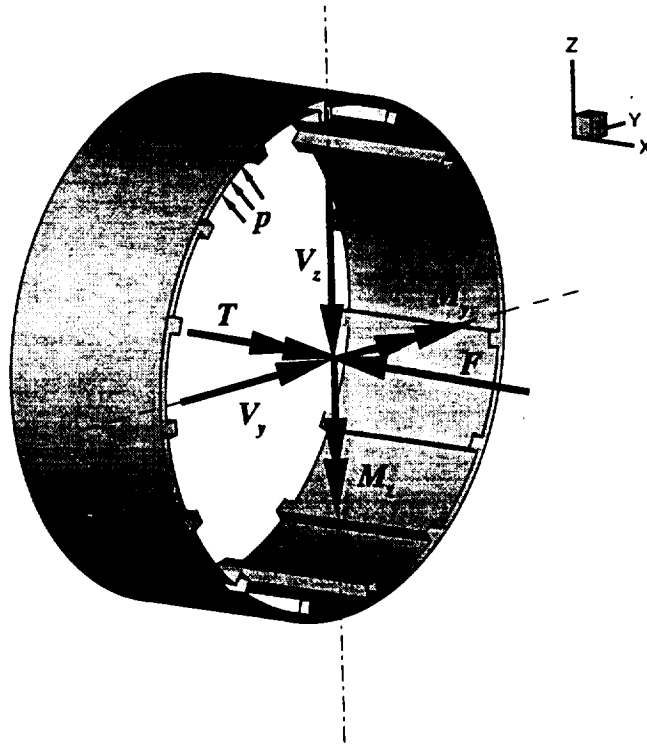


**Figure 4.1: Geometry and Loading for Short Cylinder Segment**

The one-dimensional beam equations, given in Eq. (4.3), along with their boundary conditions, Eq. (4.4), can be solved quite simply. These equations conform to a shear force-bending moment analysis of elementary beam theory:

$$\begin{aligned} M_y(x) &= \bar{M}_y - \bar{V}_z x & V_z(x) &= \bar{V}_z \\ M_z(x) &= \bar{M}_z + \bar{V}_y x & V_y(x) &= \bar{V}_y \end{aligned} \quad (4.5)$$

Note that the moments  $\bar{M}_y$  and  $\bar{M}_z$  represent the constant values applied at the ends of the cylinder, and that Eq. (4.5) holds only for the region to the left of the symmetric plane in Figure 2.9. Therefore, according to Eq. (4.5), the inclusion of transverse shear forces implies that some quantities must vary in the axial direction. For now, this axial variation of the loads will be allowed, though later the beam moments will be treated as constant values which exist at a particular axial location of the beam. These load quantities can also be related to the end rotations applied to the beam, however to develop these expressions the membrane equations must first be solved.

The solutions for the shell stress resultants are found from the integration of their equilibrium equations, which are also relatively simple. The third equation of Eq. (4.3) reveals that the circumferential stress resultant  $N_\theta$  depends only on the pressure, which is considered a constant for this investigation. Then the derivative of  $N_\theta$  with respect to  $\theta$  in the second equilibrium equation is zero, so that the shear stress  $N_{x\theta}$  must be only a function of  $\theta$ . This fact enables the integration of  $N_x$  in the first equilibrium equation, so that the total solution for the shell stress resultants is:

$$N_\theta(x, \theta) = pR \quad N_{x\theta}(x, \theta) = N_{x\theta}(0, \theta) \quad N_x(x, \theta) = -\frac{x}{R} \frac{dN_{x\theta}}{d\theta} + N_x(0, \theta) \quad (4.6)$$

The only membrane stress that varies in the axial direction is  $N_x$ , which is expected since this stress resultant is directly related to the beam moments of Eq. (4.5). As such, we will assume that this linear variation of the axial stresses is present only for the beam bending response of the structure, so that the expression for the axial strain  $\epsilon_x^o$  in Eq. (4.1) varies in the axial direction due only to the variables  $\kappa_y(x)$  and  $\kappa_z(x)$ . Thus the derivative involving  $u^o$ , representing axial extension of the cross-section, must be only a function of the circumferential coordinate, and for now this term is assumed to be a constant so that the cross-section displaces uniformly without warping. This is expressed mathematically as an assumption for the form of the axial displacement:

$$u^o(x, \theta) = \frac{\bar{U}}{L} \left( \frac{L}{2} - x \right) \quad (4.7)$$

The middle surface axial strain is then:



$$\epsilon_x^o = -\frac{\bar{U}}{L} + \kappa_y(x)R(\cos\theta - \cos\theta_{ref}) + \kappa_z(x)R\sin\theta \quad (4.8)$$

The axial stress resultant  $N_x$  is found through manipulation of the constitutive equations given in Eq. (4.2).  $N_x$  is expressed in terms of the middle surface axial strain  $\epsilon_x^o$  and the circumferential stress resultant  $N_\theta$ , equal to  $pR$  from Eq. (4.6):

$$N_x(x, \theta) = E_x(\theta)H\left[-\frac{\bar{U}}{L} + \kappa_y(x)R(\cos\theta - \cos\theta_{ref}) + \kappa_z(x)R\sin\theta\right] + v_{x\theta}(\theta)pR \quad (4.9)$$

Calculation of the total compressive force  $\bar{F}$  results in the following expression:

$$\begin{aligned} -\bar{F} = \oint N_x(x, \theta)Rd\theta = & -\frac{\bar{U}}{L}\oint E_x(\theta)HRd\theta + \kappa_y(x)HR^2\oint E_x(\theta)(\cos\theta - \cos\theta_{ref})d\theta + \\ & \kappa_z(x)HR^2\oint E_x(\theta)\sin\theta d\theta + pR^2\oint v_{x\theta}(\theta)d\theta \end{aligned} \quad (4.10)$$

For integrals around a closed contour such as these, simplifications can be made when the integrand is known to be “odd” or “even” with regards to a periodic coordinate. An “odd” function, such as  $\sin\theta$ , has opposite sign about  $\theta = 0$  and  $\pi$ , while an “even” function is a mirror image about these points, like  $\cos\theta$ . An integral around the entire closed contour for an odd function is always zero, while for an even function it is a constant (possibly zero).

For this investigation, the circumferential variation implies that all stiffness terms are even functions since they are symmetric about  $\theta = 0$  and  $\pi$ , therefore the third integral on the right-hand side of Eq. (4.10) is zero. Furthermore, the designation of the neutral surface is defined so that bending (through the beam curvature  $\kappa_y$ ) does not produce an axial force, therefore the second integral must be zero. This defines the reference angle that locates the material centroid of the cross-section:

$$\oint E_x(\theta)(\cos\theta - \cos\theta_{ref})d\theta = 0 \quad \Rightarrow \quad \cos\theta_{ref} = \frac{\oint E_x(\theta)\cos\theta d\theta}{\oint E_x(\theta)d\theta} \quad (4.11)$$

The final two integrals on the right-hand side of Eq. (4.10) contain even functions as integrands and therefore are non-zero, so that Eq. (4.10) becomes

$$\bar{F} = \frac{\bar{U}}{L}(EA) - pR^2\oint v_{x\theta}(\theta)d\theta \quad (EA) = \oint E_x(\theta)HRd\theta \quad (4.12)$$

The symbol  $(EA)$  represents a measure of the global axial stiffness of the variable stiffness structure, and is a constant for a circumferential stiffness variation. Eq. (4.12) thus relates the global end displacement of the cylinder to the loads  $\bar{F}$  and  $p$ . Of course, only one of the parameters  $\bar{U}$

or  $\bar{F}$  can be stipulated at the end of the cylinder, and the other must be found according to Eq. (4.12). Some special cases also deserve mentioning. If the force  $\bar{F}$  is zero the cylinder possesses a “free” end, since the axial stresses at the end are absent, and the displacement of the cross-section due to the Poisson effect is found from Eq. (4.12). Alternatively, a “fixed” end condition may be present, which corresponds to a prescribed value of  $\bar{U}$ , and the axial force is determined using the same equation. Closed ends cylinders also possess the possibility of a “hydrostatic” pressure, which generates a circumferential stress as well as an axial stress due to the resultant force acting on the ends. For this case, the end condition is considered “free” and the value of the axial (compressive) force with respect to the internal hydrostatic pressure is found from elementary mechanics as  $\bar{F} = -p\pi R^2$ . Due to these possibilities of load definition, and since the end displacement  $\bar{U}$  and end load  $\bar{F}$  can be easily interchanged using Eq. (4.12), the loading of the cylinder for the linear membrane solution will usually be defined by a given value of  $\bar{F}$ , and the global displacement calculated only when needed.

Using the expression for the axial force  $\bar{F}$  just derived, the axial stress resultant is

$$N_x(x, \theta) = E_x(\theta)H \left[ \frac{-\bar{F}}{(EA)} + \kappa_y(x)R(\cos\theta - \cos\theta_{ref}) + \kappa_z(x)R\sin\theta \right] + pR \left[ v_{x\theta}(\theta) - \frac{E_x(\theta)HR}{(EA)} \oint v_{x\theta}(\theta) d\theta \right] \quad (4.13)$$

The last term in this equation, containing  $pR$ , deserves some discussion. For cylinders without stiffness variation, the expression within the brackets is zero, so that the axial stress resultant does not depend on internal pressure, as expected (the discussion here is distinct from the “hydrostatic” case discussed earlier, which introduced the axial load due to pressurization through the force  $\bar{F}$ ). For variable stiffness structures, however, a general circumferential stiffness variation may possess a contribution of axial stress from this pressure. This is due to the stipulation that the cross-section displaces uniformly without warping, as assumed in Eq. (4.7). If an internal pressure is applied to the cylinder, the Poisson effect produces a “free” strain in the axial direction which varies circumferentially following the definition of  $v_{x\theta}(\theta)$ . However, this “free” axial strain is not necessarily constant around the circumference, so that demanding that the cross-section does not undergo warping requires the presence of axial stresses to produce a constant axial strain around the circumference. These axial stresses introduce a complication, for they also may produce a resultant beam bending moment for the simple case of internal pressure. Therefore to remove this unwanted possibility, the cross-section will be allowed to warp in violation of Eq. (4.7). This effectively removes the last term involving the pressure in Eq. (4.13) without changing any other expressions, except that the end displacement  $\bar{U}$  should now be considered the *average* end dis-

placement of the cross-section.

The calculation of the global beam response is now completed in a similar manner. The definition for  $M_y(x)$  in terms of  $N_x$ , as given in Eq. (4.13) with the pressure terms removed, yields:

$$M_y(x) = \oint N_x(x, \theta)(\cos \theta - \cos \theta_{ref})R^2 d\theta = \frac{-\bar{F}}{(EA)} \oint E_x(\theta)H(\cos \theta - \cos \theta_{ref})R^2 d\theta + \kappa_y(x) \oint E_x(\theta)HR^3(\cos \theta - \cos \theta_{ref})^2 d\theta + \kappa_z(x) \oint E_x(\theta)HR^3(\cos \theta - \cos \theta_{ref})\sin \theta d\theta \quad (4.14)$$

The first integral on the right-hand side is zero according to the definition of  $\theta_{ref}$  in Eq. (4.11), while the third term has an odd function as an integrand and therefore vanishes when evaluated at the limits. A similar situation arises for the calculation of  $\kappa_z$  and  $M_z$ , so that the curvatures become

$$\begin{aligned} \kappa_y(x) &= \frac{M_y(x)}{(EI_y)} & (EI_y) &= \oint E_x(\theta)HR^3(\cos \theta - \cos \theta_{ref})^2 d\theta \\ \kappa_z(x) &= \frac{M_z(x)}{(EI_z)} & (EI_z) &= \oint E_x(\theta)HR^3 \sin^2 \theta d\theta \end{aligned} \quad (4.15)$$

The bending stiffness terms  $(EI_y)$  and  $(EI_z)$  introduced in Eq. (4.15) are constants for a given circumferential stiffness variation, and represent the global bending stiffnesses of the cylindrical structure about each axis. If desired, the definitions for the cross-sectional rotations ( $\Omega_y, \Omega_z$ ) and beam deflections ( $a_z, a_y$ ) can be found through straightforward integration using Eq. (2.3)-(2.5) along with their associated boundary conditions from Eq. (4.4). For our purposes in this problem, we will use the force quantities to introduce the loading, so that the definition of the axial stress resultant  $N_x$  is now fully defined along the length of the shell as

$$N_x(x, \theta) = E_x(\theta)H \left[ \frac{-\bar{F}}{(EA)} + \frac{(\bar{M}_y - \bar{V}_z x)}{(EI_y)} R(\cos \theta - \cos \theta_{ref}) + \frac{(\bar{M}_z + \bar{V}_y x)}{(EI_z)} R \sin \theta \right] \quad (4.16)$$

The first equilibrium equation of Eq. (4.3) can now be used to determine the shear stress resultant  $N_{x\theta}$ , which is only a function of  $\theta$ .

$$\frac{1}{R} \frac{dN_{x\theta}}{d\theta} = \frac{\partial N_x}{\partial x} = E_x(\theta)H \left[ \frac{\bar{V}_z R}{(EI_y)} (\cos \theta - \cos \theta_{ref}) - \frac{\bar{V}_y R}{(EI_z)} \sin \theta \right] \quad (4.17)$$

Basic integration yields:

$$N_{x\theta}(\theta) = \frac{\bar{V}_z HR^2}{(EI_y)} \int_0^\theta E_x(\theta)(\cos \theta - \cos \theta_{ref}) d\theta - \frac{\bar{V}_y HR^2}{(EI_z)} \int_0^\theta E_x(\theta) \sin \theta d\theta + C_1 \quad (4.18)$$

$C_1$  is a constant of integration and represents the value of the shear stress at  $\theta = 0$ . Note that the periodicity of the function  $N_{x\theta}(\theta)$  is satisfied since both integrals evaluated around the whole circumference are zero, as shown earlier, so that  $N_{x\theta}(0) = N_{x\theta}(2\pi)$ . The unknown constant must be evaluated through the application of the integral equations involving the torque:

$$\begin{aligned} -\bar{T} = \oint N_{x\theta}(\theta) R^2 d\theta = \frac{\bar{V}_z H R^4}{(EI_y)} \oint \left[ \int_0^\theta E_x(\theta) (\cos \theta - \cos \theta_{ref}) d\theta \right] d\theta - \\ \frac{\bar{V}_y H R^4}{(EI_z)} \oint \left[ \int_0^\theta E_x(\theta) \sin \theta d\theta \right] d\theta + C_1 R^2 \oint d\theta \end{aligned} \quad (4.19)$$

Integration by parts is performed on the first two integrals. The first is found to be zero, while the second becomes a constant expressed as

$$\oint \left[ \int_0^\theta E_x(\theta) \sin \theta d\theta \right] d\theta = -\oint E_x(\theta) \theta \sin \theta d\theta \quad (4.20)$$

Therefore the value of  $C_1$ , which represents the shear stress resultant present at the top of the cylinder ( $\theta = 0$ ) is

$$C_1 = \frac{-\bar{T}}{2\pi R^2} - \frac{\bar{V}_y H R^2}{2\pi (EI)_z} \oint E_x(\theta) \theta \sin \theta d\theta \quad (4.21)$$

This answer is somewhat expected, since the shear stress produced by the horizontal force  $\bar{V}_y$  should be non-zero at the top and bottom, while the contribution there from the vertical shear force  $\bar{V}_z$  should be zero. In fact, the integral involving the horizontal force in Eq. (4.21) has another meaning: it determines where the shear stress due to a horizontal force is zero. This location is termed the shear center of the cross-section, and is defined as the point through which a transverse shear force must act so that it does not produce any twist, much like the reference angle  $\theta_{ref}$  separates the force and moment of the axial loading. For many structures (most typically ones with material symmetry about  $\theta = \pi/2$ ), the location of the centroid and the shear center coincide, though for general circumferential stiffness variations they may have unrelated values. Determination of the location of the shear center is accomplished by insisting that the shear flow produced by a transverse beam force does not produce a resultant twist of the cross-section. For a vertical shear force, this location is found to be at  $Y = 0$  due to symmetry, while for a horizontal force the shear center reference angle must follow the relation:

$$\int_0^{\theta_{sc}} E_x(\theta) \sin \theta d\theta = \frac{1}{2\pi} \oint E_x(\theta) \theta \sin \theta d\theta \quad (4.22)$$

Then the location of the shear center is ( $Y = 0, Z = R \cos \theta_{sc}$ ). Though not as concise as the definition of the neutral surface reference angle, it is still a solvable equation once the stiffness distribution is defined. Using this notation, along with the value for  $C_1$ , yields:

$$N_{x\theta}(\theta) = \frac{-\bar{T}}{2\pi R^2} + \frac{\bar{V}_z}{(EI_y)} \int_0^{\theta} E_x(\theta) (\cos \theta - \cos \theta_{ref}) H R^2 d\theta - \frac{\bar{V}_y}{(EI_z)} \int_{\theta_{sc}}^{\theta} E_x(\theta) \sin \theta H R^2 d\theta \quad (4.23)$$

Eq. (4.23) can be made even more concise by noting that the integral equations actually represent the first moments of area, weighted by the axial stiffness, of the variable stiffness cross-section. Therefore, we can define these quantities much like the global axial stiffness and moment of inertia parameters:

$$Q_z(\theta) = \int_0^{\theta} E_x(\theta) (\cos \theta - \cos \theta_{ref}) H R^2 d\theta \quad Q_y(\theta) = \int_{\theta_{sc}}^{\theta} E_x(\theta) \sin \theta H R^2 d\theta \quad (4.24)$$

so that the equation for the shear flow  $N_{x\theta}$  can be written in the traditional form of elementary beam theory as:

$$N_{x\theta}(\theta) = \frac{-\bar{T}}{2\pi R^2} + \frac{\bar{V}_z Q_z(\theta)}{(EI_y)} - \frac{\bar{V}_y Q_y(\theta)}{(EI_z)} \quad (4.25)$$

It can be shown that this shear stress distribution also correctly satisfies the relations:

$$\bar{V}_z = \oint N_{x\theta}(\theta) \sin \theta R d\theta \quad \bar{V}_y = \oint N_{x\theta}(\theta) \cos \theta R d\theta \quad (4.26)$$

which represent the resultant shear forces applied to the beam in each direction.

The final equation to consider involves the relationship between the applied torque and twist of the cylinder. Here we again will use the *average* amount of twist of the cross-section, since local warping does exist due to an applied pressure discussed earlier as well as shear warping from the transverse beam forces and torsional loads. For this simple result, however, we will ignore these secondary effects to find the torsional stiffness of the structure. The torque defined in terms of the shear stress resultant has already been used, and is given in Eq. (4.19) as

$$-\bar{T} = \oint N_{x\theta}(\theta) R^2 d\theta \quad (4.27)$$

To relate this to the twist of the cross-section, the constitutive relations are used to express the shear stress resultant in terms of the middle surface shear strain, which is a function of the circumferential displacement only since we are neglecting the ability to warp:

$$N_{x\theta}(\theta) = G_{x\theta}(\theta)H\gamma_{x\theta}^o = G_{x\theta}(\theta)H\frac{\partial v^o}{\partial x} \quad v^o = \frac{\bar{V}}{L}\left(\frac{L}{2} - x\right) \quad (4.28)$$

These equations correspond roughly to Eq. (4.7)-(4.12) for the compressive load and end shortening, and are expressed in their final form after integration as

$$\frac{\bar{V}}{R} = \frac{\bar{T}L}{(GJ)} \quad (GJ) = \oint G_{x\theta}(\theta)HR^3d\theta \quad (4.29)$$

This equation is merely the elementary mechanics solution for a cylinder under torsion, where  $(GJ)$  represents the torsional stiffness of the variable stiffness cylinder.

To review the linear membrane solution derived in this section, the expressions for the middle surface stress resultants and global displacements of the cross-section are repeated here in terms of the fundamental loads and stiffness measures:

$$\begin{aligned} N_x(x, \theta) &= E_x(\theta)H\left[\frac{-\bar{F}}{(EA)} + \frac{M_y(x)}{(EI_y)}R(\cos\theta - \cos\theta_{ref}) + \frac{M_z(x)}{(EI_z)}R\sin\theta\right] \\ N_\theta(\theta) &= pR \quad N_{x\theta}(\theta) = \frac{-\bar{T}}{2\pi R^2} + \frac{\bar{V}_z Q_z(\theta)}{(EI_y)} - \frac{\bar{V}_y Q_y(\theta)}{(EI_z)} \\ \bar{U} &= \frac{\bar{F}L}{(EA)} + \frac{pR^2L}{(EA)}\oint v_{x\theta}(\theta)d\theta \quad \frac{\bar{V}}{R} = \frac{\bar{T}L}{(GJ)} \end{aligned} \quad (4.30)$$

#### 4.1.2 Normalization with Respect to Classical Buckling Estimates

Normalization of these expressions is completed in the traditional manner with respect to their classical buckling values. However, it should be pointed out here that many buckling estimates are formulated by assuming a "smeared" skin with constant stiffness parameters that include the effect of the closely spaced stiffeners. This method tends to overestimate the stiffness of the shell and leads to poor estimates of the buckling load. In this investigation, the estimates are based on the average stiffness quantities of the skin only. For general stiffened shells, the buckled mode shape usually occurs with the skin buckling *between* stiffeners, so that smearing the effective stiffness of the stiffeners into the parameters determining the classical buckling estimates will surely provide significant error. Therefore, to accurately estimate when such a stiffened structure reaches its critical value due to skin buckling, we assume that the (a) the axial strain of the structure is the

same as that of the skin, and (b) longitudinal stiffeners do not carry any of the circumferential and shear loads. These assumptions makes it possible to compute the corresponding stresses in the skin in relation to the stresses of the total structure. The applied loads become unstable when the maximum skin stresses attain their critical values as calculated from the classical solutions of Section 1.2.2. Of course, since it is assumed that only the skin buckles, this critical stress must be located where no stiffener is present. However, for the purpose of normalization it is merely assumed that such a location is present, and the buckling values can then be calculated for the structure in terms of its global stiffness and geometric parameters. The classical buckling estimates for the middle surface stress resultants are given by Eq. (1.4)  $[\hat{N}_x^{cl}]$ , Eq. (1.8)  $[\hat{N}_\theta^{cl}]$ , and Eq. (1.14)  $[\hat{N}_{x\theta}^{cl}]$  in terms of the average *skin* stiffness, denoted by a hat, which for a circumferential stiffness variation is calculated as:

$$\hat{D}_{ij} = \frac{1}{2\pi} \oint D_{ij}^{skin}(\theta) d\theta \quad (4.31)$$

The first calculation is for buckling due to a compressive axial force. The axial strain for the structure is given in brackets in the first equation of Eq. (4.30), and according to assumption (a) above this strain must be equal to the strain in the skin. The critical buckling value for this strain occurs when the stress resultant in the skin reaches its classical value, where the stress-strain relationship between the skin stress resultant and strain is approximated using the average values. The solution for the critical end displacement for an unpressurized cylinder is also included:

$$\epsilon_x^{cl} = \frac{\hat{N}_x^{cl}}{\hat{E}_x H} = \frac{-\bar{U}^{cl}}{L} \quad (4.32)$$

The value of the critical force is then easily calculated by equating the strains:

$$\frac{-\bar{F}}{(EA)} = \frac{\hat{N}_x^{cl}}{\hat{E}_x H} \quad \Rightarrow \quad \bar{F}^{cl} = \frac{(EA)}{\hat{E}_x H} (-\hat{N}_x^{cl}) \quad (4.33)$$

For buckling of a cylinder due to pure bending, an approximation first introduced by Seide & Weingarten<sup>85</sup> is utilized. By solving the eigenvalue problem associated with bending of unstiffened isotropic circular cylinders of various radius-to-thickness ratios, they discovered that the buckling value of the moment occurs when the maximum bending stress is equal to the critical value of the cylinder under axial compression. A detailed discussion of the implications of this discovery will be presented in Section 4.4.1, so that for now this generalization will only be used to find the critical bending load. Therefore, applying the results of Seide & Weingarten in terms of the maximum compressive *strain* of the structure results in a similar method to find the critical

moments that was used for the axial force. Equating the maximum compressive strain of the structure (which occurs at the top, bottom, or one of the sides of the cross-section according to the direction of the beam bending moments) to the corresponding critical value for axial compressive strain from Eq. (4.32) results in the following classical estimates for the beam bending moments:

$$\bar{M}_y^{cl} = \frac{(EI_y)}{\bar{E}_x HR} (-\hat{N}_x^{cl}) \quad \bar{M}_z^{cl} = \frac{(EI_z)}{\bar{E}_x HR} (-\hat{N}_x^{cl}) \quad (4.34)$$

To make this expressions more concise, nondimensional moments of inertia are defined as:

$$\bar{I}_y = \frac{(EI_y)}{\bar{E}_x \pi HR^3} = \frac{1}{\pi} \oint \bar{E}_x(\theta) (\cos \theta - \cos \theta_{ref})^2 d\theta \quad \bar{I}_z = \frac{(EI_z)}{\bar{E}_x \pi HR^3} = \frac{1}{\pi} \oint \bar{E}_x(\theta) \sin^2 \theta d\theta \quad (4.35)$$

where the effective longitudinal modulus has been normalized with respect to the stiffness properties of the skin:

$$\bar{E}_x(\theta) = \frac{E_x(\theta)}{\bar{E}_x} \quad (4.36)$$

Thus the final form for the critical moments is

$$\bar{M}_y^{cl} = \pi R^2 \bar{I}_y (-\hat{N}_x^{cl}) \quad \bar{M}_z^{cl} = \pi R^2 \bar{I}_z (-\hat{N}_x^{cl}) \quad (4.37)$$

Note that for constant stiffness laminates the normalized moments of inertia are equal to unity.

Buckling due to an external side pressure ("side" implies that the pressure produces only circumferential stress, so that the axial stress associated with hydrostatic pressure for a closed end cylinder does not exist) can be found easily from the second equation of Eq. (4.30). Since the skin is assumed to carry all of the circumferential loads, the classical buckling pressure is merely

$$p^{cl} = \frac{\hat{N}_\theta^{cl}}{R} \quad (4.38)$$

Lastly, for torsion and shear force loading, the skin is assumed to carry the majority of the shear stresses, which vary as per Eq. (4.30). Furthermore, since the effect of the laminate stiffnesses  $D_{16}$  and  $D_{26}$  are ignored due to the use of membrane constitutive theory, then the sign of the applied loads does not matter. Thus for a constant shear stress produced by the application of an axial torque, the classical buckling value of the load and end twist is simply

$$\bar{T}^{cl} = 2\pi R^2 \hat{N}_{x\theta}^{cl} \quad \bar{V}^{cl} = \frac{2\pi R^3 \hat{N}_{x\theta}^{cl} L}{(GJ)} \quad (4.39)$$



For the vertical and horizontal beam forces, the shear stress of Eq. (4.30) is not constant but varies around the cross-section of the shell. To determine when this stress state becomes unstable, an assumption similar to the one used for cylinders under pure bending must be introduced. Few studies of a cylinder buckling under a constant beam shear force have ever been presented in the literature, for the most basic reason that the presence of the beam force produces an axial bending moment that increases linearly along the length and which usually dominates the buckling response. However, for very short cylinders under such a loading condition, Schröder<sup>86</sup> has shown that the critical buckling mode is dominated by these shear stresses. Further investigation of the resulting eigenvalue problem for an unstiffened cross-section under a constant beam shear force reveals that its formulation very closely resembles the one originally used by Seide & Weingarten<sup>85</sup> for the study of buckling under pure bending. Therefore, it is conjectured here that a similar result should occur for shear loading: that instability due to a transverse shear force occurs when the maximum shear stress is equal to the critical value of the same cylinder under a constant shear stress. As will be shown in Section 4.4.1, this hypothesis does hold true for short cylinders. Therefore, all that is needed for the calculation of the critical buckling load due to a transverse shear force is to find the maximum values of the resulting shear stress from Eq. (4.30), and equate it to the critical shear stress resultant for skin buckling. The maxima occur at  $\theta = \theta_{ref}$  and  $\theta = 0$  for a vertical and horizontal shear force, respectively, and nondimensional first moments of inertia are also defined for ease of expression. Thus the classical estimates are expressed mathematically as

$$\bar{V}_z^{cl} = \frac{(EI_y)\hat{N}_{x\theta}^{cl}}{Q_z(\theta_{ref})} = \frac{\pi R \bar{I}_y \hat{N}_{x\theta}^{cl}}{\bar{Q}_z(\theta_{ref})} \quad \bar{V}_y^{cl} = \frac{(EI_z)\hat{N}_{x\theta}^{cl}}{Q_y(0)} = \frac{\pi R \bar{I}_z \hat{N}_{x\theta}^{cl}}{\bar{Q}_y(0)} \quad (4.40)$$

where the normalized first moments of inertia are

$$\bar{Q}_z(\theta) = \frac{Q_z(\theta)}{\bar{E}_x H R^2} = \int_0^\theta \bar{E}_x(\theta) (\cos \theta - \cos \theta_{ref}) d\theta \quad \bar{Q}_y(\theta) = \frac{Q_y(\theta)}{\bar{E}_x H R^2} = \int_{\theta_{sc}}^\theta \bar{E}_x(\theta) \sin \theta d\theta \quad (4.41)$$

Thus the solution for the stress resultants and end displacements using classical membrane theory for cylinders with a circumferential stiffness variation is expressed as:

$$\begin{aligned} \bar{n}_x(\xi, \theta) &= \bar{E}_x(\theta) [-\bar{f} + \bar{m}_y(\xi)(\cos \theta - \cos \theta_{ref}) + \bar{m}_z(\xi) \sin \theta] \\ \bar{n}_\theta(\theta) &= \bar{p} \quad \bar{n}_{x\theta}(\theta) = -\bar{i} + \bar{v}_z \frac{\bar{Q}_z(\theta)}{\bar{Q}_z(\theta_{ref})} - \bar{v}_y \frac{\bar{Q}_y(\theta)}{\bar{Q}_y(0)} \\ \bar{u} &= \bar{f} + \bar{p} \cdot \frac{\hat{N}_\theta^{cl} \oint \bar{v}_{x\theta}(\theta) d\theta}{\hat{N}_x^{cl} \oint \bar{E}_x(\theta) d\theta} \quad \bar{v} = \bar{i} \end{aligned} \quad (4.42)$$

## 4.2 Stability Estimate using Membrane Prebuckling Solution

The equations governing the stability of the equilibrium state represented by Eq. (4.42) are derived in this section. The energy method formulation, outlined in Section 2.3.4, will be used with the specialization of a circumferential stiffness variation with constant loads in the axial direction. Since the equilibrium equations are based on classical membrane theory, the prebuckling deformations are neglected and the stability estimate takes the form of a linear eigenvalue problem in terms of the perturbed displacements. The strain-displacement relations for these perturbed variables are:

$$\begin{aligned} \epsilon_{x_1}^o &= \frac{\partial u_1}{\partial x} & \epsilon_{\theta_1}^o &= \frac{1}{R} \frac{\partial v_1}{\partial \theta} + \frac{w_1}{R} & \gamma_{x\theta_1}^o &= \frac{1}{R} \frac{\partial u_1}{\partial \theta} + \frac{\partial v_1}{\partial x} \\ \kappa_{x_1}^o &= \frac{\partial^2 w_1}{\partial x^2} & \kappa_{\theta_1}^o &= \frac{1}{R^2} \left( \frac{\partial v_1}{\partial \theta} - \frac{\partial^2 w_1}{\partial \theta^2} \right) & \kappa_{x\theta_1}^o &= \frac{1}{R} \left( \frac{\partial v_1}{\partial x} - 2 \frac{\partial^2 w_1}{\partial x \partial \theta} \right) \end{aligned} \quad (4.43)$$

These expressions, along with the prebuckling stress resultants given in Eq. (4.42), are inserted into the integral for the total potential energy, Eq. (2.109). Integration is then carried out analytically using the Rayleigh-Ritz technique to form the matrices for the eigenvalue problem. Even though the loads are considered constant in the axial direction, the mode shapes are assumed to vary sinusoidally along the length, much like the buckled state of the axisymmetric problem possessed harmonic waves in the circumferential direction. The assumed displacement field is:

$$\begin{aligned} u_1(x, \theta) &= -U_I(\theta) \cos\left(\frac{\beta x}{R}\right) + U_{II}(\theta) \sin\left(\frac{\beta x}{R}\right) - U_{III}(\theta) \sin\left(\frac{\beta x}{R}\right) + U_{IV}(\theta) \cos\left(\frac{\beta x}{R}\right) \\ v_1(x, \theta) &= V_I(\theta) \sin\left(\frac{\beta x}{R}\right) + V_{II}(\theta) \cos\left(\frac{\beta x}{R}\right) + V_{III}(\theta) \cos\left(\frac{\beta x}{R}\right) + V_{IV}(\theta) \sin\left(\frac{\beta x}{R}\right) \\ w_1(x, \theta) &= W_I(\theta) \sin\left(\frac{\beta x}{R}\right) + W_{II}(\theta) \cos\left(\frac{\beta x}{R}\right) + W_{III}(\theta) \cos\left(\frac{\beta x}{R}\right) + W_{IV}(\theta) \sin\left(\frac{\beta x}{R}\right) \end{aligned} \quad (4.44)$$

The parameter  $\beta$  corresponds to the axial frequency, and it can be infinitely valued or depend on the number of half-waves along the length of a finite length shell. Its value must be chosen so that the resulting eigenvalue is a minimum. Also note that for the expansion of Eq. (4.44), four modes must now be used (instead of two for the axisymmetric stability problem) due to the presence of anti-symmetric terms for the general loading of a cylindrical shell. When the integral for the total potential energy is evaluated, it can be easily shown that the axial variation of the mode shape is sufficiently represented solely by the parameter  $\beta$ . Thus any arbitrary mode shape with an axial frequency  $\beta$  can be completely defined through the form of Eq. (4.44), with the appropriate boundary conditions applied for each function of  $\theta$ . These circumferential boundary conditions

are chosen so that modes *I* and *III* represent a symmetric mode about the vertical line ( $\theta = 0, \pi$ ), while modes *II* and *IV* are anti-symmetric about this line.

In the axial direction, the possibilities for the boundary conditions are not as general. For most cases (those without shear loading and with small  $D_{16}$  and  $D_{26}$  stiffness terms), modes *I* and *IV* dominate the response, resulting in the perturbed radial displacement  $w_1$  varying as a sine function in the axial direction. If the value of  $\beta$  is constrained to be an integer multiple of a fundamental frequency, which depends on the geometry of the shell, then for this mode shape the end conditions can be shown to adhere to the S2 condition at  $x = 0, L$ . The choice of  $\beta$  for this scenario implies that an integer number of half-waves exist along the length, and can be written as:

$$\beta = m \left( \frac{\pi R}{L} \right) = m \beta_{\min} \quad m = 1, 2, 3, \dots \quad (4.45)$$

However, for the most general case, the buckled mode shape consists of (at least) two modes with equal magnitude, for instance  $\|II\| = \|IV\|$  for a cylinder under torsion. Thus the perturbed radial displacement is not zero at  $x = 0, L$  as it is for loading by normal stresses. Therefore, for loads involving shear (and laminates with large coupling terms through the  $D_{16}$  and  $D_{26}$  stiffness parameters), the end conditions do not restrict the radial deformation of the cross-section at the ends and allow substantial warping. This analysis therefore provides a lower bound of the buckling load, which should increase with the added constraint of the end restraint. An estimate of the error associated with this warping violation was presented in Section 3.5.2 within the discussion of buckling under torsion. These results must be taken into account whenever shear effects are a significant part of the loading. Further discussion concerning the correct choice of  $\beta$  and its applicability to realistic boundary conditions is presented in Section 4.4.1.

Insertion of the assumed form for the displacements into the stability equations generates a system of linear ordinary differential equations with variable coefficients, which is denoted as

$$\left( \begin{bmatrix} K_s & C & 0 & 0 \\ C^T & K_a & 0 & 0 \\ 0 & 0 & K_s & C \\ 0 & 0 & C^T & K_a \end{bmatrix} + \begin{bmatrix} N_s & S & V_s & M_s \\ S^T & N_a & M_a & V_a \\ V_s^T & M_a^T & N_s & S \\ M_s^T & V_a^T & S^T & N_a \end{bmatrix}_{dead} \right) \begin{bmatrix} I \\ II \\ III \\ IV \end{bmatrix} = -\Lambda \begin{bmatrix} N_s & S & V_s & M_s \\ S^T & N_a & M_a & V_a \\ V_s^T & M_a^T & N_s & S \\ M_s^T & V_a^T & S^T & N_a \end{bmatrix}_{live} \begin{bmatrix} I \\ II \\ III \\ IV \end{bmatrix} \quad (4.46)$$

Note that the loading matrices have been separated in terms of the dead and live loadings, which is allowable since the prebuckling solution and the eigenvalue problem is linear. The  $3 \times 3$  sub-matrices are similar to the ones given in Eq. (3.22) for the axisymmetric buckling problem, and their

mathematical expressions are supplied in Appendix B.2. The normal stress loading sub-matrices, symbolized as  $N_s$  and  $N_a$  in Eq. (4.46), now also include the beam moment about the horizontal axis, while the shear sub-matrix  $S$  similarly contains the load attributed to a shear force in the horizontal direction. These loads, along with the axial force, pressure, and torque, are symmetric about the vertical line ( $\theta = 0, \pi$ ), and can thus be fully defined by modes *I* and *II* of the buckled shape. The addition of the  $V_\alpha$  and  $M_\alpha$  sub-matrices in Eq. (4.46) need to be included for the anti-symmetric loading introduced by a vertical beam force and a bending moment about the vertical axis, respectively, and thus require additional modes *III* and *IV* to fully model the behavior. If a stiffness distribution that was not symmetric about the line ( $\theta = 0, \pi$ ) was allowed, additional terms in the stiffness portion of the matrices would appear in place of the zeroes.

The eigenvalue problem for the general loading of a circumferential variable stiffness cylinder is represented by Eq. (4.46). The numerical solution of this large system is completed using the power method along with either the finite difference technique or the Rayleigh-Ritz method. A discussion of both of these numerical methods, along with a comparison between the two solutions, is presented in Appendix A.

### 4.3 Material Failure Results for Curvilinear Fiber Paths

The results for the material failure loads of cylinders utilizing a circumferential stiffness variation that is produced by curvilinear fiber paths are presented in this section. These results are meant to mimic the analysis of Section 3.4.1 concerning the material failure loads of cylinders with an axial stiffness variation. However, one discrepancy exists between these two discussions. In the last chapter, the axisymmetric static equilibrium solution was robust and considered the correct application of the boundary conditions and the subsequent generation of a boundary layer near the ends. When a circumferential stiffness variation is used, the analysis is limited to membrane constitutive theory, thus the static solution represented by Eq. (4.42) does not include the boundary layer effect. This results in slight deviations between the critical values of the material failure loads. Fortunately, these errors do not significantly detract from the basic nature of the failure scenarios, even though the membrane theory solutions usually underestimate the correct material failure load.

The material failure results will be conducted for a one link curvilinear fiber path definition that is symmetric both vertically and horizontally within the cross-section. This translates into the existence of two variables to describe the circumferential stiffness variation:  $T_0$ , the fiber orientation angle at the top and bottom of the cross-section; and  $T_1$ , which is the value at the sides ( $\theta = \pm 90^\circ$ ). In the parlance of the linked line segment definition displayed in Figure 2.6, the varia-

tion can be described mathematically through Eq. (2.58) as:

$$N_{\text{seg}} = 1 \quad l_1 = \frac{\pi R}{2} \quad (4.47)$$

The cylindrical shell is assumed to have a  $[\pm\phi]_{6s}$  layup with  $R = 24''$ . Besides the basic axisymmetric loadings of pressure, axial force, and torsion, the circumferential analysis can also incorporate beam-type loads applied to the cross-section, therefore this section will also include the results for a bending moment about the horizontal axis and a vertical shear force.

#### 4.3.1 Axisymmetric Loading

For a cylinder cross-section with a circumferential stiffness variation, the stress resultants in terms of the three basic axisymmetric loads are expressed in nondimensional form as

$$\bar{n}_x(\xi, \theta) = -\bar{E}_x(\theta)\bar{f} \quad \bar{n}_\theta(\theta) = \bar{p} \quad \bar{n}_{x\theta}(\theta) = -\bar{i} \quad (4.48)$$

For an axial compressive force, the stress resultant varies circumferentially according to the local values of the axial stiffness parameter. For stiffer regions, the axial stress is larger than for areas with a low axial stiffness so as to produce the same axial strain for all locations. This can be thought of as carrying the loads in “parallel”, as opposed to the case of an axial stiffness variation in which the axial stresses resisted the loading in “series”. Intuitively, this implies that the circumferential stiffness variation possesses a greater chance of improving the load-carrying performance of a shell under an axial load, since the stiffer regions, which are usually the strongest as well, carry a greater fraction of the loads. This is demonstrated by the results shown in Figure 4.2,

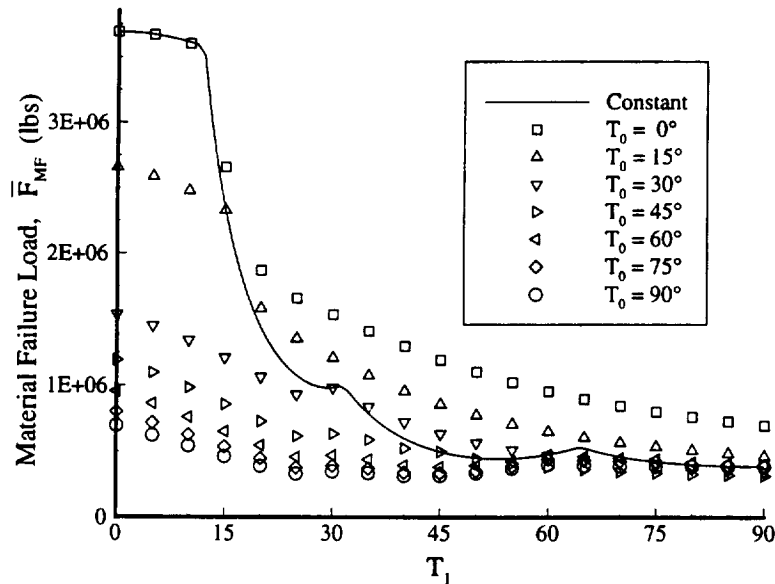


Figure 4.2: Failure Loads for Cylinders under Axial Compression

which plots the material failure loads for axial compression versus the fiber orientation angle definition for both constant and variable stiffness cylinders. This figure is the analog to Figure 3.4, which employed an axial stiffness variation for the same cylinder geometry and loading. The “weak link” philosophy that dominated those material failure results is no longer evident. Instead, Figure 4.2 reveals that the addition of stiffer regions (corresponding to a  $0^\circ$  fiber orientation angle) always increases the material failure load of the structure by transferring a fraction of the stresses away from the weaker regions. A corresponding plot of strength versus axial stiffness is shown in Figure 4.3, revealing that both the strength and the stiffness are improved for most

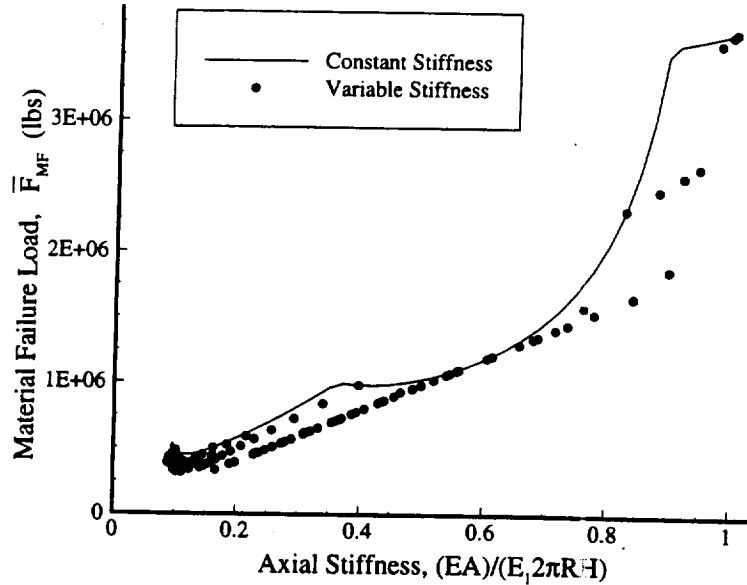


Figure 4.3: Failure vs. Stiffness for Axial Compression

designs (compare the results to Figure 3.7). Unfortunately, the results of Figure 4.2 and Figure 4.3 indicate that a constant stiffness laminate with  $\varphi = 0^\circ$  is still the stiffest and strongest when compared to the variable stiffness possibilities, however this result is considered a major consequence of the simplistic stacking sequence and the unsophisticated one link variation of the fiber orientation angle. Slightly improved results have been found for more general designs that utilize curvilinear fibers for cylinders under axial compression.

For the remaining cases of a cylindrical shell under the axisymmetric loads of internal pressure and torsion, Eq. (4.48) reveals that the corresponding stress resultants are constant around the circumference of the shell. It should be noted, however, that this is the correct solution for variable stiffness shells only when the boundary conditions in the axial direction allow warping (as discussed in Section 4.1.1). When warping is negated, some secondary effects are produced for both load cases, predominantly in the form of non-axisymmetric axial stresses. These effects will be

ignored here. Consequently, the circumferential and shear stress resultants can be considered constants, which implies that no redistribution of the stress field is produced by the variation of the stiffness parameters. Under this scenario, the results for the material failure loads correspond closely to the solutions obtained with an axial stiffness variation, which are displayed in Figure 3.5 and Figure 3.6. Since the loads are the same for all locations around the circumference, the fiber orientation angle that is most susceptible to material failure for the given loading condition limits the strength of the laminate. Thus the “weak link” concept holds true, and no improvement is exhibited by the variable stiffness concept under these loadings.

### 4.3.2 Non-axisymmetric Loading

The most likely scenario that will produce significant improvement through the use of the variable stiffness concept is for loads which vary spatially throughout the structure. Until now, the only loads considered have been axisymmetric in nature and have not been allowed to vary in either the axial or circumferential directions. Inclusion of non-axisymmetric loads, such as basic beam loading that produces normal stresses on the top and bottom of the cross-section and shear stresses on the sides, provides an excellent avenue for improving the performance of the structure by designing a variable stiffness laminate that can respond optimally to the local stress state. For instance, Figure 4.4 shows the material failure loads of constant and variable stiffness laminates

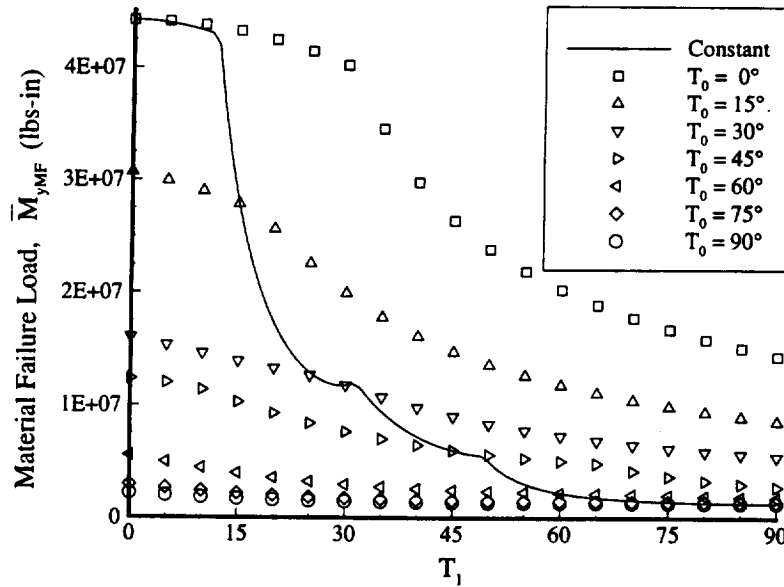
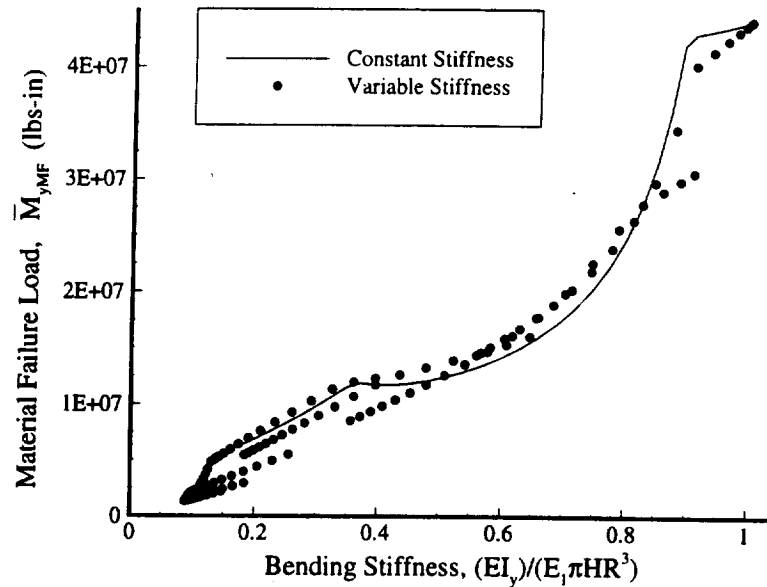


Figure 4.4: Failure Loads for Cylinders under Horizontal Bending Moment

under a pure bending moment about the horizontal axis. As with the axial compression case, the constant stiffness laminate with  $\phi = 0^\circ$  generates the highest critical load since the stresses produced from the loading are exclusively axial. However, now there are several variable stiffness

designs that rival the material load value of this optimal case. For the variable stiffness designs in general, significant improvement is exhibited by laminates that possess relatively stiff regions at the top and bottom of the cross-section (represented by smaller of values of  $T_0$ ). This is to be somewhat expected, since it is well known that a structure designed with axially stiff regions positioned farthest from the neutral axis will perform excellently under bending. A comparison of the material failure loads in Figure 4.4 with respect to the global bending stiffness of the structure is supplied in Figure 4.5. Note that now there exists some laminates that have equivalent stiffnesses



**Figure 4.5: Failure vs. Bending Stiffness for Horizontal Bending Moment**

to constant stiffness structures, yet higher material failure loads. This is quite an advantage for the designer, for it allows greater freedom to satisfy possible stiffness and strength constraints that may exist for a typical optimization problem.

As a final example, the material failure loads for a vertical shear force are displayed in Figure 4.6 as a function of the fiber orientation angles. For this loading case, the stresses are exclusively shear and are a maximum at the sides of the cross-section (the  $T_1$  location). The best resistance to the shear stress is a layup constructed of  $\pm 45$  plies, as exhibited by the curve for the constant stiffness laminates. However, the distribution of the shear stresses, calculated using the membrane solution of Eq. (4.42), depends heavily on the variation of the stiffness terms. For some of the variable stiffness designs, the circumferential stiffness variation redistributes the stress and lowers the value of the shear stress at the sides, thereby producing a design that possesses a larger material failure load when compared to the constant stiffness laminates. This is an excellent result, for it proves the effectiveness of the variable stiffness concept when applied to loads that



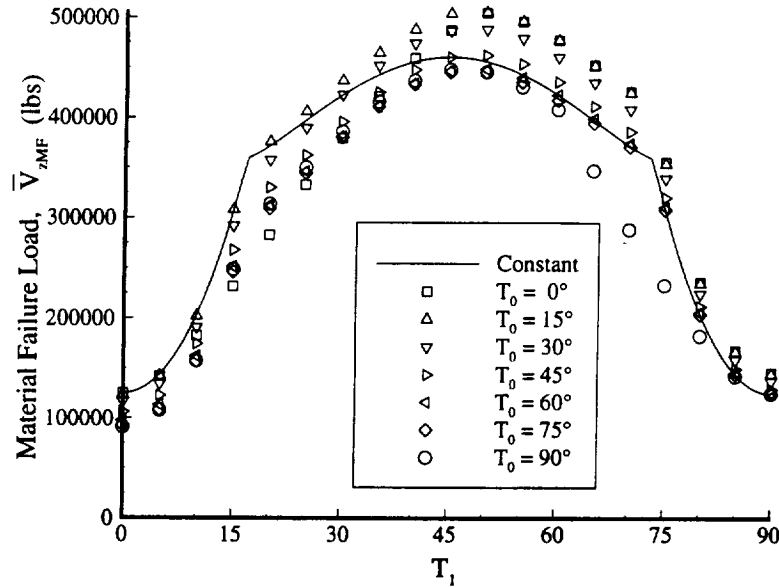


**Figure 4.6: Failure Loads for Cylinders under a Vertical Shear Force**

vary spatially throughout the structure. For loading of this type which depends heavily on the values of the stiffness parameters, the dominant loads can be effectively spread out across a larger area of the cross-section, so that the resulting stresses are reduced and the structure can withstand greater loads until material failure.

#### 4.4 Buckling Results

The results in the previous section have shown that with regard to material failure, a circumferential stiffness variation does exhibit improvement over constant stiffness laminates for load cases in which the stiffness variation is able to redistribute the stresses. Such results must also be demonstrated for buckling failure, since for many structures stability is the determining failure mechanism. Therefore, this section investigates the buckling behavior of short cylinder segments with a circumferential stiffness variation. Firstly, some general discussion regarding the correct choice of the axial buckling frequency  $\beta$  and its importance on several load cases is discussed. Variable stiffness laminates utilizing curvilinear fiber paths are then considered to determine their relative worth under all loading cases. Lastly, the stability of stiffened structures that utilize stringers and longerons is discussed to provide a comparison of these traditional structures to the novel designs of the variable stiffness concept. An in-depth optimization study is subsequently performed in the next section that utilizes all of the variable stiffness concept possibilities.

##### 4.4.1 General Loading of Constant Stiffness Structures

This section discusses the basic nature of the buckling mode shapes for the five basic types of loading shown in Figure 4.1. Some of the introductory and background information on this topic

appears in Section 1.2.2, since the classical buckling solutions use analytical methods on which these numerical solutions are based. However, there are some additional details that deserve full discussion so as to illustrate the applicability and reliability of the stability estimations presented in this section. Recall that in the formulation of the buckling eigenvalue problem, the axial frequency  $\beta$  is an additional unknown and must be determined by the numerical technique. It was shown in Eq. (4.45) that the choice of the parameter  $\beta$  in the assumed axial variation of the displacements is often determined by the length of the cylinder section. This determination is largely based on practical applications of the theory. For instance, shell structures usually possess end conditions which restrict the radial displacement through attachments to sturdy ring stiffeners or frames, therefore choosing a value of  $\beta$  that guarantees a suitable boundary condition at each end lends more credence to the solution. Similarly, there exists the theoretical concern that the membrane prebuckling solution is only valid for short cylinder sections, which implies that the value of  $\beta$  must be large. However, the numerical procedure actually places no restriction on the value of  $\beta$ , so that the correct theoretical choice for the  $\beta$  parameter is one which renders the eigenvalue to be a minimum. Thus some investigation of the relationship between the critical eigenvalue and the axial frequency  $\beta$  is warranted.

A plot of the eigenvalues for the five major beam loading cases versus the axial frequency parameter  $\beta$  is shown in Figure 4.7. These results are for an isotropic skin with  $R/H \approx 2000$ , and

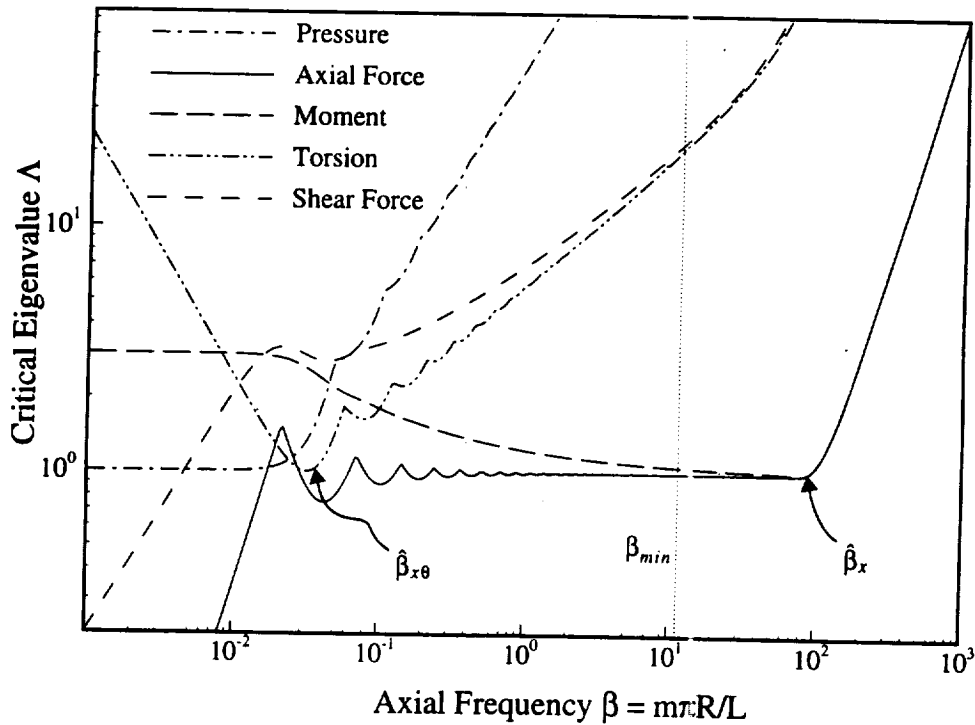


Figure 4.7: Critical Eigenvalue of Major Load Cases versus Axial Frequency  $\beta$

the loads are normalized with respect to their infinite length values. For general loading, these infinite length classical estimates can be formulated through the equations of Section 4.1.2 for each load case by using the infinite length values of  $\hat{N}_x^{cl}$ ,  $\hat{N}_\theta^\infty$ , and  $\hat{N}_{x\theta}^\infty$  given in Section 1.2.2 for the classical stress resultant buckling values. For realistic (finite length) structures, the parameter  $\beta$  is expressed as

$$\beta = m \left( \frac{\pi R}{L} \right) = m \beta_{\min} \quad m = 1, 2, 3, \dots \quad (4.49)$$

where  $\beta_{\min}$  depends on the size of the cylinder and  $m$  is an integer representing the number of half-waves along the length. For instance, the dotted vertical line in Figure 4.7 represents  $\beta_{\min}$  for a short cylinder segment with  $L/R \approx 0.25$ , and thus the only possible values for  $\beta$  would coincide with integer multiples of the minimum value  $\beta_{\min}$ .

The first problem to examine is the effect that the parameter  $\beta$  has on the buckling load under the basic loading of external pressure. The curve denoted by the dash-dot line in Figure 4.7 represents this relationship, which begins at unity for small values of  $\beta$  and rises dramatically as the axial frequency increases. The value of one for small  $\beta$  is expected, for this is the normalized classical buckling solution for an infinite length cylinder corresponding to  $\beta = 0$ . Increasing the value of  $\beta$  is analogous to increasing the frequency of the mode shape, which can be construed here as decreasing the effective length of the cylinder. It was earlier shown in Section 1.2.2 that for a pressure load, the mode shape will always attempt to achieve the lowest value of  $\beta = \beta_{\min}$ , so that only one half-wave will exist in the axial direction. It was also shown that decreasing the length tends to increase the number of circumferential waves present in the buckled mode shape. This is reflected in the series of ripples within the curve of Figure 4.7. Each ripple corresponds to a certain value of the circumferential wave number  $n$ , which increases as a positive integer as the value of  $\beta$  rises. When  $\beta$  becomes sufficiently large, the distinction between successive modes of differing circumferential wave numbers disappears, so that the dependence of the eigenvalue on the exact circumferential wave number  $n$  is eliminated. It should also be noted that the value of  $\beta$ , and thus the length-to-radius ratio of the cylinder, has a dramatic effect on the size of the eigenvalue. Therefore, to determine the *critical* eigenvalue for buckling under external pressure, an estimation of the length of the cylinder must be known. If the structure is sufficiently long, then the cylinder can be approximated as a ring under external pressure and the eigenvalue will coincide with the classical buckling estimate. For most practical structures, however, end conditions are present and only one half-wave will exist along the length, thus the value of the axial frequency will be  $\beta = \beta_{\min}$  and the eigenvalue and number of circumferential waves are determined numerically. Note that these conclusions substantiate the increased buckling performance of ring-stiffened cyl-

inders under external pressure that was shown in the optimization results of axisymmetric cylinders, since the ring stiffeners effectively reduce the length of the cylinder segment so that the buckling load increases dramatically. However, these conclusions also reveal that a similar increase for structures with a longitudinal stiffeners may not exist. This is due to two related reasons: the fact that the circumferential stiffness variation has no effect on the effective length of the cylinder; and the existence of eigenmodes with similar values of  $n$  that possess closely related eigenvalues, so that altering the circumferential mode shape will not improve the buckling load.

The next basic loading case to consider is axial compression. The relationship between the critical eigenvalue and the axial frequency  $\beta$  for a compressive axial force is denoted in Figure 4.7 by a solid line. As with the external pressure case, the resulting curve is characterized by successive ripples that represent different circumferential wave numbers of the buckled mode shape. Note that for the smallest values of  $\beta$ , the curve begins as a monotonically increasing line. This line actually represents classic Euler buckling of the cylinder as a column corresponding to one wave in the circumferential direction. For such a mode shape, the structure does not undergo the typical pattern involving wrinkling of the shell, instead the cross-section displaces in the transverse direction as a rigid body and the cylindrical structure deforms globally as a buckled column. It should be emphasized that classical cylinder equations using DMV strain-displacement equations cannot capture this "global" buckling phenomenon, but that Sanders shell theory can calculate this possible mode of buckling due to its greater accuracy for deformations dominated by slow circumferential variation. This fact is further demonstrated in Figure 4.7 for the next few successive waves of the curve, where the inaccurate DMV theory would not predict the presence of eigenvalues below the normalized value of unity. Of course, as  $\beta$  increases, so does the number of circumferential waves in the buckled mode shape, thus for larger values of the axial frequency the two theories agree. For isotropic materials, the increase in the number of circumferential waves in the buckled shape reaches a maximum near the point  $\beta = \hat{\beta}_x/2$ , and then the variation in the circumferential direction decreases until the point  $\beta = \hat{\beta}_x$  is reached. Above this value, the resulting mode shape is axisymmetric, meaning that no circumferential waves exist in the circumferential direction and the buckled cylinder is characterized by axial waves produced by the expansion and contraction of the radius of the cross-section. The results for non-isotropic materials may deviate slightly, as discussed in Section 1.2.2, since orthotropic materials possess different qualities with respect to their critical eigenvalue and resulting mode shapes.

For realistic structures with  $\beta > \beta_{\min}$ , the eigenvalue versus  $\beta$  curve for an axial compressive force resembles a horizontal line up to a particular value of the axial frequency (which corresponds to the classical buckling frequency  $\hat{\beta}_x$ ). This implies that many different mode shapes

exist for nearly identical values of the buckling load. This feature of coincident modes is distinctive to cylinders loaded under axial compression, and is a significant factor in the high sensitivity of such structures to shape imperfections, as discussed in the last chapter. For our numerical technique of eigenvalue estimation, these coincident modes do not present a problem, since the solution process relies on finding the integer multiple of  $\beta_{\min}$  that produces a minimum value of the eigenvalue, and therefore any of the closely spaced eigenvalues would suffice. For more complicated variable stiffness structures, the resulting relationship between  $\beta$  and the numerical eigenvalue may not be as simple, therefore the search for the critical buckling load usually starts at  $\beta = \hat{\beta}_x$  since that value is characteristic of the skin of the shell structure.

The foregoing discussion with regard to the buckling of cylinders under axial compression has direct relevance to the next loading case: pure bending. As alluded to earlier in this chapter, landmark work in this area was first completed for isotropic cylinders by Seide & Weingarten<sup>85</sup> using a numerical solution technique that conforms exactly to a Rayleigh-Ritz solution of the governing equations that are presented here. Their conclusion was that buckling of a circular cylindrical shell occurred when the maximum bending stress equaled the critical stress for a cylinder under axial compression, and also that the variation of the deformed mode shape in the axial direction corresponded to the classical frequency estimate under compression, namely  $\hat{\beta}_x$ . This claim was substantiated through the calculation of eigenvalues for pure bending in tabular and graphical form as a function of  $\beta$ , much like the curve shown in Figure 4.7 for an applied moment. Several  $R/H$  values were investigated, with all cases producing similar curves as the one shown (though their curves differed slightly for small  $\beta$  since they employed DMV theory instead of Sanders). One can easily see in the figure that their claims hold true: the eigenvalue, which was normalized with respect to this Seide-Weingarten criteria, has a minimum value of one at the point  $\beta = \hat{\beta}_x$ . These results are, in general, applicable to any general orthotropic shell (excluding, of course, ones with any spatial stiffness variation), though the location of the minimum and the critical value of the buckling load may differ slightly for some orthotropic laminates according to the discussion presented in Section 1.2.2. Further comparison of the relationships of an axial compressive force and a bending moment with respect to the axial frequency  $\beta$  reveals that above the value of  $\hat{\beta}_x$ , the curves actually coincide. This property is quite useful in practical applications, since determining the critical buckling load for axial compression, is, in general, simpler than calculating the eigenvalue for pure bending. This phenomena will be used extensively in Chapter 5.0 and Chapter 6.0 to estimate the buckling load of complex structures under pure bending.

The final two cases to consider from Figure 4.7 involve shear loading in the form of torsion and a transverse shear force. Of course, the results for shear loading must be augmented with the

comments concerning warping allowed at the ends. It was shown in Section 3.5.2, Figure 3.18 that the correct application of the radial restraint at the ends produces an eigenvalue that can be as much as three times the “classical” value that is calculated here. Therefore these general results for shear loading must be considered inaccurate except for general trends and order of magnitude estimations. Bearing this in mind, the relationship for torsion with respect to the axial buckling frequency is denoted in Figure 4.7 by the dash-dot-dot line. The curve possesses a minimum value at  $\beta = \hat{\beta}_{x\theta}$ , where the cylinder deforms into the traditional shape of two circumferential waves (as displayed in Figure 1.7). The value of the critical load then steadily increases with the familiar rippled pattern, with the increased value of  $\beta$  again producing higher values of the circumferential wave number, much like for the external pressure case. This is expected from our earlier discussions and results. Though not as significant as for the external pressure loading, the presence of frames that effectively increase the value of  $\beta_{\min}$  does lead to a similar increase in the buckling load under torsion.

The last load case of Figure 4.7 represents buckling by a transverse shear force, and is designated by the shorter dashed line. For small  $\beta$ , the estimated buckling load approaches zero, which represents a numerical anomaly associated with the rigid body displacement of the cross-section. However, these results are immaterial, for buckling under a transverse shear force should only be considered for short cross-sections (large values of  $\beta$ ), since it can be shown that longer cylinders are invariably unstable due to the beam moment produced by the transverse shear force. Thus, the only realistic results for this case are for values of  $\beta$  greater than  $\beta_{\min}$ , and the figure reveals that this relationship approaches that of torsion as the axial frequency is increased. This discovery is directly analogous to the axial compression and bending moment relationship first discovered by Seide & Weingarten. In fact, the formulation of the numerical equations for the determination of the buckling loads for both of these pairs of load cases is quite similar, so that these results are, in fact, expected. To illustrate the correlation further, the buckling modes under torsion and a vertical shear force are shown in Figure 4.8 for  $\beta = \beta_{\min}$ . Note that the cylinder section is short (the figures are actually elongated slightly to highlight the features along the length), and that the simple support boundary conditions at the ends are not satisfied and allow significant warping (as explained in Section 4.2). The mode shape for the cylinder under torsion is characterized by a number of helical waves traversing the length of the cylinder, where the number and spacing of the waves are uniform around the circumference of the cross-section. Conversely, the cylinder loaded by a vertical shear force produces a mode shape that only has a few of these circumferential waves, located where the shear stress is the highest. Also note that the frequency of the buckled mode shape for the shear force corresponds to that of the torsional case in both the circumferential and axial direc-

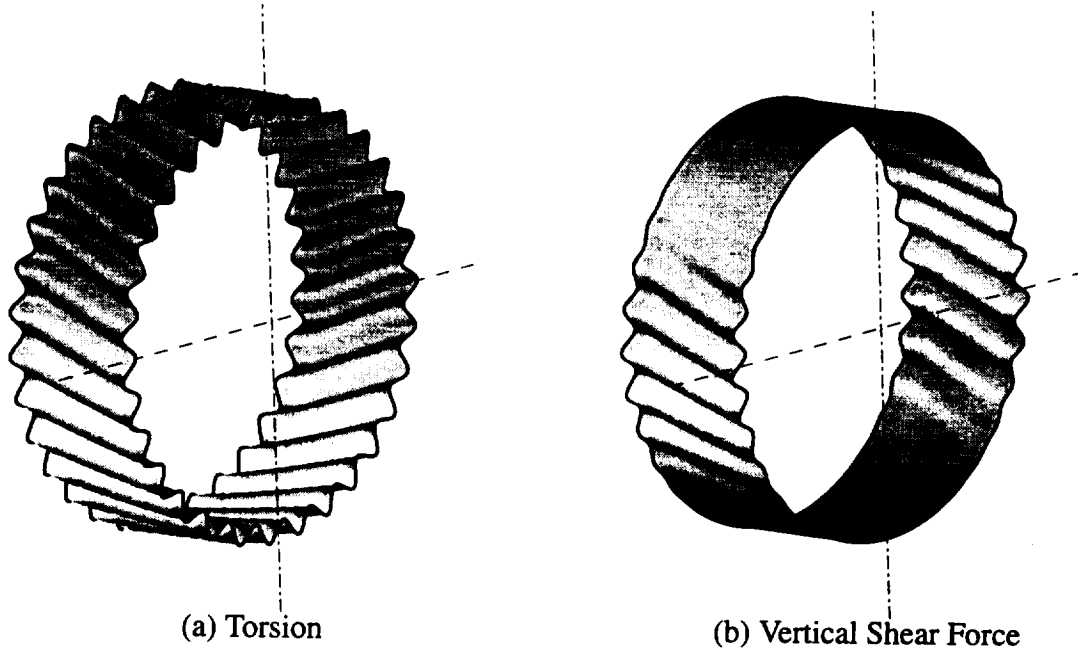


**Figure 4.8: Buckled Mode Shapes for Torsion and Vertical Shear Force,  $\beta = \beta_{min}$**

tions. Thus it can be deduced from these results that the calculation of buckling of short cylinder sections under a transverse shear force can be approximated by determining when the maximum shear stress reaches the critical value for buckling under torsion, since the local area containing the maximum shear stress is identical for both load cases. This discovery corresponds to the Seide-Weingarten criteria for cylinders under bending. An example of this for a more complicated stiffened structure is presented in Section 4.4.3.

#### 4.4.2 Curvilinear Fiber Paths using One Link Variation

The possible improvements of the buckling loads for a cross-section using a circumferential stiffness variation are investigated in this section. The results are presented in the form of contour plots of the five basic buckling loads as a function of the endpoint fiber orientation angles using a one link variation. Specific examples of the deformed cross-section are also included for each case to highlight the relevant mechanism that governs the behavior. The particular geometry of the cylindrical shell is as follows:

$$\begin{aligned} \text{Stacking sequence} &= [\pm\varphi]_{6s} & R &= 24'' & L &= 12'' \\ \varphi(\theta) &= T_0 + \frac{2\theta}{\pi}(T_1 - T_0) & 0 \leq \theta \leq \pi & \quad (\text{sawtooth function}) \end{aligned} \quad (4.50)$$

This corresponds to the  $Z_b \approx 50$  size used in the last chapter. The basic trends of the results should apply to all short and thin cylinders, so that individual optimization of the buckling loads is not deemed necessary.

**External pressure.** The level curves of the buckling pressure (normalized with respect to the best constant stiffness laminate) are shown in Figure 4.9 as a function of the endpoint angles  $T_0$

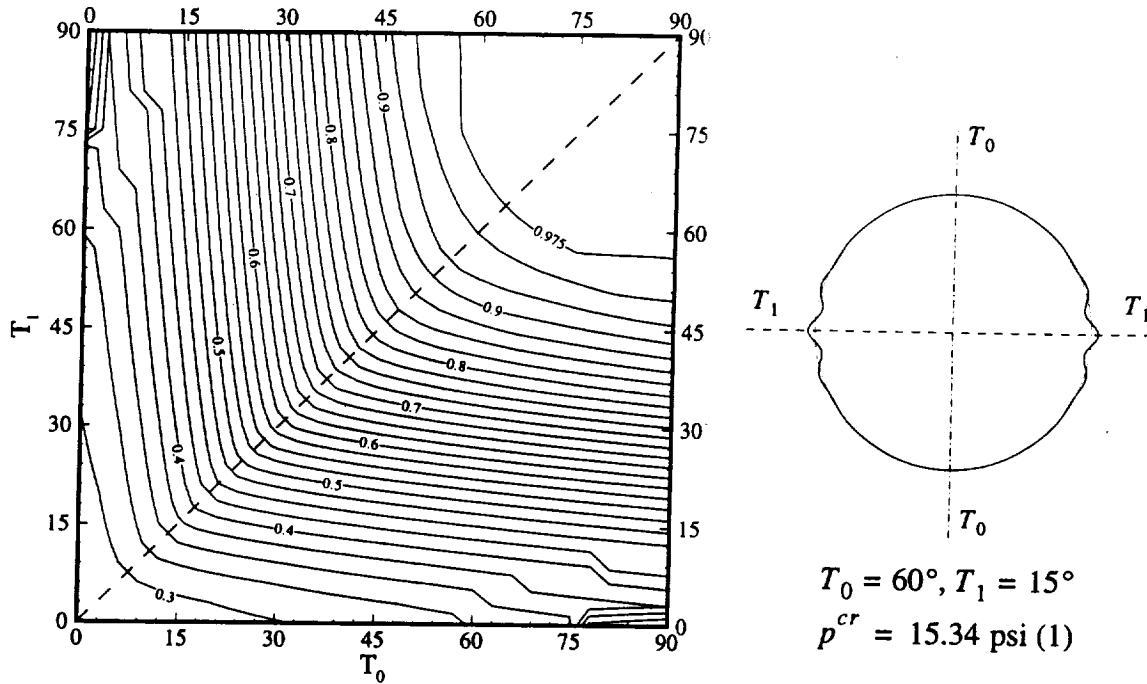


**Figure 4.9: Results for External Pressure using One Link Circumferential Variation**

and  $T_1$ . The optimal design is for a constant stiffness laminate with  $\phi = 90^\circ$ . The plot is symmetric about the diagonal constant stiffness line, which is to be expected since the periodic nature of the cylinder in the circumferential direction generates a solution that should be interchangeable with respect to the endpoint values  $T_0$  and  $T_1$ . This symmetry should also be exhibited for the axial compression and torsion cases, since none of these scenarios have a bias for any direction perpendicular to the cross-section. The external pressure case offers no improvement over the constant stiffness laminates, even for designs with a large stiffness variation. This can be attributed to the fact that for shorter cylinders, the mode shape contains many circumferential waves. Since the pressure load is constant everywhere around the circumference of the cross-section, the critical buckling mode produces the greatest deformation at the location with the least resistant stiffness properties. This deformation can be quite localized, since the circumferential buckling frequency is relatively high. For instance, the deformed cross-section for a typical variable stiffness cylinder is shown to the right in Figure 4.9, along with its buckling load and the number of axial half-waves in the mode shape (the buckled waveform also contains a sinusoidal variation along the length of the cylinder, though only the cross-section is shown here for simplicity). Note how the deformation is confined to the sides, where the  $15^\circ$  fiber orientation angle is the weakest under pressure. This is a classic example of the weak link concept, where failure occurs at the location



of least resistance. The presence of the weak link concept is also indicated by the shape of the level curves in the contour plot. Due to this phenomena, it is concluded that there is no possible improvement for short cylinders under a (constant) external pressure using a circumferential stiffness variation.

**Axial Compression.** For the axial compressive case, the solution is similar but not as straightforward. Due to the variation of the stiffness, there is some redistribution of the axial stresses since the stiffer regions carry a larger fraction of the loads. Failure still usually occurs where the stiffness parameters offer the least resistance to buckling, however the value of the stress at this critical location can now be altered since the stresses depend on the stiffness variation. For example, the level curves of the axial buckling load for the variable stiffness designs in terms of the endpoint angles is displayed in Figure 4.10. The critical values are normalized with respect to the

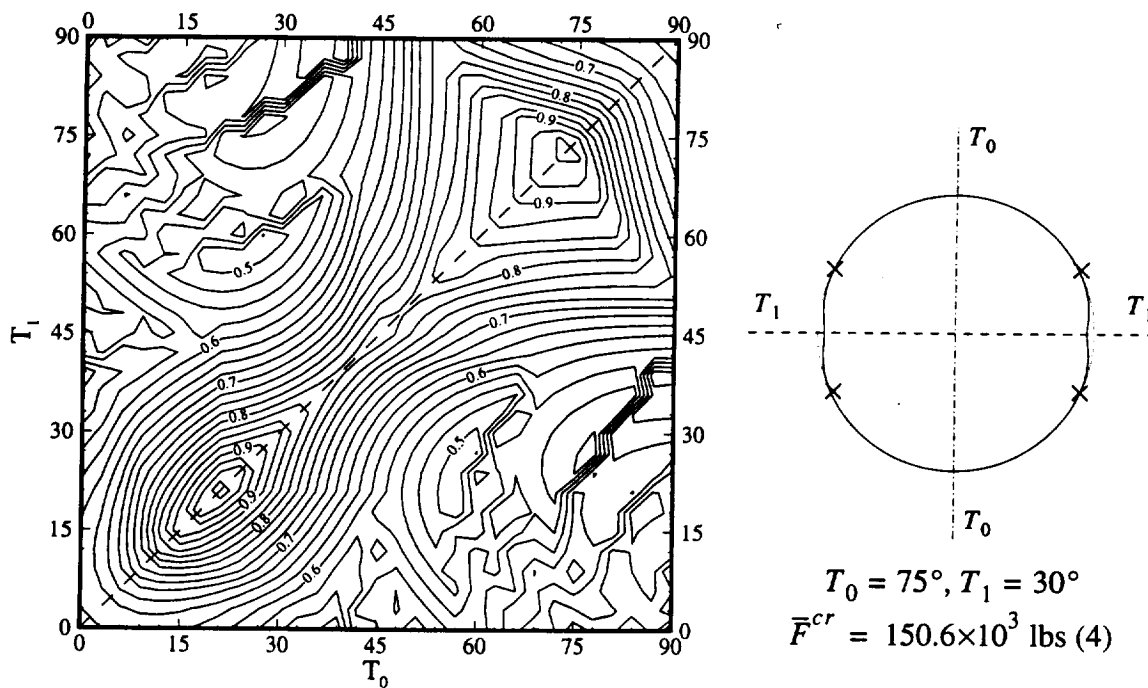


**Figure 4.10: Results for Axial Compression using One Link Circumferential Variation**

maximum constant stiffness laminate, located near  $\phi = 21^\circ$ . The results indicate that no variable stiffness laminate exists that offers an improvement to this design, and the contour lines also show quite a variation of critical load for designs with a large stiffness variation. The example variable stiffness cylinder shown in Figure 4.10 would seem to indicate that the weak link phenomenon is present, since the buckling deformation is localized to the sides of the cross-section. However, examination of the contour plot reveals that the weakest constant stiffness design under buckling occurs closer to  $\phi = 45^\circ$ . If the weak link concept rules the response, this would result in the

deformed cross-section having the largest deformation where the fiber orientation angle equals  $45^\circ$ , which is marked with the symbol  $\times$  in the figure. Instead, due to the circumferential stiffness variation the stiffer regions at the sides bear more of the axial load and becomes the critical buckling region, while the  $45^\circ$  areas are not as highly stressed and therefore do not buckle. Therefore, the concept of carrying the loads in parallel tends to improve the performance of variable stiffness laminates, though the relative increase shown for this specific geometry and laminate stacking sequence does not exist.

**Torsion.** Under a torsional load, the results agree almost exactly with the external pressure case. The weak link effect can be easily deduced from the plots shown in Figure 4.11. Again the

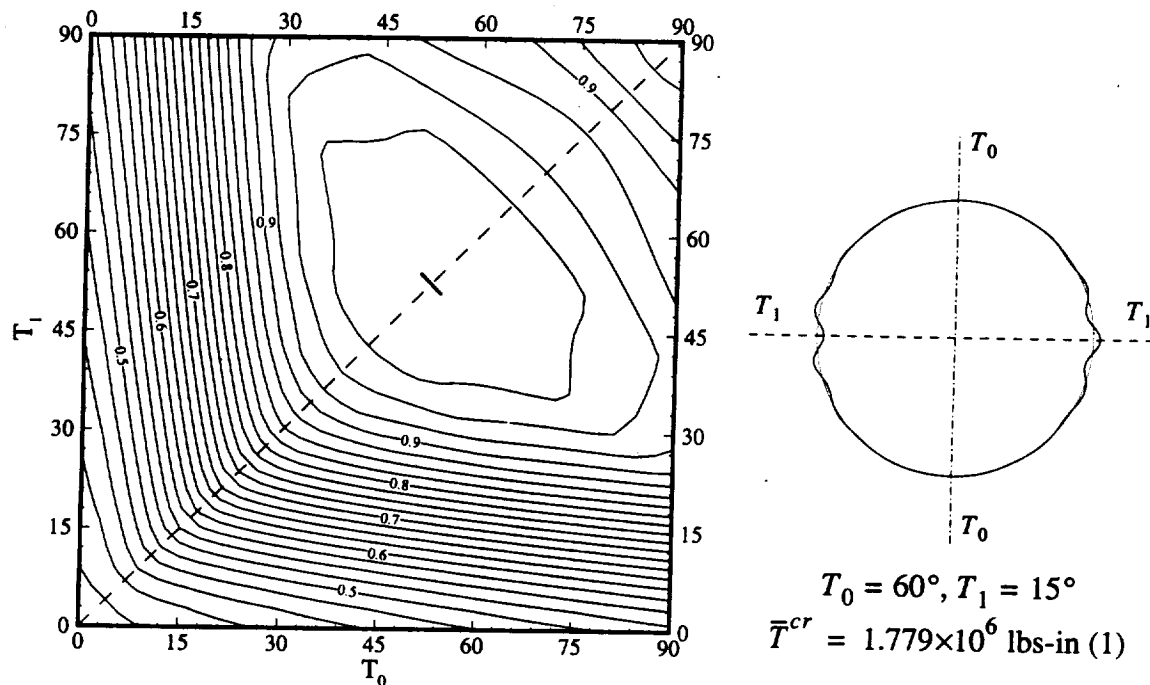


**Figure 4.11: Results for Torsion using One Link Circumferential Variation**

high frequency of the buckled shape coupled with the constant value of the shear load around the circumference results in the mode shaping itself to the weakest link in the stiffness variation. The deformed cross-section indicates the region with the largest buckling deformation, where it is implied that this mode shape varies in a helical fashion around the axis of the cylinder (as indicated by Figure 4.8). No improvements are expected for this load case.

The three previous load cases indicated no improvement possibilities for the one link curvilinear fiber definition. This was mostly due to the weak link concept and the fact that the loads contained no preferential direction within the cross-section. The next two load cases, pure bending and a transverse shear force, do possess a bias in the loading direction which restricts the buckling

deformation to a certain area. Therefore, correct variation of the stiffness parameters should produce a relative increase in load carrying capability by either redistributing the largest stresses away from these critical areas or by significantly altering the buckling deformation.

**Pure bending.** The level curves and an example deformed cross-section for a one link variable stiffness cylinder under pure bending is displayed in Figure 4.12. The first thing to notice is

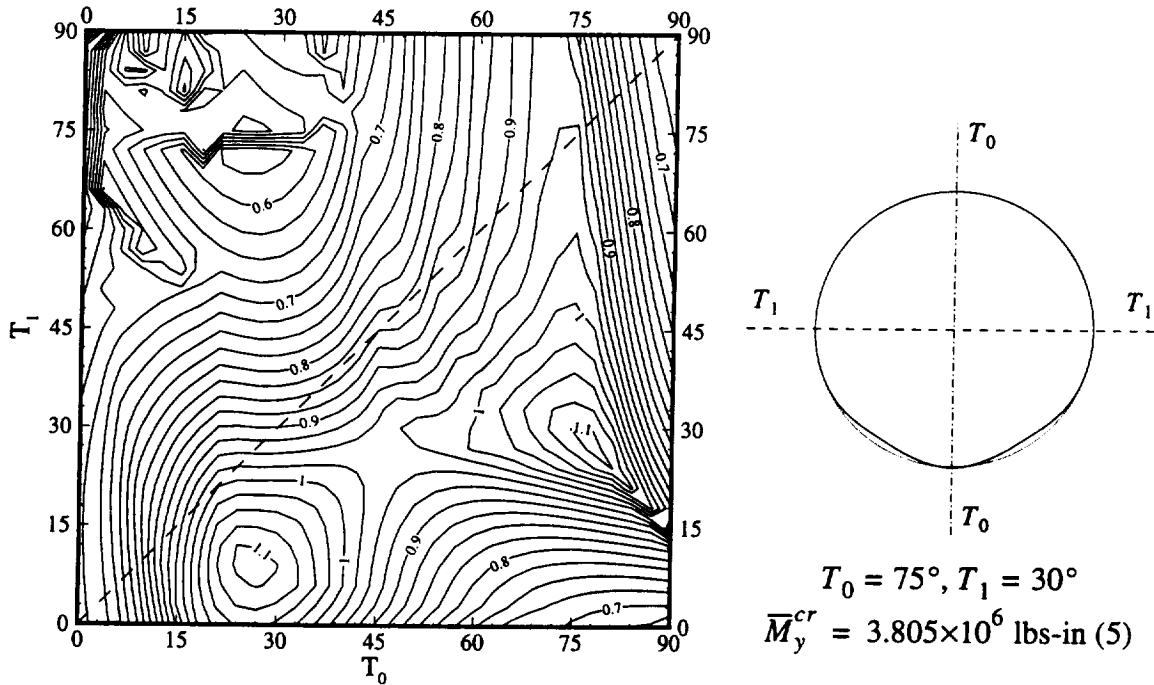


**Figure 4.12: Results for Pure Bending using One Link Circumferential Variation**

that the maximum buckling load corresponds to a variable stiffness laminate, and in fact there are actually two distinct maxima with similar critical values. The example to the right represents one of these optimal designs. The variation of the stiffness is such that the area with the largest stress (at the bottom) possesses a fiber orientation angle  $T_0 = 75^\circ$  that produces a stacking sequence that is quite resistant to buckling. Meanwhile, the linear variation of the fiber orientation angle to  $30^\circ$  at the sides produces an area near the bottom that contains fiber orientation angles that are much more susceptible to axial buckling, and therefore the maximum deformation of the critical mode shape is moved away from the region of highest stress. As one would expect, this significantly increases the global buckling value, since the stresses produced at the buckled region are not as large as those at the bottom. This feature of restricting the deformation at the point of highest stress is analogous to the presence of a “node” at that location. This will be discussed in a bit more detail in Section 4.4.3, since the idea of a node to improve the buckling load is traditionally seen through the use of stiffeners. It is actually quite promising that the curvilinear fiber format can

approximate this phenomenon so easily, and this will be taken advantage of further during the design of fuselage structures under bending. In general, the improvement under bending is achieved through this aforementioned mechanism of limiting the deformation at the point of maximum stress along with constructing a design that possesses a high bending stiffness.

**Transverse shear force.** For this last example, the force is assumed to act in the vertical direction across the cross-section. The results are displayed in Figure 4.13. The optimal design is for a

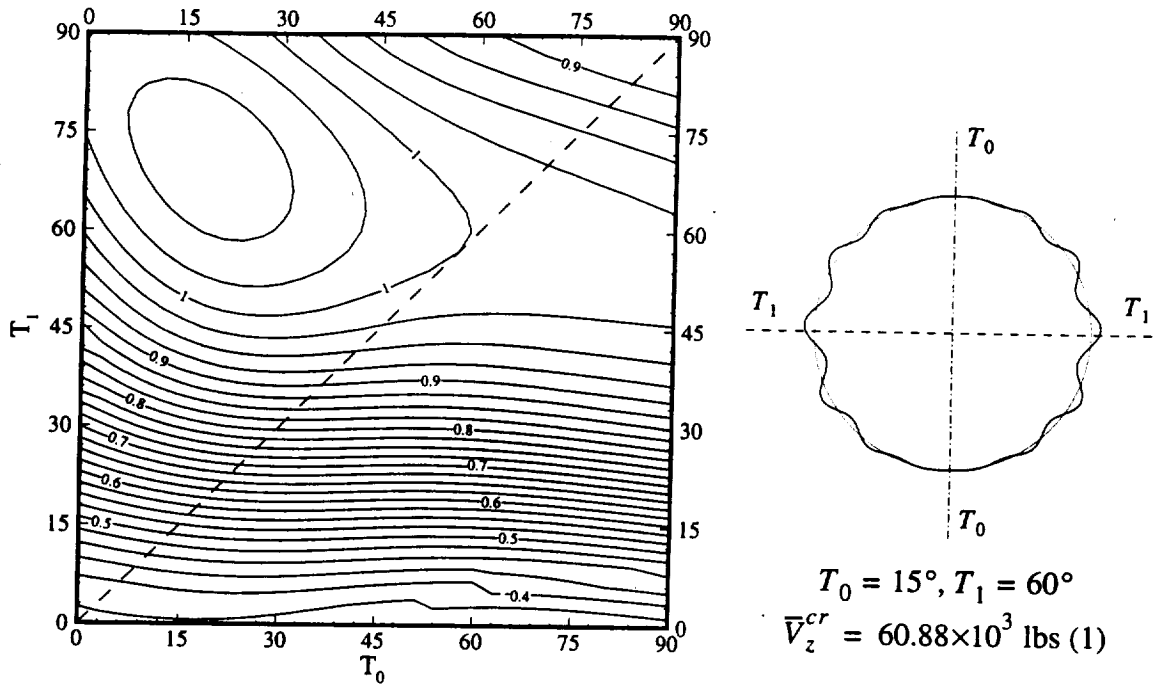


**Figure 4.13: Results for Vertical Shear Force using One Link Circumferential Variation**

variable stiffness cylinder. Also note the presence of many horizontal lines as level curves in the plot at left. These indicate that for many designs the buckling load is independent of the value of  $T_0$ . This is somewhat expected, since the shear stresses are maximum at the  $T_1$  location and the fiber orientation angles tend to follow the weak link concept under shear loading (as shown by load case of torsion). However, once the value of  $T_1$  corresponds to a fiber orientation angle that is resistant to shear buckling, the variable stiffness designs display improvements over their constant stiffness counterparts. The reason is that the stiffness variation controls the distribution of the shear stresses, therefore a proper variation should reduce the maximum stress at the critical location and increase the load required to produce instability. This is evidenced by the example cross-section at right, in which the buckling deformation is spread out over a larger area than for typical shear force buckling (see Figure 4.8). However, due to the helical type deformation pattern associated with buckling under shear, the curvilinear fiber format cannot produce sufficient stiffness

variation to enable a node to occur at the point of maximum stress. However, the results shown here do represent a definite possibility for improvement over traditional straight fiber laminates.

#### 4.4.3 Stiffened Structures

The distinguishing aspect of this study is the inclusion of spatial stiffness variations within the shell structure, usually through the inclusion of curvilinear fiber paths. However, traditional stiffened structures, such as the one displayed in Figure 4.1, can also be regarded as “variable stiffness” due to the significant addition to the stiffness properties wherever a stiffener is present. Thus a discussion of this traditional stiffening mechanism is included. For these examples, the structure will contain fifty evenly spaced stringers around the circumference, and the skin will be constructed of an isotropic material. Though the inclusion of composite materials with ply drops and curvilinear fibers may also be of interest, the basic concepts illustrated here remain the same.

The first example involves the application of a horizontal bending moment to the stiffened structure. The resulting stresses within the shell structure are axial only, and are distributed between the thin skin and the discrete axial stiffeners according to Eq. (4.30). This equation is repeated here in its normalized version as

$$\bar{n}_x(\theta) = \bar{m}_y \bar{E}_x(\theta)(\cos \theta - \cos \theta_{ref}) \quad (4.51)$$

where the normalization is completed with respect to parameters associated with the skin. For the structure under consideration, this relationship between the axial stress resultant and circumferential location is shown in Figure 4.14 for the critical buckling load of the structure. As expected,

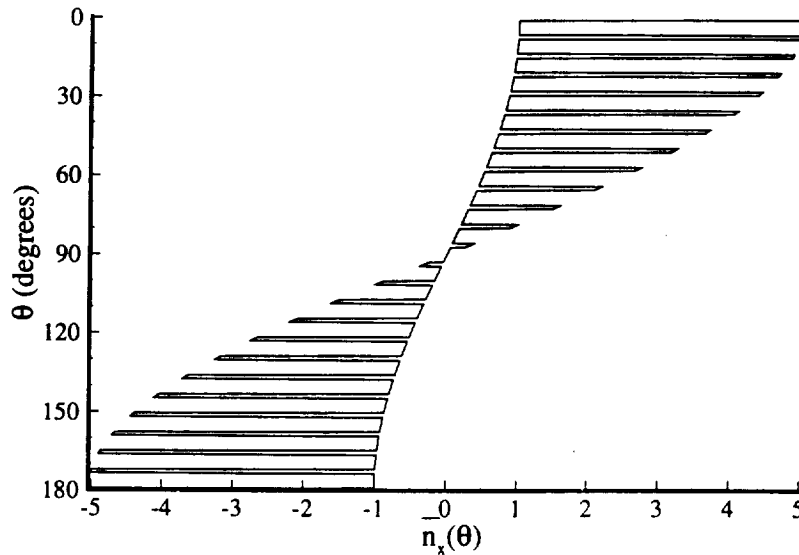


**Figure 4.14: Axial Stress Resultant Distribution for Stiffened Fuselage under Bending**

the stringers act as discrete jumps in the stiffness distribution and produce spikes in the curve. Meanwhile, the stress within the skin follows the basic cosine relationship experienced by unstiffened structures. These results lend credence to the use of the variable stiffness concept for these types of membrane loading, for the stress relationship shown in Figure 4.14 corresponds correctly to the most basic method of determining the ratios of stresses between stiffeners and skins for traditional stiffened structures. The buckled mode shape for this cylinder cross-section under a horizontal bending moment is displayed in Figure 4.15. Note how the skin has buckled between the

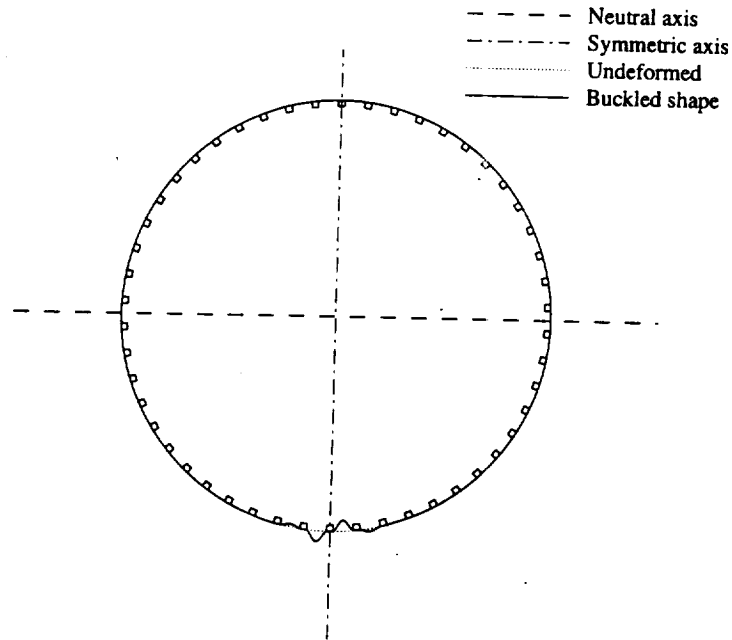


**Figure 4.15: Buckled Mode Shape for Stiffened Fuselage under Bending**

axial stiffeners, but that the sturdy stringers, which carry the majority of the axial stresses, do not undergo any substantial buckling deformation. This is a perfect example of stiffeners acting as nodes, and indicate why stiffeners are so effective in conjunction with thin shells.

Similar correlation between the variable stiffness membrane solutions and basic first-order approximations can be exhibited under transverse shear loading. The governing equation for the unnormalized shear stress resultant is given as

$$\bar{n}_{x\theta}(\theta) = \bar{v}_z \frac{\bar{Q}_z(\theta)}{\bar{Q}_z(\theta_{ref})} \quad Q_z(\theta) = \int_0^\theta E_x(\theta) (\cos \theta - \cos \theta_{ref}) H R^2 d\theta \quad (4.52)$$

This represents the shear flow of the cross-section under a transverse vertical shear force, and corresponds to the sheet-stringer analysis used in the field of mechanics of materials. Illustration of

this relationship of the shear flow of the stiffened structure under consideration is shown in Figure 4.16. The shape is roughly sinusoidal, with small slope discontinuities located at the

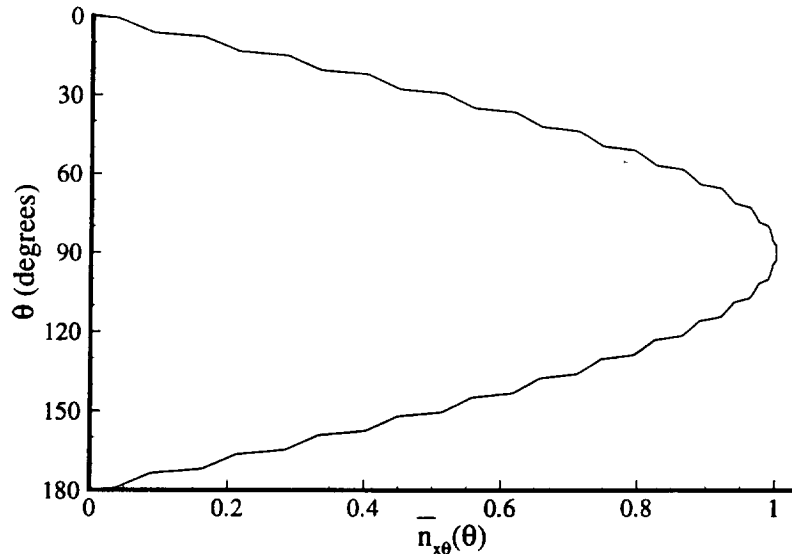


**Figure 4.16: Shear Stress Resultant Distribution for Stiffened Fuselage under Shear Force**

attachments of the stiffeners. In the classical sheet-stringer solution, these discontinuities are represented as vertical lines, since the stringers are assumed to carry none of the shear stresses and their attachment area with the skin is assumed to be infinitely small. However, the variable stiffness analysis improves upon the theory with regard to both of these remarks. Firstly, though the stiffeners are still assumed to possess negligible resistance to shear, the skin underneath the stiffener *can* carry these shear loads. Furthermore, the area over which the stiffener is attached is easily modeled under the techniques of the variable stiffness concept, so that the variation of the shear stress can be accurately portrayed within this region using the equations of Eq. (4.52).

The buckled mode shape for a short cylinder segment under the shear stress distribution of Eq. (4.52) is shown in Figure 4.17. Again note that the sturdy stiffeners remain undeformed and that the buckling is limited to the skin sections between the stiffeners. Furthermore, compare the axial and circumferential wavelengths of the buckled skin to those of the unstiffened cylinder under a vertical shear force in Figure 4.8. Though the skin is the same material and thickness for both cases, the buckled mode shapes actually differ quite substantially. This is due to the fact that the axial stiffeners tend to act as “nodes”, which are points of zero displacement for the buckled shape. It is easily apparent in the deformed shapes presented here, for both the applied bending moment and the vertical shear force, that this conclusion is warranted. Therefore, the presence of a sufficiently sturdy axial stiffener implies a node which, in general, alters the calculation of the critical eigenmode and eigenvalue of the structure. For example, the mode shape shown in

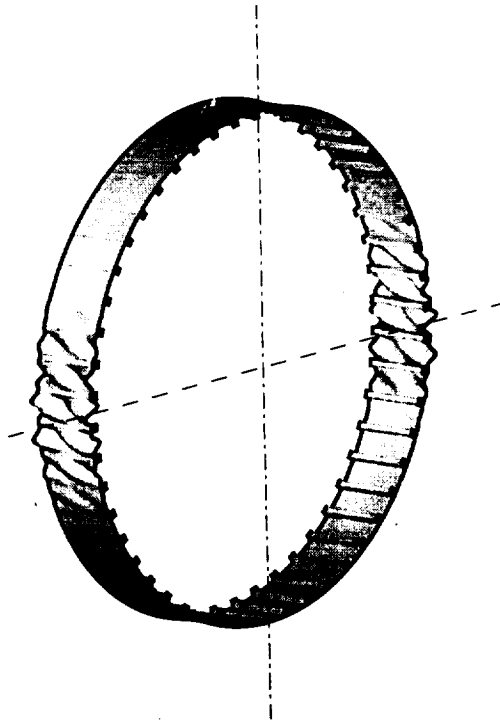


**Figure 4.17: Buckled Mode Shape for Stiffened Structure under Shear Force**

Figure 4.17 differs from the unstiffened case shown in Figure 4.8 since a higher frequency is needed in the circumferential direction to take into account the closely spaced stiffeners. This higher circumferential frequency, in turn, alters the value of the axial frequency parameter  $\beta$  that generates a minimum value of the buckling load. Therefore, though the stiffeners do not carry any substantial amount of shear stress, their presence can contribute to the buckling resistance under shear loading by serving as nodes in the deformed shape. This is also true under bending, where the circumferential variation of the buckled shape must provide for nodes where stiffeners are present, as revealed in Figure 4.15, which alters the desired buckling shape and increases the critical eigenvalue. This phenomenon of a stiffener acting as a node also exists for basic axisymmetric loading, however for these constant load cases there exist so many mode shape possibilities that the presence of the stiffeners does not appreciably alter the eigenmode and thus does little to improve the buckling performance.

#### 4.5 Design of Fuselage Cross-section for Minimum Weight

The analysis developed in this chapter is now applied to a realistic design problem that promises great possibilities for improvement. The specific problem to be studied is the design of a generic narrow body fuselage cross-section for minimum weight, where the cross-section is fabricated using traditional skin/stiffener arrangements as well as the novel variable stiffness concept utilizing curvilinear fibers. Optimization results for isotropic (aluminum) and composite materials



(graphite-epoxy) are both included. Though this study is intended to be as realistic as possible to actual loading conditions and design methods of aircraft fuselage structures, some inherent approximations will also be invoked to facilitate the design study.

#### 4.5.1 Design Criteria for General Aircraft Fuselage

The possible loading conditions experienced by aircraft components during flight is usually defined by a “flight envelope” or “ $V$ - $n$  diagram”, which classifies various flight maneuvers in terms of the airspeed  $V$  and a load parameter  $n$ . This load parameter represents the acceleration imposed upon the airplane by the aeronautical maneuver, and is most often expressed in terms of the gravitational constant  $g$ . Thus, “1  $g$ ” flight represents steady-state flight, whereas typical dives and pull-ups are denoted as  $-1\ g$  and  $2.5\ g$ , respectively. Usually, these accelerations are computed from the dynamics of the moving body and are then applied as equivalent static forces on the structure. This convention is also adopted here, and some simple assumptions concerning the resultant forces are employed so that the loading conditions under various maneuvers can be calculated from the load parameter  $n$ . Thus the design criteria for the flight envelope can be represented in terms of this load factor, and a linear relationship of the loading is assumed.

For example, the design criteria for a typical structural element of an aircraft in terms of the load parameter  $n$  is expressed graphically in Figure 4.18. The horizontal axis represents some dis-

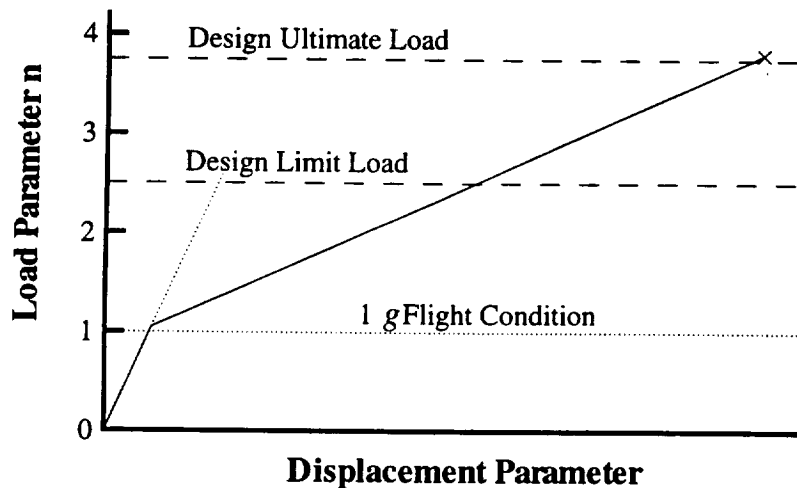


Figure 4.18: Design Criteria for Flight Envelope

placement or strain quantity, such as curvature of the fuselage or deflection of a wing tip, and the vertical axis denotes the load factor that is present due to the aeronautical maneuver. Note that the load-displacement relationship is shown here to be bilinear, where the change in slope occurs at a possible buckling point and the reduced stiffness of the post-buckled configuration produces a dif-

ferent load-displacement relationship. If the structural component is *not* allowed to buckle (for example, an aerodynamic control surface), then the load-displacement curve will follow a straight path denoted by the dotted line in the figure. To satisfy the minimum requirements of the aeronautics industry, major structural components must be able to withstand a 2.5 g limit load without inducing critical failure. For complete certification, the structure must also prove that a 3.75 g load can be attained, however this requirement is seldom used in the design process and is usually satisfied by a one-time static test of a complete aircraft. Therefore, for our purposes the limit load of  $n = 2.5 g$  is considered the actual design load of the aircraft.

However as implied earlier, for some structural components buckling is not considered critical failure, thus enforcing a buckling constraint at this limit load of 2.5 g will result in significantly heavier components and increased weight of the aircraft. Designers have therefore utilized the post-buckling strength of stiffened structures for non-control surfaces of the aircraft, such as the fuselage, so that the industry requirements are achieved while the component can be designed to be as light and efficient as possible. It should be noted though that designing with respect to a bifurcation load is quite dangerous when one is dealing with shells. This practice will often produce optimal designs which possess coincident buckling modes at the same load level, and this can lead to increased imperfection sensitivity that can result in catastrophic failure of the structure at loads well below the desired design levels. Thus, instead of the bilinear path shown in Figure 4.18 that denotes a measure of post-buckling strength, some designs may exhibit a drastic downward trend after the bifurcation point and will never attain the desired limit load. However, to include a post-buckling analysis to accurately analyze this possibility is beyond the scope of this investigation, as well as impractical for optimization studies since the nonlinear post-buckling analysis is quite involved. Even using a first approximation for the post-buckling response, which involves estimating the reduced stiffness of the buckled skin in the post-buckling region, is not practical, for the tools to calculate the altered properties of the stiffened shells do not exist in a practical formulation. For the most part, the designs presented here include stiffeners in most cases, thus we can assume that some post-buckling strength exists for the structure (which is not true for unstiffened shells). Once the optimization results are complete, the final designs can then be analyzed using more advanced tools to determine if the assumed post-buckling strength actually exists.

With regard to these comments, the proposed design criteria for the fuselage structure will be approximated in an extremely crude manner with respect to the post-buckling response. Designs will be constrained to be resistant to bifurcation buckling up to 1 g flight conditions, and the post-buckling response will not be estimated. With regards to material failure, the structure will be

assumed to follow the dotted path in Figure 4.18 up to the 2.5 g flight condition, which assumes that the post-buckling response of the structure has the same load-displacement relation and that there is no redistribution of the stresses within the cross-section. This proposed method is considerably non-conservative, in the fact that a design that can withstand the loads under these assumptions may very easily fail in the post-buckled regime due to the altered distribution of the stresses. However, without a complete post-buckling analysis this solution is the best approximation available for the desired design criteria.

Lastly, the loading represented by Figure 4.18 constitutes a pull-up maneuver of the airplane. To be complete, the fuselage must also be designed to conform to two other constraints, namely a burst pressure due to the pressurization of the fuselage, and a backload of -1 g for a dive maneuver. Other maneuvers that generate side loads and torque on the fuselage will not be considered at this time, for experience has shown that it is the bending loads due to these symmetric maneuvers that usually govern the design. This deviates considerably from realistic design, for these additional load cases contribute greatly to the non-bending aspects of the fuselage, yet they will be ignored here since some limit on the case studies must be defined so that greater detail can be directed toward the investigation of the variable stiffness concept.

#### 4.5.2 Loading Conditions for Fuselage Cross-section

The last section determined the relevant flight conditions that will be used as constraints for the fuselage design. However, these conditions must also be translated into effective loads that act on the cross-section and that can be analyzed using the techniques developed here. To this end, we will assume that the fuselage structure can be approximated as a beam, and the corresponding shear forces and moments are calculated by traditional methods that will not be included here. For this investigation, these methods are based on an approximate solution given by Niu<sup>87</sup> (example problem 5 on pages 78-79 of his text) for a generic narrow body aircraft.

The basic loads on an aircraft that result from a symmetric pull-up maneuver are shown in Figure 4.19, along with the corresponding shear and bending moment diagrams when the fuselage is treated as a beam. The load denoted as  $nW$  in the figure corresponds to an equivalent static force generated by the centrifugal acceleration of the pull-up, and is in terms of the weight of the aircraft and the load factor  $n$  (a symmetric dive maneuver would be expressed with the centrifugal force acting in the upward direction). This load acts at the center of gravity of the aircraft. There also exists a lift and moment due to the aerodynamic characteristics of the wing. Their magnitudes depend on many aerodynamic parameters including the airspeed, wing shape, angle of attack, and altitude and are usually calculated from wind tunnel tests. They are assumed to act at 25% along

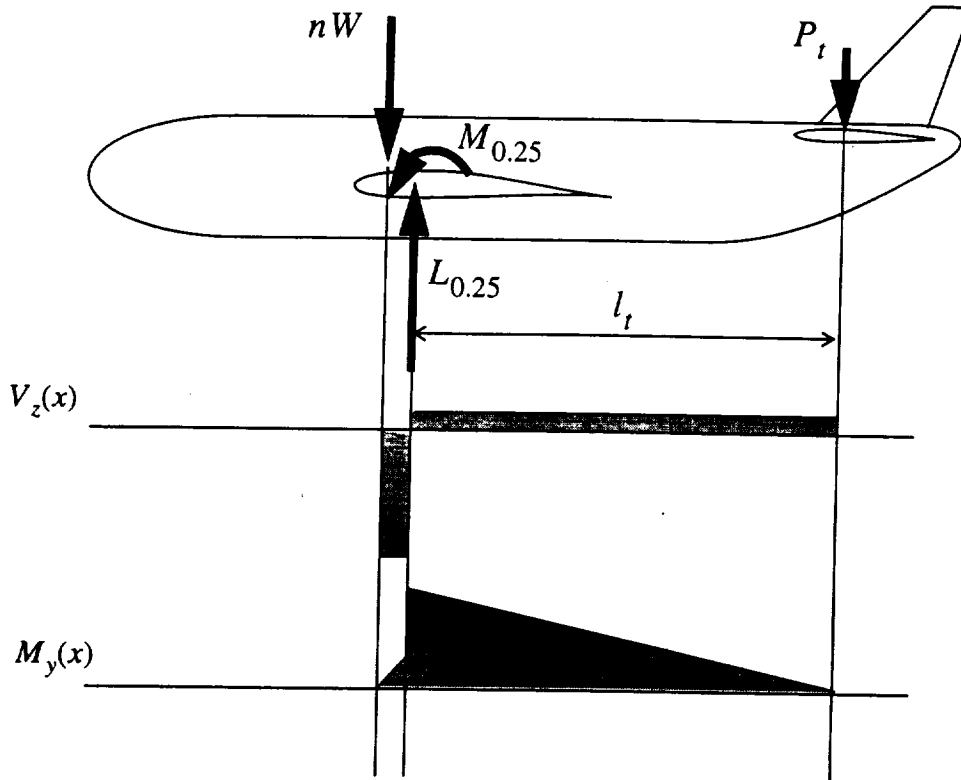


**Figure 4.19: Loads and Shear/Bending Moment Diagrams for Fuselage Structure**

the major chord length of the wing, and are thus denoted by  $L_{0.25}$  and  $M_{0.25}$ , respectively. Finally, the tail wing has an associated force  $P_t$ , which must be present to preserve equilibrium of the aircraft. These are the major forces that contribute to the stress state of the fuselage. Of course, other forces do exist, such as a tail wing moment and distributed forces along the fuselage due to the weight of the aircraft and aerodynamic pressure, however due to their relative size they will be neglected here.

In general, the fuselage is divided into three parts: the forward fuselage; the section connected to the wing; and the aft fuselage which includes the horizontal and vertical tail. Examination of the shear force and bending moment diagrams of Figure 4.19 reveal that the nature of the loads differ substantially for each section. Furthermore, it is obvious that the forward fuselage is the least critical, since there are no major flight loads that act on this section. The center section, on the other hand, must withstand major loads due to the connection with the main wing, and subsequently this section is designed to be more robust than the rest of the fuselage so that the increased stress states can be handled efficiently. This leaves the aft section, which obviously undergoes significant bending due to the flight loads, and which will be the critical location for our study. Of course, as mentioned elsewhere the analysis presented in this chapter is only applicable to “short” cylinders with constant cross-section, so that performing an analysis while taking into account the

beam-like nature of the fuselage cannot be accomplished. Instead, we will concentrate on the most critical location of the rear fuselage, which is just aft of the connection to the wing, and apply the corresponding beam forces that exist there to a constant cross-section. In the future, more advanced designs may be investigated by optimizing the fuselage cross-section at various stations along the length of the aircraft, though that will not be attempted in this investigation.

The loading displayed in Figure 4.19 suggests that the major forces acting on the aft fuselage consist of a moment about the horizontal axis and a vertical shear force. These loads are directly related by the length between the wings, denoted by  $l_w$ , and their magnitudes for the design constraints can be found using the approximate analysis referred to earlier (see Niu<sup>87</sup>). Buckling is allowed at 1 g as mentioned in Section 4.5.1. Additionally, the fuselage is assumed to be pressurized and must also satisfy a burst pressure constraint and a backload due to a -1 g dive. Therefore, the relevant load cases for the design of the fuselage are given in Table 4.1:

<b>Case 1 - Burst pressure (material failure only)</b>	
	• 16 psi internal hydrostatic pressure
<b>Case 2 - 1.0 g Pull-up (buckling failure)</b>	
	• 8 psi internal hydrostatic pressure (applied as dead load)
	• 9,000,000 lb-in horizontal moment
	• 15,000 lb vertical shear force
<b>Case 3 - 2.5 g Pull-up (material failure)</b>	
	• 8 psi internal hydrostatic pressure (applied as dead load)
	• 15,000,000 lb-in horizontal moment
	• 25,000 lb vertical shear force
<b>Case 4 - 1.0 g Dive (buckling and material failure)</b>	
	• 8 psi internal hydrostatic pressure (applied as dead load)
	• -9,000,000 lb-in horizontal moment
	• -15,000 lb vertical shear force

**Table 4.1: Load Cases for Fuselage Structure**

For cross-sections that are symmetric about a horizontal plane, Case 4 is not required since it is obviated by the constraints of Cases 2 and 3. The load cases given in Table 4.1 are translated into a nondimensional load constraint through the use of a safety factor, which is given as

$$SF = \frac{\text{Failure Load}}{\text{Design Load}} \quad (4.53)$$

where the failure load is calculated by the analysis and the design loads are given in Table 4.1. The lowest value of  $SF$  considering each load case is considered critical, and for a design to be

feasible the safety factor must be greater than or equal to unity.

#### 4.5.3 Design Strategy for Optimization of Cross-Section

The statement of the problem for the weight minimization of a generic narrow body fuselage cross-section subjected to the loads given in Table 4.1 is as follows:

$$\begin{array}{ll} \text{minimize} & W(\text{eight}) \\ \text{such that} & SF \geq 1 \end{array} \quad (4.54)$$

In addition to the weight minimization, added preference will be given to designs that exhibit greater load-carrying capability. Thus two designs that weigh nearly the same can be differentiated by their failure loads. When composite laminates are used in the design process (so that the stacking sequence is being optimized), it is assumed that laminates are constructed with  $\pm 45^\circ$  plies on the outside of the laminate, for they possess a greater resistance to damage. A penalty is also applied to laminates that are not balanced (though the symmetric laminate condition is fulfilled automatically in the design process).

The basic geometry of the cylinder cross-section and the associated axial stiffeners and tear straps is shown in Figure 4.20. The cylindrical shell is approximated as the segment of the fuse-

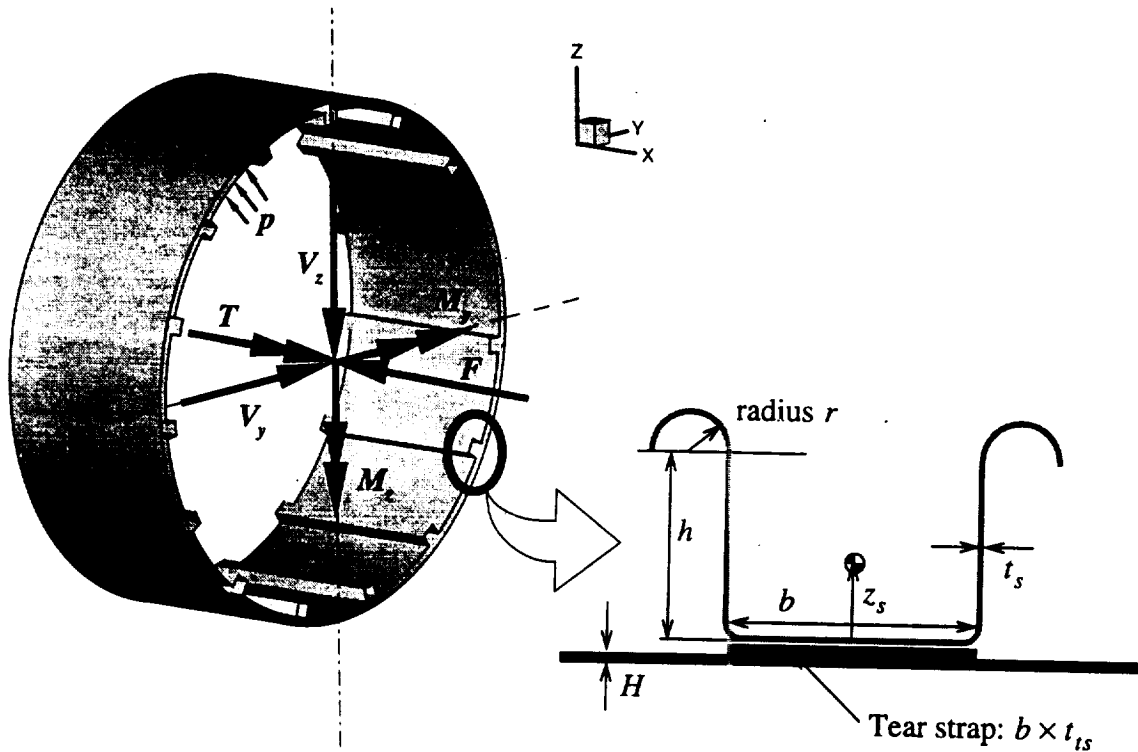


Figure 4.20: Geometry of Cross-section and Stiffener Arrangement for Short Segment

lage structure between successive frames, spaced 20 inches apart. At each stiffener location on the inside of the cylinder, there exists a tear strap which resists crack propagation and is usually the same material as the skin, and an approximate inverted hat stiffener. The thicknesses of the tear strap and stiffener will be given, but otherwise all variables, including the number and location of the stiffeners, are possible design variables. Other relevant information is supplied in Table 4.2:

<b>Fuselage</b>	
	$L = 20'' \quad R = 74''$
<b>Skin</b>	
	<ul style="list-style-type: none"> <li>• Minimum gage thickness <math>H_{min} = 0.036''</math> (Eight plies for laminate)</li> <li>• Isotropic material - Aluminum 2024-T3</li> <li>• Composite material - Graphite-epoxy</li> </ul>
<b>Tear Straps</b>	
	<ul style="list-style-type: none"> <li>• Standard thickness of <math>0.036''</math>, located beneath each stiffener</li> <li>• Isotropic material - Aluminum 2024-T3</li> <li>• Composite material - <math>[\pm 45/0]_s</math> laminate with smeared properties</li> </ul>
<b>Stiffeners</b>	
	<ul style="list-style-type: none"> <li>• Standard thickness of <math>0.027''</math></li> <li>• Minimum values</li> </ul>
	$b_{min} = 1.0'' \quad h_{min} = 0.75'' \quad r_{min} = 0.1''$
	<ul style="list-style-type: none"> <li>• Isotropic material - Aluminum 7075-T6</li> <li>• Composite Material - <math>[\pm 45/0]_s</math> laminate with smeared properties</li> </ul>

**Table 4.2: Details of Components of Cross-section**

The material information is given in Appendix C. Note, however, that the tear strap and the stiffener material as given in Table 4.2 are described as smeared laminates. In this case, the term “smeared” implies that the stiffness and strength properties of the constituent laminate are represented as a “new” orthotropic material with the effective moduli, Poissons ratio, and failure stresses associated with each laminate. Thus a stiffener can be composed of a  $[\pm 45/0]_s$  laminate that is molded into the shape of an inverted hat, and the material failure characteristics conform to the failure of such a laminate that is subjected to axial loads. The calculations for smeared laminates of this type can also be found in Appendix C.

An outline of the optimization strategy for traditional stiffened structures (not utilizing curvilinear fibers) is presented in Table 4.3. The choice of the design variables for each specific optimization case is intended to overlap with the preceding case, in that the optimal solution for the

**I: Isotropic Materials (Aluminum)**

I0. Baseline case with no stiffeners. Only design variable is skin thickness.

**Constant Skin Thickness Arrangement**

- I1. For a given number of equally spaced identical stiffeners, design variables are skin thickness and stiffener dimensions.
- I2. Same as Case I1 except that the number of equally spaced identical stiffeners is also a design variable.
- I3. Equal spacing of stiffeners is not required. However, the dimensions of the stiffeners are chosen using the results of the optimal values from Case I2. From this, a “small” and “large” stiffener are defined. Predetermined locations around the circumference of the cross-section are allowed to contain either one of these stiffener sizes, or none at all. The number of predetermined locations are varied, so that the number of each size stiffener and their locations around the circumference are unknown, as is the skin thickness.

**Crown/side/keel Arrangement**

- I4. Baseline case with no stiffeners. Cross-section is divided into three specific areas, and each can possess a different value of the skin thickness. Design variables include the section thicknesses and the locations of the transition between sections.
- I5. Crown/side/keel arrangement is again used, along with the variable stiffener spacing of Case I3.

**C: Composite Materials with Constant Stiffness Properties (Graphite/Epoxy)**

- For composite materials, Cases C0-C5 are repeated with graphite-epoxy materials used for the structural elements. The major difference that exists is the presence of the laminate stacking sequence as a design variable in place of the skin thickness. This occurs for the crown/side/keel arrangement as well, so that each section may have an independent stacking sequence including the number of plies.

**Table 4.3: Description of Optimization Cases for Traditional Stiffened Structures**

preceding case should always be a possible design for the following scenario. This is done to easily distinguish which design parameters most greatly contribute toward improved performance. Note also that the “0” and “4” cases contain no stiffeners, and are mainly used as a baseline and to determine if the unstiffened configurations are competitive with the stiffened designs. For the variable stiffness solutions using curvilinear fibers, comparisons are completed with respect to these constant stiffness composite designs without stiffeners, since the presence of the stiffeners tends to dominate the response. Further details for the curvilinear fiber designs are provided in Section 4.6.3. All optimization is performed using a genetic algorithm, which easily handles discrete variables such as stacking sequences. Several examples are also provided of the GA coding information, which is explained in the discussion of the optimization techniques in Section A.6.2.



## 4.6 Design Study Results

This section provides the detailed results of the optimization studies, divided into three subsections for the isotropic, composite, and curvilinear fiber cases. Comparisons of the design studies to reduce the total weight of the short cylinder section are summarized in Figure 4.21:

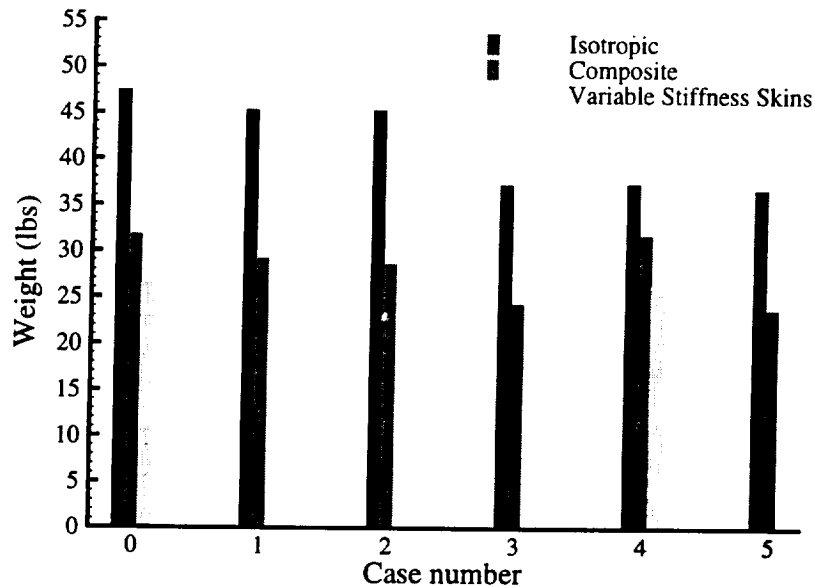


**Figure 4.21: Comparison of Weight Optimization Results for All Cases**

The first noticeable result from this figure is the significant weight reduction attained through the use of composite materials. Though this conclusion is certainly warranted, it should be noted that the improvement is predominantly due to the lower density of the graphite-epoxy composite material when compared to aluminum ( $0.057 \text{ lbs/in}^3$  versus  $0.100 \text{ lbs/in}^3$ ), as opposed to actual savings in material volume. Of course, the superior stiffness-to-weight ratio is the motivating reason for using composites in the first place, but it was found in these studies that the total amount of material required to satisfy the loading constraints was comparable for both material systems.

Another distinguishing aspect of the results of Figure 4.21 is the relative improvement for the traditional stiffened designs starting with Case 3. This is due to the fact that the critical load for almost every design was bifurcation under bending (Load Cases 2 and 4 in Table 4.1). For this loading condition, the optimizer strived to place as much material as possible at the tops and bottom of the cross-section to resist the impending instability. However, the early optimization scenarios insisted on evenly spaced properties around the circumference of the shell, therefore no noticeable improvement was found. Case 3 was the first to allow for arbitrary placement of the stiffeners, which increased the efficiency of the cross-section tremendously. Case 4 utilized the crown/side/keel arrangement, which offered similar improvements by concentrating the material

at the top and bottoms of the cross-section. It should also be noted that the (unstiffened) curvilinear fiber cases shown in the figure competes extremely well with the traditional structures.

The following three sub-sections provide the remaining details of the optimization studies. Besides reporting the weight of the optimal design, the safety factors for each load case and the effective thickness of the cross-section are also reported. The effective thickness is calculated by smearing the total amount of skin and stiffener material around the cross-section, and it provides an gauge of total material used.

#### 4.6.1 Traditional Stiffened Structures (Isotropic)

These results are broken down in terms of the case designation provided in Table 4.3. It is interesting to note the progression of the optimal solutions as additional design variables are introduced into the system.

##### Case I0: Constant thickness skin, no stiffeners

##### Design Variables: $H$

This case is mostly used as a baseline, for a monocoque isotropic shell is rarely used in a fuselage structure due to its high sensitivity to imperfections. The shell thickness is the sole design variable, and is transformed from a continuous variable to a discrete one through the following general equation:

$$\text{Variable} = \text{Minimum Value} + \text{Step Size} \times \sum_{i=1}^{\text{length}} (\text{DNA}_i - 1) \times 3^{(\text{length} - i)} \quad (4.55)$$

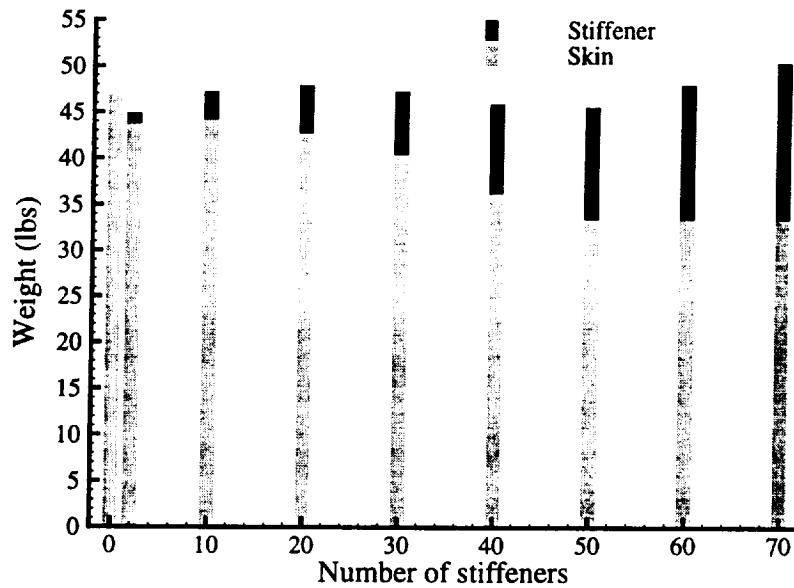
For instance, for the shell thickness variable  $H$  the minimum value (from Table 4.2) is 0.036" and the step size is chosen as 0.005".  $\text{DNA}_i$  is part of the coding of the genetic algorithm, and is allowed to be either 1, 2, or 3. The variable *length* in Eq. (4.55) represents the portion of the genetic string that is dedicated to the design variable. For this variable, the length is 4, so that the first four DNA entries in essence translate into a base-3 integer that determines the final value of the shell thickness. This strategy is used for all continuous variables. The final results are:

$$\begin{array}{lll} H = 0.0505" & SF_1 = 2.1326 & SF_3 = 2.2161 \\ W = 46.961 \text{ lbs} & SF_2 = 0.9994 & SF_4 = 0.9994 \end{array} \quad (4.56)$$

In truth, this case is not ideally suited for a genetic algorithm since the only unknown variable is continuous in nature and the actual number of designs are limited. However, using the GA for this case does provides a check on the accuracy of the genetic algorithm. Traditional root finding methods yield a solution of  $H = 0.050535"$ , which gives evidence to the robustness of the GA.

**Case I1: Constant thickness skin, given number of equally spaced stiffeners****Design Variables:**  $H, b, h, r$ 

The number of equally spaced stiffeners is defined as a constant and then subsequently incremented by ten to cover the whole range of possibilities. The scenario with two stiffeners (one each at the top and bottom) is also included since it represents a distinct jump from the unstiffened case. The design variables for the stiffener dimensions (displayed in Figure 4.20) are converted into discrete variable using Eq. (4.55) with appropriate minimal values and step sizes. The results for this case are displayed in Figure 4.22 in the form of a bar graph which plots the total and sub-

**Figure 4.22: Optimization Results for Case I1**

component weights as a function of number of stiffeners. All designs were critical with respect to Load Case 2 (buckling under bending). One can see that two optima exist: one for the two stiffener case which appears to be the global optima; and another local minimum between forty and fifty stiffeners. In general, the designs with few stiffeners tend to have larger size stringers, while the many stiffener cases have minimum values for the dimensions. This extreme is reached as the number of stiffeners increases past fifty, where both the skin and stiffener dimensions are at their minimum values and no weight improvement is observed.

**Case I2: Constant thickness skin, unknown number of equally spaced stiffeners****Design Variables:**  $H, b, h, r, N_{\text{pairs}}$ 

This next case is designed to find the optimal designs from Case I1, since now the number of pairs of stiffeners (pairs due to the vertical symmetry of the cross-section) is also a variable. Two sub-cases are investigated, which differ by the limits on  $N_{\text{pairs}}$ . The first case is limited to  $0 \leq N_{\text{pairs}} \leq 26$ , which allows for the possibility of no stiffeners, while the second has higher limits

in the range of  $10 \leq N_{\text{pairs}} \leq 36$ . The results are shown in the following figures:

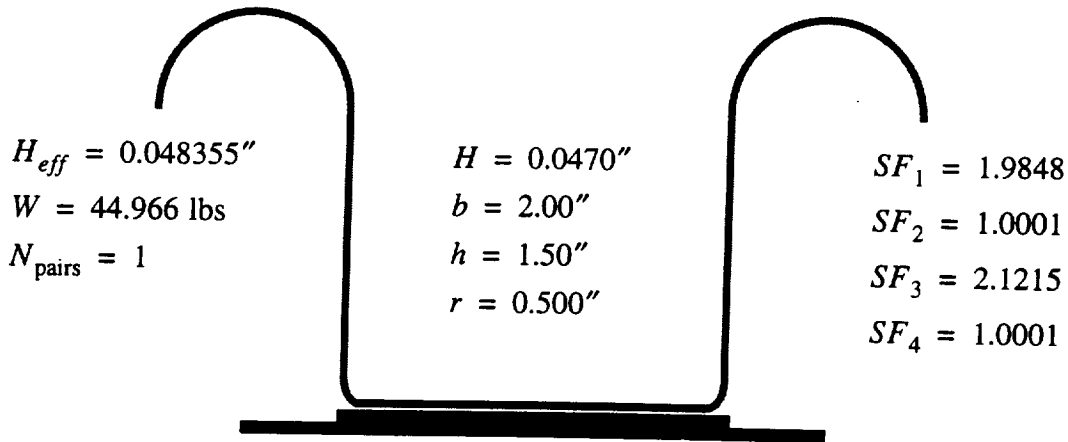


Figure 4.23: Optimization Results for Case I2,  $0 \leq N_{\text{pairs}} \leq 26$

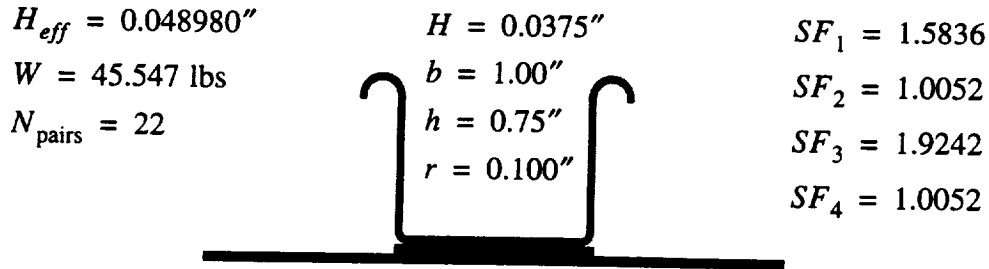


Figure 4.24: Optimization Results for Case I2,  $10 \leq N_{\text{pairs}} \leq 36$

Note that if equally spaced stiffeners are required to produce a cross-section with no directional preference, such as when the direction of the maximum bending moment is not known beforehand, the result shown in Figure 4.24 would be the best choice.

### Case I3: Constant thickness skin, unknown placement of stiffeners

**Design Variables:**  $H$ ,  $loc_{\text{stiff}}$

The optimal sizes found in Case I2 and shown in the preceding two figures are now used as the only stiffener size possibilities. This reduces the number of design variables so as to increase the numerical efficiency of the optimization algorithm. Besides the skin thickness, the only other variable is the placement of the stiffeners. To accomplish the coding of this variable, equally spaced locations are chosen around the circumference of the cross-section, with the possibility for each location to contain either a small or large stiffener (using the geometries of Figure 4.23 and Figure 4.24) or no stiffener at all. This method proved quite successful for discretizing the design space, since each location could be represented by one digit in the genetic algorithm DNA string. Several representative values of possible stiffener locations were investigated, and the optimal

design was found for stiffener locations spaced every  $5^\circ$  around the circumference with only small stiffeners being used. The numerical results and plot of the buckled shape for this design are given in Figure 4.25. As expected, the majority of the stiffeners are located at the top and bottom of the

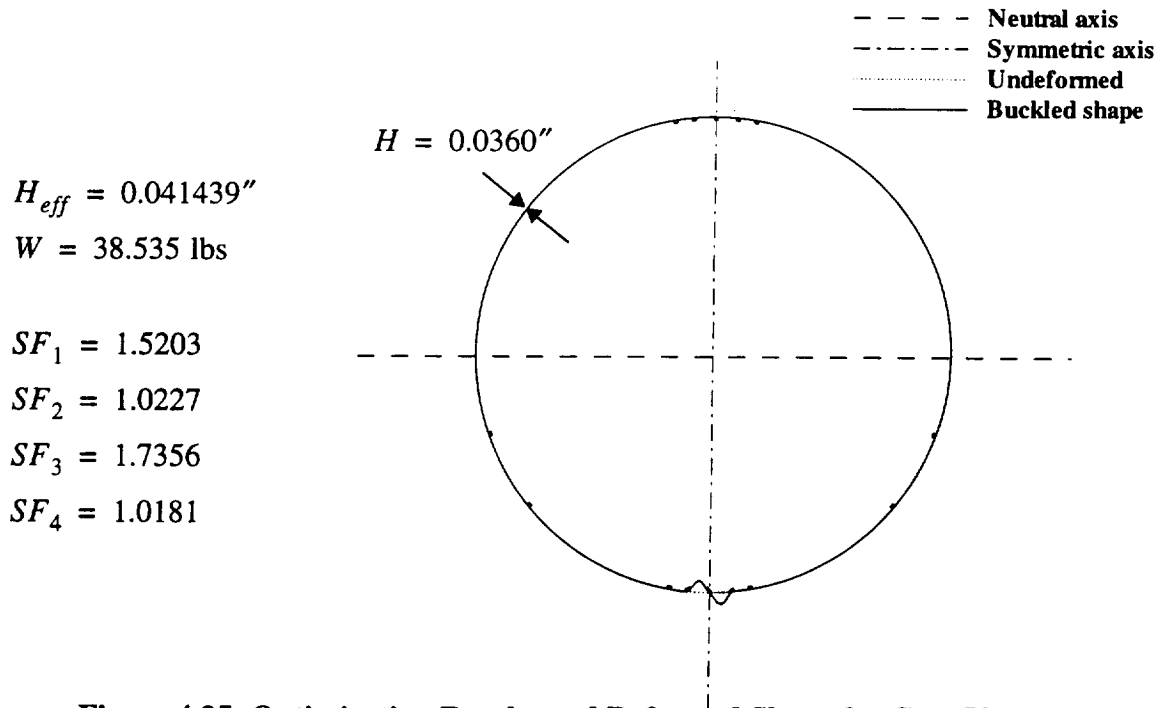


**Figure 4.25: Optimization Results and Deformed Shape for Case I3**

structure, and serve both to increase the bending resistance of the cross-section and also to serve as nodes to increase the circumferential frequency of the critical mode shape. Note also the few isolated stiffeners closer to the sides of the cross-section. Their placement is largely a function of the optimization algorithm, which is excellent at finding optimal designs in a global sense, but often lacks the precision for small details that can improve the design. For example, moving the locations of the remote stiffeners closer to the bottom generates a design with the same weight but slightly improved (less than 1%) failure characteristics.

#### **Case I4: Crown/side/keel arrangement, no stiffeners**

**Design Variables:**  $H_c, \theta_c, H_s, \theta_s, H_k$

Traditional fuselage designs are frequently constructed in four sections, namely the crown, two sides, and the keel. This cross-section design usually works best under beam-type loading, where the crown and keel are designed to withstand the large bending stresses while the sides are flimsier since they need only withstand the less critical shear stresses. Therefore, the next two cases incorporate this idea into the fuselage design study, one without stiffeners and the second with an arbitrary placement of predetermined stiffener sizes (akin to Case I3). The proposed geometry using this crown/side/keel arrangement is shown in Figure 4.26. The design variables

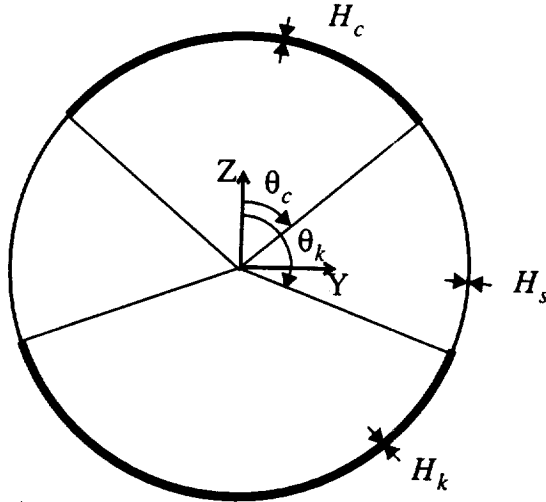


**Figure 4.26: Geometry of Crown/Side/Keel Arrangement**

now include the thickness of each section as well as the transition points between them. The thickness variables possess the same minimum value and step size as usual, while the transition angles are limited to  $25^\circ \leq \theta_c \leq 65^\circ$  and  $115^\circ \leq \theta_k \leq 155^\circ$  with a step size of  $5^\circ$ . The optimal design is:

$$\begin{array}{llll}
 H_{eff} = 0.039819'' & H_c = 0.048'' & \theta_c = 25^\circ & SF_1 = 1.5203 \\
 W = 37.028 \text{ lbs} & H_s = 0.036'' & \theta_k = 155^\circ & SF_2 = 1.0055 \\
 & H_k = 0.0515'' & & SF_3 = 1.8604 \\
 & & & SF_4 = 1.0012
 \end{array} \quad (4.57)$$

Note the asymmetry of the cross-section about the horizontal axis. This implies that this design is not the "true" optimum, since a symmetric design that would satisfy the  $SF_2$  and  $SF_4$  constraints equally would likely generate a slightly lighter and stronger structure. However, the design shown here still compares favorably with the stiffened structure of Case I3.

**Case I5: Crown/side/keel arrangement, unknown placement of stiffeners**

**Design Variables:**  $H_c, \theta_c, H_s, \theta_k, H_k, locstiff$

This last case combines the crown/side/keel arrangement with the arbitrary placement of stiffeners. This is the most general design case for the isotropic material, since all optimal designs found earlier still exist as possibilities within this design space. Again several choices for possible stiffener spacing were used. For sparser designs (those with large stiffener spacing possibilities) both the skin thickness variation and stiffener placement played a role in the optimal designs, however their total weights were still marginally greater than the design with  $5^\circ$  stiffener locations. For this case, all thickness variables attained their minimum values and small stiffeners were employed with similar distributions to those shown in Figure 4.25. Thus no significant improvement was found compared to the optimal design of Case I3.

#### 4.6.2 Traditional Stiffened Structures (Composite)

The relevant details for each case are shown here. Much of the discussion and initial setup for these cases are related to the earlier results for the isotropic study presented in Section 4.6.1, so that the conclusions presented here are quite brief to save space.

##### Case C0: Composite laminate skin, no stiffeners

##### Design Variables: *layup*

For composite laminate design, stacking sequence optimization is performed by representing each lamina as a choice of a  $0^\circ$ ,  $+45^\circ$ ,  $-45^\circ$ ,  $90^\circ$  fiber orientation angle or an empty ply designation. The laminate is assumed to be symmetric about the middle surface, so that only half of the stacking sequence needs to be represented. The genetic algorithm is designed for weight minimization of laminates so that the empty plies are pushed to the outside of the laminate during the optimization process so that empty plies do not occur near the middle surface. A penalty function also exists if the laminate is unbalanced (when the number of  $+45^\circ$  plies does not equal the number of  $-45^\circ$  plies) or if it falls beneath the gage thickness ( $0.036''$  used in this study). Furthermore, a small bonus is awarded to a laminate that contains a group of  $\pm 45^\circ$  plies on the outside of the laminate, for it has been shown that this aids in damage tolerance of the laminate. Again, this first case without stiffeners is used as a baseline, yet it also tests the stacking sequence optimization procedure of the genetic algorithm. The results are:

$$\begin{array}{lll}
 [\pm 45/0/90_3]_S & SF_1 = 1.9802 & SF_3 = 1.1838 \\
 H = 0.060'' & SF_2 = 1.0715 & SF_4 = 1.0715 \\
 W = 31.803 \text{ lbs} & & 
 \end{array} \quad (4.58)$$

Note the skin thickness is actually much larger than the corresponding isotropic design (slightly above  $0.05''$ ). The reason that the composite laminate skin cannot attain this decreased value is that the discrete jumps for stacking sequence optimization are much larger than the step size of the isotropic skin variable ( $0.005''$ ). This is due to incorporating practical construction methods within the stacking sequence designs. Enforcement of balance and symmetry of the laminate implies that each discrete jump in thickness corresponds to at least two plies of material being added, and since the nominal ply thickness is  $0.005''$  this translates into a much larger increase in weight for each variation in thickness. Thus even though stacking sequence designs with ten total plies ( $H = 0.05''$ ) produced a structure with considerable less weight, the inability of these thinner laminates to sufficiently carry the design loads forced the optimal design to contain two more plies and, subsequently, considerable more material. This phenomenon of larger step sizes for composite laminates also appears in the crown/side/keel arrangement for Case C4.

**Case C1: Composite laminate skin, given number of equally spaced stiffeners****Design Variables:** *layup, b, h, r*

The corresponding bar graph for the composite material case is shown below:

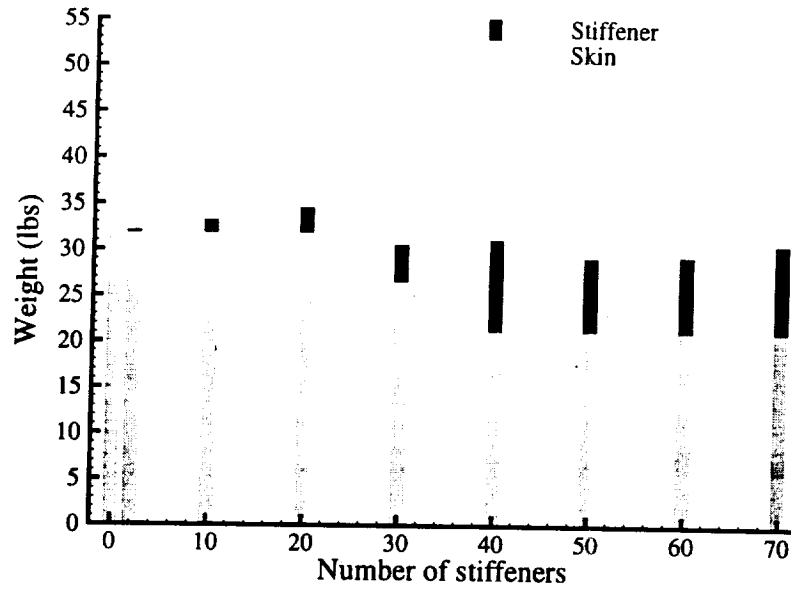


**Figure 4.27: Optimization Results for Case C1**

Most cases were critical with respect to buckling, though the designs with thinner skins often failed first due to the burst pressure constraint (Load Case 1). Note that no relative minimum exists for  $N_{\text{pairs}} = 1$ , mostly due to the fact that the laminate thickness does not decrease. The decrease in the number of plies is also quite evident, revealing that with a sufficient number of stiffeners the minimization of the skin weight is critical. The optimal value for  $N_{\text{pairs}}$  seems to lie between twenty-five and thirty. As the number of stiffeners increases, the dimensions of the stiffeners approach their minimum values as before.

**Case C2: Composite laminate skin, unknown number of equally spaced stiffeners****Design Variables:** *layup, b, h, r,  $N_{\text{pairs}}$* 

This case should isolate the optimal number of stiffeners from Case C1. The numerical results substantiate this claim, yielding as the optimal design:

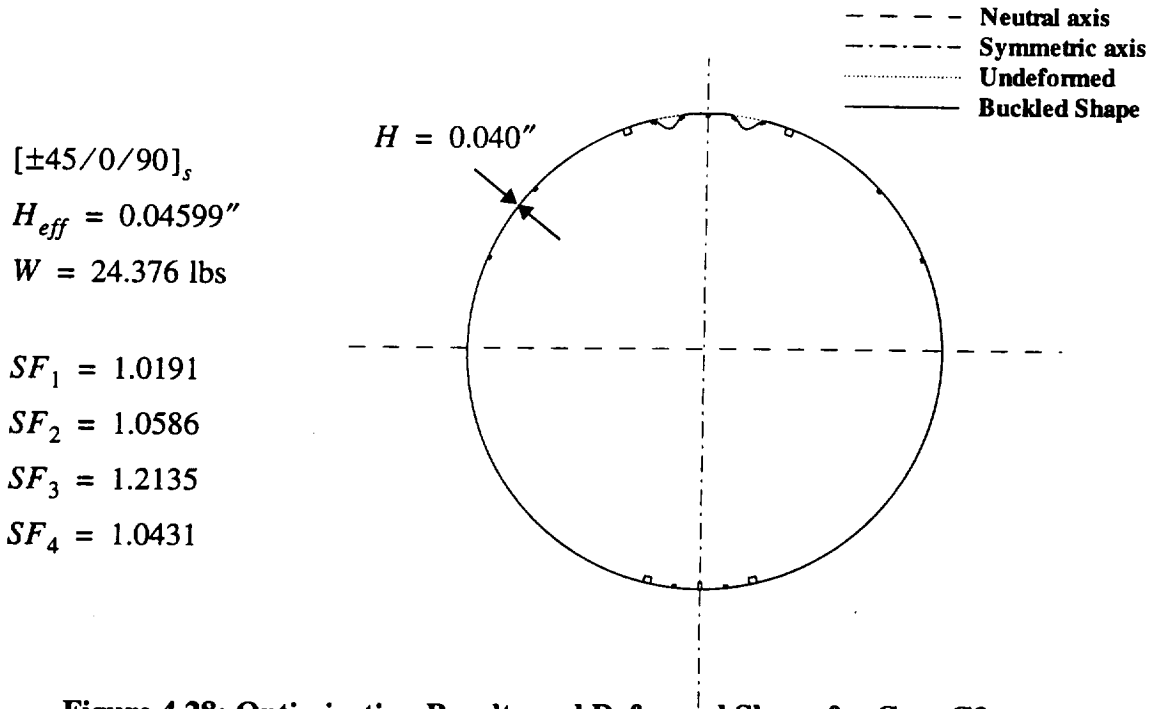
$$\begin{array}{lll}
 [\pm 45/0/90]_S & N_{\text{pairs}} = 27 & SF_1 = 1.0189 \\
 H = 0.04'' & b = 1'' & SF_2 = 1.0034 \\
 H_{\text{eff}} = 0.05399'' & h = 0.75'' & SF_3 = 1.3584 \\
 W = 28.618 \text{ lbs} & r = 0.1'' & SF_4 = 1.0034
 \end{array} \tag{4.59}$$

Note that the small stiffener geometry displayed in Figure 4.24 is also used for this case.



**Case C3: Composite laminate skin, unknown placement of stiffeners****Design Variables:** *layup, locstiff*

Since the last case only revealed one possible size for stiffeners, the alternate “large” size is assumed to be the same as for the isotropic case, shown in Figure 4.23. The optimal design here uses this sturdy stiffener to provide increased bending stiffness, and the smaller stiffeners are employed to alter the shape of the critical buckling mode. The numerical data and deformed shape for the critical buckling case are given in Figure 4.28. The constraint that is most critical here is

**Figure 4.28: Optimization Results and Deformed Shape for Case C3**

for the burst pressure, and depends predominantly on the stacking sequence of the laminate as opposed to the placement of the stiffeners. Again note the extemporaneous stiffeners located near the sides, which do little to improve the response. This indicates that slight improvements to this design likely exist.

**Case C4: Crown/side/keel arrangement, no stiffeners****Design Variables:** *layup, ply<sub>c</sub>, θ<sub>c</sub>, ply<sub>s</sub>, θ<sub>kb</sub>, ply<sub>k</sub>*

For crown/side/keel arrangements (Cases C4 & C5) using a composite material, each fuselage section should ideally possess its own stacking sequence. However, the genetic algorithm that is being used cannot optimize three different stacking sequences at the same time, for it is designed to push all the empty plies to the outside as if it were one laminate. Thus, the difference in each skin section is represented by the variable  $ply_k$  which represents a group of added plies. Each section will possess the same base stacking sequence underneath these plies according to the variable

*layup*. Each *ply* variable is represented by two integers (limited to 1, 2, or 3) in the DNA string and is interpreted in the following manner: the first integer represents the orientation angle of the added ply, much like the stacking sequence. Here, however, a “3” represents a group of two plies ( $\pm 45^\circ$ ) to preserve symmetry and balancing of the laminate. The second digit, when subtracted by one, defines the number of plies added, so that multiple thickness possibilities exist. For example:

$$\begin{array}{ll} 21 \rightarrow 90^\circ, 0 \text{ added plies} & (\text{no thickness increase}) \\ 32 \rightarrow \pm 45^\circ, 1 \text{ added group} & (\text{thickness increase of } 2 \text{ } t_{ply}) \end{array} \quad (4.60)$$

Of course, this method is unable to represent the most general definition of stacking sequences for the crown/side/keel arrangement, which possibly contributed to the poor results for this case. The optimal design for this case did not possess *any* added plies for any of the fuselage sections, and in fact the base stacking sequence was identical to the solution for Case C0. It is believed that the limited possibilities of stacking sequences, due to the inclusion of only  $0^\circ$ ,  $\pm 45^\circ$ , and  $90^\circ$  fiber orientation angles, was the main reason for these results, for it is shown in Section 4.6.3 that this geometry can show remarkable gains if the ply angles are given greater flexibility.

#### Case C4: Crown/side/keel arrangement, unknown placement of stiffeners

**Design Variables:** *layup*,  $ply_c$ ,  $\theta_c$ ,  $ply_s$ ,  $\theta_s$ ,  $ply_k$ ,  $locstiff$

This last case did incorporate the combination of added plies and stiffener placement. The results for the optimal design are shown in Figure 4.29. Note the added plies in the crown of the

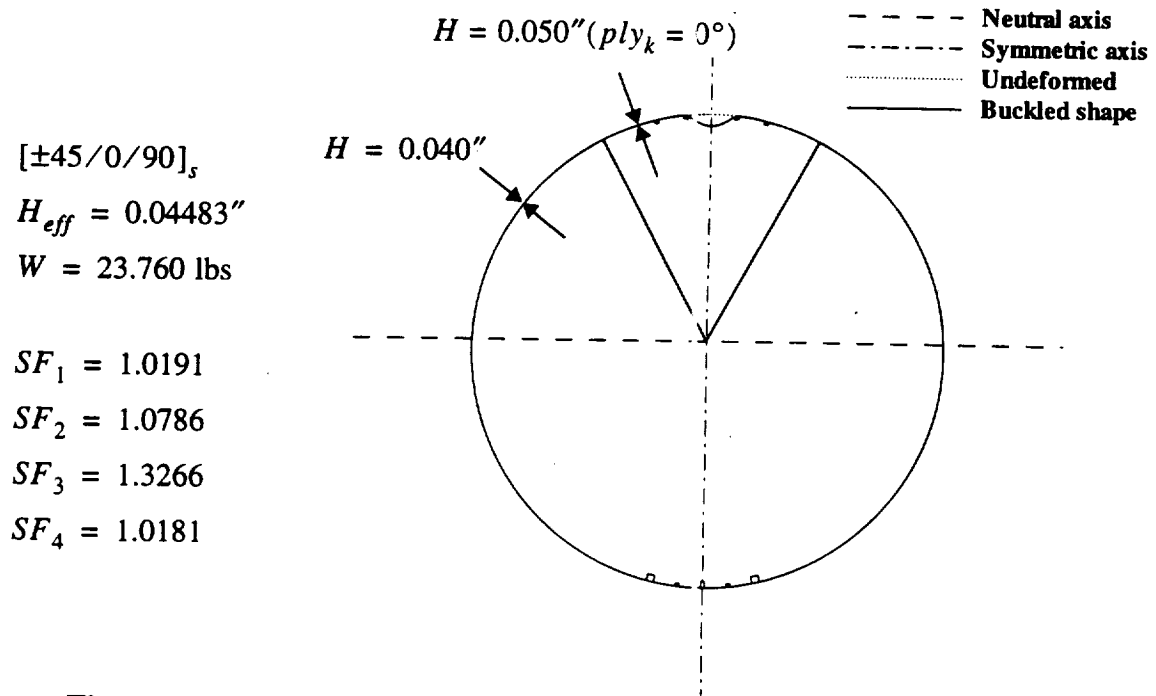


Figure 4.29: Optimization Results and Deformed Shape for Case C5

cross-section. The extra thickness there compensates for the lack of a stiffener in the middle of the symmetric wave of the buckled shape. The weight of this design is lower than any other result, however it is believed that greater improvements than this design exist if greater flexibility in the stacking sequences is available.

#### 4.6.3 Variable Stiffness Skin Designs

The inclusion of curvilinear fibers within the framework of this design problem promises to generate significant improvement over traditional constant stiffness skins. However, the results of the previous design studies have revealed that the major factor for weight minimization is the size and placement of the longitudinal stiffeners, and that for most optimal designs the skin thicknesses gravitate toward their minimum values and thus contribute little to the performance of the structure. Therefore, if stiffeners are included as design variables, they will most likely dominate the response and the flexibility of the variable stiffness skins will never come into play. Thus this section concentrates on unstiffened shells that utilize curvilinear fibers or the crown/side/keel arrangement to see if these designs can compete with the traditional structures. Though the mono-coque shells are somewhat impractical due to their lack of postbuckling strength, these design studies should give a basic indication if the curvilinear fiber format is desirable.

##### Case V0: Curvilinear Fiber Formats

**Design Variables:**  $n$ ,  $T_0$ ,  $locs$

These cases involve the use of curvilinear fibers within the stacking sequence of the laminate. The variables used to define the variation of the fiber angle are  $T_0$  and the change of the fiber orientation angle at equal spaces around the circumference. To make the solution easier to complete, stacking sequence optimization as done in Cases C0-C5 will not be completed. Instead, the results from these cases are used to determine the basic stacking sequence. Therefore, the possibilities for the stacking sequences of variable stiffness plies are limited to

$$[\pm\phi/0/90_n]_s$$

where the value of  $n$  can be 0, 1, or 2. This significantly increases the performance of the GA, since stacking sequence optimization produces a large number of design possibilities.

The path of the curvilinear fiber is defined by a base angle at the top of the cylinder ( $T_0$ ), and changes to the fiber orientation angle at equally spaced locations around the circumference ( $locs$ ). It is formulated this way for one major reason: the manufacturing constraints for the maximum curvature of the fiber path is known. If the fiber orientation angle at each location was allowed to attain whatever value it desired, then, in general, this manufacturing constraint would often be

violated, resulting in the analysis of many designs that are infeasible. However, by defining the stiffness variation in terms of the *change* in the fiber orientation angle, we can automatically satisfy the manufacturing constraint by limiting the size of the change to the acceptable value.

For example, the most basic consideration would use the base angle at the top of the cylinder, and two locations around the circumference (see Figure 4.30). The GA genetic string contains

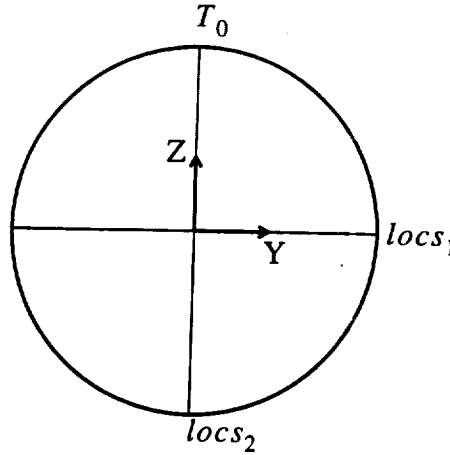


**Figure 4.30: Description of Curvilinear Fiber Definition**

variables that define the base angle  $T_0$  and the linear change of angle at each endpoint  $locs_1$  and  $locs_2$ . The angles at the endpoints thus depend on the magnitude of the preceding value, and are constrained to be either a positive, negative or zero change. The magnitude of the change of the fiber orientation angle is either the maximum allowable due to the curvature constraint or  $15^\circ$ , whichever is smaller. Increasing the number of locations around the circumference should then provide a general solution for the fiber orientation angle variation.

The results for all possibilities of curvilinear fibers produced a laminate with the same stacking sequence and weight, therefore the results are depicted as a percent increase of the load over the constant stiffness case (buckling due to bending was the critical load case constraint for all designs). However, now this constant stiffness case has more opportunities for ply angles (since it is based on  $T_0$  instead of being assumed to be  $45^\circ$ ). The result for a constant stiffness laminate is:

$$[\pm 5/0/90_2]_S \quad H = 0.050'' \quad \text{Critical } SF = 1.0097 \quad W = 26.502 \text{ lbs} \quad (4.61)$$

The rest of the designs are shown as variations of the stiffness (solid lines) and fiber orientation angle (dotted lines) along with their relative increase in load carrying capability in the following table:

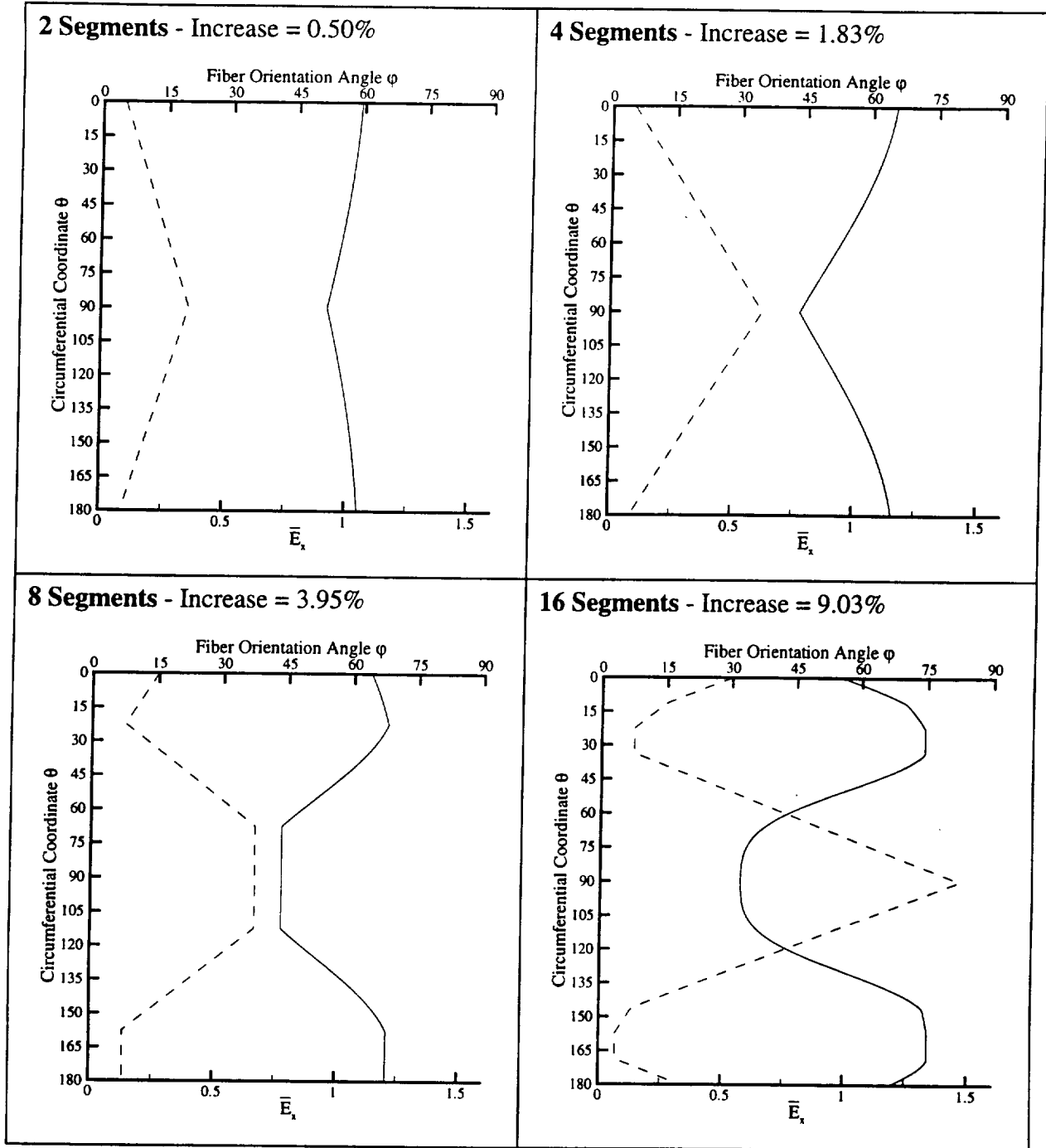


**Table 4.4: Optimization Results for Composite Skin with Curvilinear Fibers**

As one can see, the optimal designs gravitate toward an “I-beam” type structure which possesses large resistance to axial stresses at the top and bottom with shear dominated regions in the middle. The load-carrying capability can be increased even further (over 10%) by using additional links in the curvilinear fiber definition, though the shape is quite similar to the one shown for the 16 link variation. Also note how these designs compare with the traditional stiffened structures as sum-

marized in Figure 4.21. The total weight is certainly competitive, while the 10% increase in the factor of safety demonstrates the worth of this concept for fuselage structures.

#### Case V4: Crown/Side/Keel design

**Design Variables:**  $n$ ,  $T_c$ ,  $\theta_c$ ,  $T_s$ ,  $\theta_k$ ,  $T_k$

This final solution conforms to Case C4 except now the stacking sequence can change in each section due to the greater possibilities for the  $\pm\phi$  ply. Each section possess a base angle that is independent of the other, and the transitions between the sections are again additional unknowns. The results are presented in graphical form in Figure 4.31. Note how the extra flexibility of the

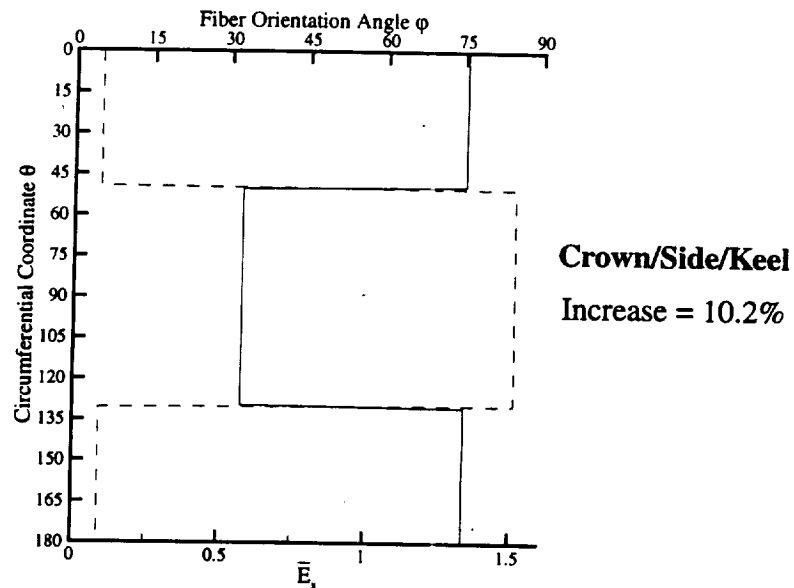


**Figure 4.31: Optimization Results for Variable Stiffness Crown/Side/Keel Arrangement**

stiffness variation generates a design that is greatly superior to the Case C4 result and that the added plies are not even needed. Slight improvements to this design are also possible by allowing the fiber orientation angle to vary within each section.

In summary, this section has demonstrated that the variation of the fiber orientation angle through curvilinear fibers or a crown/side/keel arrangement can produce unstiffened shells that show comparable performance to traditional stiffened structures. Investigation of the postbuckling response of these designs is needed in the future to determine if the designs are able to withstand the total load range as displayed in Figure 4.18, though it is believed that some longitudinal stiffening is required. Thus the combination of axial stiffeners with variable stiffness skins of this type should produce fuselage cross-sections that exhibit minimum weight with possible improvements in load-carrying capability.

## Chapter 5.0 Bending of Infinite Length Cylinders including the Brazier Effect

Attention is now focused on cylinders with a circumferential stiffness variation that are long enough so that the end conditions can effectively be ignored. The analysis of the previous chapter, employing classical membrane constitutive theory and ignoring the bending boundary layer of the shell near the ends, does not apply for longer cylinders due to the limitations of the constitutive theory. As discussed in Section 2.2.3, to accurately reflect the behavior of long cylinders the circumferential bending of the cross-section must also be included, thus this section will use semi-membrane constitutive theory. Furthermore, since we are now dealing with long cylinders, the loads cannot be assumed as constants for the particular axial location under examination, as was done in the previous chapter. Instead, the loads must *be* constant, else the configuration of an infinite length shell does not make sense. Therefore, the presence of transverse shear loads is not allowed, and to make the solution simpler the investigation will only include bending with respect to one plane. The presence of beam bending also introduces the possibility of the Brazier effect, which is an interesting nonlinear phenomena for long tubes under bending that must be included if infinite length cylinders are being considered (see Section 1.2.3 for a discussion of the physical mechanism of the Brazier effect). The governing equations of Chapter 2.0 were formulated with this nonlinearity in mind, so that this section will employ the full nonlinearity of the governing equations to solve the Brazier problem.

Therefore, this chapter begins with the nonlinear static solution of the Brazier problem for infinite length tubes under bending. Auxiliary loads of internal pressure and an axial force are also included, though the main emphasis is on the bending load. Two stability analyses are formulated, one a thorough nonlinear estimation from a perturbation of the prebuckled state, while the second approximate solution is based on a “maximum buckling stress” criterion and is applicable only to constant stiffness structures. Comparisons between these two solutions, as well as to the classic Brazier solution, are also presented, and some basic optimization is performed to determine laminate layups that can best resist this type of nonlinear deformation. The effect of stacking sequence and pressure on the nonlinear behavior is also discussed. Lastly, some basic results using variable stiffness laminates is presented.

## 5.1 Nonlinear Static Solution

An approximate analysis of nonlinear bending of long tubes, which is based on the original linearized solution of Brazier<sup>42</sup>, is often considered suitable for cross-sections that do not have a variation of stiffness around the circumference. However for more complicated structures, circumferential distributions of the bending stresses and stiffness parameters can create complex deformation patterns which cannot be accurately analyzed with the simple mode of deformation assumed by Brazier. Therefore, an accurate variable stiffness solution must fully account for the arbitrary stiffness variation and high nonlinearity. Here it is also assumed that the cylinder is infinitely long, or possesses “greased” end conditions which allow full freedom of the cross-section, so that the specialization of the governing equations can be completed by including the nonlinear terms associated with significant cross-sectional deformation while neglecting any changes in the axial direction. This stipulation implies that the stresses and strains do not change along the length of the cylinder and are only a function of the circumferential coordinate  $\theta$ . Note, however, that some displacements may still be a function of the axial coordinate since the strains depend on the derivatives of the displacements.

The basic geometry of the cross-section, along with the relevant coordinate directions and displacement components, is shown in Figure 5.1. The axial coordinate with its corresponding

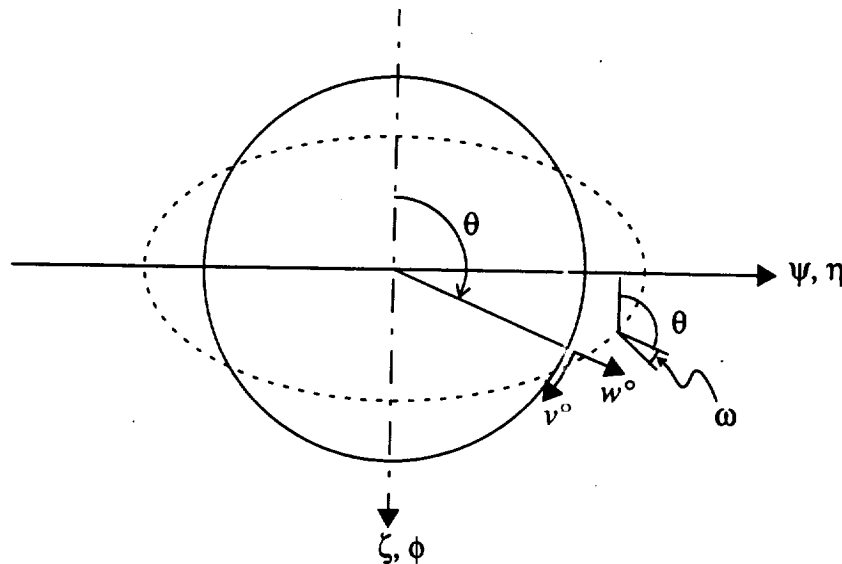


**Figure 5.1: Geometry of Cross-section for Infinite Length Cylinder**

displacement  $u^\circ$  acts in the out-of-the-page direction. The principal displacement variable used in this solution is the inextensional rotation  $\omega$ , which was first introduced in Section 2.1.3. It can be defined in terms of either the cylindrical ( $v^\circ, w^\circ$ ) or rectangular displacements ( $\phi, \psi$ ) whenever the



cross-section is considered to deform inextensionally. In such a state, application of the nonlinear Kirchhoff-Love assumption and the condition of inextensionality to the strain-displacement relations results in the following simplifications to Eq. (2.20):

$$\begin{aligned} \epsilon_x^o &= \frac{\partial u^o}{\partial x} + \kappa_y R (\cos \theta - \phi - \cos \theta_{ref}) & \epsilon_\theta^o &= 0 & \gamma_{x\theta}^o &= \frac{1}{R} \frac{\partial u^o}{\partial \theta} + \frac{\partial v^o}{\partial x} \\ \omega_\theta^o &= \sin \omega & \kappa_x^o &= \kappa_y \cos \theta & \kappa_\theta^o &= \frac{1}{R} \frac{d\omega}{d\theta} & \kappa_{x\theta}^o &= 0 \end{aligned} \quad (5.1)$$

Note that the rectangular displacement  $\phi$ , which is a function of  $\omega$  through Eq. (2.35), is used for the axial strain instead of the usual cylindrical displacements. Further simplification of Eq. (5.1) is possible since these strain quantities are assumed to be only a function of  $\theta$ . In particular, the axial and circumferential displacements can be decomposed into two portions, only one of which depends on the axial coordinate. The dependencies on  $x$  must be linear so that the axial and shear strains remain functions of  $\theta$ , so that these two displacements are written as

$$u^o(x, \theta) = \frac{\bar{U}}{L} \left( \frac{L}{2} - x \right) + u_w(\theta) \quad v^o(x, \theta) = \frac{\bar{V}}{L} \left( \frac{L}{2} - x \right) + v_w(\theta) \quad (5.2)$$

These expressions correspond roughly to the decompositions involving the *average* cross-sectional displacements used in the membrane solution, much like Eq. (4.7) and (4.28). The decompositions contain a “global” portion representing the axial displacement and circumferential rotation of the total cross-section, along with a local “warping” function. Here the warping functions are only a function of  $\theta$ . It can also be shown that the effect of the  $v_w$  function is wholly contained in the circumferential rotation  $\omega$ . Thus the strain-displacement relations are rewritten as

$$\begin{aligned} \epsilon_x^o &= -\frac{\bar{U}}{L} + \kappa_y R (\cos \theta - \phi - \cos \theta_{ref}) & \epsilon_\theta^o &= 0 & \gamma_{x\theta}^o &= \frac{1}{R} \frac{du_w}{d\theta} - \frac{\bar{V}}{L} \\ \omega_\theta^o &= \sin \omega & \kappa_x^o &= \kappa_y \cos \theta & \kappa_\theta^o &= \frac{1}{R} \frac{d\omega}{d\theta} & \kappa_{x\theta}^o &= 0 \end{aligned} \quad (5.3)$$

Only five unknown displacement parameters now exist: the axial displacement  $\bar{U}$ , which represents a constant axial strain; the beam curvature  $\kappa_y$ ; a warping function  $u_w$  and a cross-sectional rotation  $\bar{V}$ , which make up the shear strain; and the circumferential rotation  $\omega$ . For this study, the axial displacement and circumferential rotation of the cross-section are used to introduce the axial force and torsional loads on the cylinder, so that they can be considered known constants.

For the static solution, the constitutive laws are based on semi-membrane theory, discussed in Section 2.2.3. This constitutive model is ideally suited for this problem since neglecting the axial

boundary conditions effectively negates the possibility of shell bending in the axial direction, which is a basic tenet of semi-membrane theory.

$$N_x = E_x H \epsilon_x^o \quad N_{x\theta} = G_{x\theta} H \gamma_{x\theta}^o \quad M_\theta = D_{22} \kappa_\theta^o \quad (5.4)$$

These constitutive equations relate the unknown displacement variables to corresponding stress measures. The stiffness parameters  $E_x$ ,  $G_{x\theta}$ , and  $D_{22}$  are a function of  $\theta$  and are symmetric about the vertical line  $\psi = 0$ .

The shell equilibrium equations, Eq. (2.87)-(2.92), are simplified through the use of semi-membrane theory and the assumptions for an infinite length cylinder (which assume that all quantities are only a function of  $\theta$ ), and after much manipulation are written as

$$\begin{aligned} \frac{1}{R} \frac{dN_{x\theta}}{d\theta} &= 0 & Q_\theta &= \frac{1}{R} \frac{dM_\theta}{d\theta} \\ \frac{1}{R} \frac{dN_\theta}{d\theta} + \frac{Q_\theta}{R} \left(1 + \frac{d\omega}{d\theta}\right) + \frac{1}{R} \frac{d}{d\theta} \left[ \frac{M_\theta}{R} \left(1 + \frac{d\omega}{d\theta}\right) \right] + N_x \kappa_y \sin(\theta + \omega) &= 0 \\ -\frac{N_\theta}{R} \left(1 + \frac{d\omega}{d\theta}\right) + \frac{1}{R} \frac{dQ_\theta}{d\theta} - \frac{M_\theta}{R^2} \left(1 + \frac{d\omega}{d\theta}\right)^2 + p - N_x \kappa_y \cos(\theta + \omega) &= 0 \end{aligned} \quad (5.5)$$

Since no constitutive law exists for the stress resultants  $N_\theta$  and  $Q_\theta$ , they are regarded as merely intermediate variables and can be eliminated from the equations. Thus the second, third, and fourth equations in Eq. (5.5) can be combined into one equation (the dot over  $\omega$  denotes  $d/d\theta$ ):

$$\frac{d}{d\theta} \left[ \frac{\frac{d^2}{d\theta^2} \left( \frac{M_\theta}{R^2} \right)}{(1 + \dot{\omega})} \right] + (1 + \dot{\omega}) \frac{d}{d\theta} \left( \frac{M_\theta}{R^2} \right) + \frac{d}{d\theta} \left( \frac{p}{1 + \dot{\omega}} \right) = \kappa_y \left( \frac{d}{d\theta} \left[ \frac{N_x \cos(\theta + \omega)}{(1 + \dot{\omega})} \right] - N_x \sin(\theta + \omega) \right) \quad (5.6)$$

The third and final equilibrium equation is supplied by the beam equation, Eq. (2.93):

$$\frac{d^2}{dx^2} [M_y(x)] = 0 \quad \Rightarrow \quad \bar{M}_y = \oint N_x(\theta) (\cos \theta - \phi - \cos \theta_{ref}) R^2 d\theta \quad (5.7)$$

where the integration in the axial direction has been performed to find the correct equation for the constant bending moment applied to the cross-section about the horizontal axis.

The combination of the strain-displacement relations, constitutive laws, and equilibrium equations for the infinite length cylinder with a circumferential stiffness variation form a system of three ordinary differential equations for the unknown displacement parameters  $u_w$ ,  $\kappa_y$ , and  $\omega$ . However, the equation for the warping function  $u_w$  is decoupled from the other two, and the rele-

vant equations concerning this mode of shear deformation are

$$\gamma_{x\theta}^o = \frac{1}{R} \frac{du_w}{d\theta} - \frac{\bar{V}}{L} \quad N_{x\theta} = G_{x\theta} H \gamma_{x\theta}^o \quad \frac{1}{R} \frac{dN_{x\theta}}{d\theta} = 0 \quad -\bar{T} = \oint N_{x\theta}(\theta) R^2 d\theta \quad (5.8)$$

The solution of this sub-system closely follows that of Eq. (4.28) and (4.29) for the linear membrane solution, and can be solved analytically for all quantities through integration and enforcement of the periodicity condition for  $u_w(\theta)$ :

$$\begin{aligned} N_{x\theta}(\theta) &= \frac{-\bar{T}}{2\pi R^2} & u_w(\theta) &= \frac{-\bar{T}}{2\pi R H} \left[ \int_0^\theta \frac{d\theta}{G_{x\theta}(\theta)} - \frac{\theta}{2\pi} \oint \frac{d\theta}{G_{x\theta}(\theta)} \right] \\ \frac{\bar{V}}{R} &= \frac{\bar{T} L}{(GJ)} & (GJ) &= \frac{2\pi H R^3}{\frac{1}{2\pi} \oint d\theta / G_{x\theta}(\theta)} \end{aligned} \quad (5.9)$$

Notice that this definition of the torsional constant  $(GJ)$  is slightly different than before and actually more accurate for variable stiffness structures. Furthermore, the solutions in Eq. (5.9) provide an estimate of the axial warping that occurs for variable stiffness structures under torsion. Note that for a constant stiffness variation the integrals within the brackets cancel out so that the axial warping due to torsion is zero, as expected. The relevant coupling of this torsional deformation to a long cylinder under bending is only apparent when buckling is considered. For this study, this effect will not be investigated, therefore the results for torsion of a cylinder with a circumferential stiffness variation are limited to the buckling problem using a linear membrane prebuckling solution, which was presented in Chapter 4.0.

Accordingly, let us return to the main problem at hand, which involves pure bending of a long tube with auxiliary loads of pressure and axial compression. Normalization of the coupled equations governing the bending response is completed using the classical buckling parameters introduced in Section 1.2.2. Some baseline stiffness quantities are defined first. These include a typical average quantity that is related to the skin only and a global quantity that represents the axial stiffness of the variable stiffness structure:

$$\hat{E}_x = \frac{1}{2\pi} \oint E_x^{skin}(\theta) d\theta \quad \bar{E}_x = E_x / \hat{E}_x \quad (EA) = \oint E_x(\theta) H R d\theta \quad (5.10)$$

The axial and circumferential stress resultants are normalized with respect to their classical buckling values for infinite length cylinders from Eq. (1.4) and Eq. (1.6), respectively.

$$\bar{n}_x(\theta) = \frac{N_x(\theta)}{(-\hat{N}_x^{cl})} = \frac{N_x(\theta) R}{2\sqrt{\hat{D}_{11}} \hat{E}_\theta H} \quad \bar{n}_\theta(\theta) = \frac{N_\theta(\theta)}{(-\hat{N}_\theta^\infty)} = \frac{N_\theta(\theta) R^2}{3\hat{D}_{22}} \quad (5.11)$$

The stipulation that the bending load does not produce a resultant axial force on the cross-section, as discussed in Section 4.1.1, results in the expression of the reference angle that designates the neutral surface of a cylinder under pure bending. Also included here is another global stiffness quantity which represents the bending stiffness of the structure about the neutral axis.

$$\cos \theta_{ref} = \frac{\oint \bar{E}_x (\cos \theta - \phi) d\theta}{\oint \bar{E}_x d\theta} \quad \bar{I}_y = \frac{1}{\pi} \oint \bar{E}_x (\theta) (\cos \theta - \cos \theta_{ref})^2 d\theta \quad (5.12)$$

Analogous nondimensionalization in terms of the classical buckling values for the beam curvature, bending moment, internal pressure, end shortening, and resultant axial force are:

$$\begin{aligned} \bar{\alpha} &= \frac{\hat{E}_x H R \kappa_y}{(-\hat{N}_x^{cl})} & \bar{m}_y &= \frac{\bar{M}_y}{\pi R^2 \bar{I}_y (-\hat{N}_x^{cl})} & \bar{p} &= \frac{p R}{(-\hat{N}_\theta^\infty)} \\ \bar{u} &= \frac{\hat{E}_x H \bar{U}}{L (-\hat{N}_x^{cl})} & \bar{f} &= \frac{\hat{E}_x H \bar{F}}{(EA) (-\hat{N}_x^{cl})} \end{aligned} \quad (5.13)$$

Normalization in this manner renders the nondimensional end displacement  $\bar{u}$  and axial force  $\bar{f}$  equivalent. Thus the axial loading will be introduced through the normalized force  $\bar{f}$ , since this choice enables the designation of hydrostatic loading easier.

Insertion of these normalized variables into the governing equations leads to the definition of a nondimensional parameter  $\chi$  in terms of four laminate stiffness quantities:

$$\chi = \sqrt{\frac{\hat{D}_{11} \hat{E}_\theta}{\hat{D}_{22} \hat{E}_x}} \quad (5.14)$$

This symbol is termed the collapse parameter and is a function of the laminate stacking sequence. The complete nonlinear system consists of a differential equation for the circumferential rotation and an integral relation that represents the beam behavior of the cylinder. They are expressed in nondimensional form as (a dot and  $d_\theta$  represent  $d/d\theta$ )

$$\begin{aligned} d_\theta \left[ \frac{d_\theta^2 (\bar{D}_{22} \dot{\omega})}{(1 + \dot{\omega})} \right] + (1 + \dot{\omega}) d_\theta (\bar{D}_{22} \dot{\omega}) - \frac{3 \bar{p} \dot{\omega}}{(1 + \dot{\omega})^2} = \\ 4 \chi^2 \bar{\alpha} \left\{ d_\theta \left[ \frac{\bar{n}_x(\theta) \cos(\theta + \omega)}{1 + \dot{\omega}} \right] - \bar{n}_x(\theta) \sin(\theta + \omega) \right\} \end{aligned} \quad (5.15)$$

$$\bar{m}_y = \frac{\bar{\alpha}}{\pi \bar{I}_y} \oint \bar{E}_x (\theta) (\cos \theta - \phi - \cos \theta_{ref})^2 d\theta$$

The supplementary equations for the static solution are:

$$\begin{aligned}
 \bar{n}_x(\theta) &= \bar{E}_x(\theta) [\bar{\alpha}(\cos \theta - \phi - \cos \theta_{ref}) - \bar{f}] & \phi(\theta) &= \int_{\theta_{ref}}^{\theta} [\sin(\theta + \omega) - \sin \theta] d\theta \\
 \bar{n}_\theta(\theta) &= \frac{d^2_6(\bar{D}_{22}\dot{\omega})}{3(1 + \dot{\omega})} - \frac{\bar{D}_{22}\dot{\omega}}{3}(1 + \dot{\omega}) + \frac{\bar{p}}{(1 + \dot{\omega})} - \frac{4\chi^2}{3(1 + \dot{\omega})} \bar{\alpha} \bar{n}_x(\theta) \cos(\theta + \omega) \\
 \cos \theta_{ref} &= \frac{\oint \bar{E}_x(\cos \theta - \phi) d\theta}{\oint \bar{E}_x d\theta} & \bar{I}_y &= \frac{1}{\pi} \oint \bar{E}_x(\theta) (\cos \theta - \cos \theta_{ref})^2 d\theta
 \end{aligned} \tag{5.16}$$

The boundary conditions for  $\omega$  in the circumferential direction represent the line of symmetry at  $\theta = 0$  and  $\theta = \pi$ , which demands that the rotation and the shear force resultant  $Q_\theta$  are zero there.

$$\omega(0) = 0 \quad \dot{\omega}(0) = 0 \quad \omega(\pi) = 0 \quad \dot{\omega}(\pi) = 0 \tag{5.17}$$

The finite difference technique is used along with Newton's method to solve the nonlinear ordinary differential equation in terms of  $\omega$  for a given value of the normalized curvature  $\bar{\alpha}$ . Then the remaining expressions in Eq. (5.16) can be evaluated.

## 5.2 Stability Estimate with Nonlinear Prebuckling including the Brazier Effect

As mentioned in the discussion of the Brazier effect in Section 1.2.3, the solution of the preceding system results in a nonlinear moment-curvature relation which attains a limit moment due to the deformation of the cross-section. Often it is believed that this highest point on the nonlinear load path corresponds to the collapse moment for long tubes under bending. Once the maximum bending moment is surpassed, the structure has no ability to withstand the load and catastrophic failure occurs. Though this is theoretically true for *some* structures, ones in which the Brazier effect is very pronounced, most realistic tubes collapse before the limit moment is reached due to the formation of a "kink", which represents a postbuckled state. The mechanism which produces this kink is actually local buckling on the compressive side of the tube. The Brazier effect still plays a significant role in this failure mode, for the development of the kink depends substantially on the local curvature of the cross-section. To accurately determine when this local buckling occurs, a stability analysis similar to the one presented in Section 4.2 for the short cylinder case must be performed. However, the formulation of the eigenvalue problem must now consider the prebuckling deformation due to the Brazier effect, so that the numerical eigensolution must use the general nonlinear technique as opposed to the straightforward linear stability estimation.

The strain-displacement equations for the perturbed state, as defined in Eq. (2.108), are simplified with respect to two assumptions about the prebuckling deformation: inextensionality of the

cross-section and no variation in the axial direction. This reduces the relations to:

$$\begin{aligned}
 \epsilon_{x_1}^o &= \frac{\partial u_1}{\partial x} + \kappa_y(w_1 \cos \theta - v_1 \sin \theta) & \epsilon_{\theta_1}^o &= \cos \omega \left( \frac{1}{R} \frac{\partial v_1}{\partial \theta} + \frac{w_1}{R} \right) + \sin \omega \left( \frac{v_1}{R} - \frac{1}{R} \frac{\partial w_1}{\partial \theta} \right) \\
 \gamma_{x\theta_1}^o &= \frac{1}{R} \frac{\partial u_1}{\partial \theta} + \frac{\partial v_1}{\partial x} + \sin \omega \left( \frac{\partial w_1}{\partial x} \right) & \kappa_{x_1}^o &= \frac{\partial^2 w_1}{\partial x^2} & \kappa_{x\theta_1}^o &= \frac{1}{R} \left( \frac{\partial v_1}{\partial x} - 2 \frac{\partial^2 w_1}{\partial x \partial \theta} \right) \\
 \kappa_{\theta_1}^o &= \cos \omega \left( \frac{1}{R^2} \frac{\partial v_1}{\partial \theta} - \frac{1}{R^2} \frac{\partial^2 w_1}{\partial \theta^2} \right) + \frac{\cos \omega}{R} (1 + \omega) \left( \frac{1}{R} \frac{\partial v_1}{\partial \theta} + \frac{w_1}{R} \right) + \frac{\sin \omega}{R} (2 + \omega) \left( \frac{v_1}{R} - \frac{1}{R} \frac{\partial w_1}{\partial \theta} \right)
 \end{aligned} \quad (5.18)$$

The governing equations for the stability estimation are derived by inserting these expressions into the second variation of the total potential energy, Eq. (2.109). Application of the calculus of variations to the resulting integral for the three perturbed displacements generates the required system of partial differential equations. Thus the analogue to Eq. (2.110)-(2.112) for an infinite length cylinder under bending are written as:

Axial direction:

$$\frac{\partial}{\partial x} [N_{x_1}] + \frac{1}{R} \frac{\partial}{\partial \theta} [N_{x\theta_1}] = 0 \quad (5.19)$$

Circumferential direction:

$$\begin{aligned}
 &\frac{\partial}{\partial x} \left[ N_{x\theta_1} + \frac{M_{x\theta_1}}{R} \right] + \frac{1}{R} \frac{\partial}{\partial \theta} \left( \cos \omega \left[ N_{\theta_1} + (2 + \omega) \frac{M_{\theta_1}}{R} \right] \right) - \frac{\sin \omega}{R} \left[ N_{\theta_1} + (2 + \omega) \frac{M_{\theta_1}}{R} \right] + \\
 &\quad \kappa_y \sin \theta N_{x_1} + \frac{N_{x\theta_0}}{R} \left( \frac{\partial w_1}{\partial x} \right) + \left( p - \frac{N_{\theta_0}}{R} - \frac{M_{\theta_0}}{R^2} \right) \left( \frac{v_1}{R} - \frac{1}{R} \frac{\partial w_1}{\partial \theta} \right) + \\
 &\quad \frac{N_{\theta_0}}{R} \left( \frac{1}{R} \frac{\partial v_1}{\partial \theta} + \frac{w_1}{R} \right) + \frac{M_{\theta_0}}{R^2} \left( \frac{2}{R} \frac{\partial v_1}{\partial \theta} + \frac{w_1}{R} - \frac{1}{R} \frac{\partial^2 w_1}{\partial \theta^2} \right) = 0
 \end{aligned} \quad (5.20)$$

Radial direction:

$$\begin{aligned}
 &\frac{\partial^2}{\partial x^2} [M_{x_1}] + \frac{2}{R} \frac{\partial^2}{\partial x \partial \theta} [M_{x\theta_1}] + \frac{1}{R^2} \frac{\partial^2}{\partial \theta^2} \left[ \cos \omega M_{\theta_1} + \frac{M_{\theta_0}}{R^2} \left( \frac{1}{R} \frac{\partial v_1}{\partial \theta} + \frac{w_1}{R} \right) \right] - \sin \omega \frac{\partial N_{x\theta_1}}{\partial x} - \\
 &\quad \frac{1}{R} \frac{\partial}{\partial \theta} \left( \frac{\sin \omega}{R} \left[ N_{\theta_1} + (2 + \omega) \frac{M_{\theta_1}}{R} \right] \right) - \frac{\cos \omega}{R} \left[ N_{\theta_1} + (1 + \omega) \frac{M_{\theta_1}}{R} \right] + \\
 &\quad \left( p - \frac{N_{\theta_0}}{R} \right) \left( \frac{1}{R} \frac{\partial v_1}{\partial \theta} + \frac{w_1}{R} \right) - \frac{M_{\theta_0}}{R^2} \left( \frac{1}{R} \frac{\partial v_1}{\partial \theta} - \frac{1}{R} \frac{\partial^2 w_1}{\partial \theta^2} \right) - \frac{1}{R} \frac{\partial}{\partial \theta} \left[ \left( \frac{N_{\theta_0}}{R} + \frac{2M_{\theta_0}}{R^2} \right) \left( \frac{v_1}{R} - \frac{1}{R} \frac{\partial w_1}{\partial \theta} \right) \right] \\
 &\quad - \kappa_y \sin \theta N_{x_1} - N_{x_0} [\kappa_{x_1}] - N_{x\theta_0} [\kappa_{x\theta_1}] = 0
 \end{aligned} \quad (5.21)$$

The stiffness terms and “0” subscripted quantities are strictly a function of  $\theta$ , and the nonlinearity of the prebuckling solution is introduced through the semi-membrane stress resultants as well as the circumferential rotation  $\omega$  and the beam curvature  $\kappa_x$ .

To reduce the complexity of the stability solution, the perturbed displacements are assumed to vary sinusoidally in the axial direction with wavelength  $\beta$ .

$$\begin{aligned} u_1(x, \theta) &= -U_I(\theta) \cos\left(\frac{\beta x}{R}\right) + U_{II}(\theta) \sin\left(\frac{\beta x}{R}\right) \\ v_1(x, \theta) &= V_I(\theta) \sin\left(\frac{\beta x}{R}\right) + V_{II}(\theta) \cos\left(\frac{\beta x}{R}\right) \\ w_1(x, \theta) &= W_I(\theta) \sin\left(\frac{\beta x}{R}\right) + W_{II}(\theta) \cos\left(\frac{\beta x}{R}\right) \end{aligned} \quad (5.22)$$

Since the cylinder is assumed to be infinitely long, the parameter  $\beta$  has no minimum constraints dependent on the length of the cylinder, and thus  $\beta$  must be chosen so that the resulting eigenvalue is a minimum. Two modes are also considered sufficient instead of four, since no anti-symmetric loading occurs for this specialized case. Thus any arbitrary mode shape can be defined through the framework of Eq. (5.22), with the appropriate circumferential boundary conditions applied for each function. These boundary conditions are chosen so that mode *I* represents a symmetric mode about the vertical ( $\psi = 0$ ), while mode *II* is anti-symmetric about this line.

Insertion of this assumed form for the displacements into the stability equations generates a system of linear ordinary differential equations with variable coefficients, which is denoted as

$$\left( \begin{bmatrix} K_s & C \\ C^T & K_a \end{bmatrix} + \begin{bmatrix} N_s & S \\ S^T & N_a \end{bmatrix} \right) \begin{bmatrix} I \\ II \end{bmatrix} = 0 \quad (5.23)$$

The 3×3 sub-matrices are similar to the ones given in Eq. (4.46) for the short cylinder case, except that the sub-matrices for the stiffness terms ( $K_s$ ,  $K_a$ , and  $C$ ) now contain numerous nonlinear prebuckling quantities. Also note that for this chapter, torsion will not be included so that the sub-matrix  $S$  is identically zero. The mathematical expressions for the rest of the sub-matrices are supplied in Appendix B.3.

To find the eigenvalue, a perturbation from the equilibrium solution must be performed, akin to the stability estimate for the nonlinear axisymmetric problem in Section 3.2. The geometric stiffness matrix for the eigenvalue problem is formulated in terms of the derivative with respect to the load level of the total matrix given in Eq. (5.23). However, these derivatives of the terms in the

sub-matrices cannot be found analytically, since the nonlinear equilibrium solution is highly complex. Therefore, the geometric stiffness matrix is calculated through a finite difference approximation by finding the equilibrium state at closely spaced load levels. In essence, this technique produces an eigenvalue which represents the required increase in load level that produces instability. Therefore, along the nonlinear load path, a point exists for which the resulting eigenvalue is zero, and this corresponds to the buckling load of the structure.

### 5.3 Approximate Analyses for Infinite Length Cylinders

The preceding nonlinear static equilibrium solution and the eigenvalue problem for the stability estimation of an infinite length cylinder are both highly complex systems of equations that do not lend themselves to efficient solution techniques, so much so that a numerical solution is required for an accurate result. However, if the shell does not contain a circumferential stiffness variation, then history has shown that some approximations to both the equilibrium and stability solutions do exist. Therefore, this section relates the essence of simplifications that are employed to formulate these approximate analyses. Slight modifications are also introduced which attempt to incorporate some aspects of the variable stiffness effect into the stability estimate so that the numerical solutions can avoid the lengthy nonlinear eigenvalue problem. Comparisons of these approximate analyses to the full solutions are presented in the next section.

#### 5.3.1 Linearized Brazier Solution for Constant Stiffness Structures

The first approximate solution transforms the highly complex equations for the equilibrium state into simple expressions that define the cross-sectional deformation and nonlinear load-displacement relation. The simplification is based on the original solution of Brazier<sup>42,43</sup>. The formulation begins by assuming that the stiffness parameters do not change around the circumference (i.e. a constant stiffness cylinder). Though a variable stiffness solution could be formulated using these same techniques, it was found that the extra effort required to include the complete details of a general stiffness variation increased the complexity of the approximate solution enough so that its efficiency was no longer that significant when compared to the full nonlinear solution. Therefore the Brazier simplification for the equilibrium equations is confined to constant stiffness structures. The governing equation for  $\omega$  with the normalized stiffness parameters equal to unity is then simplified to:

$$d_{\theta} \left[ \frac{\ddot{\omega}}{(1 + \dot{\omega})} \right] + (1 + \dot{\omega})\ddot{\omega} - \frac{3\bar{p}\ddot{\omega}}{(1 + \dot{\omega})^2} = 4\chi^2\bar{\alpha} \left( d_{\theta} \left[ \frac{\bar{n}_x \cos(\theta + \omega)}{1 + \dot{\omega}} \right] - \bar{n}_x \sin(\theta + \omega) \right) \quad (5.24)$$

$$\omega(0) = 0 \quad \dot{\omega}(0) = 0 \quad \omega(\pi) = 0 \quad \dot{\omega}(\pi) = 0$$

This is precisely the equation found by Reissner<sup>45</sup> (for isotropic materials) in 1959, except that he



introduced the nonlinear loading terms (the right-hand-side of the equation) through a less rigorous approach. Linearization of this equation in terms of a Fourier expansion for the rotation  $\omega$  leads to an analogous form of the original ODE discovered by Brazier<sup>42</sup> in 1926. His simplistic solution establishes that the deformation varies sinusoidally around the circumference and is of the form (Wood<sup>44</sup> later included the effects of pressure):

$$\omega(\theta) = -\frac{\chi^2 \bar{\alpha}^2}{2(1 + \bar{p})} \sin 2\theta \quad (5.25)$$

The pertinent auxiliary relations from Eq. (5.16) are then easily calculated as

$$\bar{m}_y = \bar{\alpha} \left[ 1 - \frac{\chi^2 \bar{\alpha}^2}{2(1 + \bar{p})} \right] \quad \phi(\theta) = \frac{\chi^2 \bar{\alpha}^2}{12(1 + \bar{p})} (3 \cos \theta + \cos 3\theta) \quad (5.26)$$

These equations represent the Brazier solution for the moment-curvature relation and the cross-sectional deformation of a long cylinder under bending. As expected, the moment-curvature relation is nonlinear, and the limit point where the moment reaches a maximum possesses the following properties:

$$\bar{\alpha}^{lim} = \frac{1}{\chi} \sqrt{\frac{2(1 + \bar{p})}{3}} \quad \bar{m}_y^{lim} = \frac{2}{3\chi} \sqrt{\frac{2(1 + \bar{p})}{3}} \quad \phi_{max}^{lim} = \frac{2}{9} \quad (5.27)$$

The parameter  $\phi_{max}$  is a measure of the ovalization of the circular cross-section, and represents the inward displacement, normalized with respect to the radius, at the top and bottom of the cross-section. A comparison of the accuracy of these values when compared to the full nonlinear solution is presented in Section 5.4.1.

### 5.3.2 Approximate Stability Analysis Based on Maximum Compressive Stress

To determine the buckling load of a long cylinder under bending, the buckling curvature  $\bar{\alpha}^{buck}$  at which the cross-section becomes unstable is calculated using the nonlinear eigenvalue technique of Section 5.2. However, this technique is quite intensive and inefficient in a computational environment, for it involves performing a nonlinear eigenvalue analysis at many steps along the load path until the critical load level is determined. Therefore, this sub-section utilizes some previous results concerning the stability of cylinders under bending loads to develop an approximation technique for the estimation of the buckling load.

Buckling of circular cylinders under bending was most qualitatively defined by Seide & Weingarten<sup>85</sup> in 1961. They determined that the maximum critical bending stress is roughly equal to the critical buckling stress under axial compression. Local buckling occurs when the maximum compressive stress (at  $\theta = \pi$  using our definition of a positive bending moment) attains this value.

For orthotropic materials, this critical stress is found from the classical value as

$$\sigma_{cr} = \frac{-2\sqrt{D_{11}E_{\theta}H}}{\rho H} \quad (5.28)$$

Note that for this definition the stiffness parameters are not the average skin values as usual, but are allowed to vary around the circumference of the cylinder. The symbol  $\rho$  represents the local radius of curvature and is also a function of  $\theta$ . Due to the Brazier effect, the cross-section of the cylinder deforms into an oval (see Figure 5.1), and the radius of curvature at the location of highest compressive stress increases, thus *lowering* the critical buckling stress according to Eq. (5.28). Therefore, one can obtain an approximate estimate of the critical buckling moment by determining when the axial stress on the compressive side of the cylinder reaches this critical value.

Only two characteristics of the loaded cylinder need be known to determine this approximate stability criterion: circumferential curvature; and the axial stress resultant. Both quantities have been defined earlier in terms of the circumferential rotation  $\omega(\theta)$ , in Eq. (5.3) and (5.16), respectively. Then the stipulation that the maximum compressive stress must remain below the critical buckling stress to remain stable is expressed as:

$$\frac{-N_x(\theta)}{H} < \frac{2\sqrt{D_{11}(\theta)E_{\theta}(\theta)H}}{H} \left[ \frac{1}{R} + \kappa_{\theta}(\theta) \right] \quad (5.29)$$

This generates the (normalized) stability criterion for orthotropic tubes of infinite length:

$$\bar{E}_x(\theta)[\bar{\alpha}(\cos\theta - \phi - \cos\theta_{ref}) - \bar{f}] + \sqrt{\bar{D}_{11}(\theta)\bar{E}_{\theta}(\theta)}(1 + \dot{\omega}) > 0 \quad (5.30)$$

For a general variable stiffness cylinder, this equation must be evaluated at all locations around the circumference. The load which first violates the inequality is considered the critical buckling load, and the buckled mode shape should (theoretically) be concentrated around the critical location in the usual shape for buckling under a bending moment (some examples are shown in the next section). Of course, for variable stiffness structures some assumptions must be valid for this criterion to hold, namely that the stiffness variation is relatively smooth and that no axial stiffeners are present near the critical buckling location. An investigation of this stability criterion for variable stiffness cylinders that fall within this criterion is given in Section 5.5.

For constant stiffness cylinders, the approximation is simplified even further through the use of the linearized Brazier solution. The critical location at which the stability criterion of Eq. (5.30) will first be violated is now easily deduced as  $\theta = \pi$  (for a positive horizontal bending moment). The inequality is expressed solely in terms of the applied curvature, axial force, internal pressure,

and collapse parameter  $\chi$ :

$$\frac{\chi^2 \bar{\alpha}^3}{3(1 + \bar{p})} - \frac{\chi^2 \bar{\alpha}^2}{(1 + \bar{p})} - \bar{\alpha} + 1 - \bar{f} > 0 \quad (5.31)$$

Thus, the method for finding the critical bending curvature of a constant stiffness orthotropic cylinder with internal pressure and a constant axial strain consists of finding the root of a third degree polynomial. One interesting point here is that for certain values of  $\chi$  (and  $\bar{p}$ ), the critical curvature for buckling is not theoretically reached until *after* the maximum moment is attained. Some comparisons of Eq. (5.27) and (5.30) will be made in the results section to illustrate this point. Also note in Eq. (5.31) that for cylinders that do not undergo bending, buckling due to an axial force is estimated at its respective classical values. Comparisons to the full nonlinear eigenvalue solution and the original stability estimate given by Eq. (5.30) will be performed next to determine the suitability of these approximations.

## 5.4 Constant Stiffness Results

The nonlinear solutions and stability estimates developed in the previous sections represent an original form of the governing equations for infinite length cylinders. The differences to pre-existing solutions lies mainly in the normalization procedure for orthotropic laminates (which produces the nondimensional parameter  $\chi$ ) and the full inclusion of the nonlinear deformation terms in the stability estimate. Therefore, besides checking the accuracy of the approximate analyses, this section also investigates the effect of these new improvements to the Brazier problem for constant stiffness laminates. Some simple optimization is also performed in this section to determine the optimal stacking sequence to resist buckling. These optimization results are complemented by similar design studies using curvilinear fibers in Section 5.5.

### 5.4.1 Accuracy of Approximate Analyses

The first task is to compare the approximation based on the analysis of Brazier to the full nonlinear problem represented by Eq. (5.15). Here the load case is defined as pure bending ( $\bar{f} = \bar{p} = 0$ ) for a laminate with a collapse parameter  $\chi$  equal to unity. Note that this restriction on  $\chi$  basically limits the cylinder composition to either an isotropic material or an orthotropic material in which all the layers are aligned in the same direction. The comparisons between the full nonlinear solution (referred to as the Reissner solution) and the Brazier approximation are presented in Figure 5.2 in the form of a curvature-versus-moment plot of the nonlinear load path as well as the resulting cross-sectional deformation for each solution at a given load level. Each load curve also reveals the limit points and the buckling levels corresponding to the maximum buckling stress (Seide-Weingarten) criterion. As expected, the simplistic Brazier solution generates surprisingly

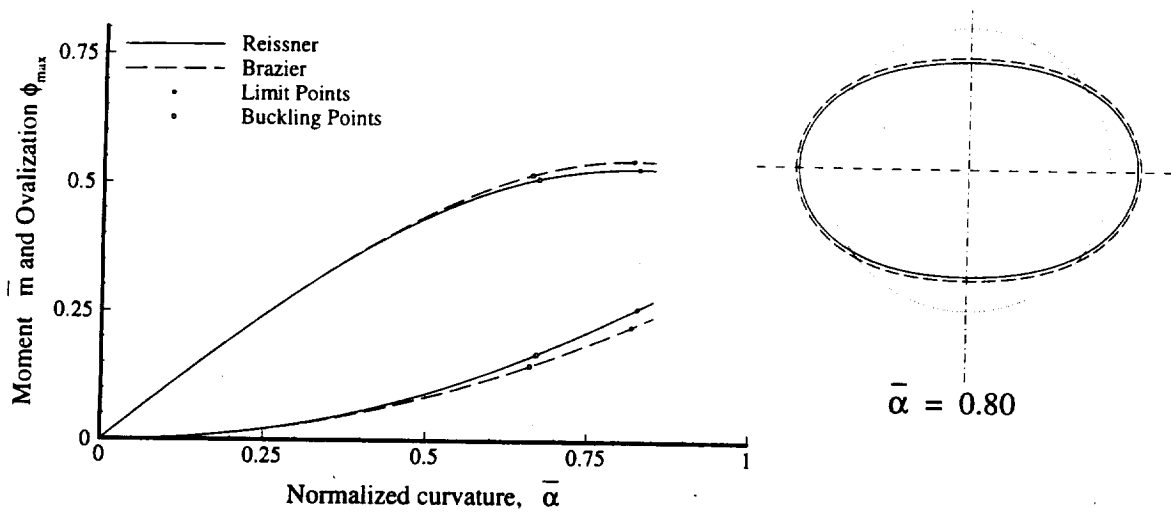


**Figure 5.2: Comparisons between Reissner and Brazier Solutions**

accurate results when matched with the full nonlinear solution. In direct comparison, the approximate technique slightly underestimates the cross-sectional deformation, which results in less nonlinearity and an increase in the calculated bending moment. However, the deformed shape of the cross-section is predicted correctly and differs only in relative magnitude. These results may seem to indicate that the level of complexity in the Reissner equation is superfluous, and that some terms may be omitted to produce a sufficiently accurate solution with less involved equations. However this is not the case. It can be shown that the linearization of the nonlinear equation that leads to the Brazier approximation does not contain an intermediate step that produces accurate results while decreasing the nonlinearity of the equations. This result is discussed in Calladine<sup>50</sup>, and he demonstrates that attempting such a solution by performing a perturbative expansion generates a corrective term to the Brazier solution that actually renders the solution less accurate, and that the next term in the expansion restores the equations to the full nonlinear form. This phenomenon is also evident in the work of Bannister<sup>49</sup>, who included some extra terms in the approximate solution that skewed the results by over 30%. Nonetheless, the approximate Brazier solution, when applied correctly, does provide an excellent alternative to the nonlinear Reissner equation, especially when comparing efficiency of the solutions.

The load-displacement response, limit and buckling points, and cross-sectional deformation shown in Figure 5.2 do not depend on the radius-to-thickness ratio of the infinite length cylinder. This is evidenced by the normalized equations (5.16), (5.26), (5.30), and (5.31) derived in the last section. However, the nonlinear eigenvalue calculation was not shown for these cylinders, particularly because it *does* depend on the relative thickness of the cylindrical shell. This phenomenon was first discerned by Fabian<sup>48</sup>, who concluded from his bifurcation analysis for isotropic cylin-

ders that the collapse of thin cylinders was governed by the maximum buckling stress criterion for thin cylinders yet better approximated by the limit load for shells with a small radius-to-thickness ratio. However, it should be noted that Fabian's stability estimation was based on shallow shell equations for a toroidal shell that did not take the full effects of the nonlinear prebuckling deformation into account. To clarify, Fabian assumed that the shell contained axial curvature due to the bending moment and circumferential curvature due to the cross-sectional ovalization, and then utilized DMV shell theory to calculate a buckling load from this deformed state. This technique possesses two differences with respect to the bifurcation analysis used in this study, namely the use of DMV theory versus Sanders equations, and the inclusion in this investigation of the prebuckling deformation that leads to a nonlinear eigenvalue problem. A comparison of the two techniques reveals that the results for thin shells are the same: the deformation is localized on the compressive side of the ovalized cross-section, and the axial buckling frequency is relatively high. For thicker shells, the buckling mode tends to spread out farther from the maximum compressive stress location, and buckles at lower circumferential and axial frequencies. This tends to increase the buckling load slightly when compared to the maximum buckling stress criterion. However Fabian's conclusion that thicker cylinders approach a limit moment before bifurcation was not substantiated by this investigation. Instead, it was found local buckling still occurred first (for the isotropic shells under consideration) but with critical curvature somewhat higher (less than 10%) than expected. Thus it was concluded that the maximum buckling stress criterion was adequate for determination of the buckling load, even for variable stiffness structures, and the remaining results in this section will utilize this approximate criterion for the buckling results.

#### 5.4.2 Influence of Laminate Stacking Sequence

Brazier's analysis applied to long cylinders constructed of orthotropic material was first completed by Kedward<sup>51</sup>. For our analysis, the nondimensional parameter  $\chi$  of Eq. (5.14) seems to describe a measure of orthotropy for any shell wall construction. However,  $\chi$  does not signify any classical measure of orthotropy, such as the ratio of the moduli in perpendicular directions. For instance, isotropic materials and cylinders fabricated from one layer of an orthotropic material *both* possess a value of  $\chi = 1$ . Clearly then, the degree of orthotropy of the material is *not* represented by  $\chi$ . A more accurate description of  $\chi$  is related to the collapse loads of the cylinder. Recall that the classical buckling moment is proportional to  $\sqrt{\hat{D}_{11}\hat{E}_\theta}$ . However, due to the Brazier effect, another mode of failure exists in the form of a limit moment on the nonlinear load path. After unnormalizing, it can be shown from Eq. (5.27) that this limit load is proportional to  $\sqrt{\hat{D}_{22}\hat{E}_x}$ . This makes physical sense, since each of the stiffness measures  $E_x$  and  $D_{22}$  contribute to the nonlinearity in different ways: a high axial membrane stiffness resists the curving of the tube

which generates the inward forces that ovalize the cross-section; while a large circumferential bending stiffness will not allow the circular cross-section to deform into an oval. Therefore,  $\chi$  is an indication of the ratio between the buckling and limit loads of a tube under bending, and is dubbed the collapse parameter. Structures with a low collapse parameter are more likely to buckle locally before the limit point is reached, while tubes with large values of  $\chi$  may attain a maximum moment before the local buckling condition is reached.

The question still remains as to what kind of structures generate different values of the collapse parameter defined by Eq. (5.14). The ratio of bending stiffness divided by the in-plane stiffness in two perpendicular directions is certainly not intuitive. As mentioned previously, any tube constructed of a single orthotropic layer possesses a value of  $\chi = 1$  and behaves identically with respect to their normalized collapse load values. To produce extreme values of  $\chi$ , the aim is to find structures that possess drastically different bending and membrane stiffness characteristics in the axial and circumferential directions. Obviously, multi-layered composites satisfy this criteria and can achieve a wide range of  $\chi$  values. For instance, a simple laminate composed of unidirectional orthotropic layers ( $E_1/E_2 \approx 11$ ) with the layup  $[0_2/\pm 45]_S$  has a collapse parameter  $\chi$  equal to 1.55. Therefore, the collapse parameter is a direct function of the stacking sequence of multi-layered shells, as well as the material properties of the constituent layers.

With this in mind, some optimization is performed to determine the limiting values of  $\chi$  that can be achieved as a function of lamina orthotropy and stacking sequence. Laminates were restricted to be symmetric, balanced, and constructed only of  $0^\circ$ ,  $\pm 45^\circ$ , and  $90^\circ$  plies. It was found that laminates with large values of  $\chi$  tend to have many  $0^\circ$  plies at the extreme locations of the laminate, with  $90^\circ$  plies at the middle surface and a transition region of  $\pm 45^\circ$  plies between the two. Conversely, small values of  $\chi$  are generated by an inner core of  $0^\circ$  plies with  $90^\circ$  layers at the extremities. The extreme value of the collapse parameter for these optimal ply configurations also depends on the orthotropy of the laminae. A plot of the maximum value of  $\chi$  as a function of material orthotropy is shown as a solid line in Figure 5.3 (here it is assumed that the shear modulus of the lamina is that of the matrix material). The relative amount of  $0^\circ$  and  $90^\circ$  plies in the laminate now varies as a function of material orthotropy, while the percentage of  $\pm 45^\circ$  layers remained about the same (around 10%). Two mechanisms to increase the value of  $\chi$  exist. For smaller values of  $E_1/E_2$ , the laminate is composed of over 50%  $90^\circ$  layers in the core of the laminate. This has the effect of making  $E_\theta$  greater than  $E_x$  without a large difference in the bending stiffnesses. However, the maximum values of  $\chi$  are not very large for this case due to the small value of the orthotropy. As the orthotropy increases, the mechanism to maximize  $\chi$  changes. The amount of  $0^\circ$  plies at the extreme locations of the laminates grows to almost 60%, thereby increas-

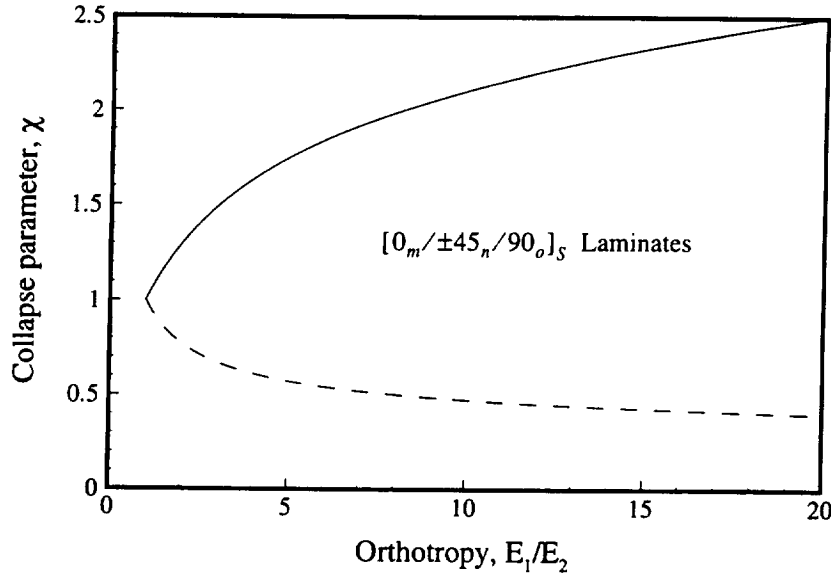


**Figure 5.3: Maximum Collapse Parameter vs. Material Orthotropy**

ing the bending stiffness in the axial direction ( $D_{11}$ ) when compared to that in the circumferential direction ( $D_{22}$ ) because of the distance of these plies from the laminate middle surface. Analogous optimization techniques for *minimum* values of  $\chi$  results in a reversal of these trends, so that the curve for the minimum value of  $\chi$  (the dashed line in Figure 5.3) follows an inverse relation (i.e.  $\chi_{min} = 1/\chi_{max}$ ). For a given material orthotropy, the range of  $\chi$  values lies between these two cases.

Representative moment versus curvature relations for various values of the collapse parameter  $\chi$  are displayed in Figure 5.4 for unpressurized cylinders. The load paths are terminated

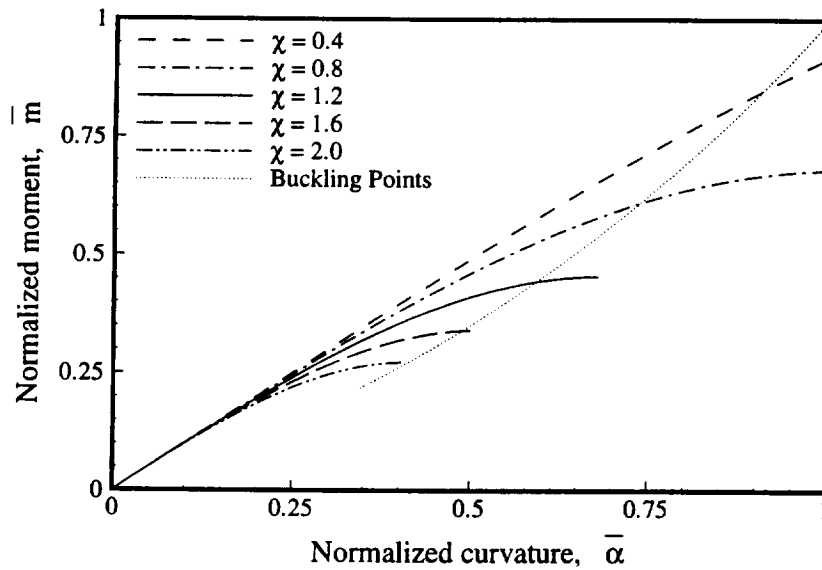


**Figure 5.4: Moment vs. Curvature for Long Orthotropic Cylinders**

when the limit point is encountered. The intersection of the dotted line with a load path represents the buckling point according to the Seide-Weingarten criterion. Note in Figure 5.4 that the tubes with higher values of the collapse parameter experience significant nonlinearity due to the Brazier effect before a buckling point is attained. Conversely, laminates possessing a small value of  $\chi$  behave more linearly and collapse when their classical buckling value is reached. Thus the limit point of the Brazier effect *cannot* be used as an accurate estimate of the collapse load for long cylinders possessing a small value of  $\chi$ . To illustrate this more clearly, critical curvatures according to limit load and local instability are plotted as a function of  $\chi$  in Figure 5.5. The lower value of

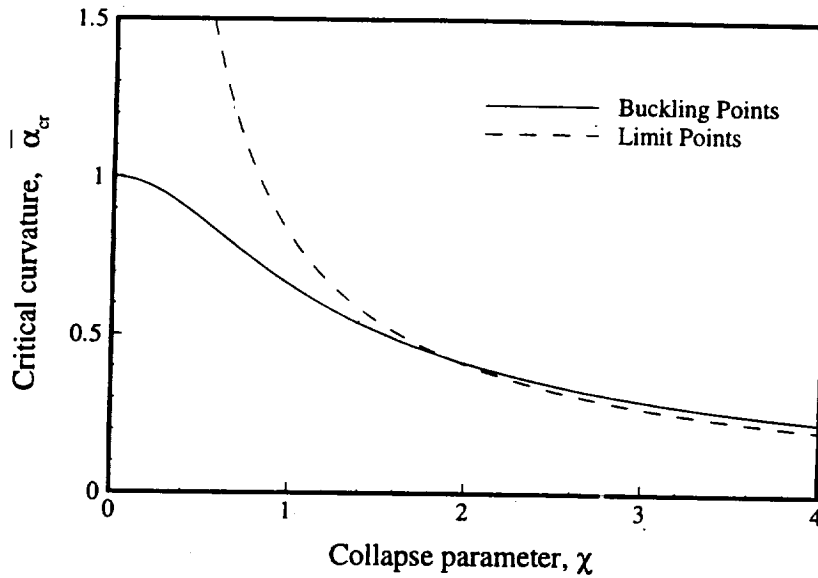


**Figure 5.5: Buckling Curvature and Limit Curvature vs. Collapse Parameter**

the two is the curvature that determines collapse. Note that for small values of  $\chi$ , the limit moment is *not* an accurate estimate of the collapse load. Furthermore, for values of  $\chi$  greater than two, the limit point is reached before the local stability condition is violated. However, it may be almost impossible to distinguish this limit load behavior from the local instability experimentally, for the buckling load remains very close to the limit load, and the catalyst to the post-buckled state may be difficult to distinguish.

### 5.4.3 Stacking Sequence Optimization to Maximize Critical Load

The results of the previous section have demonstrated that the nonlinearity for a composite laminate depends strongly on the stacking sequence of the laminate. Additionally, some optimal stacking sequences that maximized or minimized the value of the collapse parameter  $\chi$  were determined. However, it is not apparent if this nonlinearity has any effect on the optimal design of cylinders under bending, or even what the desired characteristics of the laminate should be to pro-



duce a long cylindrical structure that performs well under bending. For instance, the last chapter assumed that the cylinder section was short and the prebuckling static solution was approximated by the classical membrane solution. The optimal designs tended to increase the axial stiffness at the top and bottom of the cross-section, while the sides were relatively soft so that the stiffer sections could carry the bulk of the load. However, such a design may not perform as well as others if the cylinder is long, since the soft sides would tend to increase the Brazier effect by deforming easily circumferentially. Therefore, this sub-section illustrates the difference in optimal designs that exist between short and long cylindrical shells.

For this design study, the radius-to-thickness ratio is chosen to be 200, which qualifies as a thin shell so that the maximum buckling stress criterion can be used. The laminate is constructed of twenty-four plies of a typical graphite-epoxy material (for properties see Appendix C) that is constrained to be balanced and symmetric. This leaves twelve design variables defined as the fiber orientation angle for each lamina, which are allowed to be either 0,  $\pm 45$ , or 90 degree plies. A genetic algorithm is implemented to use these discrete design variables to find the optimal collapse moment for both a short cylinder segment and an infinite length shell. For the short segment solution, the critical bending moment is assumed to correspond to the classical buckling moment given in Eq. (5.13). Thus the optimization problem can be simply stated as maximizing the quantity  $D_{11}E_0$  for a 24-ply stacking sequence. The collapse moment of the infinite length shell is determined by the minimum value of either the limit moment or the buckling load calculated by the maximum buckling stress criterion. This can be evaluated by either finding the buckling and limit points as the curvature is increased along the load path, or using the approximate Brazier analysis expressions given in Eq. (5.27) and (5.31). Here the former choice is used due to its greater accuracy. The results for each case are displayed in Table 5.1:

Case	Stacking Sequence	$\overline{M}_y^{cl}$ (lbs-in)	$\chi$	$\bar{\alpha}_{cr}$	$\overline{M}_y^{\infty}$ (lbs-in)
<b>Short</b>	$[0_4/90_8]_S$	$8.323 \times 10^6$	1.900	0.4477	$2.313 \times 10^6$
<b>Infinite</b>	$[90_2/0/90/0_2/90_2/0_4]_S$	$5.187 \times 10^6$	0.6906	0.7883	$3.441 \times 10^6$

**Table 5.1: Results of Optimization for Maximum Bending Load (Constant Stiffness)**

Not surprisingly, the optimal designs for each case differ substantially. For the short cylinder, the buckling load is maximized by placing 0° plies at the outermost locations with many 90° plies at the core. This has the effect of simultaneously increasing the  $D_{11}$  stiffness parameter (axially stiff plies far from the middle surface) and the  $E_0$  term (due to the presence of many circumferentially stiff 90° laminae). However, this method of design produces a laminate with a large value of the

collapse parameter  $\chi$ , which implies significant nonlinearity before buckling for a long tube. The critical normalized curvature and bending moment for this stacking sequence is also calculated, and it is evident that the drop in load carrying capability is drastic (over 70%). Conversely, optimization using the infinite length solution produces a laminate with a more even distribution of  $0^\circ$  and  $90^\circ$  plies, with the larger bending stiffness in the circumferential direction. This produces a small value of  $\chi$  and a drop of only 34% from the short cylinder case. However, this design also exhibits a relative increase in load-carrying capability of over 50% when compared to the optimal short cylinder design. Thus these designs demonstrate that for long cylinders, the Brazier effect plays a significant role in the performance of the structure under bending.

#### 5.4.4 Influence of Pressure

The presence of internal or external pressure also affects the amount of nonlinearity for long tubes under bending. The effect of pressure on collapse loads for cylinders under bending was first investigated in detail by Fabian<sup>48</sup> in 1977, who also performed a full bifurcation analysis from the deformed state for infinite cylinders under bending, pressure, and axial loads. His results for various pressure loads conform exactly as those presented here, though his conclusions regarding the effect of the radius-to-thickness ratio on the mode of collapse are not evident in these results since the buckling criterion is based on the maximum buckling stress criterion. Nonetheless, plots of load-displacement curves are displayed in Figure 5.6 for typical values of pressure for thin shells with a collapse parameter equal to one. A large internal pressure creates circumferential

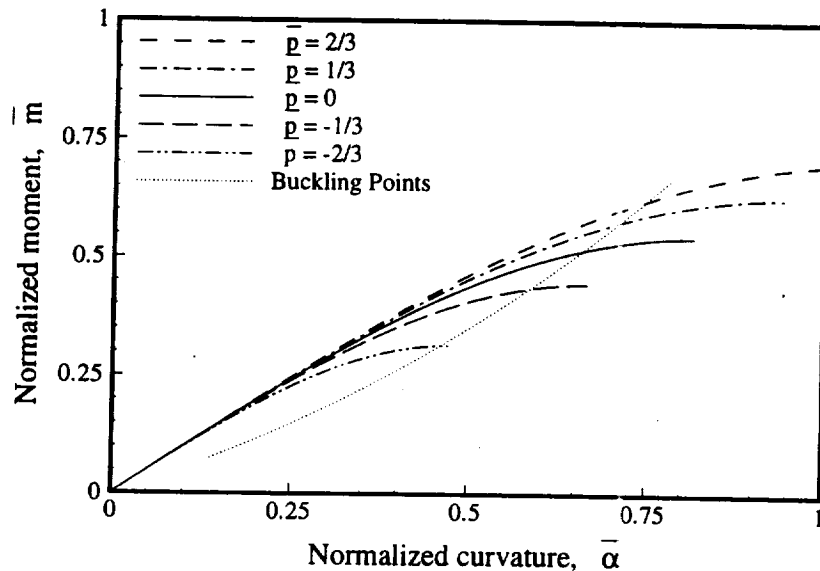


Figure 5.6: Moment vs. Curvature for Pressurized Isotropic Cylinders

stresses that dominate the bending stresses in the tube and force the cross-section to remain circu-

lar. Thus the ovalization that lowers the moment of inertia does not occur, and the nonlinearity due to the Brazier effect is lessened. Conversely, exterior pressure heightens the nonlinear effect by encouraging the cross-sectional deformation to increase. The dotted line in Figure 5.6 again corresponds to the buckling point using the Seide-Weingarten criterion. Limit points and buckling loads are compared as a function of pressure in Figure 5.7. As expected, large external pressures increase the Brazier effect, so that a limit point may occur before the local buckling phenomenon appears. Though the results shown in these figure apply only to thin shells, and it is still safely concluded that the limit load is again a poor estimate of the failure load of the structure except for extreme cases.

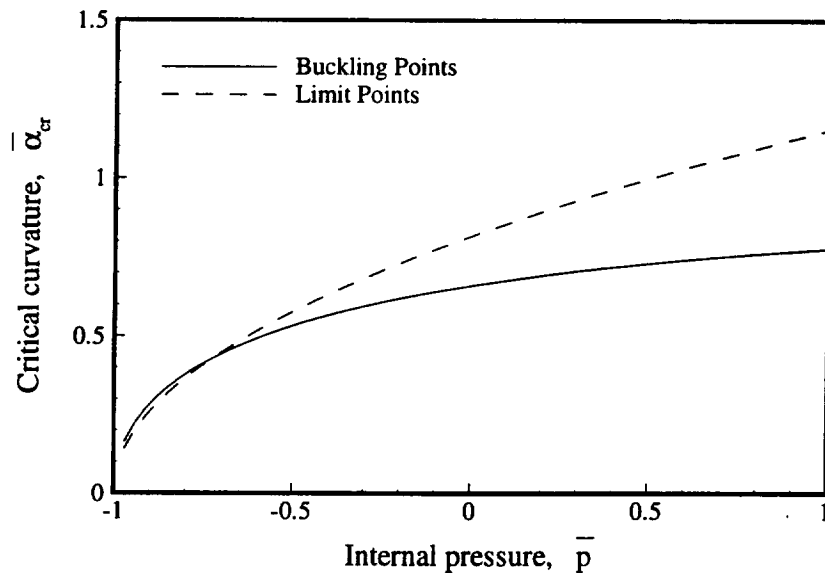


Figure 5.7: Buckling Curvature and Limit Curvature vs. Pressure

## 5.5 Variable Stiffness Concept Results

This last section analyzes infinite length cylinders constructed of variable stiffness laminates through the use of curvilinear fiber formats. Axial stiffeners are not investigated here, since their total effect is not accurately reflected for the infinite length case. Though discrete stiffeners figure significantly in the membrane and bending stiffness parameters in the axial direction, the absence of end conditions severely limits their effectiveness for this idealized problem. This is due to the “greased end” boundary conditions, for which the axial stiffeners are not rigidly attached at the boundaries and merely float in space as attachments to the skin. Therefore the resistance to cross-sectional deformation that the stiffeners *should* provide (by bending as beams) is lost by virtue of the approximate analysis in the axial direction. Nonetheless, curvilinear fiber formats and crown/side/keel arrangements are still viable possibilities for skin constructions. Therefore this section will discuss the analysis associated with such structures and their relative effectiveness in

increasing failure loads when compared to constant stiffness solutions.

To complement the optimization performed in Section 5.4.3 for constant stiffness laminates, this section utilizes a circumferential stiffness variation to improve the critical buckling load of a long cylinder under bending. The variation of the stiffness parameters is expected to provide two methods to improve the performance under bending: modification of the prebuckling deformation pattern by minimizing the circumferential bending of the cross-section; and the presence of a stacking sequence at the critical buckling location that exhibits excellent resistance to buckling due to axial stress. The cylinder geometries are chosen as  $R/H = 200$  and are constructed of 24 balanced, symmetric plies, which implies twelve fiber orientation angle design variables. The two outermost plies are constrained to be variable stiffness layers, while the remaining ten are allowed to be variable stiffness plies or straight fiber laminae with fiber orientation angles equal to  $0^\circ$  or  $90^\circ$ . Two methods of stiffness variation are used: curvilinear fibers using a linked-line segment format that are symmetric about the horizontal axis; and a crown/side keel arrangement with various locations used for the transition area between the sections. A genetic algorithm was used for the numerical optimization.

The results for the variable stiffness case are shown in Figure 5.8. The plot on the left displays the fiber orientation angle  $\varphi$  (dashed line), normalized axial stiffness  $\bar{E}_x$  (solid line), and collapse

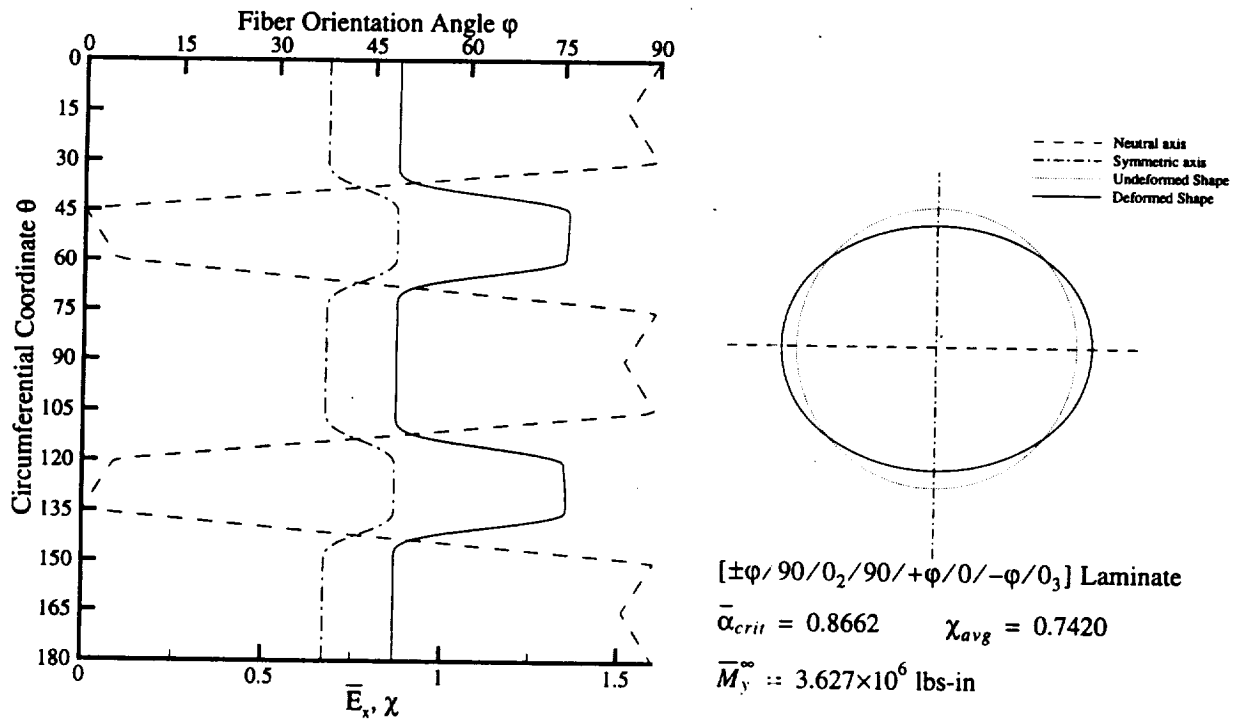


**Figure 5.8: Optimal Variable Stiffness Design for Long Cylinder under Bending**

parameter  $\chi$  (dash-dot line) as a function of the circumferential coordinate  $\theta$ . Note that the regions that experience the largest circumferential bending (the top, bottom, and sides) possess a stacking sequence with a small value of  $\chi$  which reduces the circumferential bending due to the nonlinear Brazier effect. Where the cross-sectional deformation is not as significant, the design favors an axial stiff laminate that increases the bending resistance of the structure. It is interesting to compare this optimal design with the results for a short cylinder under bending, such as those shown in Table 4.4. For those cases, the top and bottom regions required the highest stiffness possible, however for a long cylinder such a design is less valuable since it experiences increased nonlinearity. The plot to the right in Figure 5.8 shows the cross-sectional deformation of the variable stiffness design. Note that even with the drastic stiffness variation, the displacements still basically follow the  $\cos 2\theta$  deformation pattern. This is due to the fact the forcing term in the nonlinear equilibrium equation is dominated by this function, and that the variation of the circumferential stiffness parameter  $D_{22}$  is not able to significantly alter the shape of the deformed cross-section. This result was also exhibited for shells with different radius-to-thickness ratios. Thus it is concluded that though the variable stiffness concept does provide an improved design with respect to the constant stiffness solution (around 5%), the variation of the stiffness parameters is still not able to significantly alter the resulting deformation shape or failure mechanism due to the nonlinear Brazier effect.

For the crown/side/keel design case, the results were even less promising. Since both the sides and the crown/keel regions required a laminates with a small value of  $\chi$  to resist the ovalization, the resulting design turned out to be a constant stiffness laminate identical to the optimal design given in Table 5.1. This is somewhat expected from the variable stiffness results shown in Figure 5.8. Instead of a crown/side/keel arrangement, a more effective layout would contain an additional region between the sections that improved the global axial stiffness, while the sides, top and bottom would be constructed of a laminate that resisted the cross-sectional deformation.

## Chapter 6.0 Bending of Finite Length Cylinders including the Brazier Effect

The previous chapter investigated the Brazier effect for infinite length tubes under bending. Unfortunately, that analysis suffers the drawback that it is only applicable to extremely long shells that are not affected by the end conditions. For many practical structures, the presence of end restraint renders the infinite solution useless, since the end conditions play such an enormous role in retarding the deformation of the cross-section. Therefore, this chapter attempts to incorporate the end effects into the nonlinear analysis of cylinders under beam bending loads. By including the variation of the response in the axial direction, the resulting analysis can also incorporate stiffness variations along the length, akin to the axisymmetric solution of Chapter 3.0. The axisymmetric analysis formulated there constitutes a *complete* solution for the axisymmetric response, in that the inclusion of boundary layer effects, arbitrary end conditions, and stability estimations with nonlinear prebuckling solutions provides a thorough investigation of all aspects of the problem. However, retaining this amount of detail for loads that vary around the circumference of the shell, such as this particular case of beam bending, increases the complexity of the solution technique by a considerable degree. This is due to the fact that the nonlinear governing equations contain products and squares of the variables, most notably rotations of shell elements. For the axisymmetric problem, this does not present too severe of a complication, for the nonlinear terms remain functions of the axial coordinate only and the expressions governing the response are still ordinary differential equations. However, with a possible non-axisymmetric distribution of the response, the nonlinear terms generate equations which demand analysis in the circumferential direction as well. For example, traditional investigations of pure bending of cylindrical shells often rely on a harmonic expansion of the displacements, which results in a large system of coupled ordinary differential equations. Though a numerical solution is feasible (see, for instance, Fuchs<sup>88</sup>), the complexity of the method requires far greater computational time and power than that of our axisymmetric solution. Since the goal in this investigation is chiefly to explore the possibilities of the variable stiffness concept, such a highly sophisticated solution that is computationally slower will not be used. However, since the beam loading of a variable stiffness shell is still a desirable problem to solve, an approximate method will be employed. By utilizing certain

assumptions about the response in the circumferential direction, the resulting system can be maintained to be a few ordinary differential equations, though some of the desirable details of the analysis mentioned earlier will be lost.

The specific problem to be explored is pure bending of a finite length cylindrical shell with an axial stiffness variation. The most basic solution to this problem is found through the use of linear membrane theory, such as the analysis presented in Chapter 4.0. Though this solution does not consider the local boundary layer of the cylindrical shell, it still conveys an accurate representation of the beam response of the structure in a global sense. Furthermore, the neglect of the shell boundary layer near the ends removes the nonlinearity and leads to a simple closed-form solution in the axial direction. Thus for short cylinders the first approximation of the solution for pure bending corresponds to the linear membrane solution. For longer cylinders, membrane theory is not as accurate and must be augmented by the inclusion of the circumferential moment through the use of semi-membrane theory, as discussed in Section 2.2.3. This again leads to the incorporation of the Brazier effect, which was investigated in the last chapter for infinite length cylinders with a circumferential stiffness variation. However, the inclusion of an axial stiffness variation for a finite length cylinder changes the problem considerably, for now a thorough analysis must be performed in the axial direction to fully explore the ramifications of the variable stiffness concept and the effect of finite length on the nonlinear bending phenomenon. Thus the loss of the detailed analysis near the end of the cylinders due to adopting an approximate solution is tempered by the existence of a different type of nonlinear problem that is still significant for many applications.

The assumption used for the simplification of the governing equations in the circumferential direction will be based on the approximate solution of Brazier<sup>42</sup> in 1926. As discussed in the introduction and established numerically in the last chapter, Brazier's original linearized analysis for infinite length cylinders is surprisingly accurate compared to the more robust nonlinear solution. When applied to finite length cylinders, the simple assumptions transform the static equilibrium equations into differential equations that only vary in the axial direction. This produces a mathematical system that can be solved efficiently using standard numerical techniques. The application of Brazier's analysis to finite length tubes was first investigated by Aksel'rad<sup>59</sup>, who also employed semi-membrane constitutive theory to determine the effect of the cross-sectional deformation on the structure's buckling load. In this study, the approximate maximum buckling stress criterion introduced in Section 5.3.2 will likewise be used to estimate stability and the effect of the Brazier nonlinearity on collapse. Since the stiffness variation is only in the axial direction, this approximate technique should be adequate, since it was shown in the last chapter that the

approximate stability estimate is sufficiently accurate for cylinders with a smooth stiffness distribution around the circumference of the cylinder.

### 6.1 Static Equilibrium

The original Brazier solution determined that for long cylinders under bending, the line of action of the bending stresses produces an ovalization of the cross-section which varies like  $\cos 2\theta$ . Therefore for this chapter, this variation is used as the basis for the functional form of the displacements in the circumferential direction so that the magnitude of the deformation along the length of the cylinder are the unknown variables. Thus the displacements are expressed as

$$u^o(x, \theta) = u_2(x) \cos 2\theta \quad v^o(x, \theta) = v_2(x) \sin 2\theta \quad w^o(x, \theta) = -w_2(x) \cos 2\theta \quad (6.1)$$

and the resulting strain-displacement relations are assumed to be linear. The negative sign of the radial displacement is inserted so that the resulting measure of the ovalization will be positive. The resulting deformed geometry of the cylinder acting as a beam is shown in Figure 6.1.

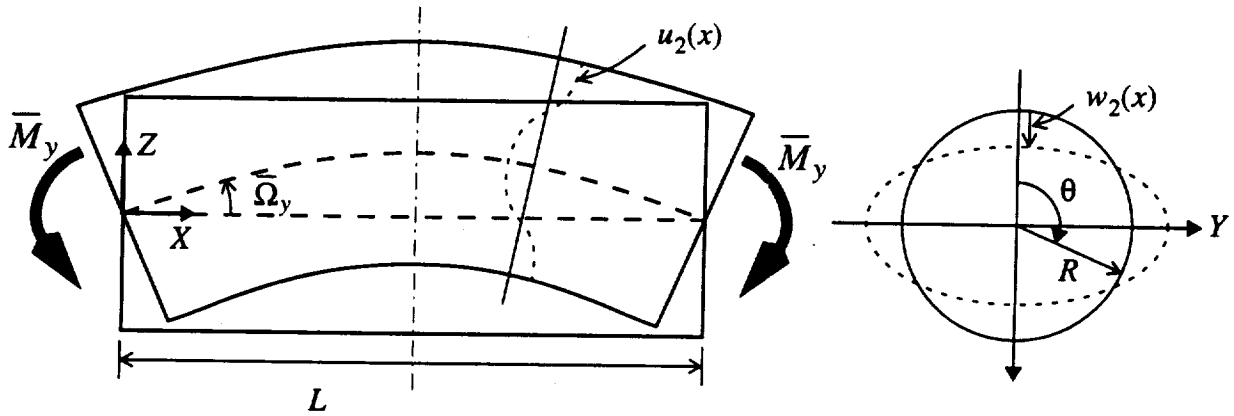


Figure 6.1: Geometry of Finite Length Cylinder under Bending

Semi-membrane theory is used to model the constitutive behavior, which corresponds to a membrane solution for the beam-like response of the cylinder that still includes the effect of circumferential bending. Since the major loading of the structure consists of beam bending which produces predominantly axial stresses, the resulting ovalization of the cross-section is assumed to be inextensional in the circumferential direction. This translates into a relationship between the circumferential and radial displacement functions that guarantees that the circumferential middle surface strain is zero, and for a linear approximation this is expressed as

$$\epsilon_\theta^o = \frac{1}{R} \left( \frac{\partial v^o}{\partial \theta} + w \right) = 0 \quad \Rightarrow \quad v_2(x) = \frac{w_2(x)}{2} \quad (6.2)$$



Therefore the circumferential displacement  $v_2$  is eliminated from the equations and the solution is formulated in terms of the radial displacement  $w_2$ . This choice is made since the radial displacement gives a great physical feel to the problem than the circumferential displacement. However, it should be noted that the resulting equations using semi-membrane theory will be *membrane* equations, and that the boundary conditions in terms of  $w_2$  are physically related to the circumferential displacement  $v_2$ .

The correct application of Brazier's approximation implies that the nonlinearity attributed to shell rotations is small and that the axial curvature due to variations of  $w_2(x)$  can be neglected. The strain-displacement relations can then be specialized from their general form from Chapter 2.0, Eq. (2.20)-(2.21), and are written here in terms of the ovalization variables:

$$\begin{aligned}\epsilon_x^o &= \kappa_y \left[ \left( R - \frac{3w_2}{4} \right) \cos \theta - \left( \frac{w_2}{4} \right) \cos 3\theta \right] + \left[ \frac{du_2}{dx} \right] \cos 2\theta & \epsilon_\theta^o &= 0 \\ \gamma_{x\theta}^o &= \left[ -\frac{u_2}{R} + \frac{1}{2} \frac{dw_2}{dx} \right] \sin 2\theta & \omega_x^o &= 0 & \omega_\theta^o &= \left[ -\frac{3w_2}{2R} \right] \sin 2\theta & e_{zz} &= 0 \\ \kappa_x^o &= 0 & \kappa_\theta^o &= \left[ -\frac{3w_2}{R^2} \right] \cos 2\theta & \kappa_{x\theta}^o &= \left[ \frac{1}{R} \left( -\frac{7}{2} \frac{dw_2}{dx} \right) \right] \sin 2\theta\end{aligned}\quad (6.3)$$

The semi-membrane constitutive equations from Eq. (2.71) are:

$$N_x = E_x H \epsilon_x^o \quad N_{x\theta} = G_{x\theta} H \gamma_{x\theta}^o \quad M_\theta = D_{22} \kappa_\theta^o \quad (6.4)$$

where the stiffness parameters are solely a function of  $x$ . The equilibrium equations for the shell and the beam, Eq. (2.87)-(2.94), become:

$$\begin{aligned}\frac{\partial N_x}{\partial x} + \frac{1}{R} \frac{\partial N_{x\theta}}{\partial \theta} &= 0 & \frac{\partial N_{x\theta}}{\partial x} + \frac{1}{R} \frac{\partial N_\theta}{\partial \theta} + \frac{1}{R^2} \frac{\partial M_\theta}{\partial \theta} + N_x \kappa_y \sin \theta &= 0 \\ \frac{1}{R^2} \frac{\partial^2 M_\theta}{\partial \theta^2} - N_x \kappa_y \cos \theta - N_\theta \left( \frac{1}{R} + \kappa_\theta^o \right) + p &= 0 \\ \frac{d^2}{dx^2} [M_{y(x)}] &= \frac{d^2}{dx^2} \left\{ \oint N_x \left[ \left( R - \frac{3w_2}{4} \right) \cos \theta - \left( \frac{w_2}{4} \right) \cos 3\theta \right] R d\theta \right\} = 0\end{aligned}\quad (6.5)$$

Note that due to the lack of stiffness variation around the circumference, the reference angle that determines the neutral surface of the cross-section is automatically calculated as  $\theta_{ref} = \pi/2$

For the boundary conditions, all constraints are homogeneous except for those dealing with

the beam variables, which introduce the loading through the application of either an end rotation or a bending moment.

$$\begin{aligned}
 u_2(0) = 0 \quad \text{or} \quad N_x(0, \theta) &= \frac{\bar{M}_y}{\pi R^2} \cos \theta & u_2(L/2) &= 0 \\
 w_2(0) &= 0 & \frac{dw_2}{dx}(L/2) &= 0 \\
 \Omega_y(0) = \bar{\Omega}_y \quad \text{or} \quad M_y(0) &= 0 & \Omega_y(L/2) &= 0
 \end{aligned} \tag{6.6}$$

For the end conditions, the axial direction provides two alternatives: a fixed condition in which the cross-section remains straight, and a free end where the stress resultant due to bending is specified and  $\cos 2\theta$  warping deformation is allowed (this is discussed in more detail shortly). The boundary condition for  $w_2$  at the ends corresponds to the stipulation that the cross-section must remain circular there, for it guarantees that the radial and circumferential displacements, through Eq. (6.2), are zero. At  $x = L/2$ , suitable symmetry conditions are used for the axial and radial displacement, which are respectively anti-symmetric and symmetric with respect to the mid-length of the cylinder.

A remark should also be made here regarding the evaluation of the end conditions. Often the governing equations for this problem are formulated solely in terms of the radial displacement  $w_2$  by assuming that the shear stress is zero. In such a situation it can be shown that the first two options for the boundary condition in the axial direction are replaced with the choices of  $dw_2/dx = 0$  or  $d^2w_2/dx^2 = 0$ . These expressions are often construed as “clamped” or “simply supported” boundary conditions due to their traditional form. However, since semi-membrane theory does not account for bending of the shell wall in the axial direction, these classifications are not appropriate for these boundary conditions. The concept of clamped versus simply supported can only be related to the structure as a beam, that is, through the designations of  $\Omega$  and  $M_y$  at the ends (for this case of pure bending, the beam would be considered clamped). Therefore, the constraints at  $x = 0$  actually correspond to membrane boundary conditions and the first two options refer to either a fixed or free end in the axial direction. The first choice demands that the axial displacement vary linearly across the cross-section, which results in axial stresses developing that vary around the circumference as  $\cos 2\theta$ . This condition occurs when the end is supported by a rigid plate or sturdy ring stiffener and it is considered the more realistic of the two. The second option corresponds to a free end or a flimsy stiffener, in which the axial displacements are allowed to vary in the  $yz$ -plane and lead to warping of the cross-section. The intended point here is that these boundary conditions are related to the axial displacement of the cross-section, and thus do not

involve the axial rotation or resultant moment of the shell element.

Returning to the formulation of the governing equations, the beam equation is solved first. The expression for the axial stress resultant in terms of the displacement parameters is

$$N_x(x, \theta) = E_x(x)H \left[ \kappa_y(x)R \left( 1 - \frac{3w_2}{4R} \right) \cos \theta + \left( \frac{du_2}{dx} \right) \cos 2\theta - \kappa_y(x)R \left( \frac{w_2}{4R} \right) \cos 3\theta \right] \quad (6.7)$$

Inserting this expression into the integral equation for the moment in Eq. (6.5) and ignoring squares of the radial displacement generates the relationship between the beam curvature and the bending moment, which is constant since we have limited the loading to pure bending.

$$\frac{\bar{M}_y}{E_x(x)\pi HR^3} = \kappa_y(x) \left( 1 - \frac{3w_2(x)}{2R} \right) \quad (6.8)$$

The beam rotation  $\Omega_y(x)$  can be found through the definition of the curvature using Eq. (2.4), and the application of the appropriate boundary conditions after integration yields the desired relation between the end rotation and moment:

$$\frac{d\Omega_y}{dx} = -\kappa_y(x) \quad \Rightarrow \quad \Omega_y(x) = \frac{\bar{M}_y}{\pi HR^3} \int_x^{L/2} \frac{dx}{E_x(x) \left( 1 - \frac{3w_2(x)}{2R} \right)} \quad \Omega_y(0) = \bar{\Omega}_y \quad (6.9)$$

The governing equations for the axial and radial displacements are determined from the combination of the shell equilibrium equations, semi-membrane constitutive laws, and strain-displacement relations.  $N_\theta$  is eliminated as an intermediate variable in these calculations, and a few other terms, involving squares and derivatives of the variable  $w_2$ , are neglected in accordance with Brazier's approximation. The resulting pair of differential equations are found from the requirement that the coefficients of the harmonics  $\sin 2\theta$  and  $\cos 2\theta$  must be equal to zero.

$$\begin{aligned} \frac{d}{dx} \left[ E_x(x)H \frac{du_2}{dx} \right] + \frac{G_{x\theta}(x)H}{R} \left( \frac{dw_2}{dx} - \frac{4u_2}{R} \right) &= 0 \\ -\frac{d}{dx} \left[ \frac{G_{x\theta}(x)H}{R} \left( \frac{1}{2} \frac{dw_2}{dx} - \frac{2u_2}{R} \right) \right] + \left( \frac{18D_{22}(x)}{R^3} + 6p \right) \frac{w_2}{R} &= \frac{3E_x(x)HR\kappa_y(x)^2}{2} \end{aligned} \quad (6.10)$$

Normalization is performed using similar parameters as those used in the axisymmetric problem. The axial coordinate and stiffness parameters are nondimensionalized as

$$\xi = \frac{2x}{L} \quad \hat{E}_x = \int_0^1 E_x^{skin}(\xi) d\xi \quad \bar{E}_x = E_x / \hat{E}_x \quad (6.11)$$

The Brazier-type displacements are normalized with respect to typical length quantities:

$$\bar{u}_2(\xi) = \frac{2L}{R} \frac{u_2(x)}{R} \quad \bar{w}_2(\xi) = \frac{w_2(x)}{R} \quad (6.12)$$

The end rotation, axial curvature, bending moment, and pressure are all normalized with respect to their classical buckling values for an infinite cylinder:

$$\bar{\alpha} = \frac{\hat{E}_x H R^2 \bar{\Omega}}{L \sqrt{\hat{D}_{11} \hat{E}_\theta H}} \quad \alpha(\xi) = \frac{\hat{E}_x H R^2 \kappa_y(x)}{2 \sqrt{\hat{D}_{11} \hat{E}_\theta H}} \quad \bar{m}_y = \frac{\bar{M}_y}{2 \pi R \sqrt{\hat{D}_{11} \hat{E}_\theta H}} \quad \bar{p} = \frac{p R^3}{3 \hat{D}_{22}} \quad (6.13)$$

This leads to the definition of three nondimensional parameters, referred to as the collapse parameter, tube length parameter, and shear length parameter, respectively:

$$\chi = \sqrt{\frac{\hat{D}_{11} \hat{E}_\theta}{\hat{D}_{22} \hat{E}_x}} \quad \lambda = \sqrt[4]{\frac{9 \hat{D}_{22} L^4}{4 \hat{E}_x H R^6}} \quad \mu = \sqrt{\frac{\hat{G}_{x\theta} L^2}{\hat{E}_x R^2}} \quad (6.14)$$

Then the coupled system for the solution of the Brazier problem for finite length cylinders with an axial stiffness variation is written as (primes denote differentiation with respect to  $\xi$ ):

$$\begin{aligned} & [\bar{E}_x(\xi) \bar{u}_2'] + \mu^2 \bar{G}_{x\theta}(\xi) (\bar{w}_2' - \bar{u}_2) = 0 \\ & - \frac{\mu^2}{4 \lambda^4} [\bar{G}_{x\theta}(\xi) (\bar{w}_2' - \bar{u}_2)] + [\bar{D}_{22}(\xi) + \bar{p}] \bar{w}_2 = \frac{\chi^2 \bar{E}_x(\xi) \alpha(\xi)^2}{3} \\ & \bar{u}_2(0) = 0 \quad \text{or} \quad \bar{u}_2'(0) = 0 \quad \bar{u}_2(1) = 0 \\ & \bar{w}_2(0) = 0 \quad \bar{w}_2'(1) = 0 \\ & \bar{m}_y = \bar{E}_x(\xi) \alpha(\xi) \left( 1 - \frac{3 \bar{w}_2}{2} \right) \quad \bar{\alpha} = \int_0^1 \alpha(\xi) d\xi \end{aligned} \quad (6.15)$$

The loading is introduced through the end rotation  $\bar{\alpha}$ , and the unknown moment is calculated through the integral relation. This displacement control procedure is used because for longer cylinders the moment versus end rotation curve has a maximum, and specifying a moment above this limit would not be feasible. Also note that the forcing term in the second equilibrium equation is a function of  $\alpha^2$ , so that the radial displacement  $w_2$  is positive. Thus the effect of the Brazier deformation leads to a decrease in the bending stiffness of the structure, as revealed by the relation between the applied bending moment and the axial curvature.

Several pertinent limiting cases of these governing equations exist in terms of the nondimensional length parameters  $\lambda$  and  $\mu$ . Firstly, as  $\lambda \rightarrow 0$ , the cylinder becomes so short that the radial

restraint totally nullifies the Brazier effect, in which case the classical membrane solution governs the response. Thus the results for this scenario agree with the short cylinder section analysis of Chapter 4.0. The other limiting case for  $\lambda$  can be represented as:

$$\lambda \rightarrow \infty \quad \Rightarrow \quad \bar{u}_2(\xi) = 0, \quad \bar{w}_2(\xi) = \text{constant} \quad (6.16)$$

This of course is the solution for an infinite length cylinder, and corresponds exactly to the approximate Brazier solution given in Eq. (5.26).

For the shear length parameter  $\mu$ , two limiting cases also exist. When  $\mu \rightarrow 0$ , the shear stresses that normally transform the deformed cross-section back into a circle at the end restraints are zero and thus the edge effects disappear. This again leads to the infinite length solution of Brazier. Conversely, the condition  $\mu \rightarrow \infty$  implies that the shear strain is zero everywhere. This is an assumption that is often invoked for this problem, and it provides another constraint which can be used to eliminate one of the unknown variables from the equations. Usually the radial displacement is still chosen as the main unknown variable, so that the constraint in terms of zero shear strain, from the third equation of Eq. (6.3), determines that

$$\bar{u}_2 = \bar{w}_2' \quad (6.17)$$

The resulting reduced system is expressed as:

$$\begin{aligned} \frac{1}{4\lambda^4} [\bar{E}_x(\xi) \bar{w}_2'']'' + [\bar{D}_{22}(\xi) + \bar{p}] \bar{w}_2 &= \frac{\chi^2 \bar{E}_x(\xi) \alpha(\xi)^2}{3} \\ \bar{w}_2'(0) = 0 \quad \text{or} \quad \bar{w}_2''(0) = 0 \quad \bar{w}_2'''(1) = 0 \\ \bar{w}_2(0) = 0 \quad \bar{w}_2'(1) = 0 \\ \bar{m}_y = \bar{E}_x(\xi) \alpha(\xi) \left( 1 - \frac{3\bar{w}_2}{2} \right) \quad \bar{\alpha} = \int_0^1 \alpha(\xi) d\xi \end{aligned} \quad (6.18)$$

A comparison of the numerical solutions for both of the systems represented by Eq. (6.15) and (6.18) will be presented in Section 6.3.

## 6.2 Approximate Stability Analysis

This section utilizes the maximum buckling stress criterion formulated in Section 5.3.2 to estimate the load which renders the finite length cylinder unstable. The most accurate solution technique to determine when this local buckling occurs is based on a nonlinear stability analysis with the prebuckling deformation due to the Brazier effect included, similar to the one presented in Section 3.2 for the axisymmetric case. However, since the loading and cross-sectional deforma-

tion is no longer axisymmetric, the eigenvalue problem becomes appreciably more complicated because the analysis must be carried out in the circumferential direction as well. In essence, this implies that the buckled mode shape is no longer separable in terms of the circumferential wavenumber  $n$ , so that the assumed form of the displacements used for the axisymmetric problem, Eq. (3.19), cannot be used unless all values of  $n$  are considered simultaneously. To do so would make the problem much larger numerically and inefficient for our purposes. However, the approximate stability analysis formulation for the infinite length case can be easily modified to handle the finite length problem. Plus the results of Section 5.4.1 indicate that this approximate technique produces excellent correlation to a full stability analysis for thin shells that do not possess a drastic variation of stiffness in the circumferential direction.

The basis of the maximum buckling stress criterion relies on determining when the axial stress due to bending reaches a critical value that depends on the local curvature of the shell. Only two characteristics of the deformed cylinder need be known to determine stability under this approximate criterion: the axial stress resultant; and the circumferential change of curvature. Both quantities have already been defined, and are reproduced here in nondimensional form as

$$\begin{aligned}\bar{n}_x(\xi, \theta) &= \bar{E}_x(\xi)\alpha(\xi)\left[\left(1 - \frac{3\bar{w}_2}{4}\right)\cos\theta - \left(\frac{\bar{w}_2}{4}\right)\cos 3\theta\right] + \frac{3\bar{E}_x(\xi)}{4\chi\lambda^2}\bar{u}_2'\cos 2\theta \\ \bar{\kappa}_\theta(\xi, \theta) &= R\kappa_\theta(x, \theta) = -3\bar{w}_2\cos 2\theta\end{aligned}\quad (6.19)$$

Then the stipulation that the maximum compressive stress (at  $\theta = \pi$  for a positive bending moment) must remain below the critical buckling stress to remain stable generates the "critical stress" stability criterion:

$$\sqrt{\bar{D}_{11}(\xi)\bar{E}_\theta(\xi)}(1 - 3\bar{w}_2(\xi)) + \frac{3\bar{E}_x(\xi)}{4\chi\lambda^2}\bar{u}_2'(\xi) - \bar{E}_x(\xi)\alpha(\xi)[1 - \bar{w}_2(\xi)] > 0 \quad (6.20)$$

This criterion must be investigated at all points along the length of the cylinder. Buckling occurs when the inequality is first violated, and the maximum deformation of the buckled mode shape should form at that axial location.

### 6.3 Numerical Results and Comparisons

The investigation of the Brazier effect for tubes of finite length begins with the constant stiffness solutions. The effects of the length parameters involved in the solution, namely the shear length parameter  $\mu$  and the tube length parameter  $\lambda$ , are still largely unexplored, therefore the results will first attempt to qualify the behavior of the system with regard to these parameters. The effects of the collapse parameter  $\chi$  and the pressure  $\bar{p}$  were already investigated in Section 5.4.2

concerning infinite length tubes. Therefore, so as to concentrate on the effect of the length parameters, the initial study is restricted to unpressurized cylindrical shells for which  $\chi = 1$ . Once this behavior is understood, composite laminates and variable stiffness designs can then be fully investigated with confidence.

The nonlinear systems of Eq. (6.15) and (6.18) are solved numerically using Newton's method along with the finite difference technique. Though analytical solutions could be obtained for certain cases of the nondimensional parameters, the numerical technique is suitably efficient to fully explore the effects of the parameters on the solution. Stability is assessed through Eq. (6.20), and the moment-end rotation curves terminate when the Seide-Weingarten maximum buckling stress criterion is violated. For finite length cylinders, this mode of failure is the critical one (as opposed to a limit load in the load-displacement curve) for virtually all designs. Most of the collapse loads are presented in terms of the end rotation as opposed to the bending moment. This enables us to distinguish between collapse points more accurately, due to the fact that near collapse the load-displacement curve flattens out as it approaches a maximum moment, thus making it harder to locate the failure point in terms of the bending moment since all values are close in magnitude.

### 6.3.1 General Solution for $\lambda$ and $\mu$

The solutions of the two systems of differential equations given by Eq. (6.15) and (6.18) are shown in Figure 6.2 for an isotropic cylinder with  $\lambda = 5$  and  $R/H = 100$ . The boundary conditions are chosen as fixed ends. Both the axial and radial displacements, as well as the normalized shear strain, are plotted as a function of the axial coordinate for a load equal to the critical buckling end-

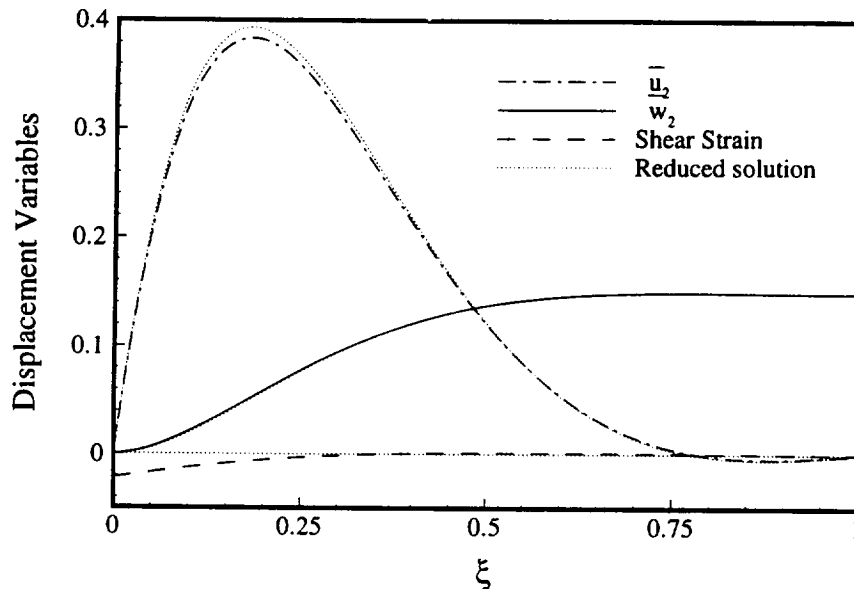


Figure 6.2: Displacement Profiles for Finite Length Cylinder under Bending

rotation of the structure. Several observations stand out from this figure. Firstly, notice the difference in the shape of the “membrane” boundary layer for the radial displacement  $\bar{w}_2$  when compared to the typical shell bending boundary layer evident in the axisymmetric results (see Figure 3.2). The membrane boundary layer extends much farther into the interior of the shell and produces a gentle transition from the maximum deformation at the mid-length to the condition of total restraint at the ends. Meanwhile, the axial warping represented by the  $\bar{u}_2$  function also possesses a “shear” boundary layer that is most easily apparent in the curve signifying the shear strain. Within this region, shear stresses develop that transform the ovalized cross-section back into a circle to satisfy the boundary conditions. It should also be noted that for the majority of the domain, the shear strain is effectively zero. The assumption of zero shear strain that is used in reduced system is denoted by the dotted lines in Figure 6.2. Note that the only region that this assumption does not hold true is near the ends, however the results indicate that the presence of the shear strain does not significantly affect the solution. The radial displacement profiles seem identical, while the axial deformation differs only slightly at its maximum value. This implies that the reduced system given in Eq. (6.18) that assumes zero shear strain everywhere may be valid for cylinders with a large shear length parameter.

Investigation of the sensitivity of the solution with respect to the length parameters is also desired. To this end, the applied bending moment as a function of end rotation is shown in Figure 6.3 for various values of  $\mu$  when  $\lambda = 1$ . Note that the smaller values of  $\mu$  increase the non-linear effect and lead to lower buckling loads. This is due to the fact that small values of the shear length parameter generate larger shear strain deformation, thereby allowing additional degrees of

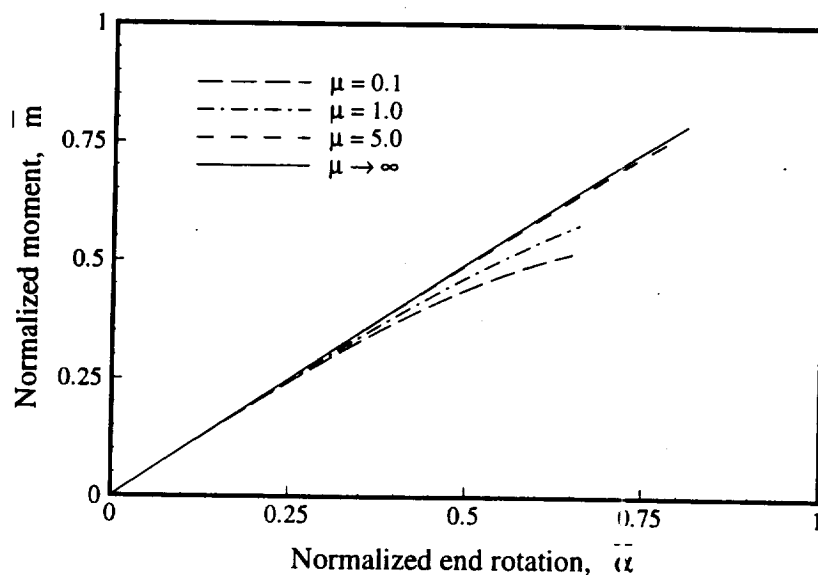
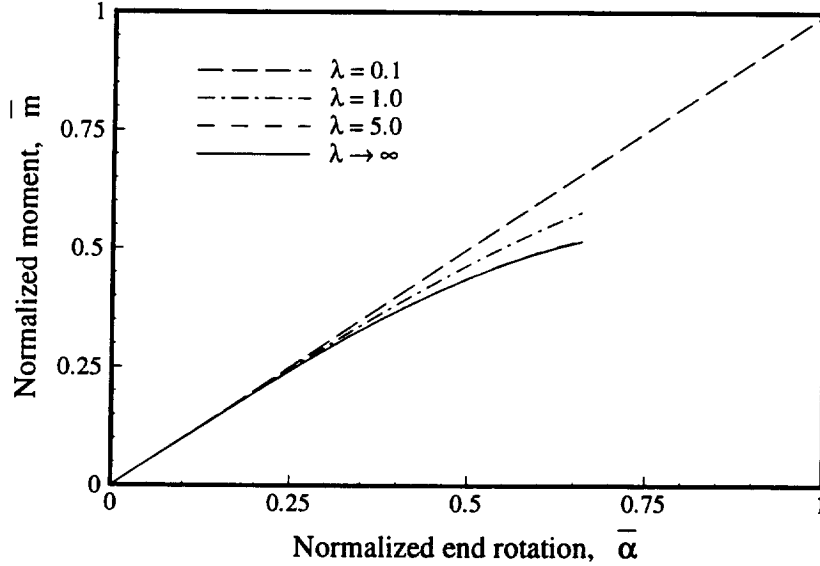


Figure 6.3: Moment vs. End Rotation for  $\lambda = 1$ , Fixed Ends



freedom and less stiff structures. In fact, the limiting case as  $\mu \rightarrow 0$  is the infinite length solution given by Eq. (5.26), where the radial displacement and axial loads do not depend on location along the length. For  $\mu > 5$  in Figure 6.3, the solution approaches the case of no shear strain ( $\mu \rightarrow \infty$ ), which corresponds to the system of Eq. (6.18).

Keeping  $\mu$  constant and choosing various values of  $\lambda$  leads to the load-displacement curves of Figure 6.4. Small values of the tube length parameter  $\lambda$  correspond to short and thin cylinders



**Figure 6.4: Moment vs. End Rotation for  $\mu = 1$ , Fixed Ends**

which do not undergo ovalization and are very susceptible to buckling, thus remaining in the linear range and collapsing at the classical value. As  $\lambda$  increases, the effect of the Brazier nonlinearity does as well, until it also approaches the infinite length solution given by Eq. (5.26). For this case, the maximum buckling stress stability criterion gives for the (isotropic) buckling loads:

$$\bar{\alpha}^{\infty} = 0.66012 \quad \bar{m}_y^{\infty} = 0.51629 \quad \bar{w}_2^{\infty} = 0.14525 \quad (6.21)$$

These values serve as a useful comparison to the finite length results.

Collapse loads due to local buckling are shown as a function of  $\lambda$  and  $\mu$  as a surface plot in Figure 6.5. The contour lines correspond to constant values of the critical buckling curvature  $\bar{\alpha}_{cr}$ . One can see that as the shear length parameter  $\mu$  increases, the contour lines become parallel, indicating that changes in the value of the shear length parameter do not significantly affect the solution once  $\mu$  is greater than five. For these regions, the collapse behavior is governed solely by the tube length parameter  $\lambda$ . Also note that many areas of the surface have critical curvatures which are *below* the infinite length value as given by Eq. (6.21). This is due to the boundary layers at the

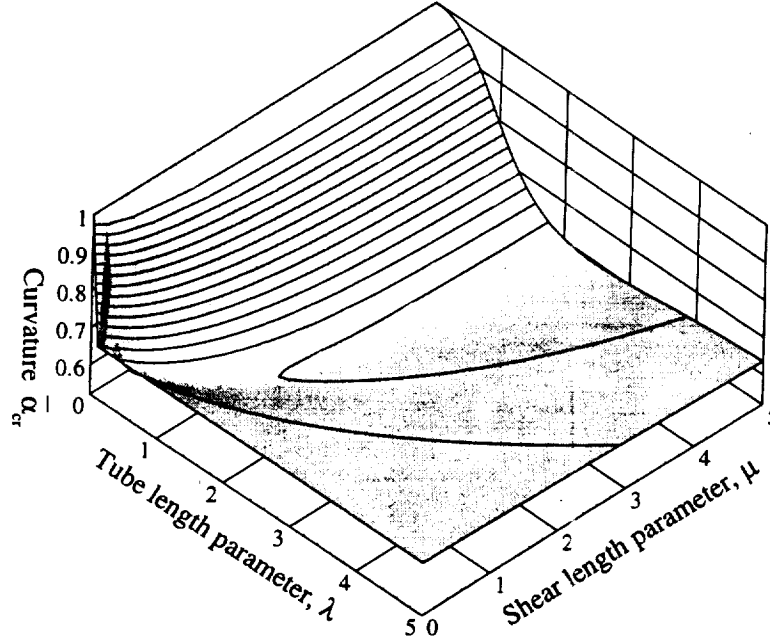


**Figure 6.5: Critical Curvature vs.  $\lambda$  and  $\mu$ , Fixed Ends**

edges which propagate throughout the structure and significantly alter the critical values of the axial stress resultant and circumferential curvature.

To provide a practical perspective of the parameters  $\lambda$  and  $\mu$ , they are expressed below in terms of a “material” and “geometric” portion:

$$\lambda = \sqrt[4]{\frac{9D_{22}^*}{4E_x^*H^3}} \cdot \frac{L}{R} \sqrt{\frac{H}{R}} \quad \mu = \sqrt{\frac{G_{x\theta}^*}{E_x^*}} \cdot \frac{L}{R} \quad (6.22)$$

Therefore, for a given material system, low values of  $\lambda$  (which produce very little Brazier effect) are generated by short and thin cylinders, and buckle according to the classical solution. Longer and thicker cylinders, which are more easily construed as “tubes”, undergo drastic Brazier nonlinearity before buckling occurs. Note how these conclusions reiterate the buckling results as a function of the radius-to-thickness ratio for an infinite length cylinder, discussed in Section 5.4.1. Additionally, the importance of the shear strain is only apparent for small values of  $\mu$ , i.e. shorter cylinders. Similar qualifying statements could be made for the material portion of Eq. (6.22), though the range of parameter values for typical material systems does not vary as greatly as those of the geometric part. To illustrate the point further, a surface plot for the critical curvatures of an isotropic cylinder as a function of length-to-radius ratio  $L/R$  and radius-to-thickness ratio  $R/H$  is displayed in Figure 6.6. As expected, short and thin cylinders undergo little Brazier nonlinearity, while the longer, thicker, tube-like cylinders behave closer to the infinite length case. Figure 6.6

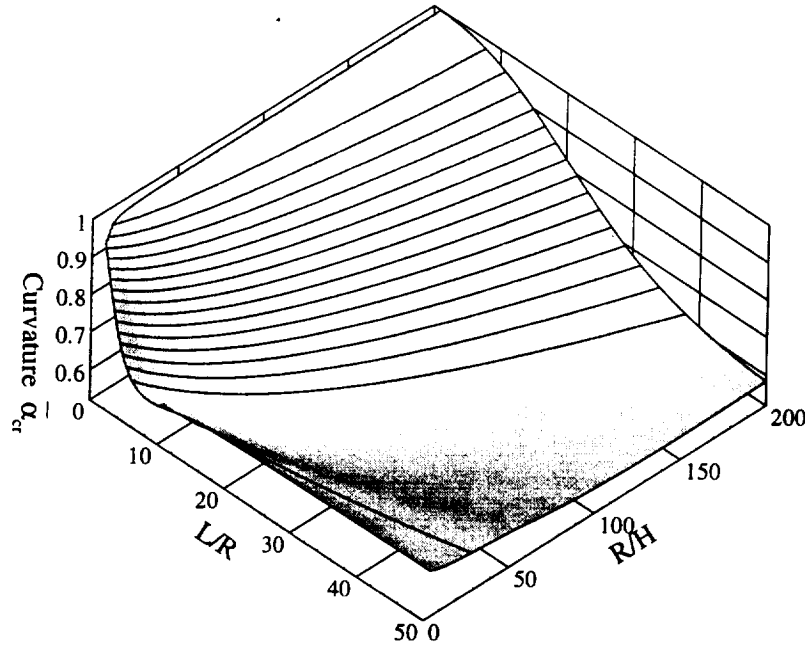


**Figure 6.6: Critical Curvature vs.  $L/R$  and  $R/H$  for an Isotropic Cylinder, Fixed Ends**

also reveals why it is preferred to employ the nondimensional parameters  $\lambda$  and  $\mu$ , as they approach a definite solution as they tend toward infinity.

### 6.3.2 Influence of Shear Length Parameter

We have seen in the previous results that the nonlinear solution does not significantly change for larger values of  $\mu$ . This must be investigated in greater detail, for if we can ignore the presence of shear strain (when  $\mu \rightarrow \infty$ ) we can reduce the system of Eq. (6.15) to the single ordinary differential equation of Eq. (6.18), thereby increasing the efficiency of the solution technique by eliminating unknown variables. To this end, the critical buckling curvature is shown as a function of the tube length parameter  $\lambda$  for various values of the shear length parameter  $\mu$  in Figure 6.7. The horizontal asymptote that the curves all approach as  $\lambda \rightarrow \infty$  is the infinite tube solution of Eq. (6.21). Small values of  $\mu$  arrive at this asymptote quite quickly, and thus for such a structure the effect of ignoring the shear strain for the Brazier problem ( $\mu \rightarrow \infty$ ) can lead to serious errors in the calculation of the buckling load. However, Figure 6.7 may be misleading in regard to the range of values that  $\mu$  can achieve. For example, specification of the material system for the cylinder under bending puts a lower bound on the value of  $\mu$  with respect to  $\lambda$ , since from Eq. (6.22)

$$\mu = \sqrt[4]{\frac{4G_{x\theta}^2 H^3}{9E_x D_{22}}} \cdot \sqrt{\frac{R}{H}} \cdot \lambda \quad (6.23)$$

The ratio of  $R/H$  must be greater than one half, else the structure is not a cylinder. Therefore, val-

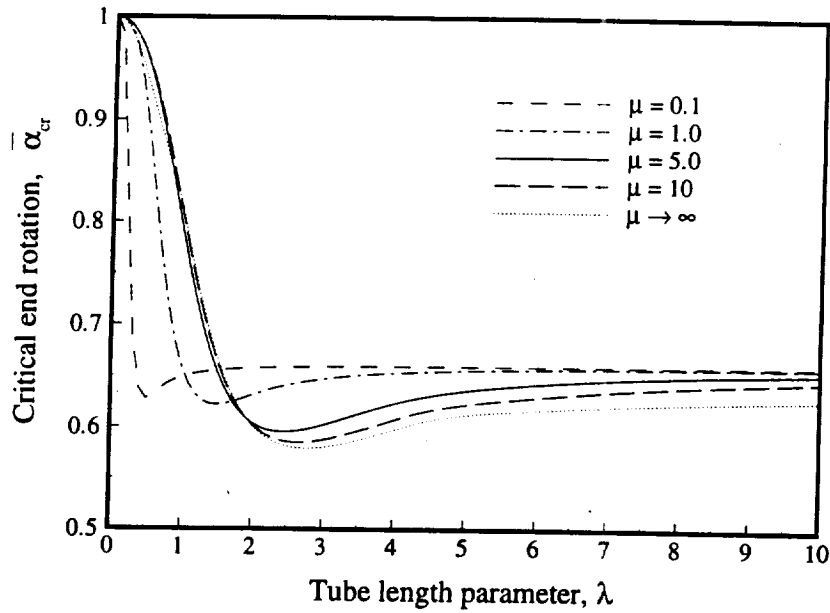


**Figure 6.7: Critical Curvature vs.  $\lambda$  for General Material, Fixed Ends**

ues of  $\mu = 1$  for large values of  $\lambda$  may not even be feasible. For instance, Figure 6.7 is reproduced for an isotropic cylinder for various values of radius-to-thickness ratios in Figure 6.8. One can see that all of the different thickness cylinders produce remarkably similar solutions, and that they all are analogous to the case which ignores the presence of the shear strain. The largest deviation from this case occurs for shorter, thicker cylinders, as expected. Similar results apply even to highly orthotropic materials, such as the graphite-epoxy AS3501 used by Corona & Rodrigues<sup>63</sup>

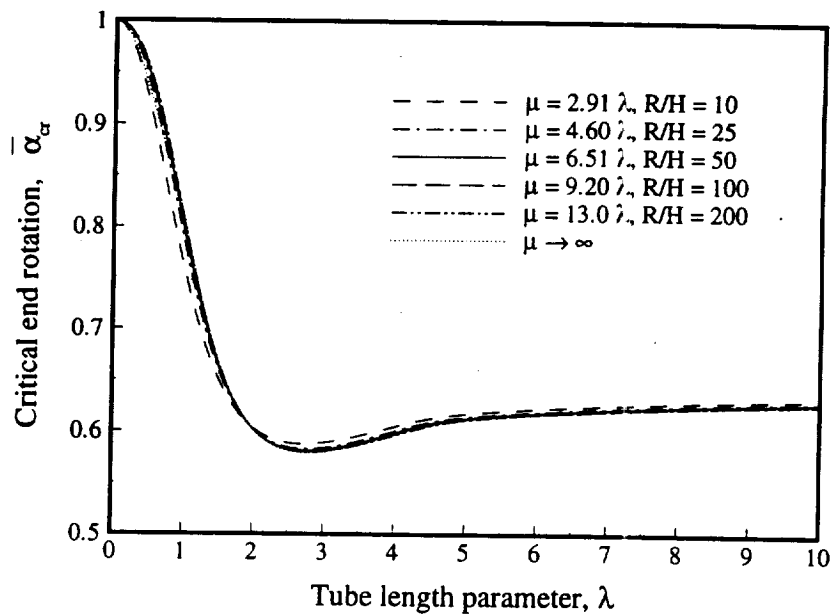


**Figure 6.8: Critical Curvature vs.  $\lambda$  for Isotropic Material  $\nu = 0.3$ , Fixed Ends**

for the study of infinite length tubes under bending. For this material,  $E_1/G_{12}$  is around 20 and  $E_1/E_2$  approximately 15, yet Figure 6.9 reveals that this material also approaches the case of no

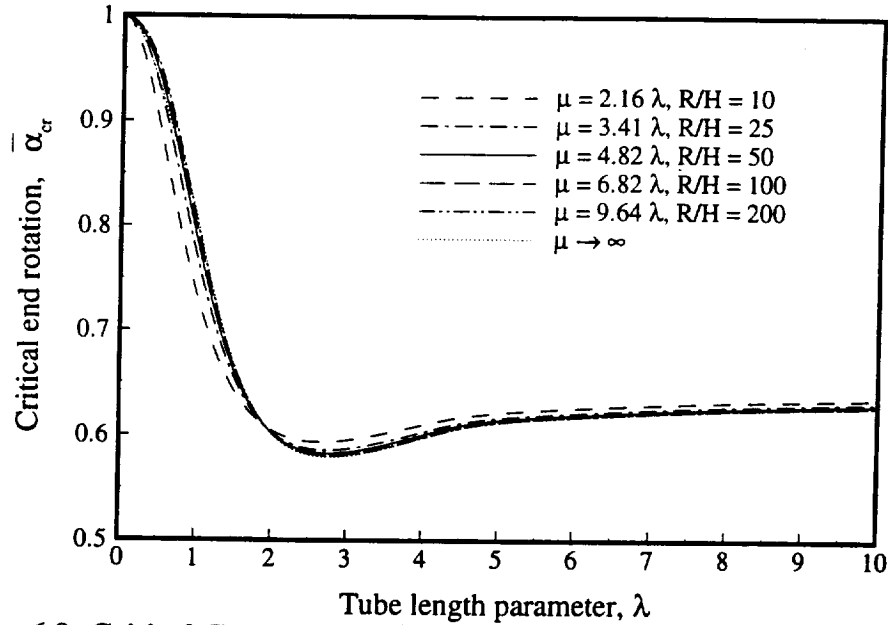


**Figure 6.9: Critical Curvature vs.  $\lambda$  for Orthotropic Material AS3501, Fixed Ends**

shear for thinner shells. Therefore, one can conclude that the shear warping due to the Brazier effect is not significant for most thin shells under pure bending, and that the simpler system of Eq. (6.18) can be used except for small values of  $\lambda$  and  $\mu$ .

### 6.3.3 Influence of Boundary Conditions

The results presented in the last two sub-sections have all been generated with the “fixed end” boundary condition. This case is considered more realistic, since most testing apparatus and structural applications involve a rigid plate or sturdy ring stiffener at the end of the cylinder. However, the “free end” boundary condition does occur in other tube bending applications, or more commonly, an elastic restraint which lies between the limiting cases of fixed and free is applied. Therefore, an investigation of the effect of the boundary conditions on the buckling characteristics and load-displacement behavior is warranted.

The surface image of Figure 6.5 for a fixed end cylinder is reproduced in Figure 6.10 as a contour plot, along with the corresponding level curves for a tube with free ends (dashed lines). Regions where the contours coincide are the values of  $\lambda$  and  $\mu$  for which the boundary effects have no effect. According to Figure 6.10, this is most easily apparent for small values of  $\mu$ , which approaches the infinite length case as it goes to zero. Though not evident on the scale of Figure 6.10, very small and very large values of  $\lambda$  also are independent of the boundary conditions. The small values of  $\lambda$  experience no Brazier deformation, while the large values generate

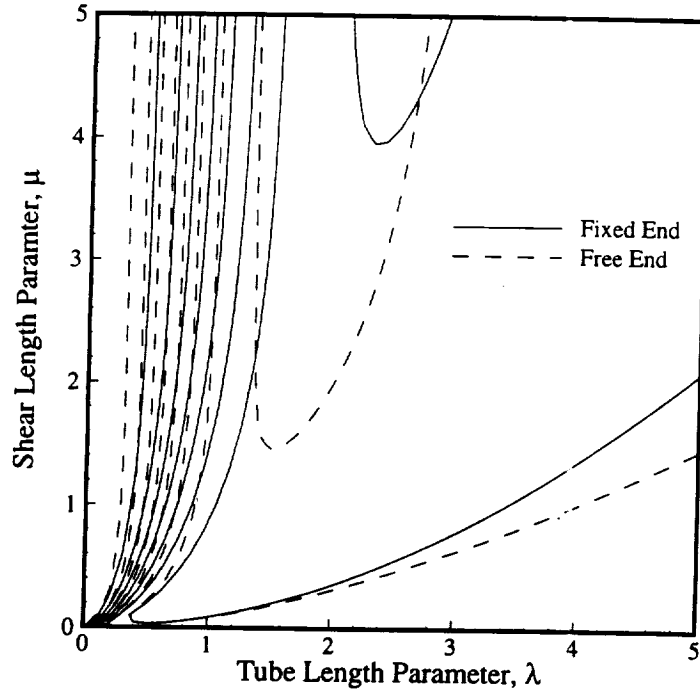


**Figure 6.10: Comparison of Critical Curvature for Fixed and Free End Condition**

the infinite case for which the boundary conditions have no effect. All intermediate values of both parameters, however, do produce solutions which vary significantly according to the end condition. In general, the free end allows for greater movement, thus producing more nonlinear ovalization and lower buckling loads. As an illustration of this, load-displacement curves and buckling load comparisons are performed for both end conditions for an isotropic cylinder with  $R/H = 100$ . First, moment and radial displacement versus end rotation for  $\lambda = 2$  are shown in Figure 6.11. As

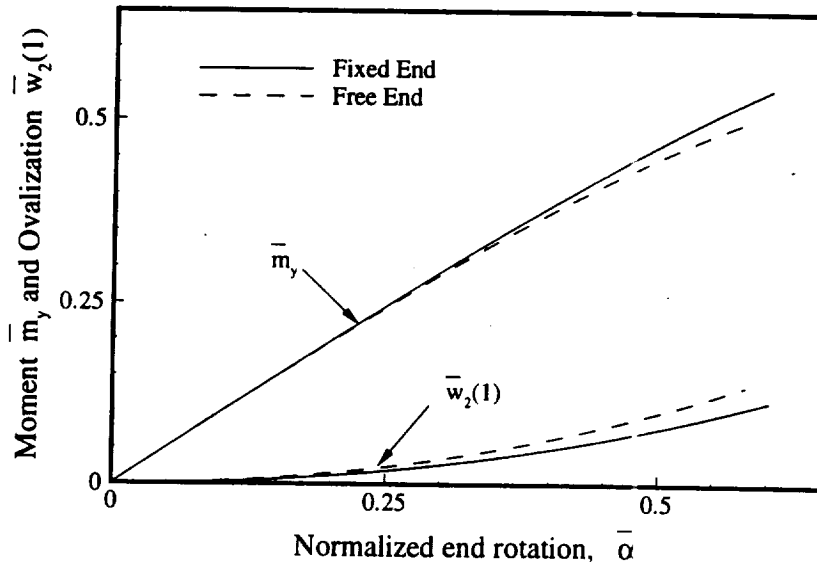


**Figure 6.11: Moment-End Rotation Curves for Fixed and Free Ends, Isotropic Material**

expected, the fixed end generates a stiffer structure due to the extra restraint applied to the displacements. Shown in Figure 6.12 is the critical end rotation and bending moment as a function

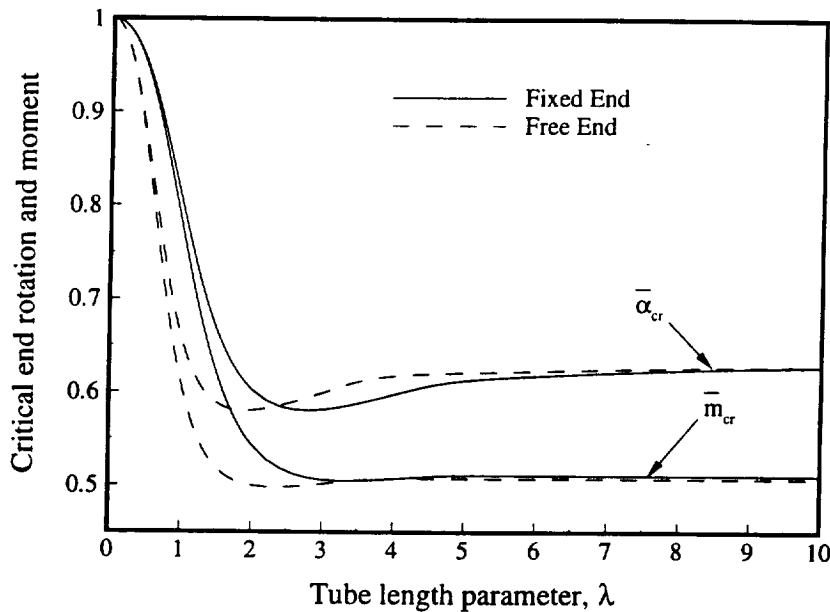


**Figure 6.12: Critical Curvature and Moment vs.  $\lambda$  for Fixed and Free Ends**

of  $\lambda$  for an isotropic material. Note how the free end case plummets much more quickly to the infinite length value as the tube length parameter is increased. This phenomenon is expected, since the fixed end provides a constraint to the deformation which leads to stiffer and more stable structures. Also note that the moments approach the asymptotic value of the infinite length case much faster than the end rotations, mostly due to the small slope of the load-displacement relation near collapse. This demonstrates the need to use the critical curvatures to define the buckling point since it provides greater distinction between different load levels.

#### 6.3.4 Comparison to Published Results

Few references exist concerning finite length tubes that are long enough for the Brazier effect to be significant. Most cylinders in structural applications are short or have ring stiffeners that inhibit the nonlinear ovalization. However, Stephens et al.<sup>66</sup> performed a nonlinear finite element analysis on various length isotropic cylinders under bending and pressure to measure the amount of ovalization and nonlinearity due to the Brazier effect. Their results were presented in terms of the amount of ovalization versus the applied bending moment, and are reproduced here in Figure 6.13 for various  $L/R$  ratios and compared to the present analysis using free end conditions. Collapse load calculations are also included (all load-displacement curves end at the critical load level), however Stephens et al. presumed that for infinite length cylinders the collapse load occurs

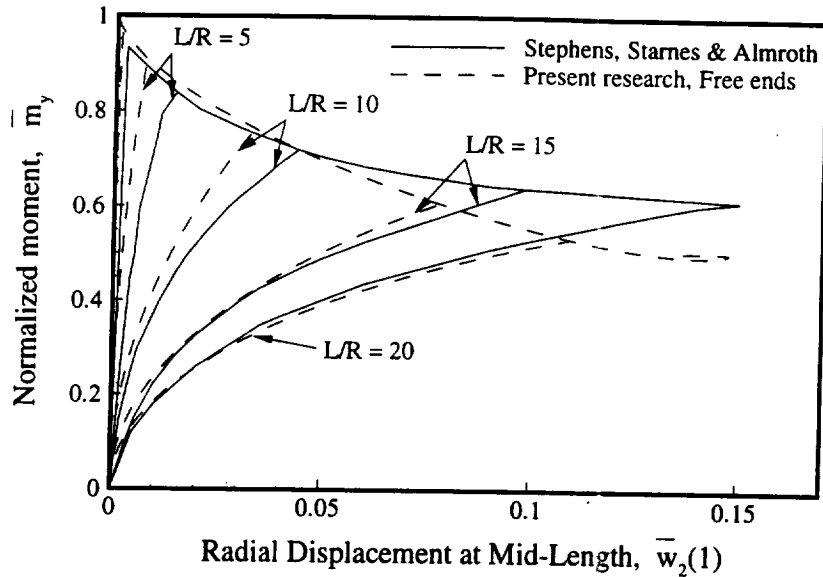


**Figure 6.13: Comparison to Stephens et al. for Moment vs. Radial Displacement**

due to the limit load of the Brazier effect. The results calculated here indicate that this is not the case (the structure experiences local buckling first) and so a discrepancy exists in Figure 6.13. Also note that the load-displacement curves use the free end condition since it was found that this boundary condition produced better correlation to the published work than the fixed end condition. This may be due to the constraints applied in the finite element solution, which did not exactly match either boundary condition. This comparison reveals that our solution agrees in principle with the published solution, though an exact match does not exist. These are attributed to two factors: the radial deformation is not as accurate a measurement of displacement as the applied end rotation; and the finite element solution offered limited choices for the buckling mode of the cylinder.

A more recent investigation of the Brazier effect for finite length tubes was performed by Libai & Bert<sup>67</sup>, who employed semi-membrane theory and the approximations of Brazier to produce systems analogous to the governing equations derived here. Approximate closed-form solutions using a simple Rayleigh analysis were generated for orthotropic tubes under the assumption that the shear strain is zero ( $\mu \rightarrow \infty$ ), and critical loads due to local buckling were estimated along the same lines as those presented here. A comparison of their closed-form solution to the numerical solution of the present work for isotropic cylinders is shown in Figure 6.14. Note that the critical load is presented in terms of the moment as opposed to the end rotation, which tends to minimize any discrepancies between the results for longer cylinders due to the small slope of the load-displacement curve near the critical point. The largest differences between the two studies



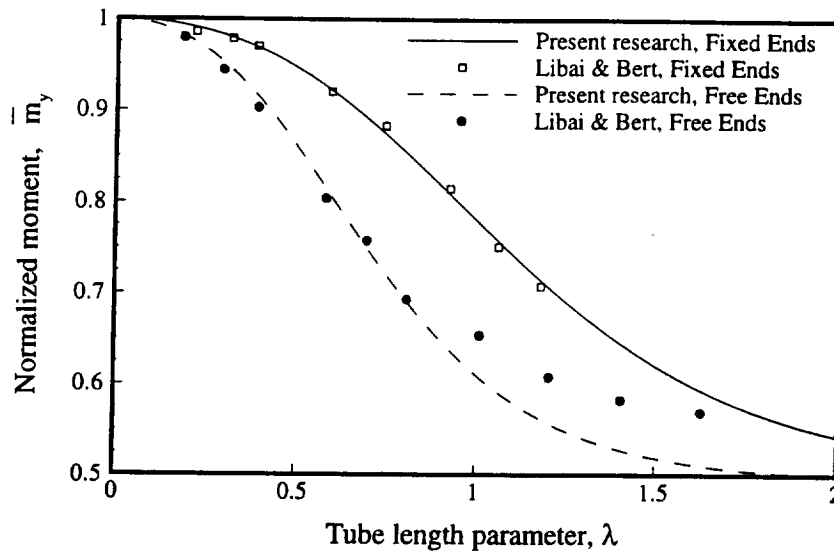


**Figure 6.14: Comparison of Libai & Bert to Present Research**

occurs for longer cylinders with the free end boundary condition. This error is due to the approximate solution technique used by Libai & Bert, which underestimates the nonlinearity for longer cylinders and overestimates the critical buckling load. Also notice that for small values of  $l$ , a slight discrepancy exists due to the inclusion of shear strain ( $\mu \neq \infty$ ) in our analysis.

## 6.4 Variable Stiffness Solutions

This section is intended to investigate the effect of variable stiffness designs on the performance of finite length cylinders under bending. In truth, the existence of the nonlinear Brazier effect is actually quite serendipitous for this investigation, for it provides an application that shows great promise for the use of the variable stiffness concept while also tying together the results of the other three specific design scenarios. Most cylindrical shells that undergo bending loads are constructed with frames and ring stiffeners which are required, among other things, to resist the ovalization associated with the Brazier effect. For such structures, the short cylinder analysis of Chapter 4.0 has demonstrated that designs with a circumferential stiffness variation exhibit a significant improvement in load-carrying capability and weight minimization. Likewise, the results of Chapter 5.0 show similar gains under bending for long cylinders with stiffness properties that vary around the cross-section. However, the application of an axial stiffness variation to a cylinder that undergoes predominantly axial stresses should follow the trends of the axisymmetric response under an axial force. Unfortunately, the conclusions from this investigation in Chapter 3.0 have revealed that little improvement is expected for an axial stiffness variation because the axial stiffness variation is bound to possess a weak link that will dominate the material failure and buckling response of the structure. These conclusions imply that an axial stiffness

variation will not enhance the response of short cylinders under bending. However, the significant cross-sectional ovalization that exists for long cylinders under bending does provide a likely avenue in which the variable stiffness concept can flourish, for the one aspect of the response that the concept is able to control is that of deformation. The main mechanism in this regard is providing an effective circumferential restraint for long cylinders that will reduce the Brazier deformation and act as an end condition. This technique should produce structures that possess greater load-carrying capabilities than constant stiffness designs, as well as more weight efficient cylinders that act as beams.

#### 6.4.1 Curvilinear Fiber Formats

To demonstrate the effectiveness of the variable stiffness concept for long cylinders under bending, this sub-section presents the results of a design study aimed at improving the buckling load of a relatively long cylinder. Curvilinear fibers are used to vary the stiffness parameters, and the path of the fiber is defined by the standard linked line segment approach. Comparisons are made to constant stiffness laminates that undergo stacking sequence optimization using a genetic algorithm. The optimization problem is represented as:

$$\begin{aligned} & \text{maximize } \bar{M}_y(T_i, \phi_k) \\ & \text{such that manufacturing constraints are satisfied} \end{aligned} \quad (6.24)$$

where the manufacturing constraints imply the maximum curvature of the tow path must not be exceeded. This design study is analogous to the curvilinear fiber path optimization presented in Section 3.6.2, so that the details need not be repeated here. The cylinder is defined to have a balanced, symmetric layup with 24 plies, which translates into twelve ply angle variables. The radius-to-thickness ratio is chosen to be 200 to correspond to the optimization for an infinite length shell (Section 5.5), and several length-to-radius ratios are investigated. The optimal constant stiffness solutions are presented in Table 6.1. The infinite length solution is also included to

<i>L/R</i> Ratio	Stacking Sequence	$\bar{\alpha}_{cr}$	$\chi$	$\bar{m}_{cr}$	$\bar{M}_y$ (lbs-in)
20	$[0_7/90_5]_S$	0.8118	2.135	0.7913	$6.111 \times 10^6$
50	$[90_2/0/90/0_5/90/0/90]_S$	0.6667	0.7877	0.6101	$3.416 \times 10^6$
100	$[90_2/0/90/0/90/0_5/90]_S$	0.7331	0.7077	0.6497	$3.420 \times 10^6$
$\infty$	$[90_2/0/90/0_2/90_2/0_4]_S$	0.7883	0.6906	0.6633	$3.441 \times 10^6$

**Table 6.1: Results of Optimization for Maximum Bending Load (Constant Stiffness)**  
show the effect of the finite length on the buckling load and the optimal stacking sequence. Note

that the applied bending moment is actually larger for the infinite length case, which is contrary to expectation. This is due to the end effects of the finite length cylinder that produce a boundary layer that is slightly less resistant to buckling than the other regions of the cylinder.

The results for the curvilinear fiber format cases, however, do not exhibit any significant improvement over any of these constant stiffness geometries. The hope is that the variation of the stiffness parameters will produce stiff regions along the length that act as ring stiffeners, so that at that location the radial deformation will be reduced and the nonlinear effect lessened. For example, shown in Figure 6.15 is the radial displacement profile of the long variable stiffness cylinder

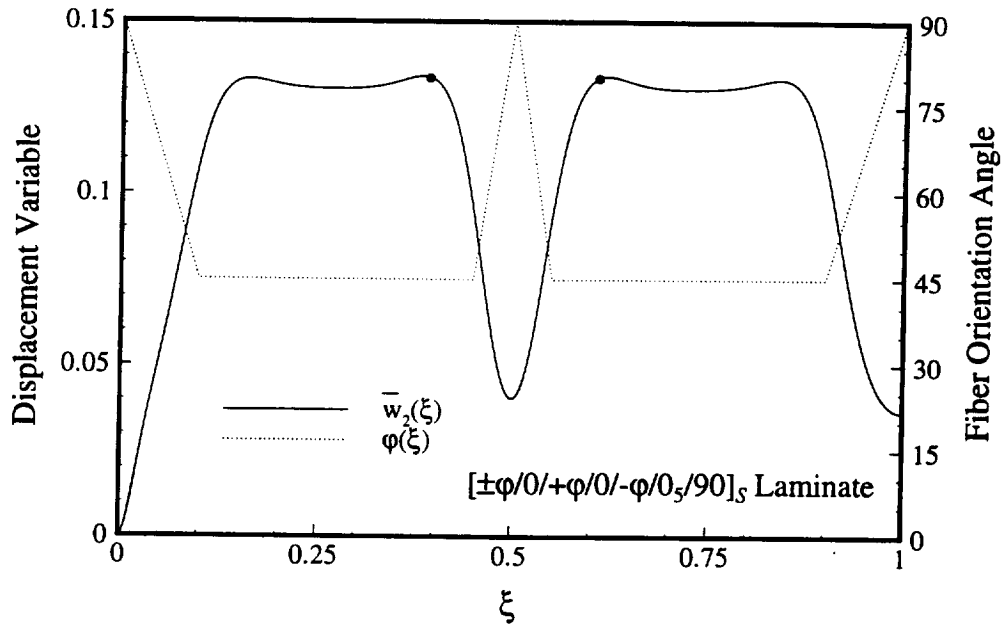


**Figure 6.15: Variable Stiffness Concept Example for Finite Length Cylinder under Bending**

( $L/R = 1000$ ) whose fiber orientation angle variation is denoted by the dotted line. As desired, the circumferentially stiff regions restrict the cross-sectional deformation to give the appearance of a ring-stiffened structure. The maximum buckling stress criterion indicates that buckling is most likely to occur at the points denoted by a filled circle. However, the critical buckling value of this design is quite low (less than 60%) when compared to the optimized value for a constant stiffness laminate. This is due to the fact that the optimal layup consists of a circumferentially stiff stacking sequence at all locations along the length. Thus to improve upon the design shown in Figure 6.15, the weak  $45^\circ$  areas should be replaced by the stiffer  $90^\circ$  layups since that stacking sequence performs the best for this geometry. This phenomenon resembles the weak link philosophy introduced for the axisymmetric case. The cylinder will buckle at the least resistance location, so that the optimal design should ideally consist of the best stacking sequence at all locations along the

length, which of course is simply a constant stiffness design. Therefore, though the application of the variable stiffness concept to this problem seemed promising, the results indicate that no significant improvement actually exists.

#### 6.4.2 Ring Stiffened Structures

Luckily, there still is a useful application for the finite length nonlinear bending problem. Though the curvilinear fibers could not produce the desired mechanism to increase the buckling load, ring stiffeners are perfectly suited for the task of decreasing the effective length of the cylinder. For example, the displacement profile of a cylinder under bending containing two sturdy ring stiffeners within the half-length is displayed in Figure 6.16. The ring stiffeners constrain the

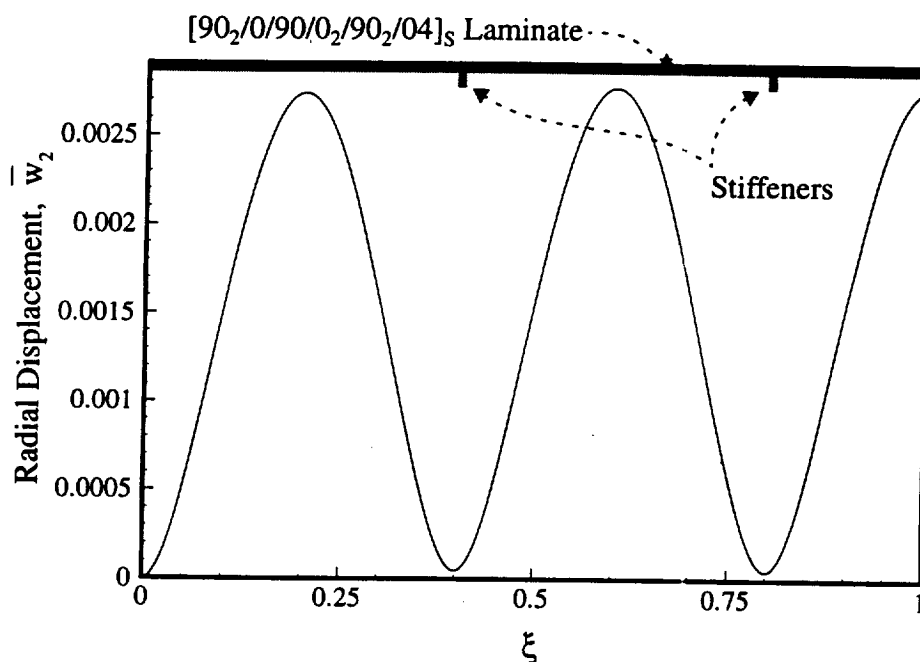
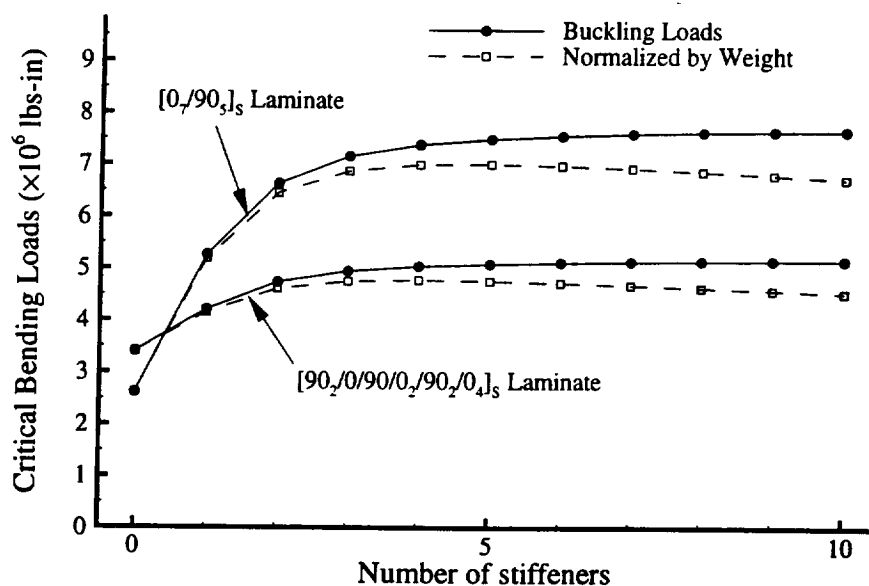


Figure 6.16: Example of Ring Stiffened Cylinder under Bending

cross-section to remain circular due to their relatively high circumferential stiffness, which decreases the span of the cylinder and improves the buckling load. The buckling locations are estimated to occur at the point midway between the stiffeners (at the point of maximum deformation). By placing the stiffeners closer together (or using more equally spaced stiffeners), one can improve the buckling load until it approaches the value for a short cylinder with no cross-sectional deformation. However, too many ring stiffeners would needlessly increase the weight of the structure, therefore a happy medium should exist with regard to the number of ring stiffeners. Therefore, this final section uses the finite length Brazier analysis to investigate the effect of ring stiffener spacing on the maximum buckling load.

The results are formulated for the  $L/R = 50$  cylinder from Table 6.1. The ring stiffeners are assumed to be blade stiffeners,  $1'' \times 2''$ , that are equally spaced along the length of the cylinder and constructed of a unidirectional graphite-epoxy material. Two stacking sequences are used, corresponding to the optimal layups for the shortest and infinite length cases from Table 6.1. The results are presented in Figure 6.17 in terms of the maximum bending moment, as well as a



**Figure 6.17: Buckling Moments versus Number of Ring Stiffeners for Finite Length Cylinder under Bending**

moment that is normalized by the relative weight of the structure. Notice that for no stiffeners, the infinite length stacking sequence provides the largest buckling moment, but once stiffeners are introduced the “short” cylinder layup is dominant. As expected, as the number of stiffeners increases, the maximum load does as well, however a limit point does exist (around five stiffeners for the short cylinder stacking sequence) after which adding stiffeners decreases the efficiency of the structure in terms of total weight. This simple design study demonstrates the worth of this analysis for ring stiffened cylinders, for it efficiently indicates the optimal stiffener spacing to use when nonlinear bending is an issue.

## Chapter 7.0 Concluding Remarks

The concluding remarks are grouped into four distinct sections, each which contains a summary of the major conclusions drawn from this investigation as well as future recommendations to further the research. The four sections deal with, respectively, the analysis of shell structures that contain general stiffness variations, the effect of an axial stiffness variation on the performance of a cylindrical shell structure, similar conclusions for a circumferential stiffness variation, and general results for nonlinear bending of long tubes.

### 7.1 Analysis of Variable Stiffness Shells

The presence of stiffness parameters that vary spatially within a shell structure demands a subtly different type of formulation than the typical constant stiffness structure. For this particular investigation, it was shown that the equilibrium equations contained derivatives of certain stiffness parameters that are not normally included in standard cylindrical shell analyses. Even when alternate formulations of the shell governing equations are used (such as a stress-based approach or the finite element method that integrates the stiffness parameters over a local region), attention must be focused on correctly including the effect of the stiffness variation. This study has successfully completed this goal for the subset of cylindrical shells with various stiffness variations and loading conditions. The method of formulation has also revealed to this author two conclusions regarding the analysis of cylindrical shell structures. First, that additional terms that do not exist in the standard formulation are required to correctly model the nonlinear bending problem for long tubes, and secondly that the best first approximation for the shell equations should be based on Sanders theory. This second conclusion is based on the fact that the numerical solutions using the Sanders-type expressions are only slightly more complicated than the Donnell-Mushtari-Vlasov shallow shell equations, yet they do not contain the inaccuracy for longer shells that DMV theory possesses. Of course, for many closed-form analytical solutions the simplicity of the shallow shell equations remains unchallenged, however it is believed that any general numerical solution should satisfy at least the level of accuracy of the Sanders approximations to be considered robust.

The introduction of the curvilinear fiber format for fiber reinforced laminates also presents some novel ideas for shell analysis and design. Firstly, the definition of the stiffness variation through the designation of the local value of the fiber orientation angle provides a meaningful

technique to ensure that the various stiffness terms represent a feasible structure. In fact, it may be advantageous to use this method to formulate a new “element” in standard finite element packages that can be defined via the spatial variation of the fiber orientation angle within the element. Typically, modern finite element codes either assume constant stiffness values within each element or require the definition of many stiffness parameters at several points within the domain, however it would be more efficient and accurate if the stiffness variation could be accounted for at the fundamental level of the fiber orientation angle. Furthermore, the representation of variable stiffness plies using the proposed curvilinear fiber definitions provides a realistic method to transform the theoretical design into actual parts through the use of the tow placement process. Coordination of the idealized fiber paths with computer controlled manufacturing techniques has been successfully demonstrated for flat panels, and can easily be extended to include general shells. Thus the use of curvilinear fibers can be a valuable tool in the design of high performance shell structures.

The analytical tools developed in this investigation possess one other advantage over many modern analysis techniques, that being the numerical efficiency of the solutions. The inclusion of ply drops and discrete stiffeners into the shell stiffness parameters (through the use of Classical Lamination Theory) provides a straightforward method to calculate the effect of these mechanisms without resorting to smearing their stiffness contributions over the total area or constructing cumbersome models that require large amounts of computational space and time. It is believed that in the future this variable stiffness technique can be used to generate an effective “global” shell analysis tool that provides excellent coordination with the detailed local models yet is still numerically efficient and able to accurately reflect the global effects of the problem. Such a tool would be a tremendous contribution to the present capabilities of modern shell analysis.

## **7.2 Axial Stiffness Variation for a Cylindrical Shell**

The investigation of cylinders containing a stiffness variation only in the axial direction revealed the most common form of material failure for variable stiffness structures, denoted here as the weak link phenomenon. In essence, the results indicated that for loads that do not change in the axial direction, the introduction of varying stiffness and strength parameters through the use of curvilinear fibers will never significantly improve the performance of the structure since it cannot effectively redistribute the applied loads. In the presence of these non-varying loads, there always exists some laminate stacking sequence that is best suited to withstand the resulting state of stress, and thus any deviation from that stiffness definition only detracts from the strength of the laminate. Though the variable stiffness concept under axisymmetric loading is able to affect the pre-buckling deformation and the critical location of failure stress, these effects did little to improve the global response of the structure. The only apparent advantage with regard to material failure was

limited to the various global stiffness and strength properties that could be achieved using curvilinear fibers, which may be advantageous in a design environment.

With regard to buckling behavior, the applicability of the axial stiffness variation produced mixed results. Firstly, it was shown that the possible negative effects of the prebuckling deformation on the nonlinear buckling load did not exist. That is, the non-flat deformation produced by the variation of the stiffness terms did not appear to act as a geometric imperfection, which severely affects the collapse behavior of cylinders under compression. Thus the membrane prebuckling solution could be used with relative confidence. Secondly, for loading that produced mainly axial stresses (such as axial compression or bending), the weak link phenomenon still applied due to the high axial frequency that exists for this type of loading. The buckling mode was simply concentrated in the region that contained stiffness properties that were the most susceptible to axial buckling, so that no improvement over constant stiffness laminates existed. Conversely, the load cases of external pressure and torsion exhibited much lower frequencies in the axial direction (dependent on the effective length of the cylinder), thus a stiffness variation that could significantly increase the axial frequency possessed the possibility of improving load-carrying performance. This basically means that the optimal stiffness variation should contain a region that is circumferentially stiff and approximates a ring stiffener. This technique was also shown to be instrumental to improve the buckling moment of long cylinders under bending, since a circumferentially stiff region could resist the ovalization due to the Brazier effect. Unfortunately, the results indicated that the stiffness variation based on varying the fiber orientation angle never produced enough stiffness disparity between regions to achieve this goal, while traditional ring stiffeners fulfilled this objective quite easily.

Though these results indicate little advantage for cylinders with an axial stiffness variation, it should be emphasized that the foregoing conclusions apply only to cases where the loads are constant along the length. For stress states that *do* vary in the axial direction, the introduction of the variable stiffness concept obviously promises tremendous advantage for the reasons just discussed. If the loading varies along the length, then each region possesses a particular stiffness configuration that is best suited to withstand that state of stress, and an excellent way to vary the local shell properties to correspond to the loading is through the mechanisms of the variable stiffness concept. Thus instead of the original desired mechanism of the variable stiffness concept, which was improving the load-carrying performance by redistributing the applied stresses, the application of an axial stiffness variation is better suited by designing the stiffness and strength properties to correspond to the local state of stress, such as cylinders acting as beams or ones with known concentrated and distributed loads acting along the length.



### 7.3 Circumferential Stiffness Variation for a Cylindrical Shell

The alternate possibility of stiffness variation presented in this investigation allows for fluctuation of the properties in the circumferential direction. For axial loading, the circumferential stiffness variation can now achieve the desired goal of redistributing the stresses so that the stronger regions carry the majority of the load. Unfortunately, this is not the case for pressure or torsion, since the distribution of the stresses from these loads do not depend on the local stiffness properties so that the failure is governed by the weak link concept. Therefore, the pressure and torsion cases do not indicate any improvement for shells with a circumferential stiffness variation. However the remaining load cases considered, namely an axial load, bending, and a transverse shear force, do depend strongly on the circumferential variation of the stiffness, and subsequently showed relative improvement over constant stiffness laminates in terms of material strength, global stiffness, and buckling characteristics. In general, the greatest improvements were realized for loads which also contained variation in the circumferential direction. For pure bending of short cylinder sections, the best designs tended to place the highest axial stiffness at the top and bottom of the cross-section, which maximized the global bending stiffness of the cylinder while simultaneously producing a region that behaved well under buckling due to an axial stress. For some designs, the stiffness variation was also able to produce a node at the top that relocated the critical buckling location away from the area of maximum stress. Likewise, for transverse shear force loading in which the maximum shear stress is located at the sides of the cylinder, the circumferential stiffness variation altered the distribution of the shear flow and spread the buckling deformation over a larger area. This tended to significantly increase the resulting buckling loads.

These preliminary positive results for a short cylinder segment with a circumferential stiffness variation lead to an in-depth optimization study of a fuselage structure under typical flight loads of internal hydrostatic pressure, an axial bending moment, and a vertical shear force. The formulation of the design problem was based on reducing the weight of a generic narrow body fuselage section that was subjected to typical flight load conditions. As a comparison, initial design studies were conducted for traditional isotropic and composite shells that also utilized longitudinal stiffeners and a crown/side/keel arrangement for fuselage construction. The results indicate that the response was dominated by the buckling characteristics of the structure under bending, and that the isotropic and composite designs were quite similar in geometry. The optimal solutions placed longitudinal stiffeners at the top and bottom to increase the stiffness and act as nodes for the buckling shapes. A comparison to these traditional design cases was conducted for (unstiffened) curvilinear fiber designs and crown/side/keel arrangements. It was found that the variable stiffness designs were both quite competitive to the traditional designs in terms of weight and structural

characteristics. Furthermore, it is believed that the variable stiffness designs also offer an advantage over the stiffened structures when it comes to production, since the curvilinear fiber shells can be constructed as one piece and do not require any further attachments. The ability of the variable stiffness shells to change their properties spatially is also a significant bonus when holes in the fuselage are required (such as doors or windows), since the laminate in that area can be designed differently from the top and bottom regions so that the effect of the hole is minimized. This feature of altering the stiffness properties can also be taken advantage of along the length of the fuselage, where the loading changes from bending to one dominated by internal pressure and the shear force. These areas do not require the added stiffness at the top and bottom of the fuselage, therefore significant weight savings and performance improvements can be achieved by combining the circumferential stiffness variation with alterations in the axial direction to produce a total variable stiffness fuselage structure.

#### **7.4 The Brazier Effect for Long Tubes**

The last problem studied in this investigation concerned the deformation resulting from pure bending of long cylinders. Due to the significant cross-sectional deformation associated with this problem, it was considered an excellent application for the variable stiffness concept due to its ability to control deformation and dictate the stiffness response. Initial investigation into this problem revealed that before the variable stiffness designs were studied, a thorough consideration of the basic mechanism was warranted since its highly nonlinear behavior needed to be quantified for general orthotropic cylinders. The formulation revealed that the standard cylindrical shell equations were not able to accurately reflect the true nature of the problem, and that additional nonlinear terms were needed in the governing equations to correctly represent the problem. Investigation of the resulting equations for infinite length and finite length constant stiffness cylinders revealed that the nonlinearity was strongly a function of cylinder length as well as stacking sequence and internal pressure, and that the usual failure mechanism was local buckling as opposed to a limit load phenomenon. However the cross-sectional deformation still played a major role in the determination of the critical load.

For variable stiffness structures, investigations of possible improvements over constant stiffness structures were attempted using both an axial and circumferential stiffness variation. The results revealed that the circumferential variation for extremely long cylinders worked reasonably well, with the optimal designs resisting the cross-sectional bending deformation yet still providing areas that could sufficiently withstand the impending axial buckling mode. However, these infinite length designs differed substantially from the short cylinder segment solutions, in which the region of maximum stress did not require any resistance to circumferential bending. This conclu-

sion was further evidenced by the results of the finite length cylinders, which indicated the disparity of the optimal stacking sequences for cylinders of various lengths. Attempts to improve the buckling load of finite length cylinders using an axial stiffness variation proved useless, since the possibility of redistributing the bending stresses or significantly restricting the cross-sectional deformation did not exist. Ring stiffeners again showed their dominance here, since their inclusion effectively reduced the length of the cylinder and negated the nonlinear deformation. Therefore, it is believed that the most effective way to increase the buckling loads of long cylinders under bending is either through a selective choice of a stacking sequence that is best suited to resist the nonlinear effect or including optimally spaced ring stiffeners to sufficiently control the cross-sectional deformation.

## References

1. Timoshenko, S. P., Woinowsky-Krieger, S., *Theory of Plates and Shells*, McGraw-Hill Book Company, New York, 1959.
2. Mishiku, M., Teodosiu, K., "Solution of an Elastic Static Plane Problem for Nonhomogeneous Isotropic Bodies by Means of the Theory of Complex Variables," *Journal of Applied Mathematics and Mechanics*, Vol. 30, No. 2, 1966, pp. 459-468.
3. Ashton, J. E., "Analysis of Anisotropic Plates II," *Journal of Composite Materials*, Vol. 3, 1969, pp. 605-615.
4. Dinardo, M. T., Lagace, P. A., "Buckling and Postbuckling of Laminated Composite Plates with Ply Dropoffs," *AIAA Journal*, Vol. 27, No. 10, October, 1989, pp. 1392-1398.
5. Pao, Y. C., "Momentless Design of Composite Structures with Variable Elastic Constants," *Journal of Composite Materials*, Vol. 3, 1969, pp. 605-615.
6. Leissa, A. W., Vagins, M., "The Design of Orthotropic Materials for Stress Optimization," *International Journal of Solids and Structures*, Vol. 14, 1978, pp. 517-526.
7. Muser, C., Hoff, N. J., "Stress Concentrations in Cylindrically Orthotropic Plates with Radial Variation of the Compliances," *Progress in Science and Engineering of Composites*, Eds. T. Hayashi, K. Kawata, and S. Umekawa, *ICCM-IV*, Tokyo, Vol. 2, 1982, pp. 389-396.
8. Martin, A. F., Leissa, A. W., "Application of the Ritz Method to Plane Elasticity Problems for Composite Sheets with Variable Fiber Spacing," *International Journal of Numerical Methods in Engineering*, Vol. 28, 1989, pp. 1813-1825.
9. Kuo, C. M., Takahashi, H., Chou, T. W., "Effect of Fiber Waviness on the Nonlinear Elastic Behavior of Flexible Composites," *Journal of Composite Materials*, Vol. 22, November, 1988, pp. 1004-1022.
10. Hyer, M. W., Charette, R. F., "The Use of Curvilinear Fiber Format in Composite Structure Design," *Proceedings of the 30th AIAA/ASME/ASCE/AHS/ASC Structures, Structural Dynamics and Materials (SDM) Conference*, New York, NY, 1989, pp. 2137-2145.
11. Hyer, M. W., Lee, H. H., "The Use of Curvilinear Fiber Format to Improve Buckling Resistance of Composite Plates with Central Holes," *Composite Structures*, Vol. 18, 1991, pp. 239-261.
12. Gürdal, Z., Olmedo, R., "Composite Laminates with Spatially Varying Fiber Orientations:

- Variable Stiffness Panel Concept," *Proceedings of the 33rd AIAA/ASME/ASCE/AHS/ASC Structures, Structural Dynamics and Materials (SDM) Conference*, Dallas, Vol. 2, April 13-15, 1992, pp. 798-808.
13. Gürdal, Z., Olmedo, R., "In-Plane Response of Laminates with Spatially Varying Fiber Orientations: Variable Stiffness Concept," *AIAA Journal*, Vol. 31, No. 4, April 1993, pp. 751-758.
  14. Tatting, B. F., Gürdal, Z., "Analysis of Variable Stiffness Composite Cylinders," *Proceedings of the Third Pan American Conference of Applied Mechanics (PACAM III)*, São Paulo, Brazil, January 4-8, 1993, pp. 608-611.
  15. Olmedo, R., "Compression and Buckling of Composite Panels with Curvilinear Fibers," M.S. Thesis, Virginia Polytechnic Institute and State University, 1992.
  16. Olmedo, R., Gürdal, Z., "Buckling Response of Laminates with Spatially Varying Fiber Orientations," *Proceedings of the 34th AIAA/ASME/ASCE/AHS/ASC Structures, Structural Dynamics and Materials (SDM) Conference*, La Jolla, CA, April 19-21, 1993, pp. 2261-2269.
  17. Waldhart, C.J., Gürdal, Z., Ribbens, C., "Analysis of Tow Placed, Parallel Fiber, Variable Stiffness Laminates," *Proceedings of the 37th AIAA/ASME/ASCE/AHS/ASC Structures, Structural Dynamics and Materials (SDM) Conference*, Salt Lake City, UT, April 15-17, 1996, pp. 2210-2220.
  18. Rice, J. R., Boisvert, R. F., *Solving Elliptic Problems Using ELLPACK*, Springer-Verlag, New York, 1985.
  19. Evans, D. O., Vaniglia, M. M., Hopkins, P. C., "Fiber Placement Process Study," *34th International SAMPE Symposium*, May 8-11, 1989, pp. 1822-1833.
  20. Enders, M. L., Hopkins, P. C., "Developments in the Fiber Placement Process," *36th International SAMPE Symposium*, April 15-18, 1991, pp. 778-790.
  21. Evans, D. O., "Design Considerations for Fiber Placement," *38th International SAMPE Symposium*, May 10-13, 1993, pp. 170-181.
  22. Eschenauer, H., Schuhmacher, G., Krammer, J., "Constructive Design Models for Multidisciplinary Optimization of Fiber Composite Structures," *Proceedings of the 4th AIAA/USAF/NASA/OAI Symposium on Multidisciplinary Analysis and Optimization*, Cleveland, OH, September 21-23, 1992.
  23. Nagendra, S., Kodiyalam, A., Davis, J.E., Parthasarathy, V. N., "Optimization of Tow Fiber Paths for Composite Design," *Proceedings of the 36th AIAA/ASME/ASCE/AHS/ASC Structures, Structural Dynamics and Materials (SDM) Conference*, New Orleans, LA, April 10-13, 1995, pp. 1031-1041.
  24. Brush, D. O., Almroth, B. O., *Buckling of Bars, Plates, and Shells*, McGraw-Hill Book Company, New York, 1975.
  25. Flügge, W., "Die Stabilität der Kreiszyinderschale," *Ingenieur-Archiv*, Vol. 3, 1932, pp. 463-

- 506.
26. Sanders, J. L., "An Improved First-Approximation Theory for Thin Shells," *NASA TR R-24*, 1959.
  27. Sanders, J. L., "Nonlinear Theories for Thin Shells," *Quarterly of Applied Mechanics*, Vol. 21, No. 1, April, 1963, pp. 21-36.
  28. Donnell, L. H., "Stability of Thin-Walled Tubes under Torsion," *NACA TR-479*, 1933.
  29. Donnell, L. H., "A New Theory for the Buckling of Thin Cylindrical Shells under Axial Compression and Bending," *Transactions of the American Society of Mechanical Engineers*, Vol. 56, November, 1934, pp. 795-806.
  30. Koiter, W. T., "The Stability of Elastic Equilibrium," Ph.D. Dissertation, Delft University, 1945. English translation by Riks, E., *AFFDL-TR-70-25*, 1970.
  31. Timoshenko, S. P., Gere, J. M., *Theory of Elastic Stability*, McGraw-Hill Book Company, New York, 1961.
  32. Batdorf, S. B., "A Simplified Method of Elastic-Stability Analysis for Thin Cylindrical Shells," *NACA Report 874*, 1947.
  33. Hoff, N. J., "The Perplexing Behavior of Thin Circular Cylindrical Shells in Axial Compression," *Israel Journal of Technology*, Vol. 4, No. 1, 1966, pp. 1-28.
  34. Bushnell, D., "Buckling of Shells - Pitfall for Designers," *AIAA Journal*, Vol. 19, No. 9, September, 1981, pp. 1183-1226.
  35. Stein, M., "The Influence of Prebuckling Deformations and Stresses on the Buckling of Perfect Cylinders," *NASA TR R-190*, February, 1964.
  36. Sobel, L. H., "Effects of Boundary Conditions on the Stability of Cylinders Subject to Lateral and Axial Pressures," *AIAA Journal*, Vol. 2, No. 8, August, 1964, pp. 1437-1440.
  37. Almroth, B. O., "Influence of Edge Conditions on the Stability of Axially Compressed Cylindrical Shells," *AIAA Journal*, Vol. 4, No. 1, January, 1966, pp. 134-140.
  38. Donnell, L. H., Wan, C. C., "Effect of Imperfections on Buckling of Thin Cylinders and Columns under Axial Compression," *Journal of Applied Mechanics*, Vol. 17, 1950, pp. 73-83.
  39. Hutchinson, J. W., Koiter, W. T., "Postbuckling Theory," *Applied Mechanics Review*, Vol. 23, 1970, pp. 1353-1356.
  40. Singer, J., Baruch, M., "Recent Studies on Optimization for Elastic Stability of Cylindrical and Conical Shells," *Proceedings of the 5th Congress of the International Council of the Aeronautical Sciences*, September, 1966, pp. 751-782.
  41. Tennyson, R. C., Hansen, J. S., "Optimum Design for Buckling of Laminated Cylinders," *Collapse: The Buckling of Structures in Theory and Practice*, University Press, Cambridge, 1982, pp. 409-429.

42. Brazier, L. G., "The Flexure of Thin Cylindrical Shells and Other 'Thin' Sections," *Late of the Royal Aircraft Establishment, Reports and Memoranda No. 1081, M.49.*, May, 1926, pp. 1-30.
43. Brazier, L. G., "On the Flexure of Thin Cylindrical Shells and Other 'Thin' Sections," *Proceedings of the Royal Society*, Vol. 116, Series A, 1927, pp. 104-114.
44. Wood, J. D., "The Flexure of a Uniformly Pressurized Circular, Cylindrical Shell," *Journal of Applied Mechanics*, Vol. 80, December, 1958, pp. 453-458.
45. Reissner, E., "On Finite Bending of Pressurized Tubes," *Journal of Applied Mechanics*, Vol. 26, September, 1959, pp. 386-392.
46. Reissner, E., "On Finite Pure Bending of Cylindrical Tubes," *Österreichisches Ingenieur-Archiv*, Vol. 15, 1961, pp. 165-172.
47. Reissner, E., Weinitschke, H. J., "Finite Pure Bending of Circular Cylindrical Tubes," *Quarterly of Applied Mechanics*, Vol. XX, No. 4, January, 1963, pp. 305-319.
48. Fabian, O., "Collapse of Cylindrical, Elastic Tubes Under Combined Bending, Pressure, and Axial Loads," *International Journal of Solids and Structures*, Vol. 13, 1977, pp. 1257-1270.
49. Bannister, K. A., "Direct Energy Minimization to Whipping Analysis of Pressure Hulls," *The Shock and Vibration Bulletin*, Vol. 54, Pt. 2, June, 1984, pp. 67-85.
50. Calladine, C. R., *Theory of Shell Structures*, Cambridge University Press, Cambridge, 1983.
51. Kedward, K.T., "Nonlinear Collapse of Thin-Walled Composite Cylinders Under Flexural Loading," *Proceedings of the 2nd International Conference on Composite Materials*, Toronto, April 16-20, 1978, pp. 353-365.
52. Spence, J., Toh, S. L., "Collapse of Thin Orthotropic Elliptical Cylindrical Shells under Combined Bending and Pressure Loads," *Journal of Applied Mechanics*, Vol. 46, June, 1979, pp. 363-371.
53. Birman, V., Bert, C. W., "Nonlinear Beam-type Vibrations of Long Cylindrical Shells," *Proceedings of the 27th AIAA/ASME/ASCE/AHS Structures, Structural Dynamics, and Materials (SDM) Conference*, San Antonio, May 19-21, 1986, pp. 564-568.
54. Stockwell, A. E., Cooper, P. A., "Collapse of Composite Tubes under End Moments," *Proceedings of the 33rd AIAA/ASME/ASCE/AHS/ASC Structures, Structural Dynamics and Materials (SDM) Conference*, Dallas, TX, April 13-15, 1989, pp. 1841-1850.
55. Tatting, B. F., Gürdal, Z., Vasiliev, V. V., "Nonlinear Response of Long Orthotropic Tubes under Bending including the Brazier Effect," *AIAA Journal*, Vol. 34, No. 9, September, 1996, pp. 1934-1940.
56. Baruch, M., Arbocz, J., Zhang, G. Q., "Imperfection Sensitivity of the Brazier Effect for Orthotropic Cylindrical Shells," *Delft University of Technology, Report LR-687*, Delft, The Netherlands, July, 1992.

57. Li, L.-Y., "Approximate Estimates of Dynamic Instability of Long Circular Cylindrical Shells under Pure Bending," *International Journal of Pressure Vessels & Piping*, Vol. 67, 1996, pp. 37-40.
58. Molyneaux, T. C. K., Li, L.-Y., "Dynamic Instability of Long Circular Cylindrical Shells under Pure Bending," *Thin-Walled Structures*, Vol. 24, 1996, pp. 123-133.
59. Aksel'rad, E. L., "Pinpointing the Upper Critical Bending Load of a Pipe by Calculating Geometric Nonlinearity," *Akademiya Nauk SSSR, Izvestia Mekhanika*, Vol. 4, 1965, pp. 133-139.
60. Reddy, B. D., Callandine, C. R., "Classical Buckling of a Thin-Walled Tube Subjected to Bending Moment and Internal Pressure," *International Journal of Mechanical Sciences*, Vol. 20, 1978, pp. 641-650.
61. Reddy, B. D., "An Experimental Study of the Plastic Buckling of Circular Cylinders in Pure Bending," *International Journal of Solids & Structures*, Vol. 15, 1979, pp. 669-683.
62. Aksel'rad, E. L., Emmerling, F. A., "Collapse Load Of Elastic Tubes Under Bending," *Israel Journal of Technology*, Vol. 22, 1984/85, pp. 89-94.
63. Corona, E., Rodrigues, A., "Bending of Long Cross-ply Composite Circular Cylinders," *Composites Engineering*, Vol. 5, No. 2, 1995, pp. 163-182.
64. Ju, G. T., Kyriakides, S., "Bifurcation and Localization Instabilities in Cylindrical Shells under Bending - II. Predictions," *International Journal of Solids & Structures*, Vol. 29, No. 9, 1992, pp. 1143-1171.
65. Karam, G. N., Gibson, L. J., "Elastic Buckling of Cylindrical Shells with Elastic Cores," *International Journal of Solids & Structures*, Vol. 32, No. 8/9, 1995, pp. 1259-1306.
66. Stephens, W., Starnes, J. H., Jr., Almroth, B. O., "Collapse of Long Cylindrical Shells under Combined Bending and Pressure Loads," *AIAA Journal*, Vol. 13, No. 1, January, 1975, pp. 20-25.
67. Libai, A., Bert, C. W., "A Mixed Variational Principle and its Application to the Nonlinear Bending Problem of Orthotropic Tubes - II. Application to Nonlinear Bending of Circular Cylindrical Tubes," *International Journal of Solids and Structures*, Vol. 31, No. 7, pp. 1019-1033, 1994.
68. Tatting, B. F., Gürdal, Z., Vasiliev, V. V., "Nonlinear Shell Theory Solution for the Bending Response of Orthotropic Finite Length Cylinders including the Brazier Effect," *Proceedings of the 36th AIAA/ASME/ASCE/AHS/ASC Structures, Structural Dynamics and Materials (SDM) Conference*, New Orleans, LA, April 10-13, 1995, pp. 966-976.
69. Tatting, B. F., Gürdal, Z., Vasiliev, V. V., "The Brazier Effect for Finite Length Composite Cylinders under Bending," *International Journal of Solids & Structures*, Vol. 34, No. 12, 1997, pp. 1419-1440.
70. Novoshilov, V. V., *Foundations of the Nonlinear Theory of Elasticity*, Greylock Press, Roches-



- ter, NY, 1953.
71. Leonard, R. W., "Nonlinear First Approximation Thin Shell and Membrane Theory," Ph.D. Dissertation, Virginia Polytechnic Institute and State University, 1961.
  72. Naghdi, P. M., Nordgren, R. P., "Nonlinear Theory of Elastic Shells," *Quarterly of Applied Mathematics*, Vol. 21, 1963, pp. 19-59.
  73. Budiansky, B., "Notes on Nonlinear Shell Theory," *Journal of Applied Mechanics*, Vol. 35, 1968, pp. 392-401.
  74. Jones, R. M., *Mechanics of Composite Materials*, Hemisphere Publishing Company, Washington D.C., 1975.
  75. Reddy, J. N., "A Review of Refined Theories of Laminated Plates," *Shock and Vibration Digest*, Vol. 22, No. 7, 1990, pp. 3-17.
  76. Tsai, S. W., Pagano, N. J., "Invariant Properties of Composite Materials," *Composite Materials Workshop*, Eds. S. W. Tsai, J. C. Halpin, and N. J. Pagano, Technomic Publishing Co., Stamford, CT, 1968, pp. 233-253.
  77. Miki, M., "Material Design of Composite Laminates with Required In-Plane Elastic Properties," *Progress in Science and Engineering of Composites*, Eds. T. Hayashi, K. Kawata, and S. Umekawa, *ICCM-IV*, Tokyo, Vol. 2, 1982, pp. 1725-1731.
  78. Gere, J. G., Timoshenko, S. P., *Mechanics of Materials*, PWS Publishing, Boston, MA, 1984.
  79. Vlasov, V. Z., *General Theory of Shells and Its Application in Engineering* (in Russian), Moscow-Leningrad, 1949. English translation NASA TT F-99, April, 1964.
  80. Vasiliev, V. V., *Mechanics of Composite Structures*, Taylor & Francis, Washington D.C., 1993.
  81. Langhaar, H. L., *Energy Methods in Applied Mechanics*, Robert E. Krieger Publishing Company, Malabar, FL, 1989.
  82. Thurston, G. A., "Roots of Lambda Matrices," *Journal of Applied Mechanics*, Vol. 45, December, 1978, pp. 859-863.
  83. Bushnell, D., "Stress, Stability, and Vibration of Complex Branched Shells of Revolution," *NASA CR-2116*, October, 1972.
  84. Nemeth, M. P., "Nondimensional Parameters and Equations for Buckling of Anisotropic Shallow Shells," *Transactions of the ASME*, Vol. 61, September, 1994, pp. 664-669.
  85. Seide, P., Weingarten, V. I., "On the Buckling of Circular Cylindrical Shells Under Pure Bending," *Journal of Applied Mechanics*, Vol. 28, March, 1961, pp. 112-116.
  86. Schröder, P., "Concerning the Stability of the Thin Walled Circular Cylindrical Shell Subjected to Shearing Force," *Über die Stabilität der querkraftbelasteten*, 1972, pp. 145-148 (Translated from German as NASA TT-21814).
  87. Niu, M. C. Y., *Airframe Structural Design*, Conmilit Press Ltd., Hong Kong, 1988.

88. Fuchs, J. P., "Numerical and Experimental Investigation of the Bending Response of Thin-Walled Composite Cylinders," Ph.D. Dissertation, Virginia Polytechnic Institute & State University, September, 1993.
89. Press, W. H., Teukolsky, S. A., Vetterling, W. T., Flannery, B. P., *Numerical Recipes in FORTRAN*, Cambridge University Press, Cambridge, 1986.
90. Meirovitch, L., *Analytical Methods in Vibrations*, MacMillan Publishing Company, New York, 1967.
91. Haftka, R. T., Gürdal, Z., *Elements of Structural Optimization*, Kluwer Academic Publishers, Boston, 1992.
92. Vanderplaats, G. N., "ADS - A FORTRAN Program for Automated Design Synthesis," NASA CR-177985, September, 1985.

# Appendix A. Numerical Techniques

This appendix presents the general solution techniques for the specialized governing equations presented in Chapters 3.0 through 6.0. Numerical methods are employed due to the relative complexity of the governing equations in terms of nonlinearity and the existence of variable stiffness coefficients. The four basic numerical techniques discussed in this appendix include the finite difference technique for the solution of linear ordinary differential equations, Newton's method for nonlinear problems, the Rayleigh-Ritz method as an auxiliary formulation of the eigenvalue problem, and the power method for the solution of the eigenvalue problem. A comparison of the finite difference technique versus the Rayleigh-Ritz method is also included. Additionally, numerical optimization techniques used for the design studies are discussed, and the accuracy and efficiency of the numerical techniques are investigated. The numerical techniques are implemented using the FORTRAN computer language, and certain numerical subroutines were obtained from the LAPACK algorithm library.

## A.1 Finite Difference Techniques for Linear ODE's

The equilibrium equations governing the static response of a variable stiffness cylindrical shell under various loading conditions are in the form of ordinary differential equations with boundary conditions specified at each end. Problems of this type are termed boundary value problems, as opposed to initial value problems which have prescribed conditions at only one point of the domain. For these initial value problems, the solution is quite straightforward, for all that is required is a step-wise numerical integration of the differential equation as the domain is traversed from the initial point. Because of the ease of this approach, numerical solutions of boundary value problems are often based on "shooting" methods, which generate an initial value problem at one end and vary some unknown parameters until the boundary conditions at the other end are satisfied. However, this method is not suitable for problems that involve complicated boundary conditions at each end, or ones in which the numerical integration of the differential equations is not easily accomplished. Therefore, the numerical technique used for our problems will instead be based on discretization methods, which solve the boundary value problem by defining the variables at discrete points within the domain that approximately satisfy the differential equations and the boundary conditions at each end. For this investigation, the finite difference technique will be

used. This choice is made due to its ease of implementation for variable coefficient differential equations, as well as its efficiency and accuracy for boundary value problems of this type. In this section, the primary concepts of the method will be discussed and illustrated with an example.

The basic premise of the finite difference method is to define the region of interest in terms of discrete points separated by a finite distance, and to approximate the unknown functions and their derivatives by the values at these given locations. The representation of the derivatives is based on the definition of differentiation through the theory of limits, which states that

$$f'(x) = \lim_{h \rightarrow 0} \frac{f(x+h) - f(x)}{h} \quad (\text{A.1})$$

For the finite difference technique, the limit parameter  $h$  is replaced by the finite distance  $\Delta$ , and the values of the function  $f$  at the two points are treated as the unknown variables:

$$f'(x) \approx \frac{f(x+\Delta) - f(x)}{\Delta} = \frac{f_{x+\Delta} - f_x}{\Delta} \quad (\text{A.2})$$

This equation conforms to a "forward difference" equation, since the derivative is based on functional values that occur in a forward direction from the original point. "Backward difference" and "central difference" equations can also be defined, where the latter can be shown to be the most accurate. Thus the central difference equations will be used here, and the higher-order derivatives, expressed in terms of  $\Delta$  and the functional values at equally spaced points  $x_i$ , are given as

$$\begin{aligned} f(x_i) &\approx f_i & f'(x_i) &\approx \frac{f_{i+1} - f_{i-1}}{2\Delta} & f''(x_i) &\approx \frac{f_{i+1} - 2f_i + f_{i-1}}{\Delta^2} \\ f'''(x_i) &\approx \frac{f_{i+2} - 2f_{i+1} + 2f_{i-1} - f_{i-2}}{2\Delta^3} & f''''(x_i) &\approx \frac{f_{i+2} - 4f_{i+1} + 6f_i - 4f_{i-1} + f_{i-2}}{\Delta^4} \end{aligned} \quad (\text{A.3})$$

Of course, the smaller the distance between points, the more accurate the derivatives become according to the theory of limits. Numerically, however, there are bounds for the value of  $\Delta$  due to the accuracy of the computing machines. If  $\Delta$  is too small, the solution may experience severe round-off errors due to the finite arithmetic used by the computer; while too large a value of  $\Delta$  will not accurately reflect the values of the derivatives.

Insertion of the approximate relations of Eq. (A.3) into a linear ordinary differential equation for the function  $f(x)$  transforms the differential equation into an algebraic one, in which the functional values  $f_i$  are the unknowns. Boundary conditions can also be expressed in terms of these unknown functional values, and the combination of the approximate differential equations in the interior of the region with the boundary conditions at the ends produces a unique solvable system

of algebraic equations. Of course, since the value of  $\Delta$  is usually small, the number of unknown variables can be quite large, thus numerical algorithms to solve large linear systems are employed. The finite difference technique has an added advantage here in that the form of the matrices used in this linear solution lends itself to efficient numerical solutions. This will become more apparent as we develop the finite difference equations with the help of an example.

To illustrate the finite difference method for a typical linear system, we use a simple example of the axisymmetric problem derived in Section 3.4, where the nonlinear terms will be ignored. This system has an independent variable of  $\xi$  and two unknown dependent variables: the radial displacement  $\bar{w}_0(\xi)$  and the constant axial force  $\bar{f}$ , and is reproduced here from the linearization of Eq. (3.15) as

$$\begin{aligned} \frac{(\bar{D}_{11}\bar{w}_0'')''}{4I^4} + \bar{E}_\theta\bar{w}_0 - \nu_{\theta x}\bar{f} &= \frac{\hat{N}_\theta^{cl}}{\hat{N}_x^{cl}}\bar{p} & \int_0^1 \left[ \frac{\bar{f}}{\bar{E}_x} + \frac{\nu_{x\theta}}{\bar{E}_x}(\bar{E}_\theta\bar{w}_0 - \nu_{\theta x}\bar{f}) \right] d\xi &= \bar{u} \\ \bar{w}_0(0) &= 0 & \bar{w}_0'(0) &= 0 \quad \text{or} \quad \bar{w}_0''(0) = 0 \\ \bar{w}_0'(1) &= 0 & \bar{w}_0'''(1) &= 0 \end{aligned} \quad (\text{A.4})$$

The system is well-posed, since we have a fourth order differential equation for  $\bar{w}_0$  along with four boundary conditions, and an algebraic (integral) equation for the solution of the constant  $\bar{f}$ . Note that the loading is introduced through the known constants  $\bar{u}$  and  $\bar{p}$ . The region of interest is defined as  $0 \leq \xi \leq 1$ , where the end point at  $\xi = 0$  is part of the boundary, and the interior region where the differential equation must be satisfied is divided by  $N$  equally spaced discrete locations, as shown in Figure A.1. Variable spacing of the finite difference points can also be used to investi-

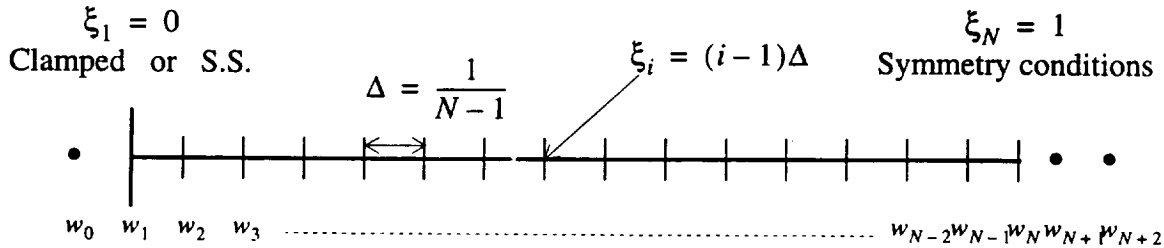


**Figure A.1: Finite Difference Representation of Region of Interest**

gate complicated regions in greater detail, though for our purposes it was found that the constant spacing was sufficient for accuracy as well as being easier to implement. Estimations of the stiffness and loading terms must be calculated at each endpoint  $\xi_i$ , and the solution will consist of

finding the values of the radial displacement at these locations. Since the differential equation is of fourth order, two finite difference points are required on both sides of each interior point. Thus, three more finite difference points must be defined so that the differential equation can be satisfied at each end of the interior domain ( $i = 2$  and  $i = N$ ), bringing the total number of unknowns to  $N+3$  plus the constant  $\bar{f}$ . The differential equation is applied at each interior finite difference location ( $\xi_i$ ,  $i = 2, N$ ), and inclusion of the integral equation and the four boundary conditions brings the total number of equations to  $N+4$  as well. Therefore we can use linear algebra techniques and formulate the problem in matrix form. All that remains is to transform the differential and integral equation into linear algebraic equations. This is accomplished using the central difference relations for the function  $\bar{w}_0$ , as well as assuming that the stiffness terms and their derivatives are fully defined at each finite difference location. Before developing the algebraic relations completely, however, we must examine the formulation for the boundary conditions and the integral equation.

The boundary conditions must also be expressed in terms of the unknown variables, which is a straightforward procedure for the problems investigated here. For example, for the axisymmetric problem the first boundary condition reveals that the left end is fixed against radial displacement, therefore we know that the value of  $\bar{w}_0(0) = w_1$  must be zero, thereby removing it as an unknown. Similarly, the clamped or simply supported boundary condition can be represented through the central difference equations, and the unknown variable  $w_0$  can be automatically calculated once the boundary condition is determined:

$$\begin{aligned} \text{Clamped: } \bar{w}_0'(0) = 0 & \Rightarrow w_0 = w_2 \\ \text{Simply Supported: } \bar{w}_0''(0) = 0 & \Rightarrow w_0 = 2w_1 - w_2 = -w_2 \end{aligned} \quad (\text{A.5})$$

Similarly at the other end, the symmetry condition also removes two unknowns:

$$w_{N+1} = w_{N-1} \quad w_{N+2} = w_{N-2} \quad (\text{A.6})$$

Thus the reduced linear problem is of order  $N$ , with  $N-1$  unknown radial displacements ( $i = 2, N$ ) and the unknown axial force coupled with  $N-1$  algebraic equations at each interior location ( $i = 2, N$ ) and the integral equation. This integral equation must also be transformed into an algebraic one, and this is accomplished by performing the integration using the trapezoidal rule:

$$\int_0^1 g(\xi, \bar{w}_0, \bar{f}) d\xi \approx \sum_{k=2}^N \left( \frac{g_k + g_{k-1}}{2} \cdot \Delta \right) \quad (\text{A.7})$$

Higher order representations of the integral for finite difference techniques do exist, however in

practice it was found that this simple trapezoidal rule generated the same results than the more accurate approximations, so its use will be retained here.

To complete the example, the algebraic system for the linear axisymmetric problem is formulated in terms of the unknown vector  $\vec{X}_i$ , where

$$\vec{X}_i = w_{i+1}, (i = 1, N-1) \quad X_N = \bar{f} \quad (\text{A.8})$$

Then the algebraic equations are presented as

$$\begin{aligned} & \left[ \frac{\bar{D}_{11} - \bar{D}_{11}'\Delta}{4(l\Delta)^4} \right] X_{i-2} + \left[ \frac{-4\bar{D}_{11} + 2\bar{D}_{11}'\Delta + \bar{D}_{11}''\Delta^2}{4(l\Delta)^4} \right] X_{i-1} + \left[ \frac{6\bar{D}_{11} - 2\bar{D}_{11}''\Delta^2}{4(l\Delta)^4} + \bar{E}_\theta \right] X_i + \\ & \left[ \frac{-4\bar{D}_{11} - 2\bar{D}_{11}'\Delta + \bar{D}_{11}''\Delta^2}{4(l\Delta)^4} \right] X_{i+1} + \left[ \frac{\bar{D}_{11} + \bar{D}_{11}'\Delta}{4(l\Delta)^4} \right] X_{i+2} + [-v_{\theta x}] X_N = \frac{\hat{N}_\theta^{cl}}{\hat{N}_x^{cl}} \bar{p} \end{aligned} \quad (\text{A.9})$$

$$\sum_{k=1}^{N-2} \left[ \left( \frac{v_{x\theta} \bar{E}_\theta}{\bar{E}_x} \right)_k \cdot \Delta \right] X_k + \left[ \left( \frac{v_{x\theta} \bar{E}_\theta}{\bar{E}_x} \right)_{N-1} \cdot \frac{\Delta}{2} \right] X_{N-1} + \left[ \int_0^1 \frac{1 - v_{x\theta} v_{\theta x}}{\bar{E}_x} d\xi \right] X_N = \bar{u}$$

where the first equation is evaluated for  $i = 1$  to  $N-1$ , and is slightly altered for  $i = 1, 2, N-2$ , and  $N-1$  due to the application of the boundary conditions. Formulation of these equations in matrix form  $A\vec{X} = \vec{B}$  reveals that the system is banded and bordered, which is displayed in schematic form in Figure A.2, where the open spaces denote zeroes of the matrix. The bandwidth for the

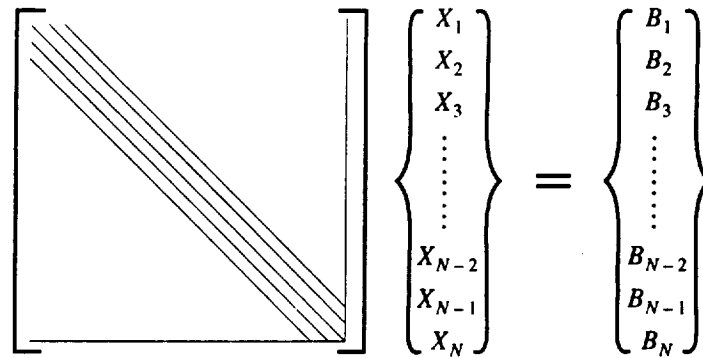


**Figure A.2: Matrix Structure for Finite Difference Technique**

matrix in this example is four, and Gaussian elimination is employed to solve for the unknown vector  $\vec{X}$ . Numerically, Gaussian elimination is much more stable and accurate than, for instance, matrix inversion by calculating determinants, and it also is quite efficient when applied to banded

matrices of this form. The bordered section of the matrix is dealt with through the use of the Woodbury formula (see Press et al.<sup>89</sup>), which preserves the banded nature of the matrix structure while still incorporating the influence of the bordered portion through the addition of a few matrix computations.

As a comparison to the example of the axisymmetric problem, the equilibrium solution for the Brazier problem for finite length cylinders with an axial stiffness variation generates a matrix of the same structure as the one shown in Figure A.2, except that the order of the matrix is  $\sim 2N$  and the bandwidth is eight due to the extra differential equation and variable present in that system. For the Brazier problem applied to infinite length cylinders, the linearized equation is even simpler because the bordered portion due to the presence of an unknown constant does not exist, therefore the Woodbury formula need not be invoked. These results for the linearized form of the nonlinear governing equations are important, for the following sections reveal that the numerical solution to these linear problems is vital to the calculation of the nonlinear response as well as the solution of the eigenvalue problem.

## A.2 Newton's Method for Nonlinear Problems

The finite difference technique discussed in the last section is one of many numerical techniques that works for linear problems, in which powers and multiplications of unknown variables do not exist. However, the equilibrium equations for a cylindrical shell undergoing loads that produce instability are usually nonlinear, for which these straightforward linear solution techniques are not applicable. In fact, it is generally believed that no generic solution techniques exist for an arbitrary nonlinear problem, for the presence of the nonlinearity produces multiple solutions of the equations which cannot necessarily be calculated using standard techniques. However, this does not mean that some important solutions to nonlinear problems cannot be found. For instance, nonlinearity in shell equilibrium solutions usually increases proportionally to the level of the applied loads. For the initial loading, the linear solution can be found; and as the load level increases the resulting nonlinear solutions can be calculated by finding a suitable configuration near the linear solution that satisfies the static equilibrium equations. This technique usually works adequately until a bifurcation point develops, for bifurcation implies a drastic change in the configuration that leads to a significant alteration in the response. Calculation of the resulting state after bifurcation is found through the application of postbuckling theory, and is beyond the scope of this investigation. Instead, we will employ nonlinear solution techniques for the prebuckling solutions, which can be based on perturbations from the linear solutions, and include the nonlinear effects to determine when bifurcation may occur. The nonlinear technique is iterative, in that it keeps updating the solution until the equilibrium equations are considered accurately satisfied. It



is based on Newton's method (also referred to as the Newton-Raphson method) for finding the roots of nonlinear equations using derivative information, which is extended to include ordinary differential equations of several variable.

A general nonlinear system containing ordinary differential equations with  $\xi$  as the independent variable and the vector  $\vec{X}$  as the dependent variable can be represented as

$$\vec{F}(\xi, \vec{X}, \vec{X}', \vec{X}'' \dots) = 0 \quad (\text{A.10})$$

where the vector  $\vec{F}$  is a system of nonlinear differential operators (for our problems of fourth order) and is a function of  $\vec{X}$  and its derivatives with respect to  $\xi$ . The system should be well-posed, so that the number of equations represented by  $\vec{F}$  is the same as the number of components in the unknown vector  $\vec{X}$ . The idea is to assume an initial solution  $\vec{X}_0(\xi)$  for the nonlinear system and use this basis to find a more accurate solution in the neighborhood of this solution. Of course, convergence depends highly on the accuracy of the initial solution. For our problems this choice is usually the linear problem, where we solve the differential equation without the nonlinear terms in  $\vec{F}$  using the finite difference technique already described.

Once an initial solution is chosen, we perturb the dependent variable such that

$$\vec{X} = \vec{X}_0 + \delta\vec{X} \quad (\text{A.11})$$

Substituting this assumed form into Eq. (A.10) and performing a Taylor series for  $\vec{F}$  about the original solution results in the following equation:

$$\left. \frac{\partial \vec{F}}{\partial \vec{X}} \right|_{\vec{X}_0} \delta\vec{X} + \left. \frac{\partial \vec{F}}{\partial \vec{X}'} \right|_{\vec{X}_0} \delta\vec{X}' + \left. \frac{\partial \vec{F}}{\partial \vec{X}''} \right|_{\vec{X}_0} \delta\vec{X}'' + \dots + O[\delta^2] = -\vec{F}(\xi, \vec{X}_0, \vec{X}_0', \vec{X}_0'' \dots) \quad (\text{A.12})$$

If the original solution is close to the correct one, then the forcing term  $\vec{F}$  on the right hand side will be small, as will be the solution to the correction  $\delta\vec{X}$ . Since these terms are small, we can neglect orders of  $\delta^2$  in Eq. (A.12). Thus we have formed a system of *linear* ODE's for the correction variables, which can be calculated using the linear solution in terms of finite difference techniques discussed in the last section. Then we can update the actual solution of  $\vec{X}$  using Eq. (A.11) and iterate until the correction terms converge to zero. Therefore the solution technique for the nonlinear problem is to solve a series of linear problems until we reach the desired accuracy, which is measured by either the relative changes of the dependent variables or the magnitude of the vector  $\vec{F}$ , where in practice both of these convergence criteria are usually considered.

For the integral equations that also arise in our nonlinear systems, a similar technique is used.

A general case can be represented as

$$\int_a^b G(\xi, \bar{X}, \bar{X}') d\xi = C_1 \quad (\text{A.13})$$

where this time  $G$  is a nonlinear function and is for our systems first-order at most. We also include the possibility of the limits  $a$  and  $b$  being unknowns. These variables must also have an initial guess, and are perturbed slightly to correct the solution:

$$a_1 = a_0 + \delta a \quad b_1 = b_0 + \delta b \quad (\text{A.14})$$

Again using a Taylor expansion for the unknowns and ignoring products of the correction terms results in the integral relation

$$\int_{a_0}^{b_0} \left( \frac{\partial G}{\partial \bar{X}} \bigg|_{\bar{X}_0} \delta \bar{X} + \frac{\partial G}{\partial \bar{X}'} \bigg|_{\bar{X}_0} \delta \bar{X}' \right) d\xi - \delta a G(a_0, \bar{X}_0, \bar{X}_0') + \delta b G(b_0, \bar{X}_0, \bar{X}_0') = C_1 - \int_{a_0}^{b_0} G(\xi, \bar{X}_0, \bar{X}_0') d\xi \quad (\text{A.15})$$

This integral is linear with respect to the correction variables  $\delta \bar{X}$  as well as  $\delta a$  and  $\delta b$ .

The relative complexity of the nonlinear solution technique is contained in the calculations of the derivatives of the nonlinear solution with respect to the unknown variables. These derivatives make up the matrix in the resulting linear system of equations, which is termed the Jacobian matrix. If the nonlinear equations are sufficiently complex, numerical techniques must also be used just to calculate the entries in the Jacobian matrix. However, for this investigation the analytical representation of the governing equations supplies the necessary relations so that the terms of the Jacobian matrix can be calculated in closed form. The order and matrix structure of the resulting system corresponds to that of the linear solution, so that the algorithms to solve the nonlinear problem consist mainly of updating the Jacobian matrix and forcing vector until the desired accuracy is attained. For the specific problems presented in this investigation, the effect of the nonlinearity did not produce any numerical problems (i.e. non-convergence due to a failure to find an equilibrium solution near the linear configuration) except for loads that were well past the bifurcation point of the structure. In fact, the nonlinear static solutions near bifurcation often hinted that a buckling point was imminent, such as the results shown in Figure 3.10.

### A.3 The Classical Rayleigh-Ritz Method for the Eigenvalue Problem

The Rayleigh-Ritz method has long been used for the solution of buckling and vibration problems in structural mechanics. Its origin began with the conception of Rayleigh's quotient to esti-

mate natural frequencies (eigenvalues) of conservative systems by assuming the resulting shape of the vibration mode. The Rayleigh-Ritz method is an attempt to improve these estimates by determining what the correct mode shape should be so that the eigenvalue calculation is more accurate. The designation of the “classical” Rayleigh-Ritz method is introduced so that the traditional procedures of this technique are differentiated from one of its popular descendants, the finite element method. An excellent introduction to the classical Rayleigh-Ritz method, as well as a discussion of its general formulation, convergence properties, and comparisons to the aforementioned finite element method, can be found in Meirovitch<sup>90</sup>. For our purposes, we will highlight only certain facts and procedures that are significant for the formulation of our buckling problems for variable stiffness cylinders.

The derivation of the governing equations for buckling (and vibration) problems using the Rayleigh-Ritz technique are usually formulated from energy methods for the system under study. For the cylindrical shell, these energy equations correspond to the expressions for potential energy and work done on the system that were introduced in Section 2.3, and contain at most second-order derivatives of the perturbed displacements  $(u_1, v_1, w_1)$ . The basis of the Rayleigh-Ritz method is to approximate the expected shape of these displacements using a linear combination of predetermined trial functions, which effectively discretizes the displacements and turns the differential eigenvalue problem into an algebraic one. The coefficients of the trial functions constitute the unknown buckling mode, so that the numerical solution using these variables generates estimates of the buckling modes and their critical values. The accuracy of the method depends greatly on the choice of the trial functions. These functions can be divided into three types, in terms of increasing accuracy: *admissible* functions, which need be differentiable only up to the order of the energy equations and only have to satisfy the geometric boundary conditions; *comparison* functions, which are differentiable to at least twice the order of the energy equations (which corresponds to the order of the governing equations in differential form) and must satisfy all the boundary conditions; and lastly, *eigenfunctions*, which fully satisfy the governing equations and boundary conditions and are linearly independent to each other. Of course, for complex systems, determination of the actual eigenfunctions is usually impossible, so that linear combinations of the admissible and comparison functions are used to approximate the true shape of the buckled mode. However, if the eigenfunctions for similar systems to the one under study are known, then the use of these as trial functions greatly improves the accuracy of this method.

It should be noted here that one of the main differences between the classical Rayleigh-Ritz method and the finite element method lies in the choice of these trial functions. The classical formulation traditionally chooses *global* functions, which are defined over the entire domain and

often belong to the same set of orthogonal functions, such as trigonometric functions or Bessel functions. As such, the requirements of differentiability are usually automatically satisfied, and the trial functions are chosen to satisfy as many boundary conditions as possible. In the finite element method, the trial functions are only defined in a *local* sense, in that each function only covers a portion of the domain, and are sometimes chosen to merely satisfy the minimum differentiability requirements. One advantage of the local aspect of the trial functions is that it can more accurately approximate abrupt changes in stiffness and loading definitions. The boundary conditions can also be rigorously satisfied using these local function definitions, however the convergence characteristics of this technique do not always follow the typical trends of the classical Rayleigh-Ritz method due to the fact that the trial functions are not linearly independent. For more detail in this matter, refer to Meirovitch<sup>90</sup>.

For this investigation, we will employ the classical Rayleigh-Ritz method for the solution of various cases involving buckling. Since exact eigenfunctions can be determined under certain loading and boundary conditions for constant stiffness cylinders, their use as comparison functions for variable stiffness cylinders generates very accurate results that converge quickly. An exception to this rule, however, is when the stiffness definition contains discrete and abrupt changes due to the presence of stiffeners or dropped plies. The global definitions for the trial functions have trouble approximating these sudden changes, as compared to the local definitions of the finite element method. However, finite difference techniques, which do not classify as Rayleigh-Ritz methods due to their nature of discretization, *can* incorporate these drastic stiffness changes since they also, in a sense, rely on local analysis of the domain. Thus it will be seen that the classical Rayleigh-Ritz method performs very efficiently for cylinders with well-behaved stiffness and loading definitions, while for structures containing significant stiffness changes the finite difference technique (or the finite element method if desired) proves more reliable.

The formulation of the Rayleigh-Ritz method for our problems can also be referred to as the assumed modes method. Examples of this technique have already been used for the solution of the classical buckling estimates of Section 1.2.2, whereby for these constant stiffness cylinders with their specialized boundary conditions the assumed modes actually turn out to be the eigenfunctions of the system. Therefore, these eigenfunctions are used as the basis for the trial functions for the general variable stiffness cylinder. The governing equations for the stability estimation of a cylindrical shell are in terms of the laminate stiffness measures, the perturbed displacements, and the rotations and stress measures which are the solution for the prebuckled state. The equations are displayed in differential form in Eq. (2.110)-(2.112), and can also be expressed as a surface integral, which is defined as the second variation of the potential energy. Neglecting the prebuck-

ling rotations (to save space here) results in

$$\begin{aligned}
 \delta^2 V = & \frac{1}{2} \int_0^L \left\{ A_{11}[(u_1')^2] + 2A_{12}[(u_1')(\dot{v}_1 + w_1)] + A_{22}[(\dot{v}_1 + w_1)^2] + A_{66}[(\dot{u}_1 + v_1')^2] + \right. \\
 & \frac{2B_{11}}{R}[(u_1')(-w_1'')] + \frac{D_{11}}{R^2}[(-w_1'')^2] + \frac{2D_{12}}{R^2}[(-w_1'')(\dot{v}_1 - \ddot{w}_1)] + \frac{D_{22}}{R^2}[(\dot{v}_1 - \ddot{w}_1)^2] + \\
 & \frac{D_{66}}{R^2}[(v_1' - 2\dot{w}_1')^2] + \frac{2D_{16}}{R^2}[(-w_1'')(\dot{v}_1' - 2\dot{w}_1')] + \frac{2D_{26}}{R^2}[(\dot{v}_1 - \ddot{w}_1)(v_1' - 2\dot{w}_1')] + \\
 & N_{x_0}[(w_1')^2] + N_{\theta_0}[(v_1 - \dot{w}_1)^2] + 2N_{x\theta_0}[(w_1')(v_1 - \dot{w}_1)] - \\
 & \left. pR[v_1(v_1 - \dot{w}_1) + w_1(\dot{v}_1 + w_1)] \right\} dx R d\theta
 \end{aligned} \tag{A.16}$$

For the Rayleigh-Ritz method, the trial functions for the perturbed displacements are in terms of trigonometric functions and divided into four modes, such that

$$\begin{aligned}
 u_1(x, \theta) &= \sum_{n=0}^N -U_I^n C_{n\theta} C_x + U_{II}^n S_{n\theta} S_x - U_{III}^n C_{n\theta} S_x - U_{IV}^n S_{n\theta} C_x \\
 v_1(x, \theta) &= \sum_{n=0}^N V_I^n S_{n\theta} S_x - V_{II}^n C_{n\theta} C_x - V_{III}^n S_{n\theta} C_x - V_{IV}^n C_{n\theta} S_x \\
 w_1(x, \theta) &= \sum_{n=0}^N W_I^n C_{n\theta} S_x + W_{II}^n S_{n\theta} C_x - W_{III}^n C_{n\theta} C_x + W_{IV}^n S_{n\theta} S_x
 \end{aligned} \tag{A.17}$$

The notation for the trigonometric functions is translated as

$$C_{n\theta} = \cos(n\theta) \quad S_{n\theta} = \sin(n\theta) \quad C_x = \cos\left(\frac{\beta x}{R}\right) \quad S_x = \sin\left(\frac{\beta x}{R}\right) \tag{A.18}$$

where the axial wavelength  $\beta$  is assumed to be an integer multiple of a base wavelength related to the length of the cylinder. Integration of Eq. (A.16) in both directions results in an expression involving squares and multiplications of the coefficients of the series expansions. For equilibrium, the derivative of the energy expression with respect to each of these independent variables must be zero. These leads to a complete system of linear algebraic equations for the unknown series coefficients for the perturbed displacements, which can be organized into standard matrix form. As such, the unknown vector  $\vec{X}$  representing these series coefficients is denoted as

$$X_{IA}^i = X[(3N + 3)(I - 1) + 3i + A] \tag{A.19}$$

where the superscript  $A$  defines which variable is being referenced ( $U = 1, V = 2, W = 3$ ) and the  $i$

and  $I$  indices represent the harmonic coefficient and mode, respectively. The terms in the stiffness and geometric stiffness matrices are likewise referenced as

$$k_{IA,JB}^{ij} = K[(3N+3)(I-1) + 3i + A, (3N+3)(J-1) + 3j + AB] \quad (\text{A.20})$$

A sample calculation of a matrix term reveals that the stiffness and loading definitions are being expressed in terms of a similar series expansion as the displacements, in this case in the circumferential direction. For instance, the  $D_{11}$  portion of one matrix entry is

$$k_{I3,I3}^{ij} = \oint_0^L \left\{ D_{11}(\theta) \beta^4 X_{I3}^i X_{I3}^j \cos(i\theta) \cos(j\theta) \sin^2\left(\frac{m\pi x}{L}\right) \right\} dx R d\theta \quad (\text{A.21})$$

The resulting integral in the circumferential direction is most easily evaluated when the stiffness term is expanded in a Fourier series, such that

$$D_{11}(\theta) = \frac{d_{11}^0}{2} + \sum_{k=1}^{\infty} d_{11}^k \cos(k\theta) \quad d_{11}^k = \frac{1}{\pi} \oint D_{11}(\theta) \cos(k\theta) d\theta \quad (\text{A.22})$$

Since the stiffness terms are symmetric about  $\theta = 0$  and  $\pi$ , only the cosine terms need to be included in the expansion. However, the prebuckling stress resultants  $N_{x_0}$ ,  $N_{x\theta_0}$  must also contain a sine term in the expansion due to the possible anti-symmetry of the beam loads. The resulting expressions for the matrix terms are given in Appendix B, and the resulting eigenvalue problem follows the matrix form for the finite difference technique. The terms in the geometric stiffness matrix are functions of the load level, so that the eigensystem becomes:

$$\begin{bmatrix} K_s & C & 0 & 0 \\ C^T & K_a & 0 & 0 \\ 0 & 0 & K_s & C \\ 0 & 0 & C^T & K_a \end{bmatrix} + \begin{bmatrix} N_s & S & V_s & M_s \\ S^T & N_a & M_a & V_a \\ V_s^T & M_a^T & N_s & S \\ M_s^T & V_a^T & S^T & N_a \end{bmatrix} \begin{bmatrix} I \\ II \\ III \\ IV \end{bmatrix} = 0 \quad (\text{A.23})$$

Two major differences do exist when compared to the finite difference formulation, in that the sub-matrices are now symmetric and full (as opposed to banded).

One advantage of using the classical Rayleigh-Ritz method for the eigenvalue problem is that it ensures that the matrices are symmetric when the expressions for the matrix elements are able to be derived from energy expressions. The symmetry of the matrices implies several favorable properties of the eigensystem. For example, it can be easily shown that the eigenvalues of real

symmetric matrices must always be real, thereby removing the need to investigate the imaginary plane. The expansion in terms of a finite sum of orthogonal functions (the Fourier series) also ensures that the inclusion principle holds. This very powerful result means that as you increase the number of terms in the expansion for the displacements, the resulting matrix includes the pre-existing eigensystem except for an addition of another row and column. The new eigenvalue that is created due to the higher order of the system will not be less than any eigenvalue from the lower order system, and in fact the old eigenvalue spectrum is “embedded” within the new one such that each eigenvalue is decreased. Thus the inclusion principle guarantees convergence from above for all eigenvalues, which is a very desirable feature for eigenvalue calculations. An iterative solution to find the lowest eigenvalue and associated eigenvector is introduced in the next section.

#### A.4 The Power Method for the Eigenvalue Problem

The eigenvalue problem using either the Rayleigh-Ritz method or finite difference techniques can be presented in a general form as

$$[K] \cdot \hat{d}_1 = \Lambda[M] \cdot \hat{d}_1 \quad (\text{A.24})$$

The eigensystem will be defined to be of order  $N$ , so that  $N$  eigenvalues and corresponding eigenvectors exist (usually the rank of  $[M]$  defines the order). However, our investigations only require an estimation of the critical, or lowest, eigenvalue and its associated mode shape, so that numerical algorithms that generate all characteristic values and buckled shapes are more robust than needed. Therefore, a method that only calculates the lowest eigenvalue and associated eigenvector is all that is desired so as not to waste computational time and expense. One such technique for the solution of the general eigenvalue problem is the power method. Not only does this method fulfill our needs of efficiency by only calculating the pertinent modes, but it also can be applied to symmetric *and* unsymmetric matrices, which occur when the finite difference technique is employed for the discretization of the domain. Systems that are not positive definite, such as when a critical load is calculated at a point along the nonlinear load path which is past the bifurcation point, can also be handled. Furthermore, the algorithms of linear algebra to solve the banded systems that occur for the static problems can again be used in the solution techniques using the power method.

The power method is based on the principle that the eigenvectors for a given matrix are linearly independent and that they represent a complete basis for the  $N$ -dimensional subspace. Thus, an arbitrary vector can be decomposed into a linear combination of the orthogonal eigenvectors:

$$\hat{d}_0 = \sum_{k=1}^N \alpha_k \hat{x}_k \quad (\text{A.25})$$

where the  $N$  eigenvectors are found from a general matrix such that

$$[A]\hat{x} = \Lambda\hat{x} \quad (\text{A.26})$$

Each eigenvector has a corresponding eigenvalue  $\Lambda_k$  associated with it, which are not necessarily distinct (i.e.  $\Lambda_1$  may be the same as  $\Lambda_2$ , but the associated eigenvectors  $\hat{x}_1$  and  $\hat{x}_2$  are still linearly independent). If we use the matrix  $[A]$  to multiply the arbitrary vector in an iterative fashion, the resulting vector can be expressed as

$$\hat{v}_p = [A]\hat{v}_{p-1} = \sum_{k=1}^N \alpha_k \Lambda_k^p \hat{x}_k \quad (\text{A.27})$$

since the eigenvectors are orthogonal to each other. Isolating the first term of the expansion and dividing by  $\Lambda_1$ , which will be defined as the largest among the  $N$  eigenvalues, results in

$$\hat{v}_p = \Lambda_1^p \left[ \alpha_1 \hat{x}_1 + \sum_{k=2}^N \alpha_k \left( \frac{\Lambda_k}{\Lambda_1} \right)^p \hat{x}_k \right] \quad (\text{A.28})$$

However, since  $\Lambda_1$  is by definition the largest eigenvalue, then the ratio in parentheses will converge to zero as the power  $p$  tends to infinity (hence the term “power method”), and the iterated vector will be equal to a scalar multiple of the eigenvector associated with the dominant eigenvalue. Convergence to this fundamental eigenvector depends greatly on the value of the ratio that is being increased exponentially. A special case exists when there are repeated eigenvalues corresponding to the largest one, but it can be shown that even for this case the resulting eigenvalue and iterated eigenvector correctly satisfy the solution to the eigenvalue problem, though convergence may be slow.

The power method applied to our specific problems follows the basic theory as presented above with some slight differences. For instance, our eigensystem is constructed of two matrices as in Eq. (A.24) instead of the single square matrix  $[A]$ . Furthermore, we desire the *smallest* eigenvalue and associated eigenvector as opposed to the largest one, and want also to speed up the convergence rate for closely spaced eigenvalues. These alterations are performed by assuming that the eigenvalue is composed of a known “shift”  $\mu_s$  plus the calculated eigenvalue  $\lambda_s$ , so that Eq. (A.24) is rewritten as

$$\Lambda = \mu_s + \lambda_s \quad ([K] - \mu_s[M]) \cdot \hat{u}_1 = \lambda_s[M] \cdot \hat{u}_1 \quad (\text{A.29})$$

Rearrangement and use of a negative power to denote matrix inversion results in



$$([K] - \mu_s[M])^{-1}[M] \cdot \hat{u}_1 = [A] \cdot \hat{u}_1 = \frac{1}{\lambda_s} \hat{u}_1 \quad (\text{A.30})$$

This form now corresponds to that of Eq. (A.26), except that now the power method will produce the largest value of  $(1/\lambda_s)$ , equivalent to the smallest value of  $\lambda_s$ . Furthermore, convergence now depends not on the ratios of the eigenvalues, but instead on the quantity

$$\left( \frac{\Lambda_k - \mu_s}{\Lambda_1 - \mu_s} \right)^p \quad (\text{A.31})$$

When the shift is chosen to be zero, the power method will find the lowest eigenvalue and associated eigenvector as shown earlier, while a constant shift will produce the eigenvalue that is closest to the value of  $\mu_s$ . Therefore, convergence can be greatly enhanced when looking for the critical eigenvalue by using a shift value that is nearest the lowest one. Of course, some care must be taken in the choice of the shift value, for if its magnitude is closer to a different eigenvalue than the resulting solution will not correspond to the critical one. It should also be noted that a value of  $\mu_s$  which exactly corresponds to an eigenvalue does not actually present a problem. This is due to the fact that the inversion of the matrix in Eq. (A.30), which is singular when the shift value is equal to any eigenvalue, is numerically performed using Gaussian elimination through *LU* decomposition, which is very stable even for nearly singular matrices. The numerical algorithm when implemented with a computer also generates some leeway in this respect, for actual equality of real numbers rarely exists when using finite arithmetic. In fact, the algorithm converges fastest when the shift value is chosen as close to an eigenvalue as possible, and this method, also known as inverse iteration, is often used to find the eigenvectors when the eigenvalues are already known.

Another factor that greatly affects the operation of the power method is the initial choice of the vector that is being iterated. If it is equal to an actual eigenvector than the iterative solution should return the same vector multiplied by a scalar corresponding to the eigenvalue, which is one factor which determines convergence. Furthermore, the initial choice of the vector can also be used to limit the possibilities of the solutions so that symmetry considerations can be fully investigated. For instance, a simplified form of the eigenvalue problem, given in Eq. (A.23), involving symmetric loading of a variable stiffness shell, can be rewritten as

$$\begin{bmatrix} K_s & C \\ C^T & K_a \end{bmatrix} \begin{bmatrix} I \\ II \end{bmatrix} = \Lambda \begin{bmatrix} N_s & S \\ S^T & N_a \end{bmatrix} \begin{bmatrix} I \\ II \end{bmatrix} \quad (\text{A.32})$$

Here we will assume that either the finite difference technique or the Rayleigh-Ritz method has

been used to transform the original differential eigenvalue problem into this algebraic one, where each sub-matrix is now  $3N \times 3N$  and the eigenvector contains a symmetric mode  $I$  and an anti-symmetric mode  $II$ . If there are no coupling effects or shear loading, the two modes become decoupled. Therefore, if the original vector used in the power method has non-zero terms only in the symmetric portion of the vector, then the resulting solution will contain the critical eigenvalue and associated eigenvector for the symmetric case only. Thus to include the possibility of an anti-symmetric buckled shape, the algorithm should be performed again with a vector containing some anti-symmetric terms. In practice, it was found that the most efficient approach was to iterate two vectors at once: one with only symmetric terms and the other with non-zero values only in the anti-symmetric portion. The overall critical eigenvalue is then the lowest of the two. This method also works well when torsion and/or coupling *are* present, for each vector tended to produce the dominant shape for each respective mode (which were sometimes identical). This technique is also used for modes  $III$  and  $IV$  associated with anti-symmetric circumferential loading.

Lastly, the efficiency of the power method is chiefly due to the fact that only one or two eigenvectors and eigenvalues are actually being calculated, as opposed to general canned subroutines which typically solve for the whole system. When the finite difference technique is used, the matrices that need be inverted are in banded form, and thus can be factored using Gaussian elimination quite efficiently. For the Rayleigh-Ritz method, the matrix structure is not banded but does possess the added advantage of symmetry, so that the inclusion principle and convergence of an eigenvalue from above, discussed in the last section, are applicable. For the non-symmetric matrices resulting from the finite difference technique, some discrepancy may occur due to the possibility of complex eigenvalues, however it was found that for our class of problems the power method did generate the results for all cases that corresponded to non-imaginary configurations.

## A.5 Finite Difference Techniques versus the Rayleigh-Ritz Method

In this section, we will contrast the use of two different numerical methods, namely the finite difference technique and the Rayleigh-Ritz method, to determine which one works most efficiently and accurately for a typical problem from this work. The example problem to be used is the linear stability estimate from Chapter 4.0. Both of these numerical techniques are used to solve the static equilibrium and eigenvalue problems detailed in that chapter (in truth, the solution of the static equilibrium equations using an expansion in terms of sines and cosines is not technically the Rayleigh-Ritz method, but will be referred to as such for this discussion). Each method has a size parameter  $N$  associated with it which represents the number of unknown variables in the problem. For the finite difference technique, this parameter  $N$  is defined as the number of finite difference points within the domain, while for the Rayleigh-Ritz technique it describes the num-

ber of terms used in the expansion of the displacements. Larger values of  $N$  should lead to increased accuracy, but also decreased efficiency with respect to the numerical algorithms. Results of the numerical techniques with respect to the size parameter are shown in Figure A.3 for a typi-

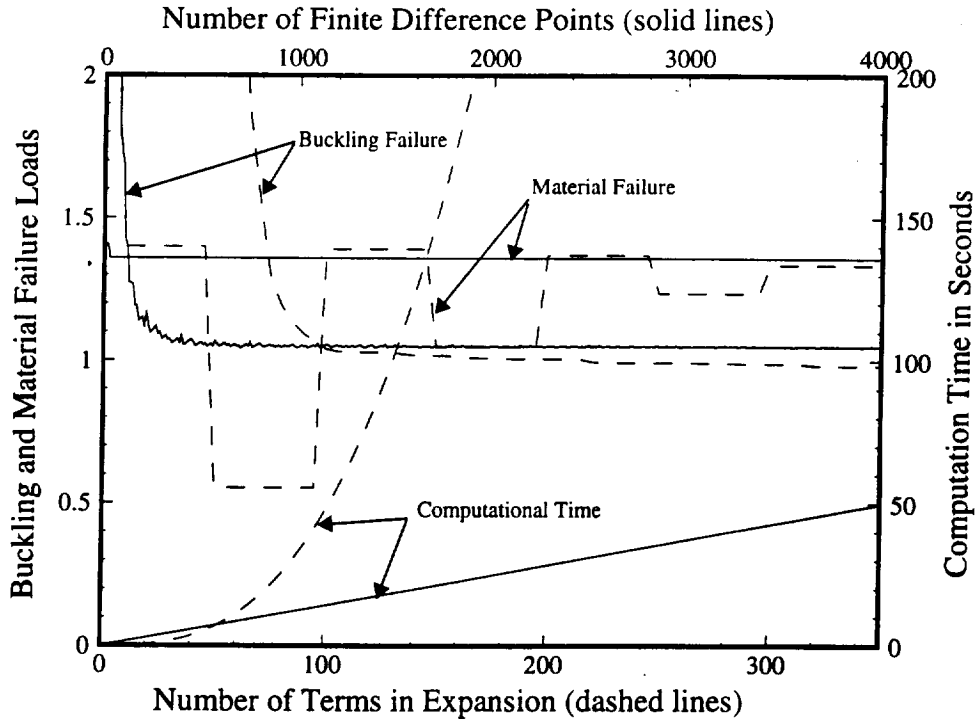


**Figure A.3: Accuracy and Efficiency versus Size Parameter for Numerical Techniques**

cal stiffened cylindrical shell under torsion. The top and bottom axes represent the size parameter  $N$  for the finite difference and Rayleigh-Ritz technique, respectively. Note that the numbering of the axes do not coincide, since each numerical method depends differently on the magnitude of  $N$ . The left axes in Figure A.3 is used to measure the failure loads of the structure, for both buckling and material failure (normalized with respect to the buckling load), while the right axes displays the computation time for each method.

The results from Figure A.3 highlight several key points. Firstly, the two curves that represent the material failure load differ quite substantially. For the finite difference technique, the solution converges quite quickly and accurately even for small values of  $N$ . However, the Rayleigh-Ritz solution exhibits very slow convergence, in fact the plot reveals abrupt changes in the material failure estimation at intervals of  $N = 50$ , with very little agreement to the correct finite difference solution until  $N$  becomes large. The reason for this is due to the fact that the structure under consideration contains fifty evenly spaced longitudinal stiffeners around the circumference of the cyl-

inder. To complete the material failure estimation, an expansion in terms of sines and cosines must be implicitly performed for the stiffness variation to determine the existing stress and strain states resulting from the applied loads. When discrete stiffeners are included, accurate convergence of this expansion may be quite slow, since abrupt changes are notoriously difficult to handle using expansion functions such as these. This is readily apparent in Figure A.3, which reveals that the accuracy and convergence of the expansion solution experiences great changes at fifty point intervals, coinciding with the most significant harmonics for a stiffness variation with fifty stiffeners. Therefore, since stiffeners will be used extensively in this study, the finite difference technique will always be used to estimate material failure.

With regards to the other two relationships compared in Figure A.3, the most significant factor involves the structure of the solution matrix for the eigenvalue calculation. This was briefly discussed earlier, where it was mentioned that the finite difference solution produced a banded, unsymmetric matrix, while the Rayleigh-Ritz technique generated a symmetric matrix that was, in general, not banded. These properties have a direct influence on the accuracy and convergence of the eigenvalue estimation as well as the computational efficiency of the numerical technique. The eigenvalue calculation using the power method involves iteratively factoring the solution matrix until the critical eigenvalue and eigenvector emerge. Thus, the finite difference technique, which produces a banded solution matrix, lends itself to extremely efficient numerical algorithms that increase linearly with respect to the size  $N$  of the matrix. Conversely, the Rayleigh-Ritz technique forms a full matrix that requires much more computational time to factor, even though it is symmetric, and it can be shown that the efficiency varies quadratically with respect to matrix size. These results are reaffirmed in Figure A.3 for both numerical methods. Therefore, since we are using these analysis techniques for rigorous optimization studies, the more efficient finite difference technique is used whenever possible due to its superior numerical efficiency.

Lastly, the numerical results of the buckling failure eigenvalue calculation for the two methods are also shown in Figure A.3. Note that the finite difference technique converges quickly to an asymptote, though the path is not perfectly smooth. The Rayleigh-Ritz solution is much smoother, and the results indicate that the correct eigenvalue is actually somewhat lower than what the finite difference calculation predicts. As explained in Appendix A, the symmetric nature of the solution matrix for the Rayleigh-Ritz method used here guarantees the convergence of the lowest eigenvalue from above, due to the inclusion principle and embedding features of the solution technique. This means that increasing the number of terms in the expansion for the displacements will always yield an improved estimation of the eigenvalue, and that any numerical result is at least an upper bound on the actual eigenvalue. The finite difference technique, however, does *not* produce

a symmetric matrix, therefore these desirable properties of convergence do not apply. Additionally, estimation of derivatives using central difference equations is not considered “exact”, and possible round off errors do exist for this method. These factors lead to the jaggedness of the curve for the eigenvalue estimation in Figure A.3. Furthermore, it can be shown that for non-axial loading (shear and torsion) when using a small value of the axial wavelength parameter  $\beta$ , the finite difference solution matrix is ill conditioned, so that for large values of  $N$  the numerical solution is unstable and often inaccurate. Of course, the test case displayed in Figure A.3 was chosen to exhibit this discrepancy, and for most of this study the loading is such that the finite difference technique generates results that completely agree with the Rayleigh-Ritz eigenvalue calculation. Therefore, though the finite difference technique does suffer some disadvantages for eigenvalue calculations, the numerical efficiency of the method far outweighs the accuracy problems that occur for limited cases, and as such we will employ the finite difference technique for all calculations while keeping in mind the areas where its accuracy may be in question.

This discussion centered around the results of Figure A.3 have demonstrated that, for our purposes, the finite difference technique is more beneficial for our problem than the Rayleigh-Ritz technique. These key points are summarized in Table A.1. It should be noted, however, that the

Numerical Technique	Stiffness Variation	Material Failure	Matrix Structure	Numerical Efficiency	Eigenvalue Analysis
<b>Finite Difference</b>	Converges quickly for all cases	Accurate for abrupt changes	Banded, but unsymmetric	$\propto N$	Inaccurate for non-axial loading with small $\beta$
<b>Rayleigh-Ritz</b>	Slow to converge	Inaccurate for abrupt changes	Full, yet symmetric	$\propto N^2$	Accurate for all cases, but often slow

**Table A.1: Summary of Numerical Technique Comparison**

finite element method actually possesses the advantages of both of these techniques, namely the discretization, bandedness and efficiency of the finite difference technique and the eigenvalue convergence of the Rayleigh-Ritz method. Therefore, future research along these lines should consider using this approach for the numerical solutions.

## A.6 Optimization Techniques

The numerical methods presented in the previous sections of this chapter have dealt exclusively with the numerical solution of the governing equations. Thus the analysis provides estimates of the stiffness, strength, and stability characteristics of a given variable stiffness cylindrical

shell, which can be translated into a suitable “performance” with regards to the application of the structure. However, in the design process, this is merely the first step, for the analysis portion has no ability to recommend possible cylinder designs or to calculate the sensitivity of the response with respect to some design parameter, such as a dimension or the laminate stacking sequence. These aspects of the design process are governed by optimization techniques, which strive to determine the best values of certain design parameters so that the performance of the structure is maximized. Of course, the number of numerical procedures and algorithms that have been developed to solve this optimization problem are vast. Here, we will only attempt to highlight the basic concepts of the optimization tools that are used for our design problems, and refer further inquiry to the text of Haftka and Gürdal<sup>91</sup>. Implementation of the traditional gradient-based techniques was accomplished through the use of ADS, designed by Vanderplaats<sup>92</sup>.

The methods used herein can be divided into two sections, one concerning traditional gradient-based methods and the other describing “genetic algorithms”. Both deal with the solution of the standard optimization problem, which can be expressed as

$$\begin{aligned} &\text{minimize } f(\mathbf{x}) \\ &\text{such that } g_j(\mathbf{x}) \geq 0, \quad j = 1, n_g \\ &\quad \quad \quad h_k(\mathbf{x}) = 0, \quad k = 1, n_e \end{aligned} \tag{A.33}$$

The vector  $\mathbf{x}$  represents the design variables of the system, while  $f$  is defined as the objective function and  $g_j$  and  $h_k$  are the inequality and equality constraints, respectively. The design variables may be either infinitely-valued, which implies continuity throughout the real numbers, or discrete-valued, for which only certain values of the variables are permitted. Examples of discrete variables include ply thicknesses and orientation angles, which may be limited due to manufacturing constraints, and integers representing the number of stiffeners included in the structure. The inequality and equality constraints divide the domain into a feasible and infeasible design space, and the correct solution of the optimization problem results in a vector  $\mathbf{x}$  which generate the minimum value of  $f$  while still being located within this feasible design space. For nonlinear objective functions, many *local* optima may exist which still satisfy all the expressions of Eq. (A.33). However, the goal of the optimization process is to find the actual *global* optimum which achieves the best performance when compared to all other feasible designs. For most optimization techniques, this assurance of global optimality can never be proven, though some techniques (most notably genetic algorithms) strive to attain this demand.

### A.6.1 Gradient-Based Methods

Analytical methods of finding extrema of functions of several variables are often based on

determining where the gradient of the functions is zero, where the constraints may be taken into account by using Lagrange multipliers. For optimization problems, techniques based on this approach are often termed gradient-based, or first-order methods, since they rely on calculating the first derivative of the objective function with respect to each variable. If the objective function and constraints can be expressed in closed form in terms of these design variables, then these methods are quite useful in determining the optimum design. However, for most realistic problems, either the complexity of the objective and constraint function evaluation or the sheer number of unknown design variables warrants a numerical solution for the optimization problem. However, the fundamental theory behind gradient-based methods remains the same, and its basic implementation and inherent shortcomings are illustrated using a simple example.

Consider the optimization problem for a highly nonlinear function of two variables, which is displayed in Figure A.4 through the use of a contour plot for the level curves of the function  $f$ . For

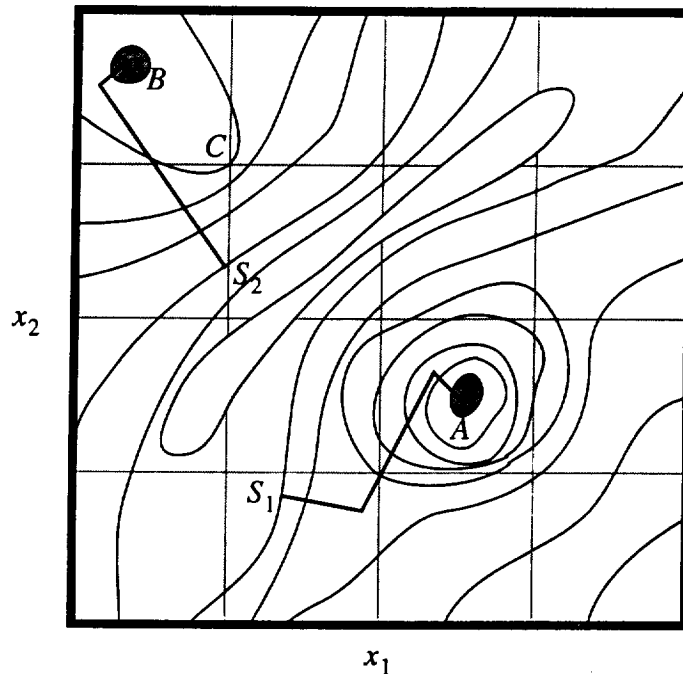


**Figure A.4: Illustration of Optimization Schemes**

clarity, the local minima are shaded dark, while the maximum ridge-like area is lightly shaded. The goal of the optimization problem is to locate the global optimum at point A, found by calculating the values of  $x_1$  and  $x_2$  so that the objective function is a minimum over the given domain. If, for instance, the initial design is chosen at the point  $S_1$ , then the gradient-based techniques will traverse the dark line “downhill” until the correct optimum is attained. Note that the downhill

course is actually made up of successive linear paths, where at the starting point (and each successive point) the direction to move is determined through the evaluation of the gradient, which is perpendicular to the level curves. However, if the initial point is instead chosen to be at  $S_2$ , then the optimization techniques will actually find a local minimum at point  $B$  since the successive gradient directions flow downhill to that location. This possibility of the calculated optimum not being the *lowest* minimum value is a constant source of uncertainty in traditional optimization methods, since for most complex problems the ability to map out the design space and determine where the global minimum is located is impossible. Of course, the optimization technique illustrated in the figure is quite basic. Typical problems also involve highly nonlinear inequality and equality constraints, which even further complicate the design space and the ability to find the optima. Furthermore, the design variables used in this example are assumed to be infinitely valued, such that they are allowed to be any real number in the feasible design space. In many problems, this luxury is not present, perhaps due to manufacturing constraints or the formulation of the problem in terms of integer variables. For example, if the design variables in Figure A.4 are only allowed to attain the values marked by the grid lines, then the optimal solution for these discrete variables is located at point  $C$ . The standard optimization techniques have no ability to find this optimum, therefore some hybrid techniques which can incorporate discrete valued variables must be used.

### A.6.2 Genetic Algorithms

One such technique is based on the concept of natural selection from the theory of evolution, which states that the best designs should evolve from a "survival of the fittest" selection process. The design variables of the problem must be represented as genetic strings, and typical biological functions, such as offspring generation and mutation, recombine the genetic strings of each individual design. The interchange of the genetic information is carried out using probability and random chance based on the fitness of the designs, and new generations are developed using these algorithms until an optimal design is found.

Several advantages of this optimization process exist for structural design problems. Firstly, the translation of the design variables into genetic strings that contain all of the information about the designs is usually accomplished by discretization of the variables. Thus the algorithm actually works best with discrete-valued design variables, therefore the design of stacking sequences with only particular ply thicknesses and orientation angles is perfectly suited for this process. Secondly, the random-based generation of designs is designed to cover the whole design space equally, where the optimal regions of the feasible space are investigated more thoroughly due to the workings of the algorithm. Therefore, the possibility of a the final design being a global opti-



mum is dramatically increased. Furthermore, this method not only produces a “best” design, but also supplies many similar designs with slightly decreased performance but often radically different design parameters. Therefore, the process may discover areas of near-optimality that gradient-based optimization methods would not discover. For example, referring to Figure A.4, if the design variables were discretized so that only the values coinciding with the grid lines were feasible alternatives, the genetic algorithm should find point *C* as the optimal point, but may also reveal that the area around point *A* also contains some meritorious designs.

The major drawback of genetic algorithms is their efficiency. For the random-based searches and probability concepts to prove effective, a large number of designs must be analyzed to ensure convergence. However, the advantages of discrete-valued variables and global optimality are very important for our design problems. This is one of the main reasons that the efficiency of the numerical solution techniques has been stressed so thoroughly - the faster the analysis, the better that the genetic algorithms will perform. For the most part, all of the design studies are completed using the genetic algorithms, even ones with continuous-valued variables. For this case, the genetic algorithm is often used to find viable starting points so that the local optimum found by the gradient-based optimization technique is a probable global solution.

## Appendix B. Stability Equations for Finite Difference Technique

This appendix details the partial differential equations that govern stability of a variable stiffness cylindrical shell, first introduced in Section 2.3.4. Three separate cases are presented, first for the axisymmetric prebuckling solution of a finite length cylinder with an axial stiffness variation, secondly for a short cylinder segment with a linear prebuckling solution and a circumferential stiffness variation, and lastly for an infinite length cylinder with stiffness changing in the circumferential direction that experiences nonlinear beam bending due to the Brazier effect. The detailed equations follow from the specialization of the general stability estimation represented by Eq. (2.106), and are formulated using either the finite difference technique or the Rayleigh-Ritz method, as noted within each section. The particular assumptions and formulations employed for each problem are referenced in the details that follow.

The notation is presented in terms of the differential operators  $d_x$  and  $d_\theta$  as well as primes and dots, which are defined as

$$d_x = ( \cdot ) = R \frac{\partial}{\partial x} \quad d_\theta = ( \cdot )' = \frac{\partial}{\partial \theta} \quad (\text{B.1})$$

and are nondimensional. When placed at the end of an expression (for finite difference formulations), the operator acts on the relevant unknown variable. To make the presentation easier to read, this section does not contain any normalization with respect to classical buckling estimates, though in practice this is performed to improve the performance of the numerical algorithms.

### B.1 Nonlinear Axisymmetric Prebuckling for an Axial Stiffness Variation

The general form of the eigenvalue problem for the stability estimation of an axisymmetric cylinder with an axial stiffness variation using the finite difference technique is represented as

$$\left( \begin{bmatrix} K_s & C \\ -C & K_a \end{bmatrix} + \begin{bmatrix} N_s & S \\ -S & N_a \end{bmatrix} \right) \begin{bmatrix} I \\ II \end{bmatrix} = 0 \quad \begin{aligned} I &\rightarrow \{U_I^i, V_I^i, W_I^i\}^T \\ II &\rightarrow \{U_{II}^i, V_{II}^i, W_{II}^i\}^T \end{aligned} \quad (\text{B.2})$$

The sub-matrices are 3×3 and contain linear operators that act on the modal displacements, repre-

sented by the roman numerals, at each finite difference location  $i$ . The subscripts  $s$  and  $a$  denote slight changes for the terms near the mid-length to account for the symmetric and anti-symmetric conditions for each function, which are not detailed here. The expressions are in terms of the CLT stiffness parameters and the prebuckling quantities, denoted by a 0 subscript, which are functions of  $x$  only. Additionally, the circumferential wavenumber  $n$  is an unknown parameter that must be determined by finding the minimum eigenvalue for all integer values of  $n$ .

The stiffness sub-matrices  $[K]$  and  $[C]$  are detailed first. They only contains stiffness terms and thus do not depend on the value of the applied load. They are represented as:

$$[K] = \begin{bmatrix} k_{11} & k_{12} & k_{13} \\ k_{21} & k_{22} & k_{23} \\ k_{31} & k_{32} & k_{33} \end{bmatrix} \quad [C] = \begin{bmatrix} 0 & 0 & 0 \\ 0 & c_{22} & c_{23} \\ 0 & c_{32} & c_{33} \end{bmatrix} \quad (\text{B.3})$$

The detailed expressions are given below. An overbar denotes some obvious normalization with respect to the cylinder radius for a few quantities to make the notation consistent and concise (for example,  $\bar{D}_{ij} = D_{ij}/R^2$ ,  $\bar{B}_{22} = B_{22}/R$ ,  $\bar{w}_0 = w_0/R$ ).

$$\begin{aligned} k_{11} &= A_{11}d_x^2 + A'_{11}d_x - n^2A_{66} & k_{12} &= n(A_{12} + A_{66})d_x + nA'_{12} \\ k_{13} &= A_{12}d_x + A'_{12} & k_{21} &= n(A_{12} + A_{66})d_x + nA'_{66} \\ k_{22} &= -(A_{66} + \bar{D}_{66})d_x^2 - (A'_{66} + \bar{D}'_{66})d_x + n^2(A_{22} + 2\bar{B}_{22} + \bar{D}_{22}) \\ k_{23} &= -n(\bar{D}_{12} + 2\bar{D}_{66})d_x^2 - 2n\bar{D}'_{66}d_x + n(A_{22} + \bar{B}_{22}) + n^3(\bar{B}_{22} + \bar{D}_{22}) \\ k_{31} &= A_{12}d_x & k_{32} &= -n(\bar{D}_{12} + 2\bar{D}_{66})d_x^2 - 2n(\bar{D}'_{12} + \bar{D}'_{66})d_x - \\ & & & n\bar{D}''_{12} + n(A_{22} + \bar{B}_{22}) + n^3(\bar{B}_{22} + \bar{D}_{22}) \\ k_{33} &= \bar{D}_{11}d_x^4 + 2\bar{D}'_{11}d_x^3 + \bar{D}''_{11}d_x^2 - 2n^2(\bar{D}_{12} + 2\bar{D}_{66})d_x^2 - 2n^2(\bar{D}'_{12} + 2\bar{D}'_{66})d_x - \\ & & & n^2\bar{D}''_{12} + A_{22} + 2n^2\bar{B}_{22} + n^4\bar{D}_{22} \\ c_{22} &= -2n\bar{D}_{26}d_x - n\bar{D}'_{26} & c_{23} &= \bar{D}_{16}d_x^3 + \bar{D}'_{16}d_x^2 - 3n^2\bar{D}_{26}d_x - n^2\bar{D}'_{26} \\ c_{32} &= \bar{D}_{16}d_x^3 + 2\bar{D}'_{16}d_x^2 + \bar{D}''_{16}d_x - 3n^2\bar{D}_{26}d_x - 2n^2\bar{D}'_{26} \\ c_{33} &= 4n\bar{D}_{16}d_x^3 + 6n\bar{D}'_{16}d_x^2 + 2n\bar{D}''_{16}d_x - 4n^3\bar{D}_{26}d_x - 2n^3\bar{D}'_{26} \end{aligned} \quad (\text{B.4})$$

Note that for a constant stiffness variation, both of the matrices are symmetric.

The expressions for the geometric stiffness matrix, or loading matrix, are detailed in a similar manner. The matrices are represented as:

$$[N] = \begin{bmatrix} 0 & n_{12} & n_{13} \\ n_{21} & n_{22} & n_{23} \\ n_{31} & n_{32} & n_{33} \end{bmatrix} \quad [S] = \begin{bmatrix} 0 & 0 & 0 \\ 0 & 0 & s_{23} \\ 0 & s_{32} & s_{33} \end{bmatrix} \quad (\text{B.5})$$

and the related equations are given below.

$$\begin{aligned} n_{12} &= -nA_{66}\bar{w}_0' & n_{13} &= A_{11}\bar{w}_0'd_x^2 + d_x(A_{11}\bar{w}_0')d_x - n^2A_{66}\bar{w}_0' \\ n_{21} &= nA_{66}\bar{w}_0' & n_{22} &= -(pR - N_{\theta_0}) + A_{66}(\bar{w}_0')^2 + d_x(A_{66}\bar{w}_0') \\ n_{23} &= -n(pR - N_{\theta_0}) + n(A_{12} + A_{66})\bar{w}_0'd_x + nA_{66}(\bar{w}_0')^2 + nd_x(A_{66}\bar{w}_0') \\ n_{31} &= -A_{11}\bar{w}_0''d_x & n_{32} &= -n(pR - N_{\theta_0}) - nA_{12}\bar{w}_0'' \\ n_{33} &= -N_{x_0}d_x^2 - (pR - n^2N_{\theta_0}) - A_{11}\bar{w}_0'\bar{w}_0''d_x + A_{12}\bar{w}_0'd_x - A_{12}1\bar{w}_0'' \\ s_{23} &= -N_{x\theta_0}d_x & s_{32} &= -N_{x\theta_0}d_x & s_{33} &= -2nN_{x\theta_0}d_x \end{aligned} \quad (\text{B.6})$$

Note that when prebuckling deformation is included, the system takes the form of a nonlinear eigenvalue problem due to the products of prebuckling rotations and curvatures in the loading matrix. When the classical membrane assumptions are used for the prebuckling solution, all terms in the loading matrix given in Eq. (B.6) are zero except for

$$\begin{aligned} n_{33} &= -N_{x_0}d_x^2 + (n^2 - 1)N_{\theta_0} \\ s_{23} &= -N_{x\theta_0}d_x & s_{32} &= -N_{x\theta_0}d_x & s_{33} &= -2nN_{x\theta_0}d_x \end{aligned} \quad (\text{B.7})$$

Now the eigenvalue problem is linear, and the loading quantities can be divided into a “dead” and “live” portion as suggested in Section 3.3. Finally, it should also be recognized that these equations reduce to the classical estimate for buckling of a constant stiffness laminate using Sanders shell theory if the displacement functions are assumed to vary sinusoidally in the axial direction with frequency  $\beta$ . In fact, this is exactly the formulation used to develop the contour plots and infinite length buckling estimates discussed in the Introduction, Section 1.2.2.

## B.2 Linear Membrane Prebuckling for a Circumferential Stiffness Variation

For this problem, both the finite difference technique and the classical Rayleigh-Ritz method were implemented to find the critical eigenvalue. This was done because the initial solution using

the finite difference technique was inaccurate for some cases (small values of  $\beta$ ), and in the course of determining the cause of the error the Rayleigh-Ritz solution was formulated for comparison (these details are presented in Section A.5). Therefore, the matrix entries for both methods are given here as further means of comparison.

Firstly, the finite difference solution is very similar to the previous one for the axisymmetric problem, though of course the stiffness parameters are now a function of  $\theta$  and the nonlinear and prebuckling deformation terms are removed. Furthermore, instead of the unknown variable  $n$ , the circumferential analysis contains the variable  $\beta$ , which represents the axial frequency of the buckled shape. The displacements are assumed to vary according to Eq. (4.44), which supplies four possible modal displacements and forms an eigensystem given as

$$\left( \begin{bmatrix} K_s & C & 0 & 0 \\ -C & K_a & 0 & 0 \\ 0 & 0 & K_s & C \\ 0 & 0 & -C & K_a \end{bmatrix} + \begin{bmatrix} N_s & S & V_s & M_s \\ -S & N_a & M_a & V_a \\ -V_s & M_a & N_s & S \\ M_s & -V_a & -S & N_a \end{bmatrix}_{dead} \right) \begin{bmatrix} I \\ II \\ III \\ IV \end{bmatrix} = -\Lambda \begin{bmatrix} N_s & S & V_s & M_s \\ -S & N_a & M_a & V_a \\ -V_s & M_a & N_s & S \\ M_s & -V_a & -S & N_a \end{bmatrix}_{live} \begin{bmatrix} I \\ II \\ III \\ IV \end{bmatrix} \quad (B.8)$$

The expressions for the linear operators in the stiffness sub-matrices are given below.

$$\begin{aligned} k_{11} &= -A_{66}d_\theta^2 - \dot{A}_{66}d_\theta + \beta^2 A_{11} & k_{12} &= \beta(A_{12} + A_{66})d_\theta + \beta \dot{A}_{66} \\ k_{13} &= \beta A_{12} + \beta^3 \bar{B}_{11} & k_{21} &= \beta(A_{12} + A_{66})d_\theta + \beta \dot{A}_{12} \\ k_{22} &= (A_{22} + \bar{D}_{22})d_\theta^2 + (\dot{A}_{22} + \dot{\bar{D}}_{22})d_\theta - \beta^2(A_{66} + \bar{D}_{66}) \\ k_{23} &= -\bar{D}_{22}d_\theta^3 - \dot{\bar{D}}_{22}d_\theta^2 + \beta^2(\bar{D}_{12} + 2\bar{D}_{66})d_\theta + \beta^2 \dot{\bar{D}}_{12} + A_{22}d_\theta + \dot{A}_{22} \\ k_{31} &= \beta A_{12} + \beta^3 \bar{B}_{11} & k_{32} &= -\bar{D}_{22}d_\theta^3 - 2\dot{\bar{D}}_{22}d_\theta^2 - \ddot{\bar{D}}_{22}d_\theta + \\ & & & \beta^2(\bar{D}_{12} + 2\bar{D}_{66})d_\theta + 2\beta^2 \dot{\bar{D}}_{66} + A_{22}d_\theta \\ k_{33} &= \bar{D}_{22}d_\theta^4 + 2\dot{\bar{D}}_{22}d_\theta^3 + \ddot{\bar{D}}_{11}d_\theta^2 - 2\beta^2(\bar{D}_{12} + 2\bar{D}_{66})d_\theta^2 - 2\beta^2(\dot{\bar{D}}_{12} + 2\dot{\bar{D}}_{66})d_\theta - \\ & & & \beta^2 \ddot{\bar{D}}_{12} + \beta^4 \bar{D}_{11} + A_{22} \\ c_{22} &= -2\beta \bar{D}_{26}d_\theta - \beta \dot{\bar{D}}_{26} & c_{23} &= -3\beta \bar{D}_{26}d_\theta^2 - 2\beta \dot{\bar{D}}_{26}d_\theta + \beta^3 \bar{D}_{16} \\ c_{32} &= -3\beta \bar{D}_{26}d_\theta^2 - 4\beta \dot{\bar{D}}_{26}d_\theta - \beta \ddot{\bar{D}}_{26} + \beta^3 \bar{D}_{16} \\ c_{33} &= -4\beta \bar{D}_{26}d_\theta^3 - 6\beta \dot{\bar{D}}_{26}d_\theta^2 - 2\beta \ddot{\bar{D}}_{26}d_\theta + 4\beta^3 \bar{D}_{16}d_\theta + 2\beta^3 \dot{\bar{D}}_{16} \end{aligned} \quad (B.9)$$

For the loading matrices of Eq. (B.8), the “dead” and “live” designations refer to predetermined

load levels chosen for each problem. The matrix entries are given below, with their corresponding load cases indicated for each linear operator:

$$\begin{aligned}
 n_{33}(p, \bar{F}, \bar{M}_y) &= \beta^2 N_{x_0} - N_{\theta_0} (1 + d_\theta^2) & m_{33}(\bar{M}_z) &= \beta^2 N_{x_0} \\
 s_{23}(\bar{T}, \bar{V}_y) &= \beta N_{x_{\theta_0}} & s_{32}(\bar{T}, \bar{V}_y) &= -\beta N_{x_{\theta_0}} & s_{33}(\bar{T}, \bar{V}_y) &= 2\beta N_{x_{\theta_0}} d_\theta \\
 v_{23}(\bar{V}_z) &= \beta N_{x_{\theta_0}} & v_{32}(\bar{V}_z) &= -\beta N_{x_{\theta_0}} & v_{33}(\bar{V}_z) &= 2\beta N_{x_{\theta_0}} d_\theta
 \end{aligned} \tag{B.10}$$

For the Rayleigh-Ritz method, integration is performed following the method outlined in Section A.3. The sub-matrices in Eq. (B.8) now represent a summation over all values of  $n$ , which is denoted by the  $ij$  superscripts for each term that is expanded. Also used to save space are four functions that utilize the Fourier expansions for the stiffness and loading terms:

$$\begin{aligned}
 \text{For } E(\theta) &\equiv \sum_{n=0}^{N_{max}} E^n \cos(n\theta) & E^n &= \frac{1}{\pi} \oint E(\theta) \cos(n\theta) d\theta \\
 CC[E^n(i, j)] &= (E^{j-i} + E^{i-j} + E^{i+j} + E^{-i-j})/2 \\
 CS[E^n(i, j)] &= (E^{j-i} + E^{i-j} - E^{i+j} - E^{-i-j})/2 \\
 SC[E^n(i, j)] &= (E^{j-i} - E^{i-j} + E^{i+j} - E^{-i-j})/2 \\
 SS[E^n(i, j)] &= (E^{j-i} - E^{i-j} - E^{i+j} + E^{-i-j})/2
 \end{aligned} \tag{B.11}$$

Then the matrix entries can be calculated utilizing the indexed notation defined in Eq. (A.21) (refer to Section A.3 for more detail). The terms in the stiffness matrix for the symmetric modes *I* and *III* are:

$$\begin{aligned}
 k_{11}^{ij} &= \beta^2 CC(A_{11}) + ij CS(A_{66}) & k_{12}^{ij} &= j\beta CC(A_{12}) + i\beta CS(A_{66}) \\
 k_{13}^{ij} &= \beta CC(A_{12}) + \beta^3 CC(\bar{B}_{11}) & k_{21}^{ij} &= i\beta CC(A_{12}) + i\beta CS(A_{66}) \\
 k_{22}^{ij} &= ij CC(A_{22} + \bar{D}_{22}) + \beta^2 CS(A_{66} + \bar{D}_{66}) \\
 k_{23}^{ij} &= iCC(A_{22} + \beta^2 \bar{D}_{12} + j^2 \bar{D}_{22}) + 2\beta^2 j CS(\bar{D}_{66}) \\
 k_{31}^{ij} &= \beta CC(A_{12}) + \beta^3 CC(\bar{B}_{11}) \\
 k_{32}^{ij} &= jCC(A_{22} + \beta^2 \bar{D}_{12} + j^2 \bar{D}_{22}) + 2\beta^2 i CS(\bar{D}_{66}) \\
 k_{33}^{ij} &= CC(A_{22}) + \beta^4 CC(\bar{D}_{11}) + i^2 j^2 CC(\bar{D}_{22}) + \beta^2 [(i^2 + j^2) CC(\bar{D}_{12}) + 4ij CS(\bar{D}_{66})]
 \end{aligned} \tag{B.12}$$

A simple transformation of  $CC \leftrightarrow CS$  results in the correct expressions for the anti-symmetric modes *II* and *IV*. Note how much simpler the expressions are since the integration could be performed symbolically.

For the coupling stiffness matrix, the matrix entries become:

$$\begin{aligned}
 c_{22}^{ij} &= \beta[iCC(\bar{D}_{26}) + jCS(\bar{D}_{26})] \\
 c_{23}^{ij} &= 2\beta ijCC(\bar{D}_{26}) + \beta j^2CS(\bar{D}_{26}) + \beta^3CS(\bar{D}_{16}) \\
 c_{32}^{ij} &= 2\beta ijCS(\bar{D}_{26}) + \beta i^2CC(\bar{D}_{26}) + \beta^3CC(\bar{D}_{16}) \\
 c_{33}^{ij} &= 2\beta^3[jCC(\bar{D}_{16}) + iCS(\bar{D}_{16})] + 2\beta ij[iCC(\bar{D}_{26}) + jCS(\bar{D}_{26})]
 \end{aligned} \tag{B.13}$$

Finally, the loading matrix is filled by likewise assuming a Fourier expansion of the membrane stress resultants, as per Eq. (B.11). However, since some of the loading is now anti-symmetric about  $\theta = 0$  and  $\theta = \pi$ , a sine expansion must also be performed. These separate expansions are denoted by a  $c$  or  $s$  superscript for the  $N_x$  and  $N_{x\theta}$  stress resultants.

$$\begin{aligned}
 n_{33}^{ij}(p, \bar{F}, \bar{M}_y) &= \beta^2 CC(N_{x_0}^c) + N_{\theta_0} \delta_{ij}[i^2 - (1 + \delta_{0i})] \\
 s_{23}^{ij}(\bar{T}, \bar{V}_y) &= \beta CS(N_{x\theta_0}^c) \quad s_{32}^{ij}(\bar{T}, \bar{V}_y) = \beta CC(N_{x\theta_0}^c) \\
 s_{33}^{ij}(\bar{T}, \bar{V}_y) &= \beta[jCC(N_{x\theta_0}^c) + iCS(N_{x\theta_0}^c)] \\
 m_{33}^{ij}(\bar{M}_z) &= \beta^2 SC(N_{x_0}^s) \\
 v_{23}^{ij}(\bar{V}_z) &= \beta SS(N_{x\theta_0}^s) \quad v_{32}^{ij}(\bar{V}_z) = \beta SC(N_{x\theta_0}^s) \\
 v_{33}^{ij}(\bar{V}_z) &= \beta[jSC(N_{x\theta_0}^s) + iSS(N_{x\theta_0}^s)]
 \end{aligned} \tag{B.14}$$

The global matrices are filled by summing over the  $i$ th row and  $j$ th column and using the previous expression. If anti-symmetric loading is not present, only the first two modes need be considered, which improves the performance time tremendously.

### B.3 Nonlinear Semi-Membrane Prebuckling for an Infinite Length Cylinder

The last specialization involves the nonlinear Brazier solution for an infinite length cylinder. Since the major loading case here is bending, the value of  $\beta$  is necessarily high due to the axial stresses that cause buckling, therefore the more numerically efficient finite difference formulation can be used without loss of accuracy. Due to the complexity of the terms in the stability matrices, the eigenvalue problem is now represented in the most basic form as:

$$\begin{bmatrix} K_s & C \\ -C & K_a \end{bmatrix} \begin{bmatrix} I \\ II \end{bmatrix} = -\Lambda \frac{d}{d\Lambda} \left( \begin{bmatrix} K_s & C \\ -C & K_a \end{bmatrix} \right) \begin{bmatrix} I \\ II \end{bmatrix} \tag{B.15}$$

In practice, the loading matrix is formed by taking a numerical derivative of the stiffness matrix, so that the definition of the stiffness matrices is all that is required here. The equations are derived from the buckling equations, Eq. (5.19)-(5.21), using the assumed form of the displacements defined in Eq. (5.22). Numerous intermediate variables are used since the equations are so complex and unwieldy. For instance, strain and curvature quantities for each mode can be defined in terms of the displacements as:

$$\begin{aligned}\epsilon_{x_I} &= \beta U_I + \bar{\kappa}_y(W_I \cos \theta - V_I \sin \theta) & \epsilon_{\theta_I} &= \cos \omega(\dot{V}_I + W_I) + \sin \omega(V_I - \dot{W}_I) \\ \gamma_{x\theta_I} &= -\dot{U}_I + \beta V_I - \beta \sin \omega W_I & \kappa_{x_I} &= \beta^2 W_I & \kappa_{x\theta_I} &= \beta(V_I - \dot{W}_I) \\ \kappa_{\theta_I} &= (2 + \dot{\omega})[\cos \omega(\dot{V}_I + W_I) + \sin \omega(V_I - \dot{W}_I)] - \cos \omega(W_I + \dot{W}_I)\end{aligned}\quad (\text{B.16})$$

For mode  $II$ , the subscripts are merely interchanged. To develop the buckling equations, the following equations are expanded in terms of the displacement quantities (for  $I \leftrightarrow II$ )

$$\begin{aligned}& \beta A_{11}[\epsilon_{x_I}] + \beta A_{12}[\epsilon_{\theta_I}] + \beta \bar{B}_{11}[\kappa_{x_I}] + d_\theta[A_{66}\gamma_{x\theta_I}] = 0 \\ & -\beta[A_{66}\gamma_{x\theta_I} + \bar{D}_{66}\kappa_{x\theta_I}] + d_\theta[A_{12}\cos \omega \epsilon_{x_I}] + d_\theta[A_{22}\cos \omega \epsilon_{\theta_I}] + \\ & d_\theta[\bar{D}_{12}\cos \omega(2 + \dot{\omega})\kappa_{x_I}] + d_\theta[\bar{D}_{22}\cos \omega(2 + \dot{\omega})\kappa_{\theta_I}] + A_{11}\bar{\kappa}_y \sin \theta[\epsilon_{x_I}] + \\ & A_{12}\bar{\kappa}_y \sin \theta[\epsilon_{\theta_I}] + \bar{B}_{11}\bar{\kappa}_y \sin \theta[\kappa_{x_I}] - A_{12}\sin \omega[\epsilon_{x_I}] - A_{22}\sin \omega[\epsilon_{\theta_I}] - \\ & \bar{D}_{12}\sin \omega(2 + \dot{\omega})\kappa_{x_I} - \bar{D}_{22}\sin \omega(2 + \dot{\omega})\kappa_{\theta_I} + (pR - N_{\theta_0} - \bar{M}_{\theta_0})(V_I - \dot{W}_I) + \\ & N_{\theta_0}(\dot{V}_I + W_I) + \bar{M}_{\theta_0}(2\dot{V}_I + W_I - \dot{W}_I) + (-1)^I\{\beta \bar{D}_{16}\kappa_{x_{II}} + \beta \bar{D}_{26}\kappa_{\theta_{II}} + \\ & d_\theta[\bar{D}_{26}\cos \omega(2 + \dot{\omega})\kappa_{x\theta_{II}}] - \bar{D}_{26}\sin \omega(2 + \dot{\omega})\kappa_{x\theta_{II}}\} = 0 \\ & \beta^2 \bar{D}_{11}[\kappa_{x_I}] + \beta^2 \bar{D}_{12}[\kappa_{\theta_I}] + \beta^2 \bar{B}_{11}[\epsilon_{x_I}] + 2\beta d_\theta[\bar{D}_{66}\kappa_{x\theta_I}] - d_\theta^2[\bar{D}_{12}\cos \omega \kappa_{x_I}] - \\ & d_\theta^2[\bar{D}_{22}\cos \omega \kappa_{\theta_I}] - d_\theta^2[\bar{M}_{\theta_0}(\dot{V}_I + W_I)] + d_\theta[A_{12}\sin \omega \epsilon_{x_I}] + d_\theta[A_{22}\sin \omega \epsilon_{\theta_I}] + \\ & d_\theta[\bar{D}_{12}\sin \omega(2 + \dot{\omega})\kappa_{x_I}] + d_\theta[\bar{D}_{22}\sin \omega(2 + \dot{\omega})\kappa_{\theta_I}] + A_{11}\bar{\kappa}_y \cos \theta[\epsilon_{x_I}] + \\ & A_{12}\bar{\kappa}_y \cos \theta[\epsilon_{\theta_I}] + \bar{B}_{11}\bar{\kappa}_y \cos \theta[\kappa_{x_I}] - \beta^2 N_{x_0} W_I + A_{12}\cos \omega[\epsilon_{x_I}] + A_{22}\cos \omega[\epsilon_{\theta_I}] + \\ & \bar{D}_{12}\cos \omega(1 + \dot{\omega})[\kappa_{x_I}] + \bar{D}_{22}\cos \omega(1 + \dot{\omega})[\kappa_{\theta_I}] - (pR - N_{\theta_0})(\dot{V}_I + W_I) + \\ & \bar{M}_{\theta_0}(\dot{V}_I - \dot{W}_I) + d_\theta[(N_{\theta_0} + 2\bar{M}_{\theta_0})(V_I - \dot{W}_I)] - \beta A_{66}\sin \omega[\gamma_{x\theta_I}] + \\ & (-1)^I\{\beta^2 \bar{D}_{16}[\kappa_{x\theta_{II}}] - 2\beta d_\theta[\bar{D}_{16}\kappa_{x_{II}}] - 2\beta d_\theta[\bar{D}_{26}\kappa_{\theta_{II}}] - d_\theta^2[\bar{D}_{26}\cos \omega \kappa_{x\theta_{II}}] + \\ & d_\theta[\bar{D}_{26}\sin \omega(2 + \dot{\omega})\kappa_{x\theta_{II}}] + \bar{D}_{26}\cos \omega(1 + \dot{\omega})[\kappa_{x\theta_{II}}]\} = 0\end{aligned}\quad (\text{B.17})$$



## Appendix C. Material Data

The material data used in this study is listed here for both isotropic and orthotropic materials.

Material Designation	Aluminum 2024-T3	Aluminum 7075-T6
Elastic Modulus, $E$ (psi)	$10.5 \times 10^6$	$10.7 \times 10^6$
Poissons ratio, $\nu$	0.33	0.33
Density, $\rho$ (lbs/in <sup>3</sup> )	0.100	0.101
Yield Stress, $S$ (psi)	$25.0 \times 10^3$	$36.5 \times 10^3$

**Table C.1: Isotropic Material Properties**

For the two laminates listed below, effective moduli and failure stresses are determined and then averaged over the thickness of the laminate, which is defined by the ply thickness in the table.

Material Designation	Graphite-Epoxy	$[\pm 45/0/90]_S$	$[\pm 45/0]_S$
Elastic Moduli, $E_1$ (psi)	$18.5 \times 10^6$	$7.42 \times 10^6$	$8.25 \times 10^6$
Elastic Moduli, $E_2$ (psi)	$1.64 \times 10^6$	$7.42 \times 10^6$	$3.73 \times 10^6$
Poissons ratio, $\nu_{12}$	0.3	0.3	0.67
Shear Modulus, $G_{12}$ (psi)	$0.87 \times 10^6$	$2.85 \times 10^6$	$3.51 \times 10^6$
Ply Thickness, $t_{ply}$ (inches)	0.005	0.04	0.03
Density, $\rho$ (lbs/in <sup>3</sup> )	0.057	0.057	0.057
Fiber Failure Stress, $X_t$ (psi)	$211. \times 10^3$	$30.1 \times 10^3$	$78.3 \times 10^3$
$X_c$ (psi)	$-204. \times 10^3$	$-81.9 \times 10^3$	$-78.3 \times 10^3$
Transverse Failure Stress, $Y_t$ (psi)	$6.1 \times 10^3$	$30.1 \times 10^3$	$15.1 \times 10^3$
$Y_c$ (psi)	$-21.4 \times 10^3$	$-81.9 \times 10^3$	$-45.4 \times 10^3$
Shear Failure Stress, $S$ (psi)	$13.8 \times 10^3$	$30.0 \times 10^3$	$37.0 \times 10^3$

**Table C.2: Orthotropic Material Properties**

